



Delft University of Technology

## Self-folding metabiomaterials

van Manen, T.

### DOI

[10.4233/uuid:c9185b1c-6f29-4bee-ab43-f59c72facdd5](https://doi.org/10.4233/uuid:c9185b1c-6f29-4bee-ab43-f59c72facdd5)

### Publication date

2022

### Document Version

Final published version

### Citation (APA)

van Manen, T. (2022). *Self-folding metabiomaterials*. [Dissertation (TU Delft), Delft University of Technology]. <https://doi.org/10.4233/uuid:c9185b1c-6f29-4bee-ab43-f59c72facdd5>

### Important note

To cite this publication, please use the final published version (if applicable).  
Please check the document version above.

### Copyright

Other than for strictly personal use, it is not permitted to download, forward or distribute the text or part of it, without the consent of the author(s) and/or copyright holder(s), unless the work is under an open content license such as Creative Commons.

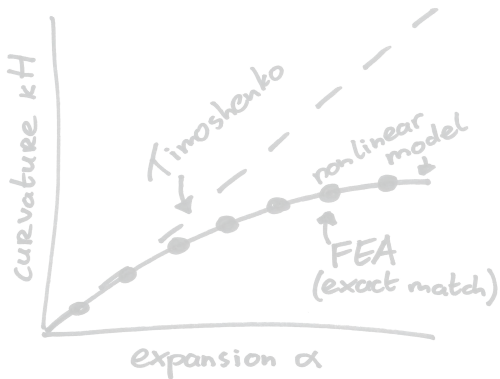
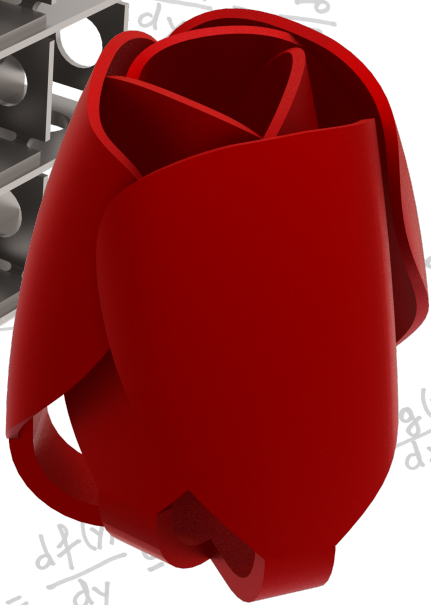
### Takedown policy

Please contact us and provide details if you believe this document breaches copyrights.  
We will remove access to the work immediately and investigate your claim.

# SELF-FOLDING METABIOMATERIALS

SELF-FOLDING METABIOMATERIALS

TEUNIS VAN MANEN

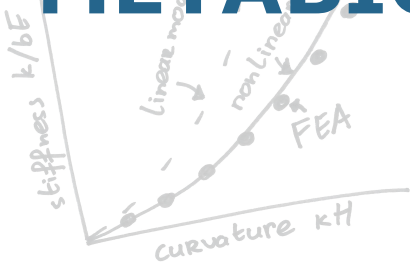


$$\vartheta = g(y)$$
$$\beta = \frac{h_2}{h_1}$$
$$\lambda \vartheta = r \frac{d\vartheta}{dx} = f(y) \frac{dg(x)}{dx} = \frac{2\vartheta r}{L_0}$$

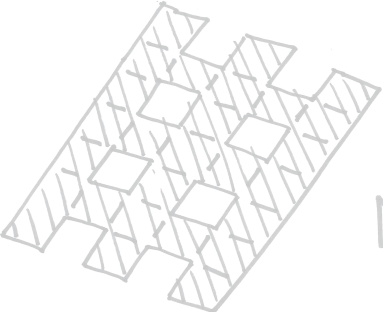
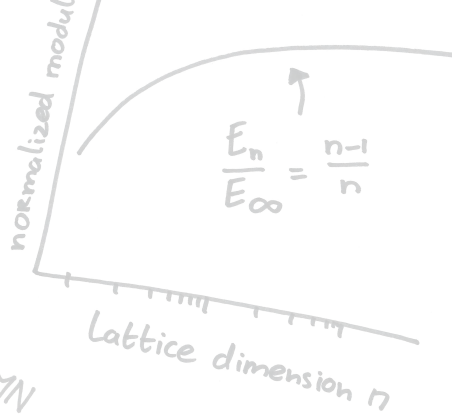
$$E_n = k_n \frac{h}{A} = \frac{n(n-1)}{n} \frac{n}{n^2} k = \frac{n-1}{n^2} k$$



$$r = f(x)$$
$$\alpha L, \beta h = \frac{1}{2} (r_0^2 - r_m^2)$$

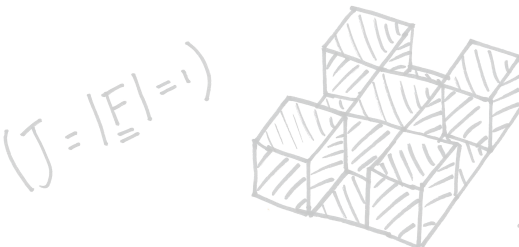


$$\gamma = \frac{G_2}{G_1}$$



$$M(\vartheta = \pm \bar{\vartheta}) = \int r \vartheta dr = \int_{r_1}^{r_2} \vartheta r dr + \int_{r_2}^{r_3} \vartheta r dr = 0$$

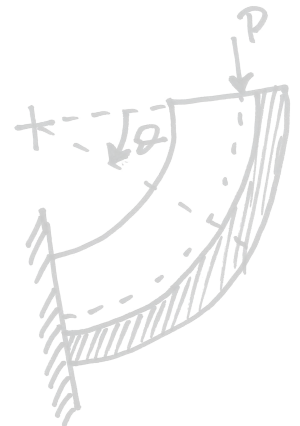
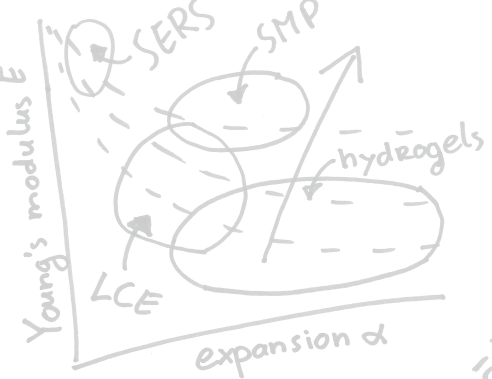
$$P(r) = \frac{G}{2} (r^2 - r_0^2) + C$$



$$(J = |F| = 1)$$

$$\frac{df(y)}{dy} f(y) \frac{dg(x)}{dx} = 1$$

$$L_1 h = \bar{\vartheta} (r_m^2 - r_i^2)$$



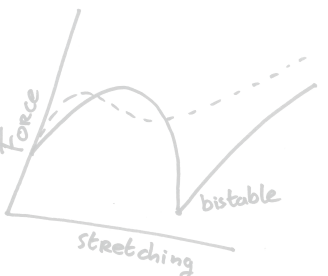
$$M(\vartheta) = P r_c (1 - \cos \vartheta)$$

$$N(\vartheta) = P \cos \vartheta$$

TU Delft



$$N(\vartheta = \pm \bar{\vartheta}) = \int \vartheta r dr$$



$$f'''' + \left[\frac{2}{r}\right] f''' - \left[n^2 a^2 r^2 + \frac{1}{r^2}\right] f'' + \left[\frac{3}{r^3} + 3n^2 a^2 r\right] f' + \left[\frac{3}{r^4} + n^2 a^4\right] (n^2 - 1) f = 0$$

TEUNIS VAN MANEN





# **Self-folding meta-biomaterials**



# Self-folding meta-biomaterials

## DISSERTATION

for the purpose of obtaining the degree of doctor  
at Delft University of Technology  
by the authority of the Rector Magnificus prof.dr.ir. T.H.J.J. van der Hagen  
chair of the Board for Doctorates  
to be defended publicly on  
30 November at 12:30 o'clock

By

TEUNIS VAN MANEN

Master of Science in Mechanical Engineering and BioMedical Engineering,  
Delft University of Technology, the Netherlands,  
born in Veenendaal, the Netherlands





This dissertation has been approved by the promotor.

Composition of the doctoral committee:

Rector Magnificus,	chairperson
Prof. dr. A.A. Zadpoor,	Delft University of Technology, promotor

*Independent members:*

Prof. dr. M.L. van Hecke	Leiden University
Prof. C.A. Dransfeld	Delft University of Technology
Prof. dr. ir. J.L. Herder	Delft University of Technology
Prof. dr. ir. H. Vallery	Delft University of Technology

*Keywords:* Self-folding, shape-shifting, 4D printing, metabiomaterials,

*Cover design:* The author

*Printed by:* Gildeprint.

The research leading to these results has received funding from the European Research Council under ERC grant agreement no. [677575].

Copyright © 2022 by T. van Manen

ISBN #####

An electronic version of this thesis is available at <http://repository.tudelft.nl/>





# Abstract

An important goal of bone tissue engineering is the development of synthetic bio-scaffolds that would eliminate the need for bone transplantation, also known as bone grafting. Bone grafting is associated with some serious limitations such, as morbidity at the donor-site and shortage of donor tissue. Therefore, scientist have been trying to develop synthetic bone substituting materials that serve as a platform for the regeneration of tissue. Despite all the effort made towards that goal, no perfect alternative has been developed yet.

The formulated requirements for the fabrication of bone scaffolds raise a serious challenge towards the development of such synthetic biomaterials. In order to mimic the structure of living bony tissue, scaffolds need to be composed of a large number of small, interconnected unit-cells, thereby providing a large surface area for cell attachment and tissue ingrowth. In addition, the mechanical properties of the scaffold should match those of the native bone tissue. A too high stiffness could lead to stress shielding and associated implant loosening while a weak scaffold offers a limited load-bearing capacity. Finally, synthetic biomaterials need to be biocompatible.

This thesis presents a number of strategies for the development of synthetic bone scaffolds using shape-shifting techniques. As compared with alternative approaches, such as additive manufacturing, self-folding materials allow for the employment of planar fabrication techniques to embed the initially flat material with a variety of surface-related functionalities. Examples of such surface-features are bactericidal or osteogenic nano-patterns. Upon activation, the initially flat construct folds to create complex 3D constructs with embedded surface-features, which are highly beneficial in the context of porous biomaterials.



The first two chapters of this thesis are related to fundamental aspects of shape-shifting materials. More specifically, in Chapter 2, we reviewed the different mechanisms for the programming of shape-shifting within flat materials. In addition, we describe the development of analytical and computational models to study the theoretical stiffness limits of self-folding hinges (Chapter 3). We found a maximum effective stiffness of 1.5 GPa for shape-memory polymers self-folding elements.

In the second part of this thesis, we present the development of three different shape-shifting techniques. The first technique is based on the 4D printing of shape-memory polymer materials. During the extrusion of the filaments, the polymers chains align along the printing direction. This deformation is then stored as memory inside the structure of the material. Heating the as-printed construct allows for the relaxation of the programmed stress. Based on the alignment of the extruded filaments, different shape-shifting behaviors can be programmed. Both the fabrication of 2D-to-3D shape-shifting materials (Chapter 4) as well the production of deployable materials and devices (i.e., 3D-to-3D shape shifting) (Chapter 5) was studied.

In Chapter 6, we focus on the development of a purely mechanical shape-shifting method. By incorporating different kirigami patterns within the material, large amounts of elastic and permanent deformations can be programmed upon stretching the material. Subsequent release of the pre-stretch allows for the recovery of the elastic deformations, driving the shape-shifting of the material. The main advantage of such a mechanical approach is that it could be applied to many different materials.

The third shape-shifting technique is inspired by sheet metal forming processes (Chapter 7). Miniaturized automated folding devices were developed for the folding of cubic lattice structures. As a demonstration, metamaterials comprising 125 cubic unit-cells with a unit-cell dimension of 2.0 mm were fabricated. In contrast to conventional self-folding methods, sharp folds can be realized in metal sheets using the presented approach. Therefore, metamaterials with a high stiffness can be folded. In addition, a variety of surface-patterns can be incorporated into the initially flat sheets. Protected by a thin layer of coating, the applied surface-related functionalities remain undamaged during the folding process. Finally, a series of cell culture experiments were performed to demonstrate the ability of the folded functionalized materials to serve as a tissue engineering scaffold.

In general, the presented shape-shifting techniques are of relevance to a variety of applications, such as optical metamaterials and 3D electronics. However, the specific aim of this thesis is the development of self-folding materials that can be applied as tissue engineering scaffolds. Considering the listed requirements, the

folding technique inspired by sheet metal forming meet the necessary requirements the best. However, additional research towards further miniaturization of the scaffolds resulting from different methods as well as an increase in their stiffness are required for application in clinical settings. In the case of the automatically folded scaffolds, the initial cell culture experiments showed promising results and the proposed folding method can, indeed, serve as a platform for further biological testing.



# Samenvatting

Een belangrijk doel van het onderzoek naar het kweken van botweefsel is de ontwikkeling van kunstmatige structuren die het transplanteren van botweefsel overbodig maakt. Er zijn namelijk enkele serieuze nadelen verbonden aan het uitvoeren van bottransplantaties zoals weefsel sterfte op de donorplaats en de beperkte beschikbaarheid van donor weefsel. Om deze reden proberen wetenschappers al langere tijd om kunstmatige structuren te ontwikkelen als vervanging van botweefsel. Deze kunstmatige materialen zouden dan moeten functioneren als een support structuur voor de regeneratie van botweefsel. Ondanks alle inspanningen is er echter nog geen perfect alternatief ontwikkeld.

De gestelde eisen aan de productie van kunstmatige biomaterialen leveren een serieuze uitdaging op. Om de structuur van botweefsel het beste na te bootsen moeten deze kunstmatige materialen bestaan uit een groot aantal kleine en onderling verbonden eenheidscellen. Op deze manier ontstaat een groot oppervlakte waarop cellen kunnen hechten en botweefsel kan ingroeien. Daarnaast moeten de mechanische eigenschappen van deze poreuze biomaterialen overeenkomen met de stijfheid van natuurlijk botweefsel. Een te hoge stijfheid kan leiden tot 'stress shielding' en als gevolg daarvan tot het loskomen van het botimplantaat. Aan de andere kant verminderd een te zwak implantaat het draagvermogen. Tenslotte moeten kunstmatige biomaterialen ook biocompatibel zijn.

Dit proefschrift presenteert een aantal strategieën voor de ontwikkeling van kunstmatige botimplantaten die gebruikmaken van zelf vervormende materialen. In vergelijking met alternatieve technieken, zoals bijvoorbeeld 3D printen, maken zelf vouwende materialen het mogelijk om gebruik te maken van 2D productie methoden om het aanvankelijk vlakke materiaal oppervlak te integreren met een verscheidenheid aan oppervlakte-gerelateerde functionaliteiten. Voorbeelden van dergelijke oppervlakte functionaliteiten zijn bacteriedodende of osteogene nanopatronen. Bij activatie vouwt het vlakke materiaal tot een complexe 3D geometrie met geïntegreerde oppervlakte functionaliteiten die veel voordelen kunnen bieden in de context van poreuze biomaterialen.



De eerste twee hoofdstukken van dit proefschrift zijn gericht op een aantal fundamentele aspecten van zelf vouwende materialen. Meer specifiek, in Hoofdstuk 2 bieden we een overzicht van de verschillende mechanismen die gebruikt kunnen worden voor het programmeren van vorm veranderingen in vlakke materialen. Daarnaast beschrijven we de ontwikkeling van analytische en numerieke modellen voor het bestuderen van de theoretische stijfheid grenzen van zelf vouwende scharnieren (Hoofdstuk 3). We hebben een maximale effectieve stijfheid van 1.5 GPa gevonden voor zelf vouwende structuren gemaakt van polymeren met vormgeheugen.

In het tweede deel van de proefschrift presenteren we de ontwikkeling van drie verschillende vorm verandering technieken. De eerste techniek is gebaseerd op het 4D printen van polymeren met vormgeheugen. Tijdens de extrusie van het filament lijnen de polymeerketens uit in de print richting. Deze vervormingen worden dan opgeslagen als geheugen in de materiaalstructuur. Opwarming van de geprinte structuur zorgt ervoor dat de geprogrammeerde spanningen kunnen relaxeren. Afhankelijk van de print richting kunnen verschillende vorm veranderingen geprogrammeerd worden. Zowel de productie van 2D naar 3D vorm veranderende materialen (Hoofdstuk 4) als de productie van uitklapbare materialen en apparaten (d.w.z. 3D naar 3D vorm veranderingen) (Hoofdstuk 5) werd onderzocht.

In Hoofdstuk 6 focussen we op de ontwikkeling van een puur mechanische zelf vouw methode. Door middel van het opnemen van verschillende kirigami patronen in het materiaal kunnen grote elastische en permanente vervormingen gerealiseerd worden tijdens het uitrekken van het materiaal. Het vervolgens loslaten van deze voorspanningen leidt tot herstel van de elastische vervormingen wat de drijvende kracht is voor de vorm veranderingen in het materiaal. Het grote voordeel van een dergelijke mechanische benadering is dat het toegepast kan worden bij veel verschillende soorten materialen.

De derde vorm verandering techniek is geïnspireerd op plaatwerk vervormingstechnieken (Hoofdstuk 7). Geminiaturiseerde zetbankjes werden ontwikkeld voor het automatisch vouwen van kubusvormige raster structuren. Als demonstratie, werden metamaterialen bestaande uit 125 kubusvormige eenheidscellen met een eenheidscel afmeting van 2.0 mm gefabriceerd. In tegenstelling tot conventionele vorm verandering methoden kunnen met de beschreven aanpak scherpe vouwen gerealiseerd worden in metaal plaatwerk. Om deze reden kunnen metamaterialen met een hoge stijfheid gevouwen worden. Daarnaast kan er een breed scala aan oppervlakte patronen geïntegreerd worden in het in eerste instantie vlakke materiaal. Beschermd door een dunne laag coating blijven de op de oppervlakte aangebrachte functionaliteiten intact tijdens het vouw proces. Tenslotte zijn er serie celkweek experimenten uitgevoerd als demonstratie van de mogelijkheid om de gevouwen gefunctionaliseerde

metamaterialen te gebruiken als support structuur voor de regeneratie van weefsel.

In het algemeen zijn de beschreven vorm verandering technieken relevant voor een verscheidenheid aan toepassingen zoals optische metamaterialen en 3D elektronica. Echter, het specifieke doel van dit proefschrift is het ontwikkelen van zelf vouwende materialen die toegepast kunnen worden als support structuur voor botweefsel regeneratie. Gezien de gestelde eisen, voldoet de vouw techniek geïnspireerd op plaatwerk vervormingstechnieken het beste aan de vereisten. Meer onderzoek gericht op zowel een verdere miniaturisering van de gevouwen structuren als een toename in stijfheid zijn nodig voor het toepassen van gevouwen botimplantaten in een klinische omgeving. In het geval van de automatisch gevouwen support structuren (Hoofdstuk 7) laten de eerste celkweek experimenten veelbelovende resultaten zien en de beschreven vouwtechniek kan gebruikt worden als platform voor verdere biologische testen.



# Table of content

	Summary	vii
	Samenvatting	xi
<b>1</b>	Introduction	1
<b>2</b>	Programming the shape-shifting of flat soft matter <i>Materials Today (2018)</i>	11
<b>3</b>	Theoretical stiffness limits of 4D printed self-folding metamaterials <i>Communications Materials (2022)</i>	55
<b>4</b>	Programming 2D/3D shape-shifting with hobbyist 3D printers <i>Materials Horizons (2017)</i>	89
<b>5</b>	4D printing of reconfigurable metamaterials and devices <i>Communications Materials (2021)</i>	109
<b>6</b>	Kirigami-enabled self-folding origami <i>Materials Today (2020)</i>	133
<b>7</b>	Automated folding of origami lattices: from nanopatterned sheets to stiff meta biomaterials <i>Small (2022)</i>	153
<b>8</b>	Outlook and conclusions	177
	Acknowledgements	189
	List of publications	193





# Introduction **1**

## 1.1 Self-folding

Folding is a well-known method for the fabrication of a large variety of objects. Examples range from folding a piece of paper into an airplane to the process of sheet metal forming in which functional parts are manufactured from flat sheets of metal. The art of paper folding, also known as origami, dates back to >1000 years ago. Origami artists have been continuously seeking to push the boundaries of what is possible to fold from a sheet of paper. Folding can also be observed in nature across a wide range of length-scales. One example at the molecular level is the folding of DNA [1, 2]. At the tissue level, the folding phenomenon can be seen in different plants, such as the tulip or *mimosa pudica* (Figure 1.1a) [3, 4]. The unfolding of tree leaves is another well-known example [5].

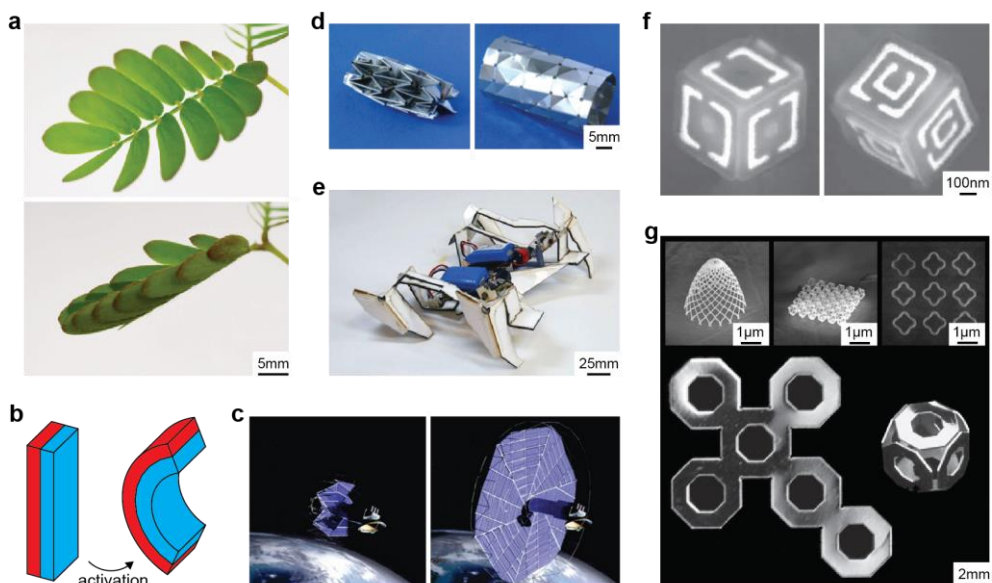
Both inspired by nature as well as the work of origami artists, scientists began to study the folding behavior of synthetic materials. One area of research is the development of techniques for the automation of the folding process. The so-called self-folding materials have been developed that can change their shape in response to certain triggering stimuli [6, 7]. The working principle of such self-folding structures may be based on different physical phenomena [6, 8, 9]. However, the most common method for the fabrication of self-folding structures is through the use of stimuli-responsive materials. These are materials that significantly change their dimensions when, for example, exposed to heat or moisture [8, 10]. Self-folding constructs can be fabricated by smart arrangements of active and passive materials. Upon the activation of these active elements, stress gradients will be generated that are eventually released through geometrical changes. One well-known example of such a shape-shifting structure is the bimorph actuator [11]. By combining two layers of material that show different amounts of expansion or shrinkage in response to a certain stimulus, the bilayer element bends (Figure 1.1b).

Self-folding materials have numerous attractive properties that are interesting for engineering applications. First of all, shape-shifting techniques can be used for the deployment of initially compact structures into large functional objects. Examples include the unfolding of solar arrays in space or the deployment of cardiovascular stents (Figure 1.1c-d) [12, 13]. The ability to program well-prescribed motions within a structure is another interesting property of shape-shifting materials. Utilizing this capability has resulted in the development of self-folding robots and biomedical drugs delivery systems (Figure 1.1e) [14-16]. Thirdly, self-folding materials can be used for the fabrication of three-dimensional objects from initially flat sheets [17-20]. The main advantage of such an approach is that planar fabrication techniques can be used both for the production of the self-folding structure as well as for incorporating surface features into the initially flat specimen (Figure 1.1f-g). Within the context of this thesis, we are particularly interested in the fabrication of self-folding bio-scaffolds with embedded

geometrical features that, for instance, stimulate tissue regeneration [21] or kill bacteria [22], as discussed in the next section.

## 1.2. Bone substituting materials

Regenerative medicine is an area of research that tries to regenerate damaged tissues or organs. Bone tissue engineering is considered to be an important sub-field of regenerative medicine not least because of the increasing incidence of major bone defects worldwide [23, 24]. For many years, bone transplantation, also known as bone grafting, was the ‘golden standard’ for the treatment of large bone defects. However, bone grafts suffer from some serious limitations, such as the shortage of donor tissue and the morbidity of the donor-site [23, 25]. The goal of tissue engineering is to resolve the issues associated with bone grafts by combining techniques that are primarily rooted in biomaterials and cell biology. For example, bio-scaffolds may be used that serve as a platform for cell attachment and subsequent tissue formation.



**Figure 1.1:** Self-folding examples both found in nature and in engineering applications. (a) The opening and closing of the *Mimosa pudica*'s leaflets. Reproduced from [4]. (b) A schematic drawing illustrating the self-folding of a bilayer specimen made of an expanding (red) and a passive layer (blue). (c) A computer-generated illustration of the deployment of an array of solar panels. Reproduced from [12] (d) Deployment of an origami stent [13]. Reproduced from [26]. (e) A fully functioning walking robot with a body folded from an initially flat sheet. Reproduced from [14]. (f) Self-folding cubes patterned with optical features. Reproduced from [17] (g) A folded origami structure embedded with a variety of surface ornaments. Reproduced from [19].

The requirements for bone substituting materials present some serious challenges for material designers. First and foremost, any type of synthetic support material needs to be biocompatible [27, 28]. Additionally, a scaffold needs to be composed of a large array of small interconnected unit cells in order to provide a large surface area for cell attachment, support cell migration, and tissue ingrowth while maintaining the permeability of the construct [28]. Next, the possibility for the surface to undergo surface treatment is of major importance because it allows for the incorporation of a variety of surface-related functionalities. Examples include geometrical features that promote cell growth or modifications to the surface chemistry to enhance cell adhesion [22, 29, 30]. Furthermore, the mechanical properties of the scaffold itself should ideally match those of the surrounding bone tissue. Especially in the case of load-bearing implants, a certain minimal stiffness (and strength) is required to maintain functionality. On the other hand, greatly exceeding the stiffness of the adjacent bone could lead to phenomena, such as stress shielding resulting in the weakening of the surrounding bone tissue [28, 31, 32]. Finally, it should be possible to physically realize scaffolds that fulfil all of these requirements.

### 1.3. Thesis aim

The combined list of requirements for the design of bio-scaffolds represents a significant challenge towards the development of synthetic bone substituting materials. The question we ask ourselves here is that whether the concept of self-folding materials is the answer to these challenges. While shape-shifting materials offer several advantages for the fabrication of such highly complex porous structures with embedded surface features, such an approach often leads to severe restrictions regarding the type of the materials that can be applied, because there is a need for at least one type of stimuli-responsive materials. In addition, it is unclear whether or not it is possible to achieve sufficiently high stiffness values when working with self-folding materials that at the same time need to be flexible in order to accommodate folding. Finally, the local control of the material behavior is of major importance for achieving a large complexity in the shape-shifting patterns. What production techniques need to be used for the fabrication of such complex self-folding materials with spatially varying properties?

The goal of this thesis is to answer these questions with the aim of *developing a shape-shifting platform for the production of synthetic bone substituting materials*. The ability to fabricate a bone scaffold embedded with highly detailed surface features allows for the biological testing and validation of the effects of surface functionalization. In summary, the central themes of this thesis is the development of shape-shifting techniques that:

1. enable the production of self-folding materials with spatially varying properties.
2. enable the self-folding of a large variety of (engineering) materials.
3. are able to fabricate large arrays of interconnected unit cells.
4. result in stiff self-folded structures.

## 1.4. Thesis outline

This thesis is structured in line with the presented research objectives. Each chapter is related to one or more of these objectives. Within this thesis, the development of several shape-shifting techniques is described. The presented methods are supported by theoretical, numerical, and experimental results.

**Chapter 2** starts by reviewing the different strategies that could be used for the programming of the shape-shifting behavior of initially flat materials. The focus of this chapter is on the different deformation mechanisms of shape-shifting from a mechanical viewpoint. These principles could be applied to different material combinations regardless of the type of the material or the activation stimulus.

Towards the development of stiff shape-shifting materials, in **Chapter 3** we search for the theoretical stiffness limits of self-folding lattices. While there exist various shape-shifting mechanisms (see **Chapter 2**), in this chapter, we focus on the most common method of using bilayer shape-shifting elements for the folding of lattices from flat sheets. Both the bending of bilayer elements as well as the resulting stiffness of the bended specimens are studied using finite element analysis and finite-deformation analytical models. Combining the bending and stiffness models allows for optimizing the design of self-folding elements in order to maximize the stiffness of the resulting curved bilayers. With the optimized designs of bilayer elements, the theoretical stiffness limits for the different types of stimuli-responsive materials are determined.

Additive manufacturing of stimuli-responsive materials, so-called 4D printing, is a recent developed approach for fabrication of shape-shifting specimens [33, 34]. In general, 3D printing allows for the spatial control of material deposition which enables the fabrication of complex structures in a single production step. In **Chapter 4 and 5** we address the first research objective by developing a novel 4D printing method for the fabrication of shape-memory polymer shape-shifting materials. The different deformation mechanisms reported in **Chapter 2** are applied for the programming of a wide range of different geometries within the as-printed structure. While **Chapter 4** covers the programming of 2D to 3D self-folding constructs, **Chapter 5** goes further and proposes a technique for the fabrication of 3D-to-3D shape-shifting materials.

**Chapter 6** is primarily focused on the second research objective. Because most shape-shifting techniques are related to a specific combination of (stimuli-responsive) materials, the wide-spread application of these techniques remains a challenge. Here, we report a purely mechanical method for the fabrication of self-folding elements, which could be applied to many different combinations of metallic and polymeric materials.

Building on the idea of using a mechanically activated self-folding technique, in **Chapter 7** proposes a production method that also meets the research objectives 3 and 4. The shape-shifting method presented in this chapter is inspired by sheet metal forming techniques. We report the development of external folding devices for the automated folding of lattice structures. One concern regarding such an approach is that the initial flat material is in physical contact with the folding devices during the process of folding, which potentially leads to damaging of the applied surface functionalities. Therefore, a method is developed to protect the embedded surface features. Finally, cell culture experiments are performed to demonstrate the osteogenic behavior of the functionalized lattice structures made from initially flat titanium sheets.

**Chapter 8** concludes this thesis by not only summarizing the main findings of the presented research but also briefly discussing the presented results in the context of the more general directions of relevant research. Furthermore, this chapter suggests a number of directions for future research.

## Bibliography

1. Dey, S., et al., *DNA origami*. Nature Reviews Methods Primers, 2021. **1**(1): p. 1-24.
2. Saccà, B. and C.M. Niemeyer, *DNA origami: the art of folding DNA*. Angewandte Chemie International Edition, 2012. **51**(1): p. 58-66.
3. Azad, A.K., et al., *Phosphorylation of plasma membrane aquaporin regulates temperature-dependent opening of tulip petals*. Plant and Cell Physiology, 2004. **45**(5): p. 608-617.
4. Wong, W.S., et al., *Mimosa Origami: A nanostructure-enabled directional self-organization regime of materials*. Science advances, 2016. **2**(6): p. e1600417.
5. Kobayashi, H., B. Kresling, and J.F. Vincent, *The geometry of unfolding tree leaves*. Proceedings of the Royal Society of London. Series B: Biological Sciences, 1998. **265**(1391): p. 147-154.
6. van Manen, T., S. Janbaz, and A.A. Zadpoor, *Programming the shape-shifting of flat soft matter*. Materials Today, 2018. **21**(2): p. 144-163.
7. Zhang, Y., et al., *Printing, folding and assembly methods for forming 3D mesostructures in advanced materials*. Nature Reviews Materials, 2017. **2**(4): p. 1-17.
8. Ionov, L., *Polymeric actuators*. Langmuir, 2015. **31**(18): p. 5015-5024.
9. Liu, Y., J. Genzer, and M.D. Dickey, "2D or not 2D": *Shape-programming polymer sheets*. Progress in Polymer Science, 2016. **52**: p. 79-106.
10. Gracias, D.H., *Stimuli responsive self-folding using thin polymer films*. Current Opinion in Chemical Engineering, 2013. **2**(1): p. 112-119.
11. Timoshenko, S., *Analysis of bi-metal thermostats*. Josa, 1925. **11**(3): p. 233-255.
12. Zirbel, S.A., et al., *Accommodating thickness in origami-based deployable arrays*. Journal of Mechanical Design, 2013. **135**(11).
13. Kuribayashi, K., et al., *Self-deployable origami stent grafts as a biomedical application of Ni-rich TiNi shape memory alloy foil*. Materials Science and Engineering: A, 2006. **419**(1-2): p. 131-137.
14. Felton, S., et al., *A method for building self-folding machines*. Science, 2014. **345**(6197): p. 644-646.
15. Fernandes, R. and D.H. Gracias, *Self-folding polymeric containers for encapsulation and delivery of drugs*. Advanced drug delivery reviews, 2012. **64**(14): p. 1579-1589.
16. Randall, C.L., E. Gultepe, and D.H. Gracias, *Self-folding devices and materials for biomedical applications*. Trends in biotechnology, 2012. **30**(3): p. 138-146.
17. Cho, J.-H., et al., *Nanoscale origami for 3D optics*. Small, 2011. **7**(14): p. 1943-1948.
18. Jamal, M., A.M. Zarafshar, and D.H. Gracias, *Differentially photo-crosslinked polymers enable self-assembling microfluidics*. Nature communications, 2011. **2**(1): p. 1-6.
19. Janbaz, S., et al., *Origami lattices with free-form surface ornaments*. Science advances, 2017. **3**(11): p. eaao1595.
20. van Manen, T., et al., *Kirigami-enabled self-folding origami*. Materials Today, 2020. **32**: p. 59-67.
21. Jamal, M., et al., *Directed growth of fibroblasts into three dimensional micropatterned geometries via self-assembling scaffolds*. Biomaterials, 2010. **31**(7): p. 1683-1690.
22. Modaresifar, K., et al., *Bactericidal effects of nanopatterns: A systematic review*. Acta biomaterialia, 2019. **83**: p. 29-36.
23. Amini, A.R., C.T. Laurencin, and S.P. Nukavarapu, *Bone tissue engineering: recent advances and challenges*. Critical Reviews™ in Biomedical Engineering, 2012. **40**(5).
24. Baroli, B., *From natural bone grafts to tissue engineering therapeutics: brainstorming on pharmaceutical formulative requirements and challenges*. Journal of pharmaceutical sciences, 2009. **98**(4): p. 1317-1375.



25. Laurencin, C., Y. Khan, and S.F. El-Amin, *Bone graft substitutes*. Expert review of medical devices, 2006. **3**(1): p. 49-57.
26. Lang, R.J., *The science of origami*. Physics world, 2007. **20**(2): p. 30.
27. Burg, K.J., S. Porter, and J.F. Kellam, *Biomaterial developments for bone tissue engineering*. Biomaterials, 2000. **21**(23): p. 2347-2359.
28. Koons, G.L., M. Diba, and A.G. Mikos, *Materials design for bone-tissue engineering*. Nature Reviews Materials, 2020. **5**(8): p. 584-603.
29. Modaresifar, K., et al., *On the Use of Black Ti as a Bone Substituting Biomaterial: Behind the Scenes of Dual-Functionality*. Small, 2021: p. 2100706.
30. Ma, Z., Z. Mao, and C. Gao, *Surface modification and property analysis of biomedical polymers used for tissue engineering*. Colloids and Surfaces B: Biointerfaces, 2007. **60**(2): p. 137-157.
31. Takizawa, T., et al., *Titanium fiber plates for bone tissue repair*. Advanced Materials, 2018. **30**(4): p. 1703608.
32. Kolken, H.M., et al., *Rationally designed meta-implants: a combination of auxetic and conventional meta-biomaterials*. Materials Horizons, 2018. **5**(1): p. 28-35.
33. Raviv, D., et al., *Active printed materials for complex self-evolving deformations*. Scientific reports, 2014. **4**(1): p. 1-8.
34. Tibbits, S., *4D printing: multi-material shape change*. Architectural Design, 2014. **84**(1): p. 116-121.





## Programming the shape-shifting of flat soft matter

# 2

Shape-shifting of flat materials into the desired 3D configuration is an alternative design route for fabrication of complex 3D shapes, which provides many benefits such as access to the flat material surface and the ability to produce well-described motions. The advanced production techniques that primarily work in 2D could then be used to add complex surface features to the flat material. The combination of complex 3D shapes and surface-related functionalities has a wide range of applications in biotechnology, actuators/sensors, and engineering of complex meta-materials. Here, we categorize the different programming strategies that could be used for planning the shape-shifting of soft matter based on the type of stresses generated inside the flat material and present an overview of the ways those mechanisms could be used to achieve the desired 3D shapes. Stress gradients through the thickness of the material, which generate out-of-plane bending moments, and compressive in-plane stresses that result in out-of-plane buckling constitute the major mechanisms through which shape-shifting of the flat matter could be programmed. We review both programming strategies with a focus on the underlying physical principles, which are highly scalable and could be applied to other structures and materials. The techniques used for programming the time sequence of shape-shifting are discussed as well. Such types of so-called “sequential” shape-shifting enable achieving more complex 3D shapes, as the kinematics of the movements could be planned in time to avoid collisions. Ultimately, we discuss what 3D shapes could be achieved through shape-shifting from flat soft matter and identify multiple areas of application.

T. van Manen, S. Janbaz & A.A. Zadpoor (2018). *Programming the shape-shifting of flat soft matter*. *Materials Today*, **21**(2), 144-163

## 2.1. Introduction

Shape-shifting of initially flat materials into programmed 3D configurations is an emerging area of research that holds a lot of promise for development of complex materials with unprecedented functionalities and properties. A wide range of shape-shifting phenomena are seen in nature and often originate from the spatial arrangement of the structural elements and their differential responses to the different types of stimuli. For example, dimensional transformation of active elements in response to external stimuli could activate the process of change in the shape of materials such as what pine cone [5, 6] and *Mimosa Pudica* [9] show via the evolution in their extracellular systems. Inspired by nature, synthetic materials have been developed that show highly complex shape transformations once triggered by certain stimuli. Combined with surface-induced functionalities, shape-shifting materials could present functionalities that are unique and relevant for multiple areas of application.

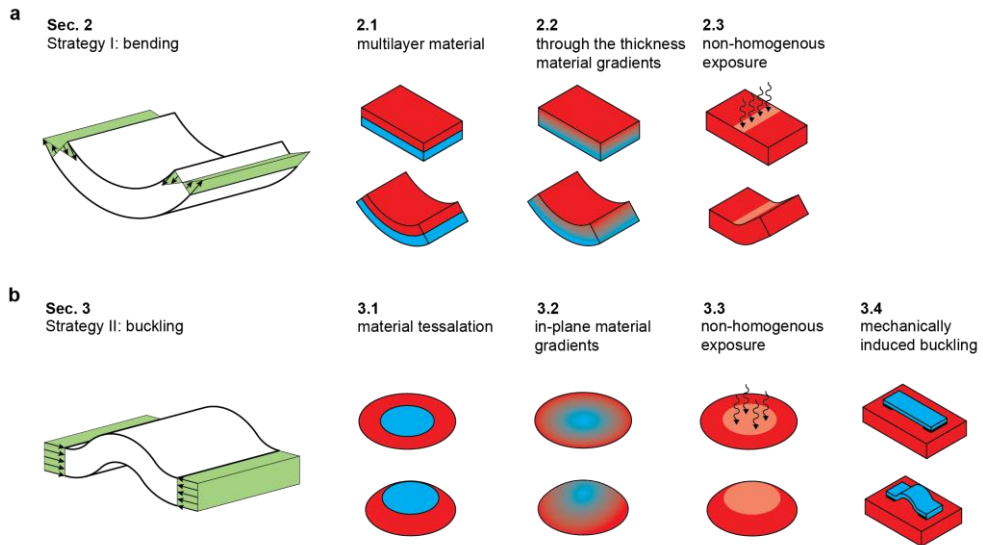
Shape-shifting in synthetic materials may be based on different physical principles such as capillary forces, residual stresses, or the energy released from active polymers [11]. Such active materials may respond to stimuli [11] such as light [13, 14], humidity [15], temperature [16], or pH [17], among others. Three main classes of stimuli-responsive polymers have been used in shape-shifting materials [18] and will be shortly introduced here. First, the swelling/de-swelling of polymer gels has been widely used as a driving force for changing the shape of materials. In response to different stimuli such as temperature or pH, the water uptake inside the crosslinked network could be changed, resulting in reversible volumetric expansion or shrinkage [18, 19]. Large swelling ratios up to four orders of magnitude could be obtained, although a large swelling ratio is often linked to a reduced stiffness [20]. However, most hydrogels have limited mechanical properties (*i.e.*  $E < 0.5$  MPa) [21], while the response time is long as compared to other active materials (*i.e.* up to several hours for material thickness of 1 mm) [22]. Many swellable polymers have good biocompatibility as well as biodegradability, which make them suitable materials for biomedical applications [23, 24]. The second class of active polymers are liquid crystalline elastomers (LCE). LCE materials are composed of a liquid crystalline material aligned inside a polymeric network [25, 26]. Because of the anisotropic alignment of those molecules, the material stiffness along the alignment direction is larger than those along other directions. Upon activation by different stimuli such as temperature or humidity, the material alignment order will decrease, resulting in highly anisotropic dimensional changes. In contrast to most swellable polymers, the response time of LCE is much shorter [26]. A third widely reported class of active materials are shape memory polymers, which exhibit the ability to store a temporary shape inside the structure of the material [27, 28]. By increasing the temperature above glass transition temperature,  $T_g$ , the material softens and can easily be deformed. After reducing the temperature below  $T_g$ , this temporary

shape will be stored as memory inside the material. Upon activation by different stimuli such as high temperature or light, the relaxation of the polymer results in recovery of the permanent shape. SMP materials exhibits good mechanical properties, although the material stiffness drops dramatically at high temperatures [29]. The main drawback of using SMP as active material is that the dimensional changes are irreversible. Moreover, the material response has to be first programmed inside the material. For a more comprehensive and in-depth review of the structure and functionalities of those and other stimuli responsive materials, the interested reader is referred to other excellent review papers [19, 26, 27].

In this paper, we review the strategies that could be used to program the shape-shifting of flat soft matter into complex 3D shapes driven by the mechanical forces induced in those active materials. Since many of the presented strategies are based on general physical principles, they could be applied regardless of the type of polymeric materials and the stimulus. Readers interested in the underlying molecular mechanisms or shape-shifting in the broader context of formation of 3D constructs are referred to other recently published reviews [11, 22, 30]. Here, we focus on the different deformation mechanisms of shape-shifting of flat soft matter from a mechanical point of view, which could serve as a guide for the rational design of shape-shifting materials.

Let us consider a slender (i.e. small thickness as compared to other dimensions) elastic body incorporating a number of active and passive elements. The deformation of such a body could be approximated using the Kirchhoff-Love assumptions [31, 32]. In this approach, the deformation of the slender body is represented by the deformation of the mid-plane consisting of the changes in the planar dimensions and curvature. The elastic energy of the plate could therefore be written as the sum of a stretching term and a bending-related term. Once triggered by the activation stimulus, both bending moments and axial forces may be generated, respectively inducing out-of-plane bending (Figure 2.1a) and out-of-plane buckling (Figure 2.1b). Creating those two types of forces are the main working principles on which the programming strategies are usually based. Both out-of-plane bending moments and axial (compressive) forces could create the out-of-plane deformations that are required for transforming the shape of a flat material to complex 3D shapes.

It is obvious why an out-of-plane bending moment will cause out-of-plane deformation. The required bending moment is often generated by inducing a gradient in the planar stresses along the thickness of the material upon activation. Different strategies may be used to program such a material response to an activation stimulus (Figure 2.1a). In the following chapter of the paper, we have categorized the reported strategies into three major categories.



**Figure 2.1:** Two different strategies for programming 2D/3D shape-shifting. (a) By generating a stress gradient along the thickness of the material, a bending moment may be generated resulting in out-of-plane bending. The different approaches have been divided into three sub-categories. (b) Compressive stresses may induce out-of-plane buckling. Four different categories have been identified within the buckling strategy.

As for the (compressive) axial forces, the material will first exhibit a pure stretching state upon activation. Since stretching energy scales linearly with the material thickness while the bending energy has a cubic dependency on the thickness, a bending configuration is energetically favorable over pure stretching for thin constructs [33]. Compressive stresses above a certain critical value will therefore induce out-of-plane buckling of the flat structure, thereby minimizing the elastic energy (Figure 2.1b). Different techniques to program the generation of compressive stresses will be reviewed in the third chapter of the paper.

We will discuss both types of the programming strategies with a focus on the mechanics of deformation and the parameters used to program and control the deformations. In addition to the final shape, the material could be programmed to undergo a specified sequence of deformations over time, thereby achieving more complex shapes. That type of so-called “sequential” shape-shifting will be discussed in the fourth chapter of this paper.

## 2.2. Bending strategy

As previously stated, a stress gradient along the thickness of the material is required for generating the bending moment. Various approaches comprising different stimuli-responsive materials have been used in the literature for creating the stress gradient, which will be discussed in this chapter.

### 2.2.1. Multilayer

A widely applied strategy for generating the bending moments is to combine two layers of different materials into a bilayer construct (Figure 2.1a). The swelling/shrinkage mismatch between both layers in response to activation stimuli, while sustaining the same strain at the interface between both layers, could result in different types of deformation. Dependent on the layer thicknesses and the induced strain, both surface wrinkling or bending may be programmed [34]. For example, surface wrinkling may be generated due to the compressive stresses applied on a thin stiff top layer by a thick soft substrate, while global bending could arise in bilayers with comparable stiffness and layer thickness. Here, only out-of-plane bending will be considered. Upon activation, the deformation of the main straining layer is constrained by the second layer and therefor one layer is loaded in tension while compressive stresses are observed in the other layer. The generated bending moment results in global bending of the constructs, thereby (partially) releasing those internal stresses. The general theory of bilayers, developed by Timoshenko [35], states that a bilayer made of two materials with different thermal expansion coefficients result in a uniform curvature, which is inversely proportional to the thickness. The normalized curvature  $\tilde{\kappa}$  can be expressed as

$$\tilde{\kappa} = \frac{\kappa h}{\Delta\alpha} = \frac{6(1+m)^2}{3(1+m)^2 + (1+mn)\left(m^2 + \frac{1}{mn}\right)} \quad (2.1)$$

where bilayer  $\kappa$  is curvature,  $h$  is thickness,  $\Delta\alpha$  is the mismatch in the thermal expansion coefficients,  $n$  is the stiffness ratio of both layers and  $m$  is the thickness ratio of both layers. Figure 2.2a depicts the dependency of the normalized bilayer curvature on the thickness ratio of layers and material stiffness ratio. A maximum value of 1.5 is found for the normalized curvature. Although this theory is derived for bi-metallic strips with small thicknesses (*i.e.*  $h \ll L$ ), its general concept is applicable also to predict the behavior of polymeric materials with different activation mechanisms [30]. In this section, we will discuss structures comprising multiple isotropic material layers as well as multilayer constructs with anisotropic material properties.

### Isotropic multiplayers

Isotropic swelling/de-swelling of polymers has been reported in many studies as the activation mechanism to drive the bending of bilayer constructs [36-46]. Guan et al. fabricated slender bilayer strips (95 x 20 x 4.8  $\mu\text{m}$ ) from hydrogels with different amounts of swelling using a soft lithography production process [38]. The curvature of the bilayer strip could be controlled based on the swelling ratios, which originate from different polymer compositions. Keeping the thickness ratio between the active and passive layers around 15, a reduction in the radius of curvature from 80  $\mu\text{m}$  to 30  $\mu\text{m}$  could be achieved based on an increase in the



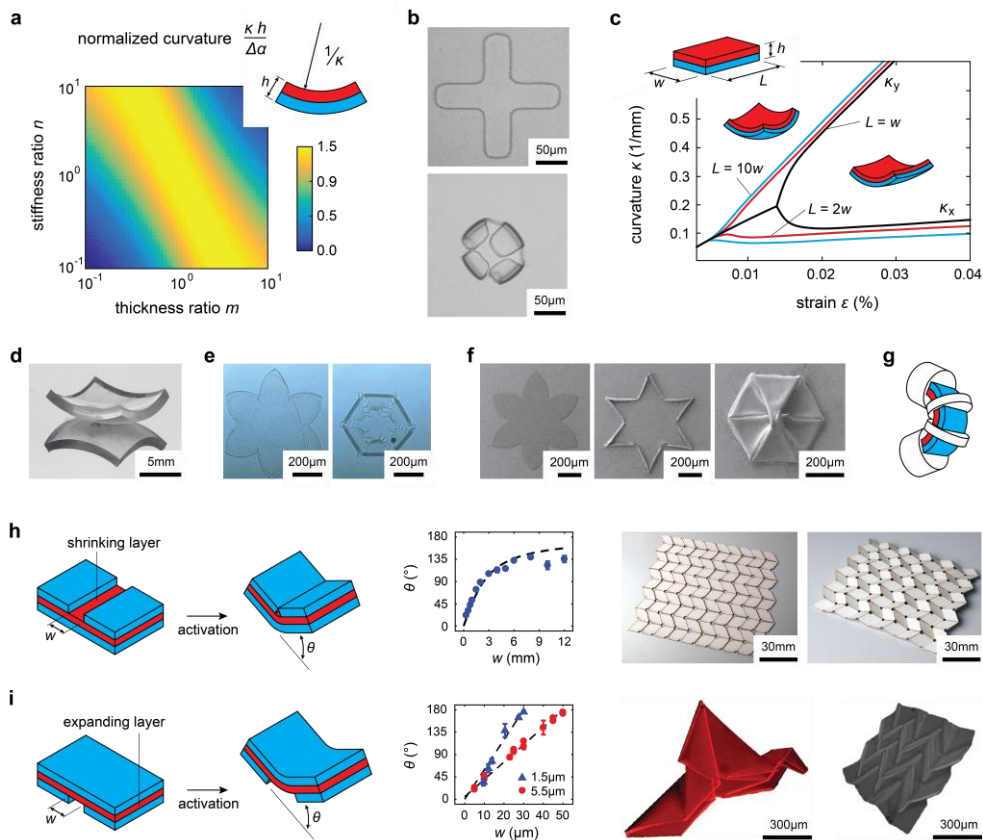
swelling ratio from 15% to 42%. Due to the increase in the swelling ratio, a larger bending moment could be generated, resulting in a larger curvature. More complex 3D microstructures could be made by different combinations of bilayers strips (Figure 2b). The effects of layer thickness on the radius of curvature is experimentally studied by Egunov et al. by varying the thickness ratio between 1/3 and 4, while keeping the thickness of the passive layer constant around 0.32 mm [37]. As the bending stiffness has a cubic dependency on the thickness, while the generated bending moment increases only quadratically with the thickness, the bilayer curvature reduces as the thickness increases. For thickness ratios close to 1, the results were in good agreement with the Timoshenko's bilayer theory and a normalized curvature of about 1.5 was achieved. In accordance to the results of Guan et al. and the general theory of bilayers, a linear relationship between the radius of curvature and swelling ratio is found [37, 38]. The other parameter influencing the radius of curvature is the material stiffness ratio, as it adjusts the resistance of the bilayer against deformation [47]. It is important to realize that swelling may strongly affect the stiffness of the active layer. In general, the thickness ratio has a stronger effect on the radius of curvature as compared with that of the stiffness ratio.

Timoshenko's bilayer theory is essentially a 2D model. Other parameters related to the 3D geometry of the actual structures, which are not captured by that theory, could influence the deformation characteristics. Both theoretical and experimental studies about bilayers of isotropic elastic materials show that the flat material adopts a double-curved shape for a small strain mismatch [37, 48-56]. For a larger strain mismatch, the resulting shape approximates a single-curve, as the in-plane stretching required for a double-curved shape is formidably high. The high levels of required in-plane strains could be seen when one tries to wrap a plastic sheet around a sphere. Rolling in one direction therefore becomes energetically favorable for strain mismatches exceeding a certain threshold (Figure 2.2c) [37, 48, 50-55]. This bifurcation from double-curvature to a major single curvature mode depends on both geometrical parameters (e.g. bilayer sheet dimensions [37, 42, 48, 50, 52, 54] and layer thicknesses [39, 51, 55]) and material properties (e.g. stiffness ratio [54, 55]), which all affect the balance between stretching and bending energies. For example, a rectangular bilayer with an aspect ratio of 1 and relatively large thickness compared with its other dimensions adopts a spherical shape (Figure 2.2d). Larger samples with the same thickness resulted in cylindrical shapes [37]. The rolling direction of the single curvature mode is determined by the aspect ratio (i.e. the ratio between the strip width and length) of the bilayers [48]. Unconstrained bilayer strips preferably curve along the shortest direction [48], which is in agreement with the observations reported by Guan et al [38]. Numerical investigation of shape-shifting for different shapes of flat bilayers showed that the geometry highly influences the curvature direction as well [57]. A star-shaped polymeric bilayer produced by the deposition of a 4  $\mu\text{m}$  layer of passive polymer on top of a thermo-

responsive swellable polymer with equal thickness has been proposed for reversible encapsulation and release of cells (Figure 2.2e) [40]. The isotropic swelling of the active layer in an aqueous environment in response to temperature changes resulted in the bending of the star arms towards each other.

Controlling the diffusion pattern of water into the swellable polymeric bilayer could be used to program the activation pattern [41, 43]. A star-like bilayer of active and passive polymer produced based on the deposition of active and passive layers on top of a flat silicon substrate has been used to restrict the diffusion directions [41]. The water could only diffuse inside the active layer from the edges, which results in the deformation being dependent on the outer contour of the initially flat bilayer. Because of the small bilayer thickness ( $< 1.5 \mu\text{m}$ ), rolled tubes with small radii of curvature will form along the perimeter of the bilayer followed by bending of the arms at the intersection of adjacent tubes (Figure 2.2f). In contrast to unconstrained bilayers, the edge-activation and the adhesion of the polymer to the substrate cause the bilayer to preferably curve along the longest direction [58].

Multi-material 3D printing provides additional freedom to program the printed construct through spatial arrangement of the active and passive materials. Raviv et al. printed bilayer structures with an isotropic swellable layer and a passive soft polymer layer [59, 60]. In-series arrangement of bending bilayers and passive disks, which act as stoppers, have been proposed to control the level of deformation. The folding angle could then be set by changing the distance between the passive disks (Figure 2.2g). An in-plane arrangement of active architected elements could then form a planar grid-like structure, which could produce curved structures upon activation. The same principle of using end-stops has been also applied in multiple trilayer structures as a technique to control the amount of deformation [61-69]. By sandwiching a shrinking layer between two structural layers, the deformation of the active layer is constrained, while small gaps in one of the structural layers allow for local bending (Figure 2.2h). By applying a global stimulus, the generated stress in the active layer is locally transformed into a bending moment, resulting in bending along the folding lines. Self-folding of origami structures have been reported based on the rational patterning of hinge gaps on both structural layers of a sandwich material with a heat-shrink polymer core [67, 69]. The edges of the gaps in the structural layers act as mechanical stoppers and allow for programming the desired folding angle by adjusting the gap width [67, 69]. Accurately control of folding angles up to about  $120^\circ$  has been reported (Figure 2.2h) [69]. A swelling polymer, upon increase of humidity, has been also used as the active material to fold origami structures at microscale [70, 71]. By adjusting the gap width in one of the structural layers the length of the remaining bilayer could be set resulting in a linear relation between gap width and folding angle (Figure 2.2i). Folding angles ranging from  $0$  up to  $180^\circ$  have been reported [71].



**Figure 2.2:** (a) The normalized curvature of bilayer samples according to the Timoshenko's theory. (b) Shape-shifting of a cross-shaped bilayer into a 3D constructs. Reproduced with permission from [38]. Copyright 2005 by the American Chemical Society. (c) The two principal curvatures of rectangular isotropic bilayer samples as a function of the strain mismatch between both layers. Two regimes with different deformation modes are shown for a bilayer with a thickness of 145 nm. Adapted with permission from [48]. Copyright 2011 by the American Chemical Society. (d) A double-curved bilayer sample photographed on a reflective surface. Reproduced from [37] with permission from The Royal Society of Chemistry. (e) The curving of a star-shaped bilayer construct. Reproduced from [40] with permission from The Royal Society of Chemistry. (f) Two-step folding of a star-shaped bilayer specimen [41]. Copyright 2013 by John Wiley & Sons, Inc. Reproduced by permission of John Wiley & Sons, Inc. (g) Schematic illustration of using passive disks to control the folding angle. (h) Trilayer constructs with a heat-shrinking core. The dashed line indicates the expected folding angle as a function of the gap width. Experimental results are indicated with blue dots [69]. Reproduced by permission of IOP Publishing. (i) Trilayer samples with a swelling core. The linear dependency of the folding angle on the gap width has been verified by experiments using different thicknesses of the expanding core [71]. Copyright 2015 by John Wiley & Sons, Inc. Reproduced by permission of John Wiley & Sons, Inc.

### Anisotropic multilayers

In order to program more complex shape transformations, one additional programming parameter could be included in the form of anisotropic material properties. By inducing stresses only in the desired direction, the deformation characteristics (e.g. the direction of rolling) could be decoupled from the geometry of the initially flat material (e.g. aspect ratio or outer contour) [72]. Self-helixing elements have been fabricated using a (mainly) uniaxial expanding/shrinking active layer for a nonzero angle  $\varphi$  between the main straining direction of the active layer and the main axis of the bilayer strip (Figure 2.3a) [73, 74]. Inspired by the opening of chiral seed pods, not only self-bending and self-helixing bilayers but also self-twisting strips could be made through combining two similar anisotropic active layers with main straining directions that are perpendicular to each other (Figure 2.3b) [1, 10, 75, 76]. Dependent on the dimensionless strip width  $\tilde{w} = w\sqrt{\kappa_0/t}$ , twisting or helixing will be the dominant deformation mode, where  $w$  is the strip width,  $t$  is the bilayer thickness, and  $\kappa_0$  is the reference curvature (i.e. the curvature induced along the main straining direction, Figure 2.3b). The twisting mode is dominated by in-plane stretching, while bending is dominant in helixing bilayers [1, 75, 77]. By increasing the widths of self-twisting samples, the stretching energy increases very rapidly while the bending energy of helixing constructs is only linearly related to the sample width [75, 77]. Twisting is therefore energetically favorable for small widths, while self-helixing strips will be formed for  $\tilde{w} \gg 1$ . Based on the angle  $\varphi$  and the strip width  $w$ , both self-helixing and self-twisting could be programmed with different values of radius  $r$  and pitch  $p$  (Figure 2.3c) [1].

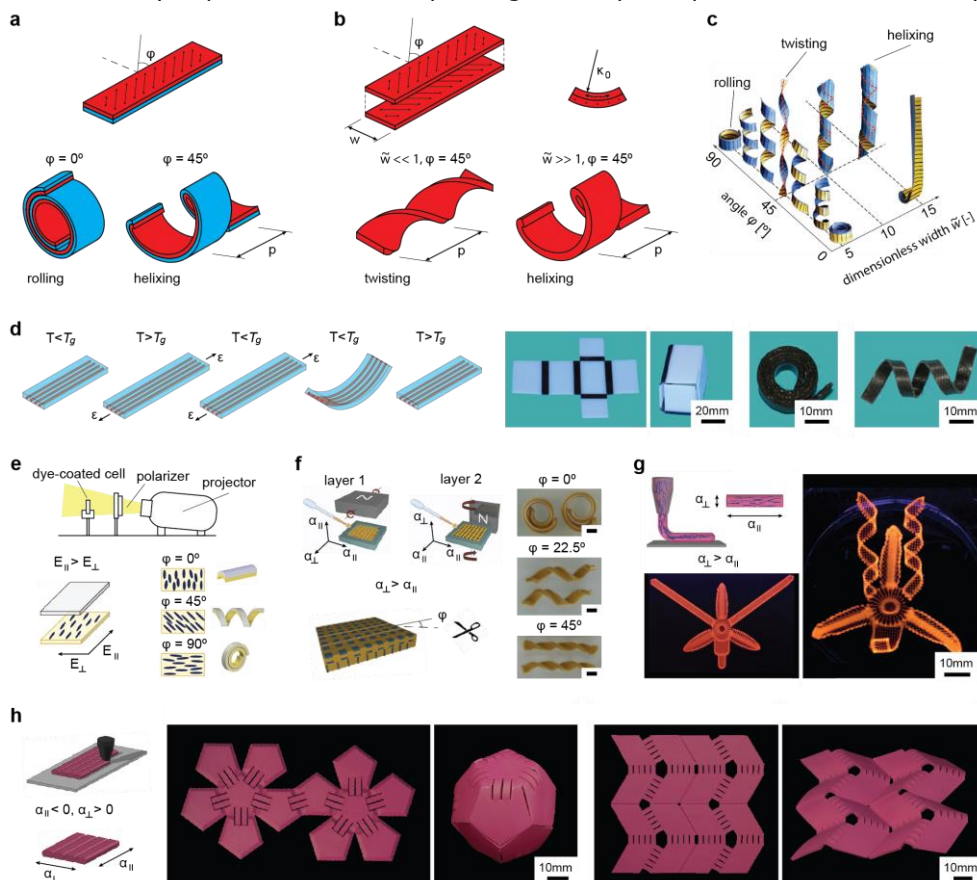
Different methods have been reported for the inclusion of anisotropy within the multilayer samples. A widely reported approach is programming SMP material through uniaxial stretching. For example, multi-material 3D printing has been used to produce bilayer strips of elastomeric materials with SMP fibers embedded in one of the layers (Figure 2.3d) [3, 78]. The samples were stretched at high temperatures and cooled down below  $T_g$ , while maintaining the straining. The programmed stress is stored as memory inside the SMP fibers, while being retained as elastic energy in the elastomer. The release of the stress causes the elastomeric layer to recover, resulting in the bending of the strip [3]. Reheating the sample will release the frozen memory, thereby recovering the original flat shape. The active self-bending elements have been integrated with passive panels to create a self-folding box (Figure 2.3d). The same research group reported 3D printing of bilayer specimens comprising two elastomeric layers and embedding SMP fibers with different  $T_g$  values [79]. The specimens revealed similar programming and recovery cycles, but shape-shifting could be activated with temperature instead of the release of the pre-strain [79]. A maximum normalized curvature of  $\sim 0.75$  has been realized [79]. Using both approaches, a linear relationship between the programming strain and curvature was found, while the

orientation of the SMP fibers within the elastomeric strip could be changed in order to program self-helixing instead of self-rolling (Figure 2.3d) [78, 79]. This approach has been further extended through production of initially curved bilayers comprising two SMP layers with different  $T_g$  values [80]. The samples have been programmed by concurrent flattening and stretching at elevated temperatures, thereby enabling the formation of both upward and downward curvatures upon activation. Uniaxially pre-programmed SMP material could be used as well as the active material in bilayer specimens [73]. Combined with a passive elastomeric layer, self-rolling and self-helixing have been realized by increasing the temperature. Finally, confined swelling of an isotropic hydrogel could be used for directional programming of SMP [81]. Trilayer strips have been printed using a multi-material 3D printer with a top layer of SMP, a middle layer of porous elastomeric material embedded with hydrogel, and an elastomer bottom layer. Submersion in water results in the swelling of the hydrogel layer, while the increase in temperature reduces the stiffness of the SMP layer. Driven by the swelling of the hydrogel, the stiffness difference between the SMP and elastomer causes the specimen to curve along its shortest direction, thereby uniaxial stretching the SMP layer. After cooling and drying the sample, reheating leads to shape-recovery of the SMP layer and the strip curves back to its initial flat state [81]. As the shape-shifting is driven by the swelling of hydrogel, the process is reversible.

Uniaxial alignment of liquid crystal in a polymer network offers another strategy to introduce anisotropic mechanical properties in the active layer [7, 18, 74, 82, 83]. Boothby et al. used a spatially patterned photoresponsive dye coating on top of a glass slide for programming molecular orientation during the synthesis of a 30  $\mu\text{m}$  thick layer of LCE material [7]. By using a digital projector of polarized light, a patterning resolution of 30 x 30  $\mu\text{m}$  could be achieved (Figure 2.3e). The LCE layer has been combined with a layer of an isotropic swellable polymer, resulting in different types of shape-shifting based on the anisotropic stiffness of the LCE upon submersion in water (Figure 2.3e) [7]. Multiple shapes could be programmed in the same bilayer upon activation by high temperature, resulting in the shrinkage of the LCE layer along its molecular direction and expansion in the orthogonal direction.

Alignment of anisotropic additions in a hydrogel solution has been also reported for material reinforcement [10, 84, 85]. Erb et al. used a rotating magnetic field to align anisotropic platelets in a layer of hydrogel during the curing process (Figure 2.3f) [10, 84]. The platelets stiffen the material mostly in one direction, which causes the hydrogel composite to show anisotropic swelling upon submersion in water. After curing, a second layer was deposited with a different anisotropy direction to create a composite bilayer [10]. This approach has been incorporated in multi-material 3D printing through different alignment of the metallic additions within each layer of liquid resin [85]. Another strategy used for

localized programming of anisotropy is 3D printing of swellable polymer ink embedded with cellulose fibrils, which align in the extrusion direction [12]. The printed fibers exhibit anisotropic swelling upon submersion in water [12]. Bilayer structures have been printed, which show both self-rolling and self-twisting as well as combinations of those basic shape-shifting modes [12] (Figure 2.3g). We have recently reported a new 4D printing technique capable of simultaneously



**Figure 2.3:** The methodology and production of anisotropic bilayers. (a) Dependency of the pitch  $p$  on the alignment angle  $\phi$ . (b) Both twisting and helixing could be programmed in anisotropic bilayers. (c) The effect of alignment angle  $\phi$  and strips width have been investigated using paper models [1]. Reproduced with permission from AAAS. (d) Programming of SMP bilayers by manually stretching of the sample has been used for different shape-shifting structures. Reproduced from [3] with the permission of AIP Publishing. (e) Spatial programming of LCE material using a digital projector. Reproduced from [7] with permission from The Royal Society of Chemistry. (f) Alignment of anisotropic platelets using a rotating magnetic field. Scale bars: 5 mm. Reproduced by permission from Macmillan Publishers Ltd: Nature Communications [10], copyright 2013. (g) Extrusion of hydrogels embedding fibrils to program anisotropic swelling. Reproduced by permission from Macmillan Publishers Ltd: Nature Materials [12], copyright 2015. (h) Simultaneous programming and fabrication of anisotropic shrinkage in SMP filament. Reproduced from [8], published by The Royal Society of Chemistry.



fabricating and programming of SMP constructs [8]. During the process of FDM printing, directional strains (up to 40%) could be programmed inside the SMP material along the printing direction, thereby enabling programming of shape-shifting using the printing pattern. This approach has been used for printing of bilayer bending actuators as well as monolayer passive panels, which could be integrated to form origami constructs (Figure 2.3h).

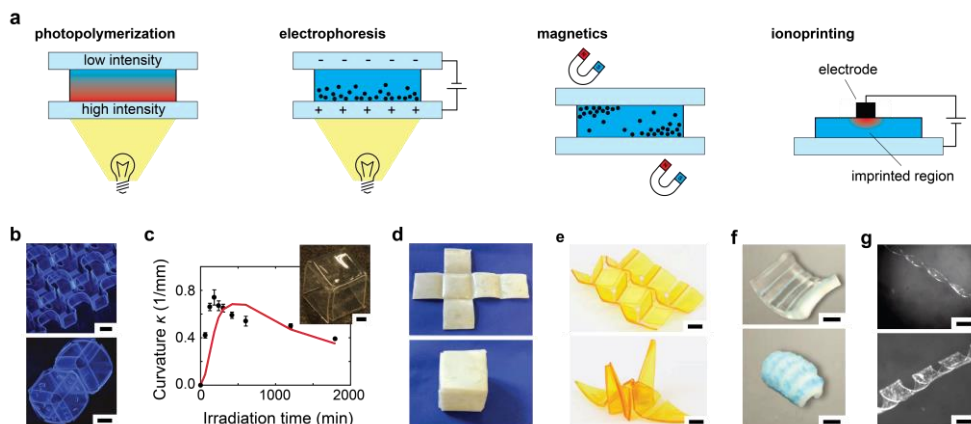
### 2.2.2. Material gradients

Instead of combining multiple different materials into a multilayer construct, a gradient in the material properties of a monolayer construct could be used to generate a stress gradient along the thickness of the material. This programming strategy offers some advantages as compared to bilayer structures. Firstly, the high shear stresses at the interface of two different materials will be avoided, thereby eliminating the risk of delamination and/or interfacial sliding. Secondly, fabrication of multilayer structures often requires multiple fabrication steps, which could be reduced in the case of a single material layer.

Based on the above-mentioned programming strategy, polymerization of a photocurable polymer resin has been reported in several studies as a simple approach for production of self-rolling structures [86-88]. During the polymerization process, the light is exposed from one side while being partially absorbed by the polymer, which results in a gradient in light intensity along the material thickness (Figure 2.4a). Jamal et al. used this approach to create a gradient in the crosslinking density of a layer of swellable material [86]. The stiffness of the material increases with higher crosslinking density, thereby reducing the swelling ratio of the material. Submersion in water therefore results in curving. Passive panels have been made by using high energy light exposure, giving rise to fully cross-linked materials [86, 87]. Bidirectional curving has been achieved by light exposure from both the top and bottom sides. Different patterns of light exposure have been used for production of complex constructs comprising passive panels with thicknesses of about 10  $\mu\text{m}$  and bidirectional folds with radii of curvature of  $\approx 200 \mu\text{m}$  (Figure 2.4b) [86]. A similar technique of using laser for partial relaxation of pre-strained polymer sheets has been used for programming stress gradients [89, 90]. Semi-transparent samples were pre-strained at high temperatures (above  $T_g$ ) and were exposed from one side to light to trigger stress relaxation [89]. Light absorption in the semi-transparent polymer results in a difference in light intensity at the top and bottom sides of the sample, thereby programming a different amount of stress relaxation through the thickness of the material. After programming the stress relaxation, the release of the pre-strain results in the curving of the specimen. Dependent on the irradiation duration and intensity, the desired stress gradient could be programmed, while non-irradiated passive panels are produced using a photomask (Figure 2.4c) [89]. Manual programming of a single layer of SMP material has also been reported [91].

Flattening of a 3D deployable SMP sample above its  $T_g$  has been used for programming the desired stress gradient, which is stored in the material by lowering the temperature. Upon temperature increase above  $T_g$ , the desired 3D shape recovers (Figure 2.4d). The concept of volume shrinkage of a photocurable polymer resin during the polymerization process has been recently reported as shape-shifting technique [92]. Based on the light intensity gradient along the thickness of material, a stress gradient could be created, which results in spontaneous curving of the structure after release from the substrate. This technique has been used for assembly of origami structures at the macroscale (Figure 2.4e) [92].

A gradient in the material properties could also be generated by creating a gradient of particles along the thickness of an active material in order to locally reduce the swelling/shrinkage ratio [93-97]. Asoh et al. used electrophoresis during the photo-polymerization process to program a gradient of electrically



**Figure 2.4:** (a) Four different techniques which have been reported for production of shape-shifting materials with a through-the-thickness gradient in material properties. (b) Self-assembly of different origami and kirigami constructs. Scale bars: 500  $\mu\text{m}$ . Reproduced by permission from Macmillan Publishers Ltd: Nature Communications [86], copyright 2011. (c) Self-folding of a cubic box. The radius of curvature could be tuned based on the irradiation time. Scale bar: 2 mm. Reproduced from [89] with the permission of AIP Publishing. (d) Self-folding of a manually programmed SMP box [91]. Copyright 2010 by John Wiley & Sons, Inc. Reproduced by permission of John Wiley & Sons, Inc. (e) Folding of complex origami constructs. Scale bars: 5 mm. Reproduced from [92]. (f) Curving of a hydrogel strip after ionoprinting. Drying of the sample results in curving in the opposite direction. Scale bars: 5 mm. Reproduced by permission from Macmillan Publishers Ltd: Nature Communications [98], copyright 2013. (g) Self-helical and self-twisting specimens. Scale bars: 5 mm. Reproduced from [99].



charged particles in a swellable polymer (Figure 2.4a) [93]. Deswelling of the polymer, in response to increase in temperature, is inhibited by the charged particles, resulting in curving of the material [93]. Liu et al. used a magnetic field to create a gradient of magnetic nanoparticles in a swellable polymer (Figure 2.4a) [94]. An increased particle concentration increases the deswelling rate while reducing the deswelling ratio, resulting in curving of the initially flat material in one direction followed by curving in the opposite direction [94]. The intensity and orientation of the applied magnetic field is used to spatially program the magnetic nanoparticles gradient, which gives local control of the curvature of the material upon deswelling.

Ionoprinting offers another strategy for programming of a bending moment in a single layer of material [98, 100]. By applying a potential field, metallic ions could be embedded inside hydrogel layers. The ions will diffuse from the electrode and bond to the hydrogel network, thereby enhancing the localized crosslinking and resulting in stiffening and deswelling of the material [98, 100]. Subsequent drying of the hydrogel may induce a second shape transformation as further deswelling in the imprinted region is inhibited due to the high amount of crosslinking (Figure 2.4f).

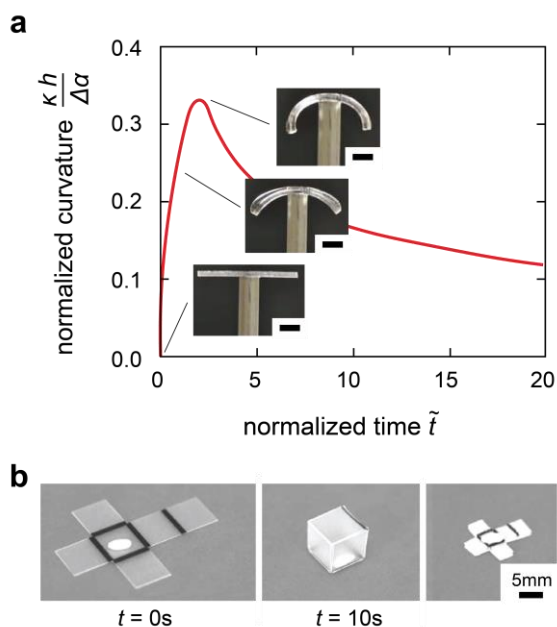
A gradient in the nematic direction of liquid crystals in a polymer network could be used as well to program self-rolling and self-helixing strips in response to temperature change and humidity [99, 101-107]. In this approach, the main straining direction (and not the amount of swelling/shrinkage) is varied over the thickness of the material. Similar to the bilayer strips with two active anisotropic layers, both self-helixing and self-twisting could be programmed dependent on the strip width and angle  $\varphi$  (Figure 2.4g) [99, 103].

### 2.2.3. Localized activation

Non-homogenous exposure of the material to the activation stimulus is another strategy to induce a stress gradient along the thickness of a monolayer material. Using this strategy, a dynamic gradient in swelling/shrinkage could be created inside the material, as the diffusion of the applied stimulus (e.g. heat or solvent) inside the material takes time. Continuous exposure to the activation stimulus will cause the diffusion to be completed, resulting in uniform swelling/shrinkage through the material thickness, thereby inhibiting out-of-plane bending.

One-sided activation of initially flat material by exposure to humidity is reported by Holmes et al [108]. Placing a droplet of a favorable solvent at one side of a thin elastic planar material leads to the localized swelling of the material. Dependent on the viscosity of the solvent, the time at which the maximum curvature is reached has been shown to vary over two orders of magnitude ( $\sim 0.1 - 10$  s) for a beam with a thickness of about 1 mm. Soon after activation, the curvature attains its maximum value of about 0.33 which is only 22% of the

theoretical limit for bilayer constructs (Figure 2.5a). Similar trend of deformation is found by Reyssat et al. and a maximum curvature equal to 40% of the theoretical maximum could be achieved [109]. In contrast to humidity, light could be applied with both high spatial and temporal resolutions, thereby offering an attractive approach for accurate programming of shape-shifting [110]. Wang et al. produced a hydrogel monolayer, which at one side was embedded with nanoparticles to transform the irradiated light into heat, resulting in localized deswelling of the hydrogel. The direction of bending was determined by the microstructure (i.e. through the thickness gradient of nanoparticle concentration), while the amount of deformation depended on the exposure time and irradiation power density [111]. A similar approach has been used for relaxation of 0.3 mm thick pre-strained SMP sheets, which were completely covered by black ink [112]. One-sided irradiation with laser (beam width: 500 – 1700  $\mu\text{m}$ ) locally heats the black ink, thereby heating the underlying polymer above its glass transition temperature,  $T_g$ , leading to strain recovery. Using this method, the desired shape-shifting pattern could be “written” in the material with a laser [112].



**Figure 2.5:** (a) Normalized curvature as a function of time, normalized by the effective diffusivity  $D$  and material thickness  $h$  as follows:  $\tilde{t} = tD/h^2$ . Scale bars: 3 mm. Reproduced from [108] with permission from The Royal Society of Chemistry. (b) Self-folding of a cubic box activated by exposure to infrared light. Continuous exposure results in the entire material being activated. Reproduced from [113] with permission from The Royal Society of Chemistry.

Instead of using a localized stimulus, the material sensitivity to a global activation stimulus could be programmed in the material as well [113, 114]. Liu et al. patterned optically transparent sheets of pre-strained SMP with black lines, which transform the global exposure to infrared light to localized increase in the temperature (Figure 2.5b) [113]. Folding angles up to  $120^\circ$  could be achieved by changing the width of the patterned lines, which sets the length of the curving region. By increasing the exposure time, the structure will curve back to the flat state, while exhibiting uniform shrinkage. Both sides of the transparent material could be patterned with black lines in order to program bidirectional folding, thereby creating a powerful tool for production of origami and kirigami constructs [115]. The bending direction of similar constructs could be also programmed by patterning the hinge regions with a thin structural layer covered with black ink [116]. Upon activation, shrinkage at the top side is constrained and the material will curve in the opposite direction, once the heat has diffused through the thickness of the construct [116].

An interesting direction for further research would be tuning the dynamic behavior of the constructs through spatial programming of the diffusion of activation stimuli. By programming the microstructure of material, both the diffusion rate and diffusion patterns could be set as desired.

### 2.3. Buckling strategy

In this approach, there is no need for through-the-thickness gradient in the material properties. By programming the in-plane arrangement of different active and passive elements, the desired compressive stresses could be generated upon activation. Externally generated compressive forces are used as well to induce out-of-plane buckling in a layer of passive material. Both methods have been implemented in a wide range of shape-shifting materials.

The local distances between the adjacent points on a surface are described by the metric tensor  $g$  of that sheet. By programming the in-plane dimensional changes, a target metric  $\bar{g}$  is prescribed and compressive stresses could be generated. Those in-plane stresses could be relieved when the construct adopts a 3D shape, thereby minimizing its elastic energy which can be expressed as the surface integral of the elastic energy density function  $w$  (for the sake of simplicity written for the one-dimensional case):

$$w = \frac{1}{8}Et(g - \bar{g})^2 + \frac{1}{24}Et^3\kappa^2 \quad (2.2)$$

where  $E$  is the material stiffness tensor,  $t$  is the material thickness, and  $\kappa$  is the surface curvature [31, 117]. As presented in the introduction, it could be seen that the elastic energy is composed of a stretching term, which is a function of

the in-plane stretching and a bending term which is related to the surface curvature. In the case of an infinitesimal thickness, the bending term is negligible and a stress-free state could be obtained when the metric tensor of the surface matches the target metric. However, such a stress-free configuration does not always exist, which results in a shape as close as possible to the target metric. By increasing the material thickness, the balance between the stretching and bending energies results in deviations from the target metric.

The buckling strategy is observed in nature as well in the form of differentially growing soft tissues [118-120]. For example, simple in-plane growth processes provide the mechanism for the shaping of leaves and other thin membranes.

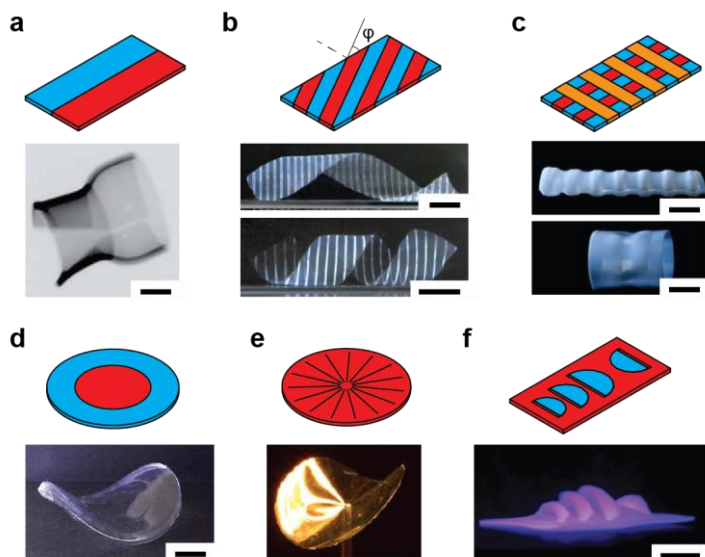
### 2.3.1. Material tessellation

Instead of stacking multiple layers which exhibit different dimensional changes in response to certain stimuli, the different materials could be tessellated in a single layer construct as well. A widely-used method for production of material tessellations is the photo-polymerization of swellable hydrogels. Controlled by the amount of light exposure, the conversion of monomers and the degree of crosslinking are enhanced, thereby increasing the material stiffness. When submerged in an aqueous medium, the swelling ratio of the hydrogel is dependent on the crosslinking density. By controlling the pattern and amount of light exposure, regions with different swelling ratios could be created to generate in-plane compressive stresses upon activation.

One simple example of a swellable material tessellation in single layer constructs is the parallel alignment of two hydrogel strips with high and low swelling ratios (volumetric expansion of 4.3 and 2.2, respectively) [121]. Swelling in an aqueous environment results in self-rolling around the width direction of the bistris, which allows the high-swelling strip to adopt a longer length as compared to the low-swelling strips, thereby minimizing its strain energy (Figure 2.6a). The balance between the stretching and bending energies at the interface of both strips results in a transition region whose dimensions have been found to be dependent on the thickness and width of the individual strips [122, 123]. Samples with parallel arrangement of multiple strips with alternating high and low swelling ratios have been prepared as well [124-126]. Dependent on the orientation of the strips with respect to the longitudinal direction of the sample, self-rolling and self-helical elements could be created (Figure 2.6b) [125, 126]. This concept may be extended by producing samples with strips in both the length and width directions of the sample, which are responsive to different stimuli (e.g. temperature and pH). In this way, multiple shape transformations could be programmed in initially flat structures (Figure 2.6c) [125-127]. However, this approach seems to be limited to cylindrical shapes while the minimum feature size (i.e. width of

individual strips) has to be larger than about 5 times the sample thickness in order to achieve global buckling, which is a serious restriction on the minimum sample

dimensions [122]. For smaller strips, the samples remain flat, although anisotropic in-plane deformations have been observed as well. In contrast to multilayer self-rolling structures, there is a nonlinear relationship between the rolling radius on the one hand and the mismatch in swelling ratio and sample thickness on the other, resulting in a normalized curvature that is dependent both on the swelling mismatch and thickness [122]. The experimental results of Byun et al. show a maximum normalized curvature of about 0.1 for a sample thickness of 11  $\mu\text{m}$  and a linear swelling mismatch of 2.0 [122]. Given the nonlinear dependence on both parameters, further reduction of the thickness and increase of swelling mismatch may result in larger values of the normalized curvature.



**Figure 2.6:** Multiple material tessellations resulting in different shape-shifting materials. (a) A bistrip of differentially swelling strips adopts a cylindrical shape upon submersion in an aqueous environment. Scale bar: 200  $\mu\text{m}$ . Reproduced from [121] with permission from The Royal Society of Chemistry. (b) Parallel alignment of multiple strips could be used to program self-helical dependent on the orientation angle  $\phi$ . Scale bar: 1 cm. Reproduced by permission from Macmillan Publishers Ltd: Nature Communications [126], copyright 2013. (c) Programming of multiple shape transformations using different responsive materials. Scale bar: 1 cm. Reproduced with permission from [125]. Copyright 2013 by the American Chemical Society. (d) Axisymmetric material tessellations used for programming of a negative Gaussian curvature. Scale bar: 1 cm. Reproduced from [37] with permission from The Royal Society of Chemistry. (e) Alignment of a liquid crystal in a single layer of material resulting in a saddle-like shape [128]. Copyright 2012 by John Wiley & Sons, Inc. Reproduced by permission of John Wiley & Sons, Inc. (f) Incorporation of cuts in the material tessellation allows for programming more complex shapes including the Sydney opera house. Scale bar: 1 cm. From [129]. Copyright 2016 by John Wiley & Sons, Inc. Reproduced by permission of John Wiley & Sons, Inc.

Axisymmetric material tessellation is another approach used for programming shape shifting to double-curved 3D geometries into flat materials [37, 129-131]. For example, a high-swelling disk surrounded by a low-swelling ring results in a dome-shaped surface upon activation, while a saddle-shaped surface could be created by interchanging the material properties of the disk and ring (Figure 2.6d) [37, 131]. In both cases, the maximum curvature could be achieved when the diameter of the inner disk is about 75% of the outer ring diameter [129, 131]. Similar surfaces could be generated by using a disk with azimuthal alignment of liquid crystals in a polymer network [106]. Upon temperature increase, the disks shrinks in the tangential direction, while it expanding in the radial direction, resulting in a conical shape. A saddle-like shape could be created when using the radial alignment of the liquid crystals (Figure 2.6e) [106].

Another study reported the use of a digital projector for 3D printing of hydrogels [129]. By programming the light exposure at every 'pixel' of a monomer solution in between two glass slices, the cross-linking density of the material was spatially controlled [129]. A large variety of double-curved surfaces could be programmed in flat hydrogels using this strategy (Figure 2.6f) [129].

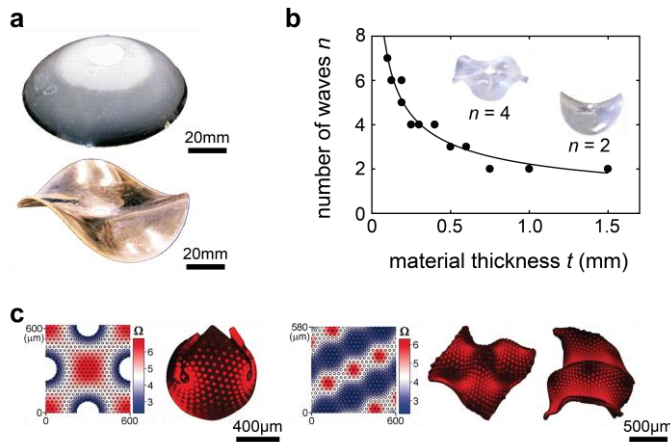
By patterning a single layer of material, both cylindrical and double curved shapes could be created based on the pattern of material tessellation. In most cases, hydrogels have been used as the active material in such designs, meaning that the applications are limited by the low-stiffness values and the requirement to have an aqueous environment. Moreover, the reported examples are limited to simple geometries. Given the programmed in-plane swelling/shrinkage, the 3D configuration could be predicted through minimization of the elastic energy. This forward problem has been solved for some of the presented examples [121, 122, 131]. However, being able to solve the inverse problem, i.e. what deformations have to be programmed for generation of a desired shape, would be required for practical applications and is an promising direction for further research.

### 2.3.2. In-plane material gradients

In contrast to the previously discussed discrete variations in the in-plane swelling/shrinkage ratios, smooth gradients in swelling/shrinkage ratios could be used for generation of stress-free 3D shapes. Sharon et al. used the injection of a solution with controllable monomer concentration into a Hele-Shaw cell to program radial gradients in the swelling ratio into a thin disk (thickness: 0.3-0.5 mm, radius: 50 mm) [132, 133]. Dependent on the programmed gradient, both wave-shaped and dome-shaped surfaces were formed upon submersion in a high temperature water bath (Figure 2.7a). The axisymmetric dome-shaped configuration deviates only slightly from the desired stretch-free state as the bending energy content is limited due to the small material thickness [133]. In the case of a negative Gaussian curvature, the effect of material thickness on the final shape is more dominant as is clear from the number of wrinkles for different

thicknesses. An increasing number of wrinkles corresponds to a larger bending component as well as decreased stretching energy [133]. The number of wrinkles were therefore found to be roughly proportional to  $t^{-0.5}$ , where  $t$  is the material thickness (Figure 2.7b) [134].

Another approach is to use a gradient in the grey values of the photomask during the photo-polymerization process to program smooth gradients in the cross-linking of a swellable polymer disk [125, 135]. The localized swelling ratio could also be programmed through lithography to pattern highly cross-linked dots in a swellable polymer with a low cross-link density matrix [136]. By controlling the amount of highly cross-linked dots as well as the dimensions of the dots in a certain area, the average swelling ratio could be programmed. A nearly closed spherical shape could be made by programming gradients in areal swelling ratios ranging from 2 to 8 (Figure 2.7c) [136]. Potentially, arbitrarily complex shapes could be made using this technique, which is illustrated by an example comprising both regions with positive and negative Gaussian curvatures (Figure 2.7c). As the buckling direction is determined by small imperfections, different surfaces could be obtained after activation for similarly programmed flat materials (Figure 2.7c) [136]. Complex surfaces with non-constant Gaussian curvatures are therefore difficult to create.



**Figure 2.7:** (a) A radial gradient in swelling ratio could be used for programming of both dome-shapes and saddle-shapes [133]. Reproduced with permission from AAAS. (b) Experimentally obtained dependency of the number of wrinkles on the material thickness. Reproduced with permission from [134]. Copyright 2011 by the American Physical Society. (c) Complex patterns of in-plane swelling ratios have been used for programming of a spherical shape as well as a surface comprising multiple regions with positive and negative Gaussian curvatures [136]. Reproduced with permission from AAAS.

### 2.3.3. Non-homogenous exposure

Non-homogenous exposure to the activation stimuli has been also used for programming a large variety of shape transformations. As the shape-shifting is not programmed inside the material but is based on the 'pattern of activation', many different configurations could potentially be realized within the same construct. One example is the embedding of nanoparticles inside a hydrogel sheet, which enables transformation of the illuminated light into heat, thereby promoting the deswelling of the hydrogel [137]. Complex double-curved surfaces could be programmed based on the pattern of light exposure [137]. The same approach of "light writing" for programming of shape-shifting has been used for local relaxation of pre-strained SMP through laser-assisted heating [138]. Attaching stretchable micro-electrodes to a single sheet of thermo-responsive hydrogel allows for the local control of temperature using Joule heating, thereby enabling the programming of different swelling/de-swelling ratios [139]. Multiple shape transformations may then be programmed in one structure by controlling the input power of each electrode [139].

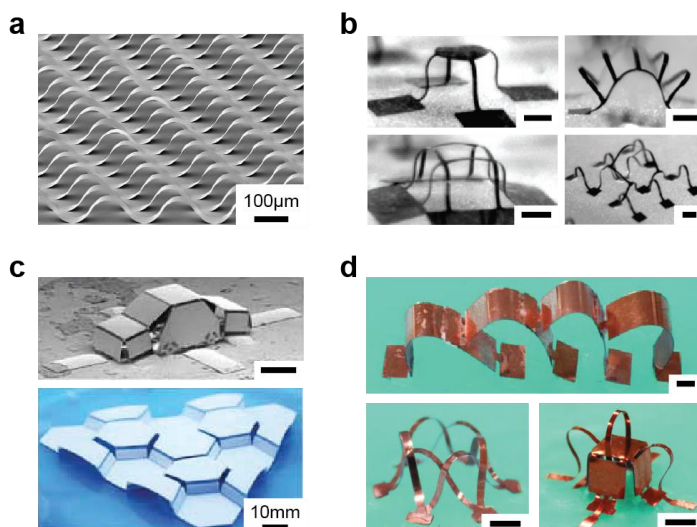
### 2.3.4. Mechanically induced buckling

Compression of a stiff top layer by induced dimensional changes in a soft substrate is widely used to induce surface wrinkling [30, 140-142]. Buckling of the thin top layer is energetically favorable over compression, causing the wrinkles to pop-up. Further compression of the bilayer could also cause delamination at the interface of both layers, resulting in buckle-delamination instead of surface wrinkling dependent on the stiffness ratio of both materials and the interfacial defects [143]. By spatially programming the adhesion between the layers, delamination occurs in a controlled manner, thereby offering a strategy for out-of-plane shape-shifting (Figure 2.8a). Spontaneous delamination has been reported as well but will not be considered here [144].

Controlled out-of-plane buckling of nanoribbons was first reported by Sun et al. using a pre-strained soft substrate (thickness  $\approx 4$  mm) locally bonded to semiconductor nanoribbons (thickness  $\approx 500$  nm) [145]. Upon releasing the substrate, the thin top layer will be subjected to compressive forces, resulting in out-of-plane buckling (Figure 2.8a). The semiconductor material behaves like a flexible material as the thickness of the top layer is very thin and shows a low bending stiffness. The same approach but using different top layer geometries and well-defined bonding sites is reported for production of complex 3D shapes at the mesoscale on top of a soft substrate (Figure 2.8b) [146]. Additional complexity could be added in the form of spatial variations in thickness of the top layer in order to locate the folding lines, thereby allowing for programming of both origami and kirigami constructs (Figure 2.8c) [147]. Another study reported the addition of multiple overlapping top layers to create more complex topologies (Figure 2.8d) [148]. More details on the shape-shifting strategy of mechanically induced



buckling could be found in other reviews [11, 149]. An interesting future direction may be the use of different active materials as a substrate, which allows for spatial variations in the amount of compression, thereby offering the ability to program more complex 3D topologies.



**Figure 2.8:** Mechanically induced buckling used for programming of different 3D constructs. (a) Thin nanoribbons on top of a thick substrate. Reproduced by permission from Macmillan Publishers Ltd: Nature Nanotechnology [145], copyright 2006. (b) Complex 3D structures at the micro-scale [146]. Scale bar: 200  $\mu\text{m}$ . Reproduced with permission from AAAS. (c) Two kirigami structures made by addition of folding lines. Scale bar: 200  $\mu\text{m}$ . From [147]. Copyright 2015 by John Wiley & Sons, Inc. Reproduced by permission of John Wiley & Sons, Inc. (d) Complex 3D configurations made using multiple releasable stiff top layers. Scale bar: 2 mm. Reproduced from [148].

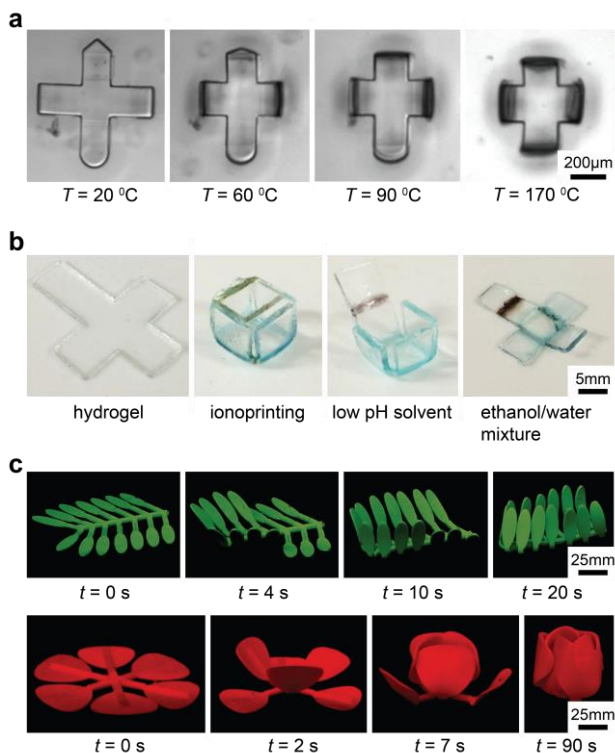
## 2.4. Sequential shape-shifting

Different strategies to program 3D shapes in initially flat constructs have been discussed so far. To achieve more sophisticated shapes, it is desirable to not only program individual shape transformations but also the time sequence of the deformations. For example, this type of sequential folding could be applied in rigid panel origami to fold highly complex structures without locking the deformation by self-collisions. Moreover, appropriate locking mechanisms could be incorporated in folded structures to improve the structural/mechanical integrity of the target configuration.

Local application of the stimulus is one approach for programming the sequence of folding [62, 64, 138, 150]. This strategy has been applied in a pre-stressed bilayer strip patterned with a stiff polymer layer which prevents curving of the construct [150]. Softening of the polymer layer upon heating by a laser allows for bending of the bilayer strip [150]. The sequence of folding is programmed by

controlling the pattern of laser light exposure. The same strategy but using Joule heating instead of laser light has been reported as well [62, 64]. The hinges are activated one by one by controlling the power input at different electrodes, which allows for the self-assembly of highly complex structures.

Another strategy to program the folding sequence is to tune the material response to a time-dependent global stimulus by locally controlling the material properties [2, 151-153]. 3D printing of origami structures with hinges made from a SMP with different  $T_g$  is reported in several studies as a tool for programming the sequence of folding [151-153]. Slowly increasing the temperature causes the hinges to start folding one by one dependent on their  $T_g$ . Both the  $T_g$  of each hinge and the time-dependent increase in the temperature are parameters that could be used to program the folding sequence. The same approach but using a swellable polymer has been reported by So et al [2]. The temperature dependency of the thermos-responsive polymer could be programmed based on the polymer composition,



**Figure 2.9:** Sequential shape-shifting. (a) Sequentially closing of a box based on the environmental temperature. Reproduced with permission from [2]. Copyright 2017 by the American Chemical Society. (b) Selective unfolding of a 3D printed hydrogel box based on the solvent. Reproduced from [4]. (c) Sequential shape-shifting based on different responses to the same activation stimulus. Reproduced from [8]. Published by The Royal Society of Chemistry.

resulting in sequential shape transformation by a time-dependent increase or decrease in the temperature (Figure 2.9a). Another variant of programming sequential (un)folding based on change in activation stimulus is ionoprinting of hydrogel using electrodes of different materials. It is then possible to imprint regions with different cations that show different deswelling behaviors based on the pH and hydrophilicity of the solvent (Figure 2.9b) [4].

A third approach is to spatially program the diffusion rate of a global stimulus in the active material [8, 154-156]. One study reported the patterning of lines with different greyscale at one side of a transparent pre-stained SMP sheet, which were activated by exposure to UV light [154]. Light absorption at the patterned lines leads to localized increase in the temperature. Dependent on the greyscale of the patterned lines, different amount of light energy is transformed into thermal energy thereby programming the onset time of the folding as the shape-recovery starts when the temperature approaches  $T_g$ . Because the patterned lines are applied only on one side of the material, the induced shape-recovery leads to out-of-plane curving [154]. A similar method has been reported based on using different color inks that can selectively absorb different spectrum of light which provide more freedom for controlling the process of shape-shifting [155]. Another study reported programming of the time-dependent shape-recovery of pre-stained SMP material embedded in a polymer matrix based on the interfacial area between the polymer matrix and the active material [156]. By increasing the interfacial area, the heat transfer from environment to the active SMP core could be enhanced, thereby controlling the onset time of the shape-shifting. Another method for programming the heat transfer inside SMP material is by tuning both the porosity and thickness of the 3D printed SMP bilayers [8]. The shape recovery will only commence when (almost) the whole element approaches  $T_g$ , as the stiffness of the material is much higher at low temperatures. Using this strategy, sequential folding has been incorporated into different designs (Figure 2.9c).

## 2.5. Discussion

Two main strategies to program shape-shifting in initially flat materials were identified based on the type of internally generated stresses. Both strategies offer design routes towards generation of 3D constructs from soft flat matter but differ in their programmability options and the achievable shape transformations. Depending on the type of application and the design requirements, one of the programming strategies may be favored over another. In this chapter, we will discuss the benefits and difficulties of both approaches and the areas where they could be applied (as summarized in Table 2.1).

### 2.5.1. Programming parameters

The shape-shifting materials within the bending strategy all rely on the programming of a stress gradient along the thickness of the material. Not only the geometrical parameters and material properties but also the programming

and activation conditions could be used to program the desired 3D configuration in initially flat materials. Both the bending stiffness of the structure and the induced stress gradient may be tuned to program the desired radius of curvature of bending elements. In agreement with the Timoshenko's bilayer model, the bending curvature increases with reduced material thickness [35]. Other geometrical parameters such as the width and aspect ratio of the hinge influence the bending stiffness as well. Besides the geometrical parameters, several material properties have been changed and are shown to influence the shape-shifting. For example, the bending stiffness is influenced by the stiffness of the bulk material while the desired stress gradient is generated by the dimensional changes of the active material. The activation conditions such as the exposure time and activation energy, among other parameters are also used to program the stress gradient. In addition to the deformation amplitude (e.g. the radius of curvature) the direction of deformation (e.g. rolling or helixing) could be programmed as well. For example, the aspect ratio is shown to determine the rolling direction, if isotropic materials are used. Depending on the direction of material anisotropy, the desired pitch of a self-helixing structure could be also programmed. Finally, the shape of the target configuration may be changed by adjusting pattern of the exposure to the activation stimulus. Although the programming of bending structures has been mostly discussed within the context of multilayer constructs, these general concepts are also applicable to the other bending approaches. For example, programming parameters such as thickness or direction of anisotropy will affect the shape-shifting in a qualitatively similar way as discussed for bilayers.

As opposed to the bending strategy, buckling is programmed through in-plane variations in swelling/shrinkage ratios, thereby generating the required compressive stresses. Based on the programmed target metric (i.e. induced in-plane dimensional changes), the structure will adopt a 3D shape by out-of-plane buckling. The buckled surface adopts a curved shape with a curvature based on the balance between the stretching and bending energies, which could be adjusted by changing the material thickness. Similar to the what was discussed for the other strategy, the activation parameters (e.g. exposure time or exposure pattern) could be used to program the in-plane compressive stress.

### 2.5.2. Programmable shapes

By inducing a stress gradient along the thickness of the material, a bending moment is generated which inherently leads to single-curved structures. Using the bending strategy, mostly deployable shapes (i.e. zero Gaussian curvature) have been created as such shapes possess (almost) no stretching energy which is energetically favorable for thin constructs. Under certain conditions, such as small strain or relatively large thickness, non-cylindrical shapes could be created as well.

Table 2.1a: Summary of the bending programming strategies

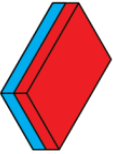
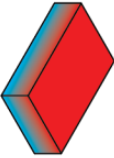
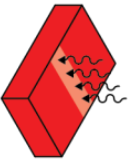

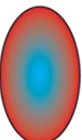
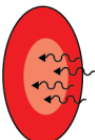

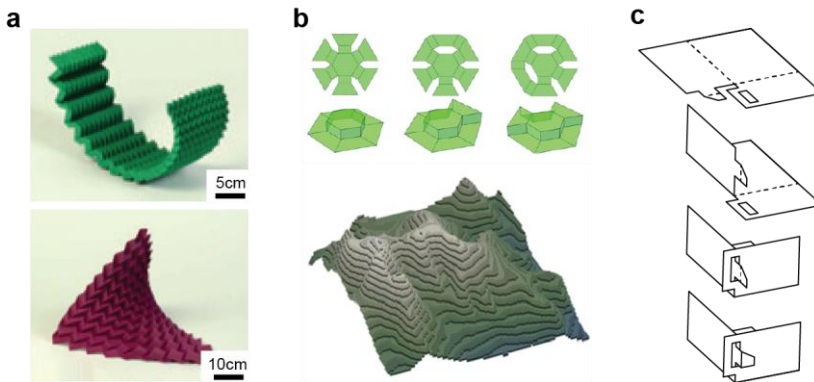
Achievable shapes	Strategy	Advantages	Limitations	Potential applications
<ul style="list-style-type: none"><li>• Tube</li><li>• Helix</li><li>• Twisted shape</li><li>• Combinations of basic modes can create complex 3D geometries</li></ul>	 Multilayer (Sec 2.2.1)	<ul style="list-style-type: none"><li>• Highest curvature</li><li>• Accurate control of both direction and amount of curving based on dimensions and material properties</li><li>• Versatility in selection of material</li></ul>	<ul style="list-style-type: none"><li>• High shear stresses at interface between layers</li><li>• Multiple fabrication steps</li></ul>	<ul style="list-style-type: none"><li>• Folding of metamaterials [157–160]</li><li>• Drugs delivery / cell encapsulation [161]</li><li>• 3D tissue scaffolds [162]</li><li>• Microgrippers [163–166]</li><li>• Deployable constructs [63, 167]</li><li>• Sensors/actuators [26]</li></ul>
	 Material gradient (Sec 2.2.3)	<ul style="list-style-type: none"><li>• Single material</li><li>• No risk of delamination</li></ul>	<ul style="list-style-type: none"><li>• Limited curvature</li><li>• Complex fabrication process</li></ul>	
	 Localized activation (2.2.3)	<ul style="list-style-type: none"><li>• Single curvature</li><li>• Simple fabrication</li><li>• Possibility of programming multiple shapes in same material based on activation</li></ul>	<ul style="list-style-type: none"><li>• Limited curvature</li><li>• Accurate control over activation necessary</li></ul>	

Table 2.1b: Summary of the buckling programming strategies

Achievable shapes	Strategy	Advantages	Limitations	Potential applications
<ul style="list-style-type: none"><li>• Shapes with nonzero Gaussian curvature</li><li>• Local double curved shapes which show globally a developable shape</li></ul>	 <p>Material tessellation (Sec 2.3.1)</p>	<ul style="list-style-type: none"><li>• Few fabrication steps</li><li>• In-plane resolution limited to about 5-10 times the material thickness [122, 136]</li></ul>	<ul style="list-style-type: none"><li>• High shear stresses at interface between two materials</li><li>• Considerable amount of residual stresses remain after buckling</li><li>• Imperfection sensitive</li></ul>	<ul style="list-style-type: none"><li>• Sensors/actuators [128]</li><li>• Shaping of sophisticated 3D shapes [129, 136]</li></ul>
	 <p>In-plane material gradients (Sec 2.3.2)</p>	<ul style="list-style-type: none"><li>• Single material</li><li>• No risk of delamination</li><li>• (almost) stress-free 3D configurations possible</li></ul>	<ul style="list-style-type: none"><li>• Complex fabrication process</li><li>• Imperfection sensitive</li></ul>	
	 <p>Localized activation (Sec 2.3.3)</p>	<ul style="list-style-type: none"><li>• Single curvature</li><li>• Simple fabrication</li><li>• Possibility of programming multiple shapes in same material based on activation</li></ul>	<ul style="list-style-type: none"><li>• Accurate control over activation necessary</li><li>• Imperfection sensitive</li></ul>	
	 <p>Mechanically induced buckling (Sec 2.3.4)</p>	<ul style="list-style-type: none"><li>• Highly complex geometries can be made [146]</li></ul>	<ul style="list-style-type: none"><li>• Multiple fabrication steps</li><li>• Structures remain connected to large substrate</li></ul>	<ul style="list-style-type: none"><li>• Flexible electronics [145, 168, 169]</li></ul>



**Figure 2.10:** (a) Approximation of smooth (double-) curved surfaces using tessellations of the Miura-ori origami. Reproduced by permission from Macmillan Publishers Ltd: Nature Materials [170], copyright 2015. (b) Kirigami elements could be used for folding of complex double-curved surfaces. Reproduced from [171]. (c) Locking elements could be implemented using sequential folding.

Examples are a dome-shaped surface in case of isotropic swelling/shrinkage and self-twisting elements when the main straining direction of the anisotropic materials is varied through the thickness. As the programming strategy based on the generation of bending moment inherently results in structures with zero Gaussian curvatures, while the desired folding angle could be controlled by many different parameters, the strategy is a suitable candidate for folding of (semi-) rigid panels. Especially, trilayer constructs are often used for folding of origami structures [69, 71]. It has been shown that smooth surface with varying curvature could be approximated by folding of a flat sheet using origami tessellations (Figure 2.10a) [170]. Folding of kirigami elements (i.e. voids are included in the flat material) could also be used for algorithmic design of a large range of discretized target shapes including double-curved surfaces (Figure 2.10b) [171]. Other techniques based on for example curved creases or concentric pleats could also result in geometries with apparent intrinsic curvature [172]. Ornamented with a secondary level of 3D nanolattices these lattices can serve as a general platform for fabrication of functionalized metamaterials.

Compared with the bending strategy, buckling provides access to a wide range of shapes incorporating both mean and Gaussian curvature. For example, nearly developable surfaces (i.e. zero Gaussian curvature) could be created through the parallel alignment of strips with different swelling ratios, although the samples locally adopt a double-curved shape. Furthermore, simple dome-shapes and saddle-shapes have been reported, which could be generated through programming of an axisymmetric target metric. By incorporating cuts in flat materials, more complex 3D configurations have been created such as a 3D theater complex similar to the Sydney Opera House (Figure 2.6f) [129]. However,

as the buckling strategy is instability-driven, the direction of out-of-plane deformation is difficult to control. Because of this, (almost) no buckled constructs exhibiting multiple regions with both negative and positive Gaussian curvature have been reported. As programming the in-plane dimensional changes generally will lead to buckled surfaces with nonzero Gaussian curvature, the folding direction and folding angle could be accurately controlled using bending elements, which shows how combining both strategies could enable expanding the range of achievable target shapes.

Sequential folding has only been reported as a tool in the folding of (semi-)rigid panels. By planning the sequence of folding, the space of achievable shapes could be largely extended as self-collision between the panels may be avoided (Figure 2.9c). In addition to increasing the range of achievable shapes, the integrity of the resulting (origami) structures may be improved as illustrated in Figure 2.10c. Using sequentially folded collar faces, the stability and controllability of rigid panel folding could be enhanced as well [88].

### 2.5.3. Applications

Using shape-shifting of initially flat material for the production of 3D shapes offers two promising advantages, which give rise to many new applications. First of all, shape-shifting provides access to the material surface, thereby allowing the use of 2D production techniques (Figure 2.11a). Secondly, the presented techniques could be used for programming well- prescribed motions. A number of biomedical applications as well as other applications, which benefit from those advantages, will be highlighted here.

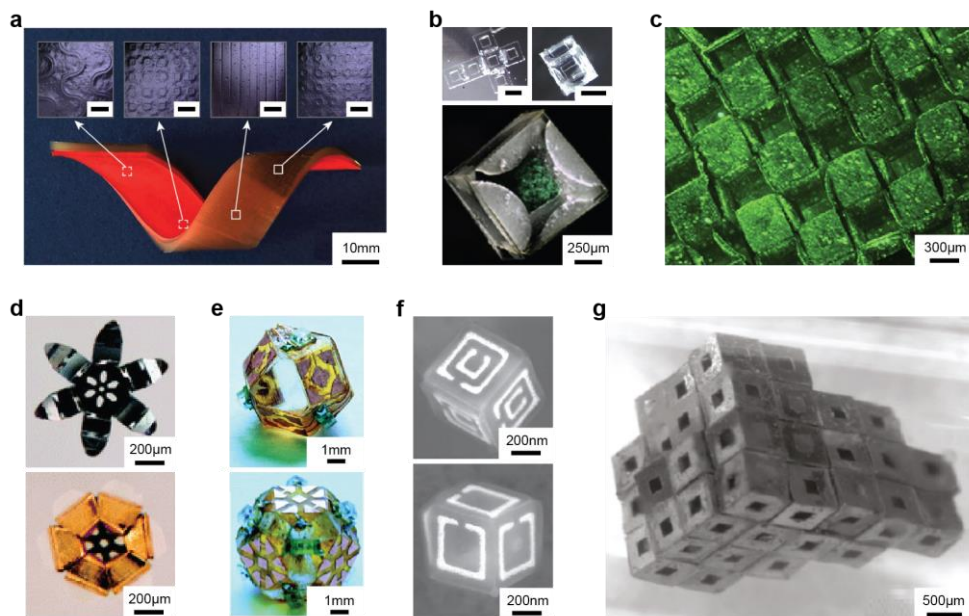
#### Medical applications

Multiple areas for biomedical application of shape-shifting have been identified by Randall et al [173]. Packaging and delivery of drugs has been mentioned as one of those applications [174]. Important features of drugs delivery systems are size, shape, porosity, and surface texture, among other attributes which are necessary for accurate control of both targeting and release of drugs [175-178]. The usage of high-tech 2D production systems makes it possible to incorporate many of those features into a flat construct. Upon activation, hollow polyhedral containers could be created that incorporate those important surface features. For example, self-assembly of hollow constructs with precisely-patterned porosity is reported, which allows for a well-controlled release of drugs [179]. Self-folding devices may be applied in cell encapsulation as well [180]. Cell encapsulating systems are used to create a safe microenvironment to protect the encapsulated cells from the outside environment while acting as a platform for drugs delivery [181]. Once more, the ability to produce flat structures with highly detailed surface features using conventional 2D production techniques makes the application of self-folding



devices attractive. Successful implementation of self-folding devices with the aim of cell capturing has been also reported (Figure 2.11b) [161].

Tissue engineering has been also pointed out as a field for application of self-folding devices [173]. 3D tissue scaffolds mimic the *in vivo* situation the best while being able to control the formation of tissue through adjustment of the scaffold properties [182, 183]. For example, mechanical properties as well as the scaffold geometry influence the differentiation of stem cells [184-186]. Cell differentiation is also facilitated by the nanotopography of the 3D scaffold [187-189]. The challenge to produce 3D scaffolds with well-controlled mechanical and geometrical properties makes shape-shifting materials an attractive alternative to other 3D production techniques. The ability to grow cells on a self-assembled 3D scaffold is reported by Jamal et al [162, 190]. By patterning different materials on top of an initially flat material, a 3D scaffold with well-controlled curvature could be created (Figure 2.11c) [162].



**Figure 2.11:** The potential applications of shape-shifting materials. (a) A self-helical bilayer strip decorated with different surface patterns. Scale bars inset: 1 mm. Reproduced from [73]. Published by The Royal Society of Chemistry. (b) A self-folding box used for encapsulation of living fibroblast cells. Scale bars: 1 mm. Reproduced from [161] with permission from Springer. (c) Fibroblast cells growing on a self-folded scaffold. Reproduced from [162] with permission from Elsevier. (d) Closing of a microgripper. Reproduced with permission from [164]. Copyright 2010 by the American Chemical Society. (e) Self-folding polyhedron embedded with electric circuits [191]. Reproduced with permission from AAAS. (f) Two self-folded cubic boxes embedded with optical features [160]. Copyright 2011 by John Wiley & Sons, Inc. Reproduced by permission of John Wiley & Sons, Inc. (g) Self-assembly of multiple unit-cells. Reproduced with permission from [160]. Copyright 2010 by the American Chemical Society.

Miniaturized medical devices are the third area of biomedical application which will be discussed here. In this application area, shape-shifting materials are utilized because of their ability to produce well-controlled and programmed motions. Production of self-folding micro-grippers as a surgical tool is reported in several studies (Figure 2.11d) [163-166]. The devices could be manipulated using external magnetic fields, while different types of stimuli (e.g. thermal or chemical) may be used to activate the gripper. Shape-shifting materials have also other applications in biotechnology such as the unfolding of a stent or wound-closure using shrinking sutures [192, 193].

### **Other applications**

Shape-shifting materials could be exploited also in many non-medical applications including sensors/actuators [26] and self-folding devices [63, 167]. Two main areas of application will be discussed here, namely 3D electronics and origami-based metamaterials.

Both access to the flat surface and the ability to produce 3D shapes make shape-shifting materials attractive for production of 3D electronics [191, 194]. Panels embedded with different types of circuits have been, for example, folded into the target the shape to form an electrical network in 3D (Figure 2.11e) [191]. Self-assembly is also used for fabrication of stretchable electronics [145, 168, 169]. Thin nanoscale ribbons acting as electrical connections could be created on top of a flexible substrate using out-of-plane buckling [145]. Stretching or bending of the substrate ensures that the thin electrical connection is only bent without any stretching so as to prevent any damage to the circuit. The self-folding of individual 3D electrical components (*i.e.* inductors and capacitors) has been also reported [67]. Similar to the case of electronics, shape-shifting could be applied in optics as well to create functionalized 3D shapes by embedding the flat panels with optical nanoscale features revealing different reflection spectra (Figure 2.11f) [160].

Finally, folding of flat sheets may be used to create metamaterials with mechanical functionalities. For example, the Miura-ori pattern offers some unusual properties such as negative Poisson's ratio [157, 158, 195, 196] while other folding patterns exhibit bi-stability [197, 198]. Metamaterials with optical functionalities could be folded and assembled from flat material as well [159]. Folding of origami structures is also used in other applications such as metamaterial absorbers [199], energy storage [200], and deformable solar cells [201].

### **2.5.4. Challenges and limitations**

While bending is a well-described strategy for programming out-of-plane shape-shifting, buckling has been only recently recognized as a suitable programming strategy, which is reflected in the relatively limited number of studies using that

approach. The buckling strategy is limited in the sense that only structures with nonzero Gaussian curvature could be made and that the direction of out-of-plane buckling depends on small imperfections that are difficult to control. Another limitation of buckling is that this strategy is merely reported using hydrogels as active material with only a few exceptions of using LCE [7, 74, 83, 105, 106] or SMP [8]. By using hydrogels as active material, shape-shifting could only be induced in aqueous environments [202]. Other limitations are the low mechanical properties (*i.e.*  $E < 0.5$  MPa) of hydrogels [21] and a long activation time (up to several hours for a material thickness of 1 mm) due to the slow diffusion of water inside the material [22]. Those limitations have been tried to overcome by addition of different inclusion in the material. Examples are carbon nanotube-hydrogel hybrids for enhancement of the activation time [44], hydrogels with fiber reinforcements in order to increase the material stiffness [203, 204], and the introduction of other hydrogel composites [205]. The bending strategy has been, however, reported for a larger range of active and passive materials, which could be activated in different environmental conditions using a wide range of activation stimuli. The shape-shifting performance of different bending approaches may be compared in terms of maximum achievable curvature. For bilayer samples, the two materials could be selected such that the difference in swelling/shrinkage in response to the activation stimuli is maximized. Given the materials and bilayer thickness, the layer thickness ratio may be tuned in order to optimize the curvature. Theoretically, a maximum normalized curvature of 1.5 could be obtained. Using the gradient approach, the maximum achievable curvature is restricted as only one single material could be used, thereby limiting the range of swelling/shrinkage mismatch. Furthermore, linear stress gradients generate bending moments that are only half of the bending moment generated in bilayer constructs with similar dimensions and swelling/shrinkage mismatches. The same limitations hold for the bending strategy when localized activation of responsive materials is used.

Shape-changing materials offer a powerful tool for the incorporation of sophisticated planar micro- and nano-fabrication techniques in 3D constructs. While multiple (potential) applications have been highlighted, many remaining challenges need to be overcome before widespread implementation of shape-shifting materials can be realized. First, shape-shifting techniques have been mostly used at the macro-scale, while many applications require shape-shifting structures with dimensions less than 1 mm. For example, 3D tissue engineering scaffolds with unit-cell dimensions of a few hundred micron could be used as a template for tissue regeneration or as a platform for studying the effects of geometrical cues on cell function [162]. Second, little to no complex assemblies of shape-shifting materials (e.g. comprising multiple unit-cells or large variations in Gaussian curvature) have been reported yet. Despite the large library of shape-shifting techniques, the production of complex 3D origami structures comprising multiple unit-cells remains challenging. Several studies reported the possibility to

program the time sequence of deformation which could tremendously increase the complexity of the possible 3D configurations. Accurate modelling tools that capture both the complex folding kinematics as well as the kinetics might be also helpful for realizing complex shape-shifting constructs. Another strategy could be the self-assembly of self-folded unit-cells, thereby eliminating the need for complex kinematics and accurate bending elements. For example, Randhawa et al. reported the self-assembly of hollow cubic unit-cells in an aqueous environment guided by the hydrophobic patterns at the outer surfaces of the cubes (Figure 2.11g) [206]. Those patterns could be applied at the flat material surfaces prior to the self-folding process of the unit-cells. Because many reported shape-shifting materials require multiple and complex fabrication steps, simple manufacturing processes need to be developed to make the widespread application of those materials possible. The emerging field of so-called '4D-printing' might be a promising direction for single-step production of complex shape-shifting materials. By precisely controlling the locations of the (different) printed material(s), highly complex shape-shifting materials could be fabricated. Further development of those high resolution additive manufacturing techniques might allow for producing shape-changing materials at the micro-scale. In addition to the limited complexity of the 3D shapes achieved with shape-shifting, they rarely incorporate functionality-inducing surface features. The effects of those surface features (*e.g.* micro- and nano-topographies) on the shape-shifting behavior and vice versa are therefore not well understood. For example, differential shrinkage/expansion of the material might distort the applied surface patterns. All important aspects such as surface functionalities and complex shape-shifting constructs at small scales have to be integrated into one shape-changing material in order to fully exploit the promising concept of 2D to 3D shape-shifting.

## 2.6. Conclusion

The strategies used for programming the shape-shifting behavior could be classified as being either based on bending or buckling. Many studies have focused on generating bending moments to enable shape-shifting while out-of-plane deformation by buckling is a relatively new programming strategy. Both strategies differ mainly in the achievable target shapes. Integration of both strategies to benefit from the best of both worlds is recommended to increase the number of possible target configurations. Sequential folding could be also used for increasing the range of achievable shapes, while it could be used as a tool to improve the integrity and stability of the final shapes as well. Different applications are highlighted, which utilize the possibility of using conventional 2D techniques as well as the opportunity to create deployable structures with complex target configurations upon activation by a single scalar signal.

## Bibliography

1. Forterre, Y. and J. Dumais, *Generating helices in nature*. science, 2011. **333**(6050): p. 1715-1716.
2. So, S. and R.C. Hayward, *Tunable Upper Critical Solution Temperature of Poly (N-isopropylacrylamide) in Ionic Liquids for Sequential and Reversible Self-Folding*. ACS Applied Materials & Interfaces, 2017. **9**(18): p. 15785-15790.
3. Ge, Q., H.J. Qi, and M.L. Dunn, *Active materials by four-dimension printing*. Applied Physics Letters, 2013. **103**(13): p. 131901.
4. Baker, A.B., D.F. Wass, and R.S. Trask, *4D sequential actuation: combining ionoprinting and redox chemistry in hydrogels*. Smart Materials and Structures, 2016. **25**(10): p. 10LT02.
5. Dawson, C., J.F. Vincent, and A.-M. Rocca, *How pine cones open*. Nature, 1997. **390**(6661): p. 668-668.
6. Studart, A.R., *Biologically inspired dynamic material systems*. Angewandte Chemie International Edition, 2015. **54**(11): p. 3400-3416.
7. Boothby, J. and T. Ware, *Dual-responsive, shape-switching bilayers enabled by liquid crystal elastomers*. Soft Matter, 2017.
8. van Manen, T., S. Janbaz, and A.A. Zadpoor, *Programming 2D/3D shape-shifting with hobbyist 3D printers*. Materials Horizons, 2017.
9. Volkov, A.G., et al., *Mimosa pudica: electrical and mechanical stimulation of plant movements*. Plant, cell & environment, 2010. **33**(2): p. 163-173.
10. Erb, R.M., et al., *Self-shaping composites with programmable bioinspired microstructures*. Nature communications, 2013. **4**: p. 1712.
11. Zhang, Y., et al., *Printing, folding and assembly methods for forming 3D mesostructures in advanced materials*. Nature Reviews Materials, 2017. **2**: p. 17019.
12. Gladman, A.S., et al., *Biomimetic 4D printing*. Nature materials, 2016.
13. Lendlein, A., et al., *Light-induced shape-memory polymers*. Nature, 2005. **434**(7035): p. 879-882.
14. Lee, K.M., et al., *Photodriven, flexural-torsional oscillation of glassy azobenzene liquid crystal polymer networks*. Advanced Functional Materials, 2011. **21**(15): p. 2913-2918.
15. Ma, M., et al., *Bio-inspired polymer composite actuator and generator driven by water gradients*. Science, 2013. **339**(6116): p. 186-189.
16. Shen, X., et al., *Large negative thermal expansion of a polymer driven by a submolecular conformational change*. Nature chemistry, 2013. **5**(12): p. 1035-1041.
17. Brannon-Peppas, L. and N.A. Peppas, *Equilibrium swelling behavior of pH-sensitive hydrogels*. Chemical Engineering Science, 1991. **46**(3): p. 715-722.
18. Ionov, L., *Polymeric actuators*. Langmuir, 2014. **31**(18): p. 5015-5024.
19. Lendlein, A. and V.P. Shastri, *Stimuli-Sensitive Polymers*. Advanced Materials, 2010. **22**(31): p. 3344-3347.
20. White, E.M., et al., *Advances in smart materials: Stimuli-responsive hydrogel thin films*. Journal of Polymer Science Part B: Polymer Physics, 2013. **51**(14): p. 1084-1099.
21. Jeon, O., et al., *Photocrosslinked alginate hydrogels with tunable biodegradation rates and mechanical properties*. Biomaterials, 2009. **30**(14): p. 2724-2734.
22. Jeon, S.-J., A.W. Hauser, and R.C. Hayward, *Shape-morphing materials from stimuli-responsive hydrogel hybrids*. Accounts of chemical research, 2017. **50**(2): p. 161-169.
23. Liu, F. and M.W. Urban, *Recent advances and challenges in designing stimuli-responsive polymers*. Progress in Polymer Science, 2010. **35**(1): p. 3-23.
24. De las Heras Alarcón, C., S. Pennadam, and C. Alexander, *Stimuli responsive polymers for biomedical applications*. Chemical Society Reviews, 2005. **34**(3): p. 276-285.

25. Woltman, S.J., G.D. Jay, and G.P. Crawford, *Liquid-crystal materials find a new order in biomedical applications*. Nature materials, 2007. **6**(12): p. 929-938.
26. Ohm, C., M. Brehmer, and R. Zentel, *Liquid crystalline elastomers as actuators and sensors*. Advanced Materials, 2010. **22**(31): p. 3366-3387.
27. Zhao, Q., H.J. Qi, and T. Xie, *Recent progress in shape memory polymer: new behavior, enabling materials, and mechanistic understanding*. Progress in Polymer Science, 2015. **49**: p. 79-120.
28. Lendlein, A. and R. Langer, *Biodegradable, elastic shape-memory polymers for potential biomedical applications*. Science, 2002. **296**(5573): p. 1673-1676.
29. Ratna, D. and J. Karger-Kocsis, *Recent advances in shape memory polymers and composites: a review*. Journal of Materials Science, 2008. **43**(1): p. 254-269.
30. Liu, Y., J. Genzer, and M.D. Dickey, *"2D or not 2D": Shape-programming polymer sheets*. Progress in Polymer Science, 2016. **52**: p. 79-106.
31. Efrati, E., E. Sharon, and R. Kupferman, *Elastic theory of unconstrained non-Euclidean plates*. Journal of the Mechanics and Physics of Solids, 2009. **57**(4): p. 762-775.
32. Efrati, E., E. Sharon, and R. Kupferman, *The metric description of elasticity in residually stressed soft materials*. Soft Matter, 2013. **9**(34): p. 8187-8197.
33. Sharon, E. and E. Efrati, *The mechanics of non-Euclidean plates*. Soft Matter, 2010. **6**(22): p. 5693-5704.
34. Cendula, P., et al., *Bending and wrinkling as competing relaxation pathways for strained free-hanging films*. Physical Review B, 2009. **79**(8): p. 085429.
35. Timoshenko, S., *Analysis of bi-metal thermostats*. Josa, 1925. **11**(3): p. 233-255.
36. Bassik, N., et al., *Photolithographically patterned smart hydrogel based bilayer actuators*. Polymer, 2010. **51**(26): p. 6093-6098.
37. Egunov, A., J. Korvink, and V. Luchnikov, *Polydimethylsiloxane bilayer films with an embedded spontaneous curvature*. Soft matter, 2016. **12**(1): p. 45-52.
38. Guan, J., et al., *Self-folding of three-dimensional hydrogel microstructures*. The Journal of Physical Chemistry B, 2005. **109**(49): p. 23134-23137.
39. Hu, Z., X. Zhang, and Y. Li, *Synthesis and application of modulated polymer gels*. Science, 1995. **269**(5223): p. 525.
40. Stoychev, G., N. Puretskiy, and L. Ionov, *Self-folding all-polymer thermoresponsive microcapsules*. Soft Matter, 2011. **7**(7): p. 3277-3279.
41. Stoychev, G., et al., *Hierarchical multi-step folding of polymer bilayers*. Advanced Functional Materials, 2013. **23**(18): p. 2295-2300.
42. Kim, J., et al., *Reversible self-bending soft hydrogel microstructures with mechanically optimized designs*. Chemical Engineering Journal, 2017. **321**: p. 384-393.
43. Stoychev, G., et al., *Hole-Programmed Superfast Multistep Folding of Hydrogel Bilayers*. Advanced Functional Materials, 2016. **26**(42): p. 7733-7739.
44. Zhang, X., et al., *Optically-and thermally-responsive programmable materials based on carbon nanotube-hydrogel polymer composites*. Nano letters, 2011. **11**(8): p. 3239-3244.
45. Oh, M.S., et al., *Control of Reversible Self-Bending Behavior in Responsive Janus Microstrips*. ACS applied materials & interfaces, 2016. **8**(13): p. 8782-8788.
46. Naficy, S., et al., *4D printing of reversible shape morphing hydrogel structures*. Macromolecular Materials and Engineering, 2017. **302**(1).
47. Guo, W., M. Li, and J. Zhou, *Modeling programmable deformation of self-folding all-polymer structures with temperature-sensitive hydrogels*. Smart Materials and Structures, 2013. **22**(11): p. 115028.
48. Alben, S., B. Balakrishnan, and E. Smela, *Edge effects determine the direction of bilayer bending*. Nano letters, 2011. **11**(6): p. 2280-2285.
49. Chen, Z., et al., *Nonlinear geometric effects in mechanical bistable morphing structures*. Physical review letters, 2012. **109**(11): p. 114302.



50. Finot, M. and S. Suresh, *Small and large deformation of thick and thin-film multi-layers: effects of layer geometry, plasticity and compositional gradients*. Journal of the Mechanics and Physics of Solids, 1996. **44**(5): p. 683-721.
51. Mansfield, E. *Bending, buckling and curling of a heated thin plate*. in *Proceedings of the Royal Society of London A: Mathematical, Physical and Engineering Sciences*. 1962. The Royal Society.
52. Dunn, M.L., Y. Zhang, and V.M. Bright, *Deformation and structural stability of layered plate microstructures subjected to thermal loading*. Journal of Microelectromechanical Systems, 2002. **11**(4): p. 372-384.
53. Freund, L., *Substrate curvature due to thin film mismatch strain in the nonlinear deformation range*. Journal of the Mechanics and Physics of Solids, 2000. **48**(6): p. 1159-1174.
54. Harper, B.D. and W. Chih-Ping, *A geometrically nonlinear model for predicting the intrinsic film stress by the bending-plate method*. International journal of solids and structures, 1990. **26**(5-6): p. 511-525.
55. Salamon, N. and C.B. Masters, *Bifurcation in isotropic thinfilm/substrate plates*. International journal of solids and structures, 1995. **32**(3-4): p. 473-481.
56. Lin, S., et al., *On the shape transformation of cone scales*. Soft Matter, 2016. **12**(48): p. 9797-9802.
57. Alben, S., *Bending of bilayers with general initial shapes*. arXiv preprint arXiv:1110.1007, 2011.
58. Stoychev, G., et al., *Shape-programmed folding of stimuli-responsive polymer bilayers*. ACS nano, 2012. **6**(5): p. 3925-3934.
59. Raviv, D., et al., *Active printed materials for complex self-evolving deformations*. Scientific reports, 2014. **4**: p. 7422.
60. Tibbitts, S., *4D printing: multi-material shape change*. Architectural Design, 2014. **84**(1): p. 116-121.
61. An, B., et al. *An end-to-end approach to making self-folded 3D surface shapes by uniform heating*. in *Robotics and Automation (ICRA), 2014 IEEE International Conference on*. 2014. IEEE.
62. Felton, S., et al., *Self-folding with shape memory composites at the millimeter scale*. Journal of Micromechanics and Microengineering, 2015. **25**(8): p. 085004.
63. Felton, S., et al., *A method for building self-folding machines*. Science, 2014. **345**(6197): p. 644-646.
64. Felton, S.M., et al., *Self-folding with shape memory composites*. Soft Matter, 2013. **9**(32): p. 7688-7694.
65. Miyashita, S., et al. *An untethered miniature origami robot that self-folds, walks, swims, and degrades*. in *Robotics and Automation (ICRA), 2015 IEEE International Conference on*. 2015. IEEE.
66. Miyashita, S., et al. *Self-folding printable elastic electric devices: Resistor, capacitor, and inductor*. in *Robotics and Automation (ICRA), 2014 IEEE International Conference on*. 2014. IEEE.
67. Miyashita, S., et al., *Self-folding miniature elastic electric devices*. Smart Materials and Structures, 2014. **23**(9): p. 094005.
68. Miyashita, S., C.D. Onal, and D. Rus. *Self-pop-up cylindrical structure by global heating*. in *Intelligent Robots and Systems (IROS), 2013 IEEE/RSJ International Conference on*. 2013. IEEE.
69. Tolley, M.T., et al., *Self-folding origami: shape memory composites activated by uniform heating*. Smart Materials and Structures, 2014. **23**(9): p. 094006.
70. An, N., M. Li, and J. Zhou, *Predicting origami-inspired programmable self-folding of hydrogel trilayers*. Smart Materials and Structures, 2016. **25**(11): p. 11LT02.
71. Na, J.H., et al., *Programming reversibly self-folding origami with micropatterned photo-crosslinkable polymer trilayers*. Advanced Materials, 2015. **27**(1): p. 79-85.
72. Chen, Z., et al., *Mechanical self-assembly of a strain-engineered flexible layer: wrinkling, rolling, and twisting*. Physical Review Applied, 2016. **5**(1): p. 017001.

73. Janbaz, S., R. Hedayati, and A. Zadpoor, *Programming the shape-shifting of flat soft matter: from self-rolling/self-twisting materials to self-folding origami*. Materials Horizons, 2016. **3**(6): p. 536-547.
74. de Haan, L.T., et al., *Humidity-responsive liquid crystalline polymer actuators with an asymmetry in the molecular trigger that bend, fold, and curl*. Journal of the American Chemical Society, 2014. **136**(30): p. 10585-10588.
75. Armon, S., et al., *Geometry and mechanics in the opening of chiral seed pods*. Science, 2011. **333**(6050): p. 1726-1730.
76. Guo, Q., et al., *Shape selection and multi-stability in helical ribbons*. Applied Physics Letters, 2014. **104**(21): p. 211901.
77. Armon, S., et al., *Shape selection in chiral ribbons: from seed pods to supramolecular assemblies*. Soft Matter, 2014. **10**(16): p. 2733-2740.
78. Ge, Q., et al., *Active origami by 4D printing*. Smart Materials and Structures, 2014. **23**(9): p. 094007.
79. Wu, J., et al., *Multi-shape active composites by 3D printing of digital shape memory polymers*. Scientific reports, 2016. **6**.
80. Chen, S., et al., *Simple triple-state polymer actuators with controllable folding characteristics*. Applied Physics Letters, 2017. **110**(13): p. 133506.
81. Mao, Y., et al., *3D printed reversible shape changing components with stimuli responsive materials*. Scientific reports, 2016. **6**: p. 24761.
82. Zhou, J. and S.S. Sheiko, *Reversible shape-shifting in polymeric materials*. Journal of Polymer Science Part B: Polymer Physics, 2016. **54**(14): p. 1365-1380.
83. Agrawal, A., et al., *Shape-responsive liquid crystal elastomer bilayers*. Soft Matter, 2014. **10**(9): p. 1411-1415.
84. Erb, R.M., et al., *Composites reinforced in three dimensions by using low magnetic fields*. Science, 2012. **335**(6065): p. 199-204.
85. Kokkinis, D., M. Schaffner, and A.R. Studart, *Multimaterial magnetically assisted 3D printing of composite materials*. Nature communications, 2015. **6**.
86. Jamal, M., A.M. Zarafshar, and D.H. Gracias, *Differentially photo-crosslinked polymers enable self-assembling microfluidics*. Nature communications, 2011. **2**: p. 527.
87. Yoon, C., et al., *Functional stimuli responsive hydrogel devices by self-folding*. Smart Materials and Structures, 2014. **23**(9): p. 094008.
88. Zhao, Z., et al., *Desolvation Induced Origami of Photocurable Polymers by Digit Light Processing*. Macromolecular Rapid Communications, 2016.
89. Ryu, J., et al., *Photo-origami—Bending and folding polymers with light*. Applied Physics Letters, 2012. **100**(16): p. 161908.
90. Danielson, C., et al., *Fabrication and characterization of self-folding thermoplastic sheets using unbalanced thermal shrinkage*. Soft Matter, 2017.
91. Behl, M., M.Y. Razzaq, and A. Lendlein, *Multifunctional Shape-Memory Polymers*. Advanced materials, 2010. **22**(31): p. 3388-3410.
92. Zhao, Z., et al., *Origami by frontal photopolymerization*. Science Advances, 2017. **3**(4): p. e1602326.
93. Asoh, T.a., et al., *Fabrication of Temperature-Responsive Bending Hydrogels with a Nanostructured Gradient*. Advanced Materials, 2008. **20**(11): p. 2080-2083.
94. Liu, Y., et al., *Programmable responsive shaping behavior induced by visible multi-dimensional gradients of magnetic nanoparticles*. Soft Matter, 2012. **8**(12): p. 3295-3299.
95. Morales, D., et al., *Bending of Responsive Hydrogel Sheets Guided by Field-Assembled Microparticle Endoskeleton Structures*. Small, 2016. **12**(17): p. 2283-2290.
96. Konotop, I.Y., et al., *Novel pH-responsive hydrogels with gradient charge distribution*. Soft Matter, 2010. **6**(8): p. 1632-1634.
97. Tokuyama, H., M. Sasaki, and S. Sakohara, *Preparation of a novel composition-gradient thermosensitive gel*. Colloids and Surfaces A: Physicochemical and Engineering Aspects, 2006. **273**(1): p. 70-74.



98. Palleau, E., et al., *Reversible patterning and actuation of hydrogels by electrically assisted ionoprinting*. Nature communications, 2013. **4**: p. 2257.
99. Sawa, Y., et al., *Shape selection of twist-nematic-elastomer ribbons*. Proceedings of the National Academy of Sciences, 2011. **108**(16): p. 6364-6368.
100. Lee, B.P. and S. Konst, *Novel hydrogel actuator inspired by reversible mussel adhesive protein chemistry*. Advanced Materials, 2014. **26**(21): p. 3415-3419.
101. Harris, K.D., C.W. Bastiaansen, and D.J. Broer, *A Glassy Bending-Mode Polymeric Actuator Which Deforms in Response to Solvent Polarity*. Macromolecular rapid communications, 2006. **27**(16): p. 1323-1329.
102. Iamsaard, S., et al., *Conversion of light into macroscopic helical motion*. Nature chemistry, 2014. **6**(3): p. 229-235.
103. Sawa, Y., et al., *Shape and chirality transitions in off-axis twist nematic elastomer ribbons*. Physical Review E, 2013. **88**(2): p. 022502.
104. Mol, G.N., et al., *Thermo-Mechanical Responses of Liquid-Crystal Networks with a Splayed Molecular Organization*. Advanced Functional Materials, 2005. **15**(7): p. 1155-1159.
105. de Haan, L.T., et al., *Accordion-like Actuators of Multiple 3D Patterned Liquid Crystal Polymer Films*. Advanced Functional Materials, 2014. **24**(9): p. 1251-1258.
106. de Haan, L.T., et al., *Engineering of complex order and the macroscopic deformation of liquid crystal polymer networks*. Angewandte Chemie International Edition, 2012. **51**(50): p. 12469-12472.
107. Lee, D.-W., J. Phadikar, and M.R. Shankar, *Multiplicity of shape selection in functionally graded liquid crystalline polymers*. RSC Advances, 2017. **7**(37): p. 23046-23054.
108. Holmes, D.P., et al., *Bending and twisting of soft materials by non-homogenous swelling*. Soft Matter, 2011. **7**(11): p. 5188-5193.
109. Reyssat, E. and L. Mahadevan, *How wet paper curls*. EPL (Europhysics Letters), 2011. **93**(5): p. 54001.
110. Tomatsu, I., K. Peng, and A. Kros, *Photoresponsive hydrogels for biomedical applications*. Advanced drug delivery reviews, 2011. **63**(14): p. 1257-1266.
111. Wang, E., M.S. Desai, and S.-W. Lee, *Light-controlled graphene-elastin composite hydrogel actuators*. Nano letters, 2013. **13**(6): p. 2826-2830.
112. Liu, Y., et al., *Three-dimensional folding of pre-strained polymer sheets via absorption of laser light*. Journal of Applied Physics, 2014. **115**(20): p. 204911.
113. Liu, Y., et al., *Self-folding of polymer sheets using local light absorption*. Soft Matter, 2012. **8**(6): p. 1764-1769.
114. Davis, D., et al., *Self-folding of polymer sheets using microwaves and graphene ink*. RSC Advances, 2015. **5**(108): p. 89254-89261.
115. Zhang, Q., et al., *Origami and kirigami inspired self-folding for programming three-dimensional shape shifting of polymer sheets with light*. Extreme Mechanics Letters, 2017. **11**: p. 111-120.
116. Cui, J., et al., *Controlling the self-folding of a polymer sheet using a local heater: the effect of the polymer-heater interface*. Soft Matter, 2017.
117. Efrati, E., E. Sharon, and R. Kupferman, *Buckling transition and boundary layer in non-Euclidean plates*. Physical Review E, 2009. **80**(1): p. 016602.
118. Liang, H. and L. Mahadevan, *Growth, geometry, and mechanics of a blooming lily*. Proceedings of the National Academy of Sciences, 2011. **108**(14): p. 5516-5521.
119. Dervaux, J. and M.B. Amar, *Morphogenesis of growing soft tissues*. Physical review letters, 2008. **101**(6): p. 068101.
120. Eran, S., M. Marder, and H.L. Swinney, *Leaves, flowers and garbage bags: making waves*. American Scientist, 2004. **92**(3): p. 254.
121. Kim, J., et al., *Thermally responsive rolling of thin gel strips with discrete variations in swelling*. Soft Matter, 2012. **8**(8): p. 2375-2381.
122. Byun, M., C.D. Santangelo, and R.C. Hayward, *Swelling-driven rolling and anisotropic expansion of striped gel sheets*. Soft Matter, 2013. **9**(34): p. 8264-8273.

123. Moshe, M., E. Sharon, and R. Kupferman, *Pattern selection and multiscale behaviour in metrically discontinuous non-Euclidean plates*. *Nonlinearity*, 2013. **26**(12): p. 3247.
124. Bae, J., et al., *Edge-defined metric buckling of temperature-responsive hydrogel ribbons and rings*. *Polymer*, 2014. **55**(23): p. 5908-5914.
125. Thérien-Aubin, H.I., et al., *Multiple shape transformations of composite hydrogel sheets*. *Journal of the American Chemical Society*, 2013. **135**(12): p. 4834-4839.
126. Wu, Z.L., et al., *Three-dimensional shape transformations of hydrogel sheets induced by small-scale modulation of internal stresses*. *Nature communications*, 2013. **4**: p. 1586.
127. Thérien-Aubin, H., et al., *Shape transformations of soft matter governed by bi-axial stresses*. *Soft Matter*, 2015. **11**(23): p. 4600-4605.
128. de Haan, L.T., et al., *Engineering of complex order and the macroscopic deformation of liquid crystal polymer networks*. *Angewandte Chemie*, 2012. **124**(50): p. 12637-12640.
129. Huang, L., et al., *Ultrafast digital printing toward 4D shape changing materials*. *Advanced Materials*, 2017. **29**(7).
130. Long, K.N., et al., *Photo-induced deformation of active polymer films: Single spot irradiation*. *International Journal of Solids and Structures*, 2011. **48**(14): p. 2089-2101.
131. Pezzulla, M., et al., *Morphing of geometric composites via residual swelling*. *Soft Matter*, 2015. **11**(29): p. 5812-5820.
132. Efrati, E., et al., *Spontaneous buckling of elastic sheets with a prescribed non-Euclidean metric*. *Physica D: Nonlinear Phenomena*, 2007. **235**(1): p. 29-32.
133. Klein, Y., E. Efrati, and E. Sharon, *Shaping of elastic sheets by prescription of non-Euclidean metrics*. *Science*, 2007. **315**(5815): p. 1116-1120.
134. Klein, Y., S. Venkataramani, and E. Sharon, *Experimental study of shape transitions and energy scaling in thin non-euclidean plates*. *Physical review letters*, 2011. **106**(11): p. 118303.
135. Na, J.-H., et al., *Grayscale gel lithography for programmed buckling of non-Euclidean hydrogel plates*. *Soft matter*, 2016. **12**(22): p. 4985-4990.
136. Kim, J., et al., *Designing responsive buckled surfaces by halftone gel lithography*. *Science*, 2012. **335**(6073): p. 1201-1205.
137. Hauser, A.W., et al., *Photothermally reprogrammable buckling of nanocomposite gel sheets*. *Angewandte Chemie International Edition*, 2015. **54**(18): p. 5434-5437.
138. Chen, T., et al., *A "writing" strategy for shape transition with infinitely adjustable shaping sequences and in situ tunable 3D structures*. *Materials Horizons*, 2016. **3**(6): p. 581-587.
139. Yu, C., et al., *Electronically Programmable, Reversible Shape Change in Two-and Three-Dimensional Hydrogel Structures*. *Advanced Materials*, 2013. **25**(11): p. 1541-1546.
140. Chen, D., et al., *Stimuli-responsive buckling mechanics of polymer films*. *Journal of Polymer Science Part B: Polymer Physics*, 2014. **52**(22): p. 1441-1461.
141. Rodríguez-Hernández, J., *Wrinkled interfaces: Taking advantage of surface instabilities to pattern polymer surfaces*. *Progress in Polymer Science*, 2015. **42**: p. 1-41.
142. Yang, S., K. Khare, and P.C. Lin, *Harnessing surface wrinkle patterns in soft matter*. *Advanced Functional Materials*, 2010. **20**(16): p. 2550-2564.
143. Mei, H., et al., *Buckling modes of elastic thin films on elastic substrates*. *Applied Physics Letters*, 2007. **90**(15): p. 151902.
144. Vella, D., et al., *The macroscopic delamination of thin films from elastic substrates*. *Proceedings of the National Academy of Sciences*, 2009. **106**(27): p. 10901-10906.
145. Sun, Y., et al., *Controlled buckling of semiconductor nanoribbons for stretchable electronics*. *Nature nanotechnology*, 2006. **1**(3): p. 201-207.

146. Xu, S., et al., *Assembly of micro/nanomaterials into complex, three-dimensional architectures by compressive buckling*. Science, 2015. **347**(6218): p. 154-159.
147. Yan, Z., et al., *Controlled Mechanical Buckling for Origami-Inspired Construction of 3D Microstructures in Advanced Materials*. Advanced Functional Materials, 2016.
148. Yan, Z., et al., *Mechanical assembly of complex, 3D mesostructures from releasable multilayers of advanced materials*. Science Advances, 2016. **2**(9): p. e1601014.
149. Yan, Z., et al., *Deterministic assembly of 3D mesostructures in advanced materials via compressive buckling: A short review of recent progress*. Extreme Mechanics Letters, 2016.
150. Laflin, K.E., et al., *Laser triggered sequential folding of microstructures*. Applied Physics Letters, 2012. **101**(13): p. 131901.
151. Ge, Q., et al., *Multimaterial 4D printing with tailorable shape memory polymers*. Scientific Reports, 2016. **6**.
152. Mao, Y., et al., *Sequential self-folding structures by 3D printed digital shape memory polymers*. Scientific reports, 2015. **5**: p. 13616.
153. Yu, K., et al., *Controlled sequential shape changing components by 3D printing of shape memory polymer multimaterials*. Procedia IUTAM, 2015. **12**: p. 193-203.
154. Lee, Y., et al., *Sequential folding using light-activated polystyrene sheet*. Scientific reports, 2015. **5**: p. 16544.
155. Liu, Y., et al., *Sequential self-folding of polymer sheets*. Science Advances, 2017. **3**(3): p. e1602417.
156. Razzaq, M.Y., et al., *Triple-Shape Effect in Polymer-Based Composites by Cleverly Matching Geometry of Active Component with Heating Method*. Advanced Materials, 2013. **25**(38): p. 5514-5518.
157. Schenk, M. and S.D. Guest, *Geometry of Miura-folded metamaterials*. Proceedings of the National Academy of Sciences, 2013. **110**(9): p. 3276-3281.
158. Lv, C., et al., *Origami based mechanical metamaterials*. Scientific reports, 2014. **4**.
159. Randhawa, J.S., et al., *Three-dimensional surface current loops in terahertz responsive microarrays*. Applied Physics Letters, 2010. **96**(19): p. 191108.
160. Cho, J.H., et al., *Nanoscale origami for 3D optics*. Small, 2011. **7**(14): p. 1943-1948.
161. Azam, A., et al., *Self-folding micropatterned polymeric containers*. Biomedical microdevices, 2011. **13**(1): p. 51-58.
162. Jamal, M., et al., *Directed growth of fibroblasts into three dimensional micropatterned geometries via self-assembling scaffolds*. Biomaterials, 2010. **31**(7): p. 1683-1690.
163. Breger, J.C., et al., *Self-folding thermo-magnetically responsive soft microgrippers*. ACS applied materials & interfaces, 2015. **7**(5): p. 3398-3405.
164. Bassik, N., et al., *Enzymatically triggered actuation of miniaturized tools*. Journal of the American Chemical Society, 2010. **132**(46): p. 16314-16317.
165. Gultepe, E., et al., *Biopsy with Thermally-Responsive Untethered Microtools*. Advanced materials, 2013. **25**(4): p. 514-519.
166. Leong, T.G., et al., *Tetherless thermobiochemically actuated microgrippers*. Proceedings of the National Academy of Sciences, 2009. **106**(3): p. 703-708.
167. Mu, J., et al., *Origami-inspired active graphene-based paper for programmable instant self-folding walking devices*. Science advances, 2015. **1**(10): p. e1500533.
168. Rogers, J.A., T. Someya, and Y. Huang, *Materials and mechanics for stretchable electronics*. science, 2010. **327**(5973): p. 1603-1607.
169. Zhang, Y., Y. Huang, and J.A. Rogers, *Mechanics of stretchable batteries and supercapacitors*. Current Opinion in Solid State and Materials Science, 2015. **19**(3): p. 190-199.
170. Dudte, L.H., et al., *Programming curvature using origami tessellations*. Nature materials, 2016. **15**(5): p. 583-588.
171. Sussman, D.M., et al., *Algorithmic lattice kirigami: A route to pluripotent materials*. Proceedings of the National Academy of Sciences, 2015. **112**(24): p. 7449-7453.

172. Callens, S.J. and A.A. Zadpoor, *From flat sheets to curved geometries: Origami and kirigami approaches*. Materials Today, 2018. **21**(3): p. 241-264.
173. Randall, C.L., E. Gultepe, and D.H. Gracias, *Self-folding devices and materials for biomedical applications*. Trends in biotechnology, 2012. **30**(3): p. 138-146.
174. Fernandes, R. and D.H. Gracias, *Self-folding polymeric containers for encapsulation and delivery of drugs*. Advanced drug delivery reviews, 2012. **64**(14): p. 1579-1589.
175. Champion, J.A., Y.K. Katare, and S. Mitragotri, *Particle shape: a new design parameter for micro-and nanoscale drug delivery carriers*. Journal of Controlled Release, 2007. **121**(1): p. 3-9.
176. Gratton, S.E., et al., *The effect of particle design on cellular internalization pathways*. Proceedings of the National Academy of Sciences, 2008. **105**(33): p. 11613-11618.
177. He, C., et al., *Effects of particle size and surface charge on cellular uptake and biodistribution of polymeric nanoparticles*. Biomaterials, 2010. **31**(13): p. 3657-3666.
178. Win, K.Y. and S.-S. Feng, *Effects of particle size and surface coating on cellular uptake of polymeric nanoparticles for oral delivery of anticancer drugs*. Biomaterials, 2005. **26**(15): p. 2713-2722.
179. Kalinin, Y.V., J.S. Randhawa, and D.H. Gracias, *Three-Dimensional Chemical Patterns for Cellular Self-Organization*. Angewandte Chemie International Edition, 2011. **50**(11): p. 2549-2553.
180. Randall, C.L., et al., *Self-folding immunoprotective cell encapsulation devices*. Nanomedicine: Nanotechnology, Biology and Medicine, 2011. **7**(6): p. 686-689.
181. Orive, G., et al., *Application of cell encapsulation for controlled delivery of biological therapeutics*. Advanced drug delivery reviews, 2014. **67**: p. 3-14.
182. Cukierman, E., et al., *Taking cell-matrix adhesions to the third dimension*. Science, 2001. **294**(5547): p. 1708-1712.
183. Tibbitt, M.W. and K.S. Anseth, *Hydrogels as extracellular matrix mimics for 3D cell culture*. Biotechnology and bioengineering, 2009. **103**(4): p. 655-663.
184. Engler, A.J., et al., *Matrix elasticity directs stem cell lineage specification*. Cell, 2006. **126**(4): p. 677-689.
185. Guilak, F., et al., *Control of stem cell fate by physical interactions with the extracellular matrix*. Cell stem cell, 2009. **5**(1): p. 17-26.
186. Pelham, R.J. and Y.-I. Wang, *Cell locomotion and focal adhesions are regulated by substrate flexibility*. Proceedings of the National Academy of Sciences, 1997. **94**(25): p. 13661-13665.
187. McNamara, L.E., et al., *Nanotopographical control of stem cell differentiation*. Journal of tissue engineering, 2010. **1**(1): p. 120623.
188. Yim, E.K., S.W. Pang, and K.W. Leong, *Synthetic nanostructures inducing differentiation of human mesenchymal stem cells into neuronal lineage*. Experimental cell research, 2007. **313**(9): p. 1820-1829.
189. Dobbenga, S., L.E. Fratila-Apachitei, and A.A. Zadpoor, *Nanopattern-induced osteogenic differentiation of stem cells—A systematic review*. Acta biomaterialia, 2016. **46**: p. 3-14.
190. Jamal, M., et al., *Bio-Origami Hydrogel Scaffolds Composed of Photocrosslinked PEG Bilayers*. Advanced healthcare materials, 2013. **2**(8): p. 1142-1150.
191. Gracias, D.H., et al., *Forming electrical networks in three dimensions by self-assembly*. science, 2000. **289**(5482): p. 1170-1172.
192. Kuribayashi, K., et al., *Self-deployable origami stent grafts as a biomedical application of Ni-rich TiNi shape memory alloy foil*. Materials Science and Engineering: A, 2006. **419**(1-2): p. 131-137.
193. Ward Small, I., et al., *Biomedical applications of thermally activated shape memory polymers*. Journal of materials chemistry, 2010. **20**(17): p. 3356-3366.
194. Pandey, S., et al., *Assembly of a 3D Cellular Computer Using Folded E-Blocks*. Micromachines, 2016. **7**(5): p. 78.

195. Kolken, H.M. and A. Zadpoor, *Auxetic mechanical metamaterials*. RSC advances, 2017. **7**(9): p. 5111-5129.
196. Zadpoor, A.A., *Mechanical meta-materials*. Materials Horizons, 2016. **3**(5): p. 371-381.
197. Hanna, B.H., et al., *Waterbomb base: a symmetric single-vertex bistable origami mechanism*. Smart Materials and Structures, 2014. **23**(9): p. 094009.
198. Silverberg, J.L., et al., *Origami structures with a critical transition to bistability arising from hidden degrees of freedom*. Nature materials, 2015. **14**(4): p. 389-393.
199. Shen, Y., et al., *Origami-inspired metamaterial absorbers for improving the larger-incident angle absorption*. Journal of Physics D: Applied Physics, 2015. **48**(44): p. 445008.
200. Song, Z., et al., *Origami lithium-ion batteries*. Nature communications, 2014. **5**: p. 3140.
201. Tang, R., et al., *Origami-enabled deformable silicon solar cells*. Applied Physics Letters, 2014. **104**(8): p. 083501.
202. Ahn, S.-k., et al., *Stimuli-responsive polymer gels*. Soft Matter, 2008. **4**(6): p. 1151-1157.
203. Lin, S., et al., *Design of stiff, tough and stretchy hydrogel composites via nanoscale hybrid crosslinking and macroscale fiber reinforcement*. Soft matter, 2014. **10**(38): p. 7519-7527.
204. Bakarich, S.E., et al., *Three-dimensional printing fiber reinforced hydrogel composites*. ACS applied materials & interfaces, 2014. **6**(18): p. 15998-16006.
205. Chen, J. and K. Park, *Synthesis and characterization of superporous hydrogel composites*. Journal of Controlled Release, 2000. **65**(1): p. 73-82.
206. Randhawa, J.S., et al., *Importance of surface patterns for defect mitigation in three-dimensional self-assembly*. Langmuir, 2010. **26**(15): p. 12534-12539.





# Theoretical stiffness limits of 4D printed self-folding metamaterials **3**

4D printing of flat sheets that self-fold into architected 3D structures is a powerful origami-inspired approach for the fabrication of multi-functional devices and metamaterials. However, the opposite stiffness requirements for the folding process and the subsequent loadbearing of 3D structures impose an intrinsic limitation in designing self-folding metamaterials: while a low stiffness is required for the successful completion of the self-folding step, a high stiffness is needed for utilizing the folded structure as a load-bearing mechanical metamaterial. Here, we present a nonlinear analytical model of self-folding bilayer constructs composed of an active and passive layer. This finite-deformation theoretical model predicts the curvature of activated bilayers, establishes their stability limits, and estimates the stiffness of folded bilayers, yielding the theoretical stiffness limits of self-folding bilayers. We use our model to identify the optimal combinations of geometrical and mechanical properties that result in the highest possible stiffness of folded constructs. We then compare the predictions of our analytical model with computational results, and validate our theory with experimental realizations of 4D printed structures. Finally, we evaluate the theoretical stiffness limits of bilayer constructs made using the most common types of stimuli-responsive materials. Our analysis shows that a maximum effective modulus of  $\approx 1.5$  GPa can be achieved using the currently available shape-memory polymers.

T. van Manen, V.M. Dehabadi, M. C. Saldívar, M.J. Mirzaali & A.A. Zadpoor (2022). *Theoretical stiffness limits of 4D printed self-folding metamaterials*. Communications Materials, **3**: 43.



## List of variables

$\alpha$	Expansion ratio
$\beta$	Thickness ratio
$\beta_c$	Thickness ratio of the curved beam
$\gamma$	Stiffness ratio
$\delta$	Displacement of the point of application of force $P$
$\Delta x$	Lattice compression
$\epsilon$	Strain
$\bar{\theta}$	Half bent angle of the curved beam
$\kappa$	Curvature
$\lambda$	Principle stretch
$\sigma$	Cauchy stress tensor
$\Sigma$	First Piola Kirckhoff stress tensor.
$\tau$	Shear stress
$a$	Outer dimensions of a cubic lattice
$A_i$	Cross-section area of layer $i$
$b$	Width of a bilayer folding element
$\mathbf{B}$	Left Cauchy–Green deformation tensor
$C$	Bound on thickness ratio and stiffness ratio
$C_{10}^{(i)}$	Neo-Hookean material constant of layer $i$
$E_i$	Young’s modulus of layer $i$
$E_L$	Effective modulus of a cubic lattice
$F$	Lattice compression force
$\mathbf{F}$	Deformation gradient
$G_i$	Shear modulus of layer $i$
$h_i$	Thickness of layer $i$
$H$	Total thickness of the activated bilayer in the flat state
$H_c$	Total thickness of the activated bilayer in the curved state
$J$	Jacobian
$k_{\text{total}}$	Total lattice stiffness
$k_{\text{hinge}}$	Hinge stiffness
$\mathbf{L}$	Gradient of the incremental displacement field $\mathbf{u}$
$L_i$	Length of layer $i$ in the activated flat state
$M$	Moment at the beam cross-section
$N$	Normal force at the beam cross-section
$p$	Pressure
$P$	Applied compressive force at a curved beam
$r_c$	Centroid of the composite bilayer beam
$r_i$	Inner radius
$r_m$	Interface radius
$r_n$	Radius of neutral axis
$r_o$	Outer radius
$\mathbf{u}$	Incremental displacement field
$U$	Total internal energy
$V$	Shear force at the beam cross-section
$W$	Strain energy density function

### 3.1. Introduction

Folding initially flat materials into 3D objects through origami-inspired approaches is a highly promising approach for the fabrication of functionalized metamaterials [1]. One example is the production of 3D hollow polyhedral structures with integrated electronics [2]. Other examples include optical metamaterials made of porous polymer structures patterned with metallic split-ring resonators [3, 4] or tissue engineering scaffolds with different types of (nano)topographical features [5, 6]. What all these examples have in common is that those specific surface features were applied to the surface of an initially flat construct. In this way, planar fabrication techniques (e.g., nanolithography) can be used for small-scale, highly precise ornamentation of the construct surface or for the incorporation of other surface features. Subsequently, self-folding techniques are used for the transformation of the functionalized flat sheets into the desired, complex 3D geometries. Using such an approach, multi-functional, 3D-architected materials can be realized.

Various strategies have been developed for the self-folding of flat sheets into 3D structures [7-9]. The vast majority of such strategies rely on the use of the so-called stimuli responsive materials [9, 10] that exhibit dimensional change upon exposure to a specific stimulus. Two well-known stimuli include temperature that is used for the activation of shape-memory polymers and humidity that induces swelling in hydrogels [7, 11]. A wide range of other responsive materials activated by a variety of different stimuli is reported in the literature [11, 12]. To fabricate self-folding elements, such active materials can be combined with other (*i.e.*, passive) materials to design a specific shape-shifting behavior. A widely applied strategy is to combine two layers of different materials into a bilayer construct [7, 9, 13]. Upon activation, the mismatch in the shape-shifting behaviors of both materials results in the bending of the bilayer specimen. While the fabrication of bilayer constructs can be performed manually, such manual processes are often very laborious and time consuming. The advent of 4D printing processes have made it possible to fabricate bi- and multi-layer constructs fully automatically [14-17]. When combined with rational geometrical design, 4D printing can yield complex shape-shifting behaviors [15, 17] that are otherwise very difficult, if not impossible, to achieve. Moreover, 4D printing can nowadays be performed using inexpensive (*i.e.*, hobbyist) printers and widely available, off-the-shelf, inexpensive materials [17, 18]. 4D printing is, therefore, developing into the *de facto* technique for the production of shape-shifting materials, such as bi-layer constructs.

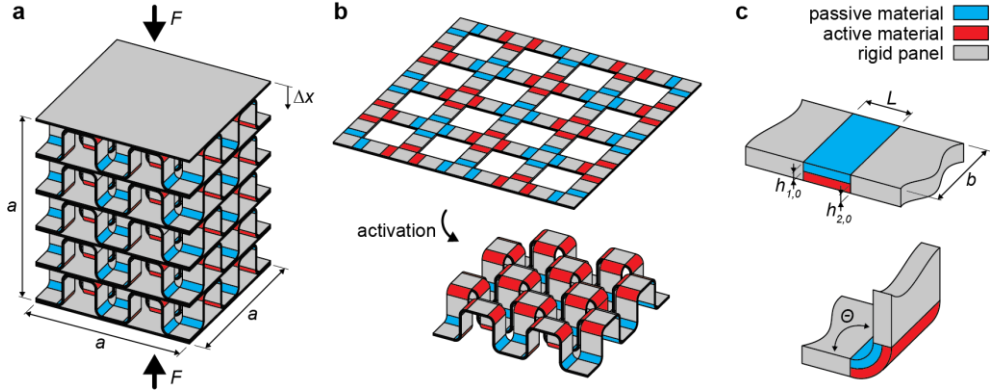
Depending on their ultimate application, self-folding materials and devices need to satisfy various design requirements. One particularly important requirement, particularly in the context of mechanical metamaterials, is the stiffness of the folded construct. For example, the desired shape of reconfigurable metamaterials

needs to be maintained under specific loading conditions to guarantee performance [19-22]. Another example is meta-biomaterials that need to match the mechanical properties of the native bone [5, 6].

The limited stiffness of self-folded constructs is due to an inherent contradiction between the design requirements of the self-folding and load-bearing steps: while a thinner construct with a lower stiffness is required in the self-folding step, a thicker construct is essential for maximizing the load-bearing capacity of the folded structure. One approach to circumvent this inherent stiffness contradiction is the use of folding elements with tunable stiffness. Upon the completion of the folding process, the hinges are stiffened to enhance the load-bearing capacity of the folded structure. One example of such a tunable stiffness element is a so-called 'layer-jamming' mechanisms in which a stack of thin folding elements is pressed together to increase its stiffness in the bent configuration [23, 24]. Yet another alternative is the use of additional locking elements to increase the rigidity of the folded structure [25]. However, both techniques highly increase the complexity of the folding elements, thereby limiting the scalability of the design. As far as pure self-folding materials (*i.e.*, without additional design complexity) are concerned, not much attention has been paid to these contradictory design requirements and their implications for the stiffness of the resulting metamaterial. Here, we present a nonlinear (*i.e.*, finite deformation hyperelastic) analytical model that can be used to establish the theoretical stiffness limits of self-folded structures and answer the fundamental question: 'given a specific geometrical design and material selection, what is the maximum stiffness that bilayer self-folded structures can achieve?' We demonstrate the validity of our analytical model by comparing its results with those of our dedicated computational models and experiments.

### 3.2 Results and Discussion

The starting point of our analysis is a cubic lattice consisting of  $n \times n \times n$  unit cells loaded under compression (Figure 3.1a). Such lattices can be fabricated from arrays of  $n \times n \times 1$  unit cells that are folded from initially flat constructs [26] (Figure 3.1b). The flat sheets are made of an assembly of bilayer elements (red and blue materials in Figure 3.1) connected by square panels (gray). Driven by the mismatch in the shape-shifting behaviors of the active and passive elements, the panels fold into the programmed 3D geometry upon activation. The initial length,  $L$ , of the bilayer elements are designed such that folding angles,  $\theta$ , of  $90^\circ$  are achieved (Figure 3.1c). The other design parameters are the thicknesses of the active and passive layers as well as the material selection for both layers. The width  $b$  of the folding elements can be adjusted as well to change the size of the unit cell. The final cubic lattice can be fabricated by stacking the folded arrays either by connecting the individual slices with additional self-folding elements or using other assembly techniques [6, 27-29].



**Figure 3.1:** Self-folding cubic lattice. (a) A schematic illustration of the compression of a self-folding lattice. (b) Folding of a single array from a flat sheet comprising self-folding bilayer elements (blue and red) and rigid panels (grey). (c) Two rigid panels (grey) connected by a self-folding bilayer element (blue and red).

Assuming the panels to be rigid as compared to the bilayer element, the total stiffness of the cubic lattice only depends on the stiffness,  $k_{\text{hinge}}$ , of the folding elements as well as the arrangement of the bilayer elements within the lattice. Considering the lattice depicted in Figure 3.1a that is made of  $n \times n \times n$  unit cells and with the outer dimensions  $a \times a \times a$  mm, the effective elastic modulus,  $E_L$ , of the structure can be determined as follows:

$$E_L = \frac{F}{a^2} \frac{a}{\Delta x} = \frac{1}{a} k_{\text{total}} \quad (3.1)$$

where  $k_{\text{total}}$  is the total stiffness of the lattice in  $\text{N} \cdot \text{mm}^{-1}$ . The total lattice structure depends on the number of bilayer hinges in series and parallel and equals:

$$k_{\text{total}} = \frac{2n^2}{2n} k_{\text{hinge}} = n k_{\text{hinge}} \quad (3.2)$$

Assuming the hinge width  $b$  to equal  $a/n$  and by combining Equations 1 and 2, the effective lattice modulus,  $E_L$ , equals the hinge stiffness normalized by the hinge width,  $k_{\text{hinge}}/b$ . In the remainder of this chapter, we focus on determining the hinge stiffness of a general bilayer element that folds into a curved beam with a  $90^\circ$  folding angle. The results can, then, be applied to any type of self-folding lattice (of the type shown in Figure 3.1) using the presented approach.

The analytical model we present here consists of three elements: a finite deformation thick-beam analysis of the bending behavior of bi-layers to relate the geometry, shape shifting response, and mechanical properties of both layers to the curvature of the resulting self-folding construct, a stability model that establishes the limits of stable shape-shifting behavior to avoid wrinkling, and a

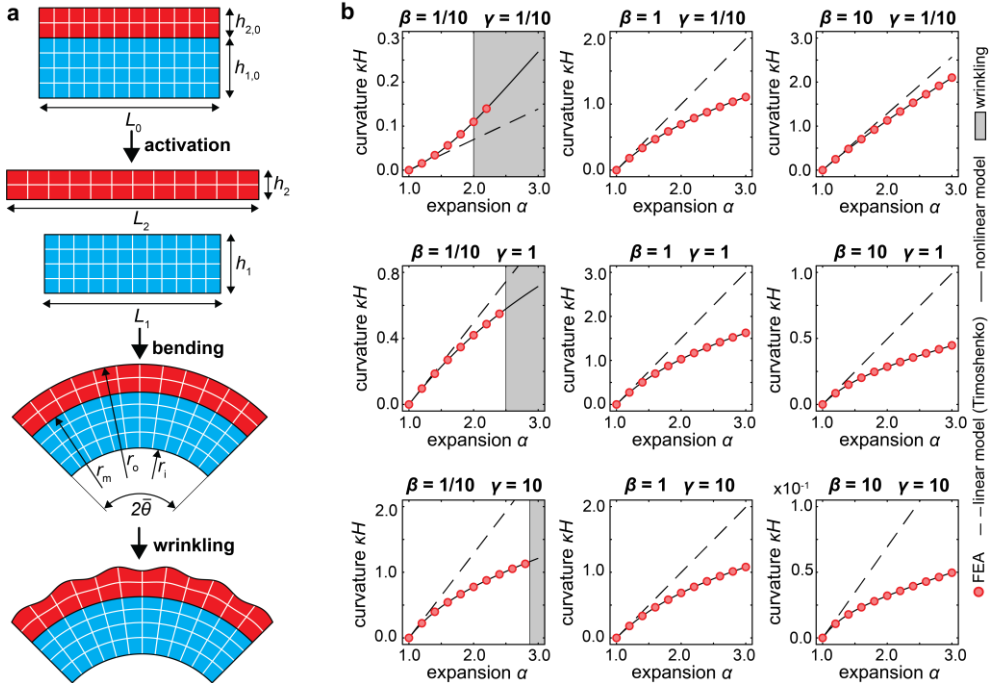
stiffness prediction model that predicts the stiffness of a self-folded construct given the design parameters of the bilayer. A detailed treatment of all three models and the relevant literature [30–36] is presented in Section 3.4 (Materials and Methods).

### 3.2.1. Bilayer bending

Studying the stiffness of self-folded elements requires us to first consider the bending of a general bilayer element. The starting point for our analysis is the plain strain bending of a thick incompressible hyperelastic beam (Figure 3.8). Following the Rivlin’s normality assumptions, the following kinematic relations are imposed [37]:

$$r = f(x) \quad \theta = g(y) \quad (3.3)$$

Because we are only interested in the final configuration of the activated bilayer, the bending analysis can be decoupled into two separate steps: (a) the free shape-shifting behaviors of the individual layers (b) followed by the bending of the activated layers while enforcing the tie condition at the interface of both layers (Figure 3.2a). Independent from the underlying shape-shifting mechanism, the following dimensionless parameters can be defined in the activated state:



**Figure 3.2:** Bending and wrinkling analysis of self-folding bilayers. (a) A schematic illustration of the folding and wrinkling of a bilayer element. (b) Theoretical and FEA results for bilayers with varying thickness ratio,  $\beta$ , and stiffness ratio,  $\gamma$ .

$$\alpha = \frac{L_2}{L_1} \quad \beta = \frac{h_2}{h_1} \quad \gamma = \frac{G_2}{G_1} \quad (3.4)$$

where  $G_i$  is the shear modulus of layer  $i$ . Following the imposed kinematics, while adopting an incompressible Neo-Hookean material model for both layers, the static balance equations can be numerically solved. As a result, the normalized curvature of the interface between both layers,  $\kappa H$ , can be obtained, where  $H$  is

the combined thickness of the activated layers (*i.e.*,  $H = h_1 + h_2$ ). The normalized bending curvature of the beam is, therefore, a function of only three dimensionless parameters,  $\alpha$ ,  $\beta$ , and  $\gamma$ .

### 3.2.2. Stability analysis

We also performed a stability analysis, using the method of incremental deformation, to determine how far the bilayer element can bend before the appearance of wrinkles on one of its surfaces. In the case of a bilayer assembled from a thin stiff layer and a thick compliant layer, instabilities can occur for small values of  $\alpha$  [38]. The results of the bending analysis serve as an input for the stability analysis (see Section 3.4) while a numerical method is employed to detect the bifurcation point.

### 3.2.3. Stiffness analysis

Based on the described nonlinear bending theory, the initial bilayer dimensions that are required to achieve folding angles of  $90^\circ$  can be determined. The next step is to evaluate the stiffness of the bilayer elements in their folded configuration using the Castigliano's second theorem according to which the small enough displacements resulting from any given force can be calculated as [35, 36]:

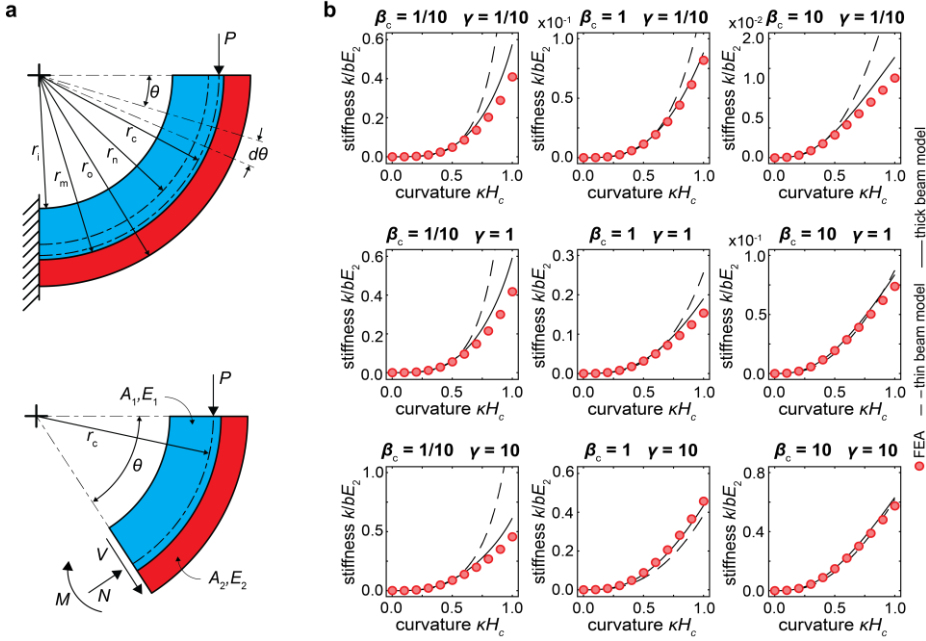
$$\delta = \frac{\partial U}{\partial P} \quad (3.5)$$

where  $\delta$  is the displacement of the point of application of force,  $P$ , along its direction and  $U$  is the total strain energy of the elastic system (Figure 3.3a). The strain energy function of a thick curved bilayer beams is given by the following relationship:

$$U_{\text{thick beam}} = \frac{1}{2} \int_{\theta} \frac{M^2}{C_M} d\theta + \int_{\theta} \frac{MN}{C_N} d\theta + \frac{1}{2} \int_{\theta} \frac{N^2 C_C}{C_N^2} d\theta + \frac{1}{2} \int_{\theta} \frac{V^2 C_S}{C_M^2} d\theta \quad (3.6)$$

The constants  $C_M$ ,  $C_N$ ,  $C_C$ , and  $C_S$  are provided in Section 3.4. The reaction loads (*i.e.*, normal force  $N$ , shear force  $V$ , and moment  $M$ ) at cross-section  $\theta$  are a function of the applied load  $P$  and centroid axis,  $r_c$ , of the beam. Differentiation of the strain energy with respect to the applied force  $P$  gives the hinge deformation as a function of the applied force  $P$ , the dimensions  $b$ ,  $r_i$ ,  $r_m$ , and  $r_o$ , and the elastic

moduli of both layers,  $E_i$ . The deformation  $\delta$  is a linear function of  $P$ ,  $b$ , and  $E_i$ . The normalized stiffness  $\tilde{k}_{\text{hinge}}$  can, therefore, be calculated as  $\tilde{k}_{\text{hinge}} = k_{\text{hinge}} b^{-1} E_2^{-1}$  where  $k_{\text{hinge}}$  is the hinge stiffness and equals  $P\delta^{-1}$ . Normalizing all dimensions with respect to the total thickness of the curved beam  $H_c$  reveals that the normalized stiffness  $\tilde{k}_{\text{hinge}}$  of a bi-layer quarter-circle beam remains unchanged as the bilayer hinge is scaled and is only a function of the parameters  $\alpha$ ,  $\beta_c$ , and  $\gamma$ , where  $\beta_c$  is the thickness ratio in the curved configuration.



**Figure 3.3:** Stiffness analysis of curved bilayer elements. (a) A schematic illustration of a folded bilayer specimen. (b) Theoretical and FEA results for bilayers with varying thickness ratio,  $\beta_c$ , and stiffness ratio,  $\gamma$ .

### 3.2.4. Computational models

To validate the described theories, a series of finite element analyses (FEA) were performed. First, the results of the plane-strain bending FEA simulations were compared with the theoretical results for the different combinations of  $\beta$  and  $\gamma$  (Figure 3.2b). Only the FEA results without the presence of wrinkles are plotted while the gray areas indicate the expansion values for which wrinkling occurs according to the theory. The bending theory is in excellent agreement with FEA while a good agreement between the wrinkling analysis and FEA can be observed as well (Figure 3.2b). For reference, the predictions of the well-known Timoshenko bilayer bending theory (a linear model) [39] are plotted as well (Figure 3.2b). Especially for the higher values of  $\alpha$ , large discrepancies are observed between the linear Timoshenko theory and the nonlinear theory developed here, indicating the need for the described nonlinear theories. Additional simulations were

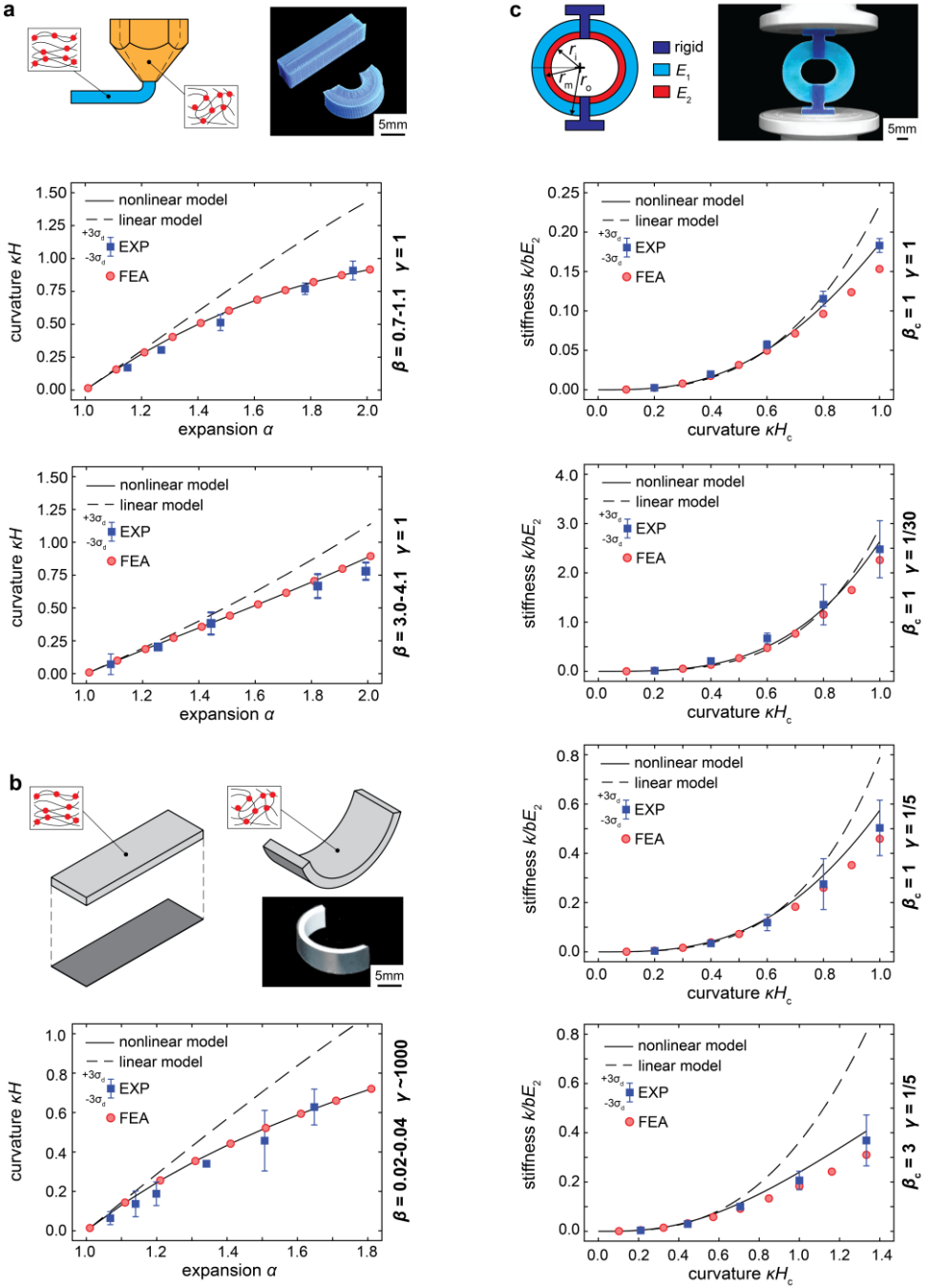
performed to compare the results of the wrinkling analysis with those of the computational models for the different combinations of  $\beta$  and  $\gamma$ . In general, the wrinkling theory is capable of capturing both the onset of wrinkling and the number of wrinkles appearing on the surface of the bilayer (Table 3.1).

Another series of FEA simulations were performed to compare the theoretical stiffness values with the computational results. For small ratios of the initial beam thickness to the radius of the interface, the theories for both thin and thick beams are in good agreement with the FEA results (Figure 3.3b). While the linear model exhibits very large discrepancies with the computational results when the total beam thickness starts to approach the interface radius, the finite deformation model continues to yield high-fidelity predictions. The advantages of the finite deformation model are particularly clear for the small values of  $\beta_c$  where the thin-beam approximation grossly overestimates the stiffness (Figure 3.3b). This effect is more significant for  $\beta_c$  values  $\ll 1$  because the thickness of the inner layer (*i.e.*,  $r_m - r_i$ ) approaches the total beam thickness, meaning that  $r_i$  approaches zero for  $\kappa H_c$  values close to 1. This is, however, an extreme case for which it is expected that FEA results should deviate from a model that assumes the bilayer elements to behave like a beam. There is, however, a very good agreement between the computational results and the results of the thick-beam model even when the ratio of the initial thickness to the interface radius approaches 1 (Figure 3.3b).

### 3.2.5. Experimental validation

As a final validation of both the bending and stiffness theories, we performed several experiments. We 4D printed bilayer bending elements from shape-memory polymers [17] (see Section 3.4). The bilayers consist of one shrinking layer on top of a semi-passive layer (*i.e.*, a layer with minimal deformation characteristics). For both layers, the longitudinal expansion/shrinkage is coupled to some degree of transverse and vertical deformation (see Table 3.3). Specimens with an expansion ratio  $a$  ranging between 1.1 and 2.0 and a thickness ratio ranging between  $\sim 1$  and  $\sim 4$  were produced. For both sets of the specimens,  $\beta$  varied slightly which originates from the fact that samples with fixed initial layer thicknesses were produced resulting in a different layer thickness in the activated states. In addition, polymer-metal bilayer samples were produced to validate the bending model for large stiffness ratios. The specimens consisted of a thin metal layer adhesively bonded to a thick heat-shrinking polymer layer (see Materials and Methods). Similar to the 4D printed samples, the longitudinal shrinkage of the polymer layer is coupled to some degree of vertical deformation. Different expansion ratios were realized by activating the samples at different temperatures (see Table 3.4). There was generally a very good agreement between the prediction of the finite deformation model and the experimental results (Figure 3.4a), demonstrating the ability of the plane strain analytical model to capture the 3D deformation characteristics of actual self-folding specimens.





**Figure 3.4:** Experimental validation. (a) The theoretical and experimental bending results of 4D printed bilayers ( $n = 4$ ). (b) The theoretical and experimental stiffness results of polymer-metal self-folding bilayers ( $n=4$ ). (c) The theoretical and experimental stiffness results of curved bilayer element ( $n = 4$ ).

To validate the stiffness predictions of the model, various specimens were produced using a multi-material 3D printer working on the basis of UV-curing of multiple types of jetted polymers (the Polyjet technology, see Section 3.4). To perform compressive mechanical testing without a need for additional clamps, the specimens included two parallel sets of soft ( $E \approx 1.4$  MPa) quarter-circle beams in series and two rigid clamps (Figure 3.4c). Because of this arrangement of the beams, the overall sample stiffness equals the stiffness of a single quarter-circle beam. Specimens with different combinations of layer thickness (*i.e.*,  $\beta_c$ ) and stiffness ratios were fabricated. The ratio of the interface radius to the total beam thickness was varied between 0.2 and 1.0. Once more, there was a very good agreement between the stiffness values predicted by the finite deformation analytical model and our experimental observations (Figure 3.4c).

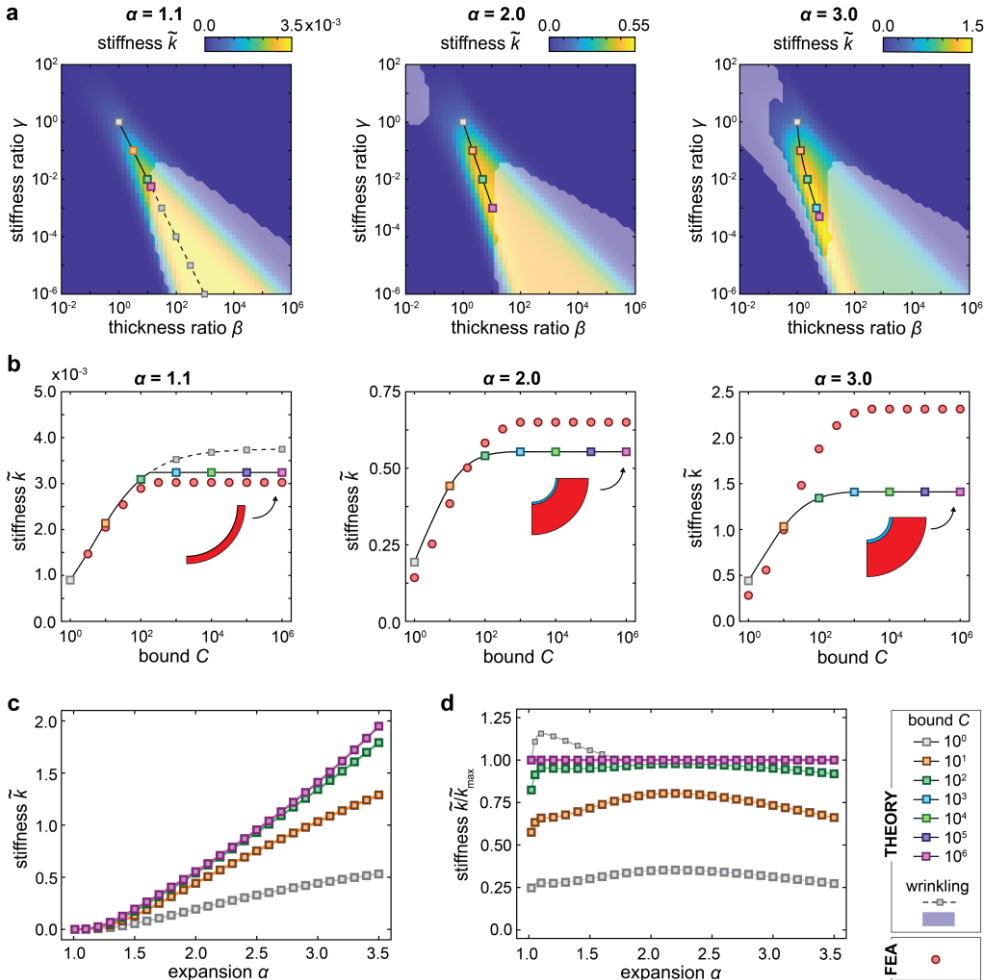
### 3.2.6. Combined analysis

Combining the three aspects of the analytical model developed here allows for estimating the normalized stiffness of the folded hinges as a function of the three dimensionless parameters  $\alpha$ ,  $\beta$ , and  $\gamma$  (see Figure 3.10). For the different values of  $\alpha$ , the theoretical normalized stiffness can be plotted against the layer thickness ratio,  $\beta$ , and the stiffness ratio,  $\gamma$  (Figure 3.5a). The results indicate that the stiffness of bilayer hinges can be greatly improved through a proper selection of  $\beta$  and  $\gamma$ . Using  $\beta$  and  $\gamma$  equal to 1 as the starting point, at least a three-fold increase in the stiffness could be realized by selecting the optimum values of  $\beta$  and  $\gamma$  (Figure 3.5a).

Depending on the expansion ratio,  $\alpha$ , the results of our analysis suggest that the maximum stiffness is achieved for  $\beta$  values between 1 and  $10^3$  and  $\gamma$  values between  $10^{-6}$  and  $10^{-3}$ . In practice, however, it is challenging to realize bilayer specimens with such a large difference in the layer thickness or stiffness. We, therefore, conducted an analysis to search for the maximum stiffness that can be reached while upholding the different bounds limiting the choice of  $\beta$  and  $\gamma$  values. The upper and lower limits of both  $\beta$  and  $\gamma$  are defined as  $1/C \leq x \leq C$  where  $x$  is  $\beta$  or  $\gamma$  and the boundary  $C \geq 1$ , respectively. For the different values of  $\alpha$ , we plotted the maximum stiffness as a function of the limit  $C$  (Figure 3.5b) and found that limiting the maximum stiffness ratio to  $10^2$  will be sufficient for realizing at least 80% of the theoretical maximum stiffness (Figure 3.5c-d). Therefore,  $\beta$  values between 2 and 10 (depending on  $\alpha$ ) and a stiffness ratio  $\gamma$  of 0.01 would often be a practical choice for the fabrication of bilayer hinges with a near-maximum stiffness.

For small expansion ratios, wrinkling occurs in the bilayers with optimized stiffness (Figure 3.5a-b). Limiting the feasible values of  $\beta$  and  $\gamma$  to the stable region only slightly decreases the theoretical maximum stiffness (Figure 3.5d). It can, therefore, be concluded that optimizing the bilayer design is not significantly hampered by the onset of instabilities.

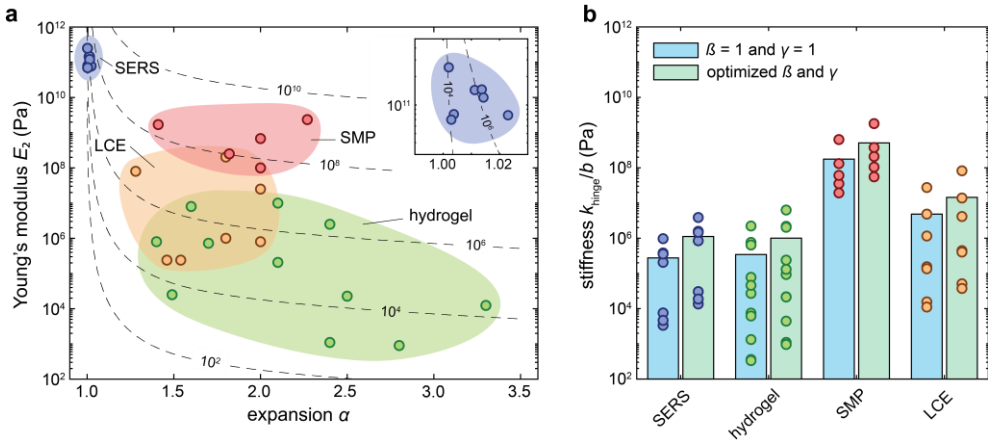
The stiffness of bilayers with optimized designs were validated using FEA simulations as well. For large values of  $\alpha$ , the analytical model underestimates the stiffness as compared with FEA (Figure 3.5b). For stiffness ratios below 0.01, the observed discrepancies are particularly high. It is important to notice that for such a large  $\alpha$ , the total beam thickness to the interface radius ratio exceeds 1.5, which is beyond the validity limits of a beam-based model. Combined with the effects of a stiffness ratio below  $10^{-3}$ , the differences between the theoretical model and FEA predictions may even reach 70% (Figure 3.5b). That said, both theory and FEA exhibit the same overall trends. Moreover, limiting the stiffness ratio to  $10^{-2}$  reduces the discrepancies between both models to a maximum of 40%.



**Figure 3.5:** Combined bending and stiffness analysis. (a) Theoretical normalized stiffness values for different combinations of thickness ratio,  $\beta$ , and stiffness ratio,  $\gamma$ . (b) The maximum theoretical stiffness subjected to different limits for  $\beta$  and  $\gamma$ . (c) The maximum normalized stiffness for different bounds  $C$  as a function of the expansion ratio,  $\alpha$ . (d) The maximum normalized stiffness normalized by the stiffness values with  $C = 10^6$ .

### 3.2.7. Practical implications

In the previous section, the bending and stiffness theories were combined to search for the theoretical maximum stiffness of bilayer hinges. For different amounts of expansion, the optimized combinations of  $\beta$  and  $\gamma$  values were determined. The optimized stiffness of folded bilayer elements only depends on the expansion coefficient,  $\alpha$ , and the elastic modulus,  $E_2$ . While it is clear that the combination of a high elastic modulus and a large expansion ratio would result in a high stiffness of folded bilayers, the selection of stimuli-responsive materials is, in practice, a trade-off between the amount of expansion and the material stiffness. Active materials with a high elastic modulus often have small expansion values while the opposite holds true for materials with large expansion coefficients. To estimate the maximum achievable stiffness of bilayer hinges, we need to identify both the elastic modulus and expansion coefficients of the different types of stimuli-responsive materials. Towards that end, we performed a literature study to identify the active materials that are most commonly used for the fabrication of shape-shifting structures. Only studies that reported the fabrication of bilayer folding elements as well as the stiffness and expansion coefficients of the applied materials were included. Four classes of stimuli-responsive materials were identified: i) semiconductor materials with engineered residual stresses (SERS) [40-45], ii) hydrogels [46-54], iii) shape-memory polymers (SMP) [17, 55-62], and iv) liquid crystal elastomers (LCE) [63-69]. The material properties we found for each of those classes of materials are presented in Figure 3.6a. Assuming that these active materials can be combined with any desired layer of a passive material, the optimized hinge stiffness normalized by the hinge width can be calculated as  $k_{\text{hinge}}/b = \tilde{k}_{\text{hinge}} E_2$ . The black dashed lines in Figure 3.6a indicate the constant values of the optimized stiffness  $k_{\text{hinge}}/b$ .



**Figure 3.6:** Stiffness for different active materials. (a) The elastic moduli and expansion values reported in the literature for the common types of stimuli-responsive materials. The black dashed lines indicate the constant values of  $k_{\text{hinge}}/b$ . (b) The hinge stiffness of non-optimized and optimized bilayer configurations for the different types of stimuli-responsive materials.

Comparing the theoretical maximum stiffness values calculated for the different classes of active materials clearly indicates that SMP outperform the other material types (Figure 3.6b). The combination of moderate expansion coefficients (*i.e.*,  $\alpha \sim 2.0$ ) and elastic moduli up to 2.5 GPa results in a maximum hinge stiffness of  $\approx 1.5$  GPa (Figure 3.6b). Even for  $\beta$  and  $\gamma$  values equal to 1, the maximum stiffness of SMP bilayer hinges is at least one order of magnitude higher than that of any other optimized bilayer hinge. The bilayers made from SERS or hydrogels display a maximum theoretical stiffness of up to 10 MPa while a somewhat larger stiffness could be achieved using LCE.

Although these estimated values give a good indication of the achievable hinge stiffness values, some other practical considerations need to be taken into account. First of all, it is assumed that these common types of stimuli-responsive materials could be combined with any sort of passive materials with any desired properties. In the case of SERS materials, however, it is challenging to find a material with a much higher stiffness value. Hence, the optimized stiffness ratios can hardly be realized in practice. One concern regarding SMP is a dramatic drop in their stiffness during their activation [70]. The passive layer should exhibit a similar drop in its stiffness in order to maintain the desired stiffness ratio and realize the theoretically predicted curvature. In practice, this could be achieved by combining the SMP layer with another SMP material. This approach, however, also limits the feasible stiffness ratio. A similar effect can be observed for LCE materials [63, 65, 69]. On the other hand, different types of stimuli-responsive materials could be combined into a bilayer structure to increase the bending curvature. For example, an expanding and a shrinking layer could be combined to create a bilayer with a larger effective expansion ratio,  $\alpha$ . The combined effects of these practical considerations are highly dependent on the limitations of the specific materials and production techniques and are, thus, difficult to predict.

Finally, we searched for the optimal combination of the parameters  $\alpha$ ,  $\beta$ , and  $\gamma$  to reach the highest possible stiffness of the bilayer hinges. However, other design restrictions imposed by the problem at hand may require the selection of another set of design parameters. Examples of such restrictions are the need for folding elements with different folding angles or a requirement regarding the time-dependent behavior of the individual folding elements and their synchronization to achieve a certain overall deformation of the self-folding array. These aspects are highly dependent on the specific design of the self-folding array.

### 3.3 Outlook and conclusions

In summary, we presented a finite deformation theory for predicting the bending behavior of bilayer elements, establishing their stability limits, and determining their stiffness. The inputs for the bending analysis are the normalized dimensions of both layers of the composite beam in the activated state that are described by

the length ratio  $\alpha$ , thickness ratio  $\beta$ , and stiffness ratio  $\gamma$ . As a result, the normalized radius of the curved bilayer can be calculated, which serves as an input to the stiffness model. For bilayer beams with a  $90^\circ$  folding angle, the normalized stiffness,  $\tilde{k}_{\text{hinge}}$ , can be obtained as a function of  $\alpha$ ,  $\beta$ , and  $\gamma$ . The design of self-folding elements could be optimized in terms of their load-bearing capacity by combining all three aspects of the analytical model. In general, the selection of a thickness ratio  $\beta$  between 2 and 10 and a stiffness ratio  $\gamma$  of  $\approx 10^{-2}$  resulted in a three-fold increase in the hinge stiffness as compared with the default (and naïve) choice of  $\beta$  and  $\gamma$  values equal to 1. As a final step, the optimized bilayer stiffness values were determined for four types of commonly used stimuli-responsive materials.

The presented theoretical analysis is based on several underlying assumptions. First of all, we performed the analysis based on a cubic self-folding origami-inspired lattice (e.g., similar to the ones presented in [26]). The effective lattice stiffness was found to be equal to the hinge stiffness normalized by the hinge width,  $b$ . The width  $b$  is assumed to be equal to the average width of a unit cell  $a/n$ . In practice, both the radius and thickness of the folding elements have finite dimensions and the actual hinge width will be smaller than the average unit cell size. A more realistic estimate for the hinge width,  $b$ , would be possible by subtracting the hinge radius (i.e.,  $b = a/n - r_i$ ). The effective modulus of a cubic lattice (Figure 3.1a) then equals:

$$E_L = \left(1 - \frac{n}{a}r_i\right) \tilde{k}_{\text{hinge}} E_2 \quad (3.7)$$

The presented analysis on self-folding bilayers indicates that the stiffness of the bilayer folding elements remains unchanged when all the hinge dimensions are uniformly scaled. A small hinge thickness can, therefore, be selected to reduce the hinge radius, thereby approaching  $E_L \approx \tilde{k}_{\text{hinge}} E_2$ . It is important to note that for any other arrangements of shape-shifting elements within the self-folding structures, a different relationship between the effective stiffness of the lattice structure and the hinge stiffness may be applicable. In addition to the design of self-folding elements, the arrangement of these elements can be also used as a tool to tune the overall stiffness of self-folding lattices. One example is the use of rectangular elements instead of cubic unit cells to enlarge the effective lattice modulus along one direction.

The finite deformation bending model we presented is based upon several assumption. First, a Neo-Hookean material model was used. Given that the Neo-Hookean material model is only accurate for moderate strain levels, additional FEA simulations were performed using different materials models. A Mooney-Rivlin model, a 2<sup>nd</sup> order Ogden model, and a Yeoh material model were implemented. Comparing the results of those additional models with the theoretical analysis

performed using a Neo-Hookean material model indicates that the effects of the selected material model on the predicted response is very limited (Figure 3.8). In addition, the development of a second curvature in the width direction are not captured by our analytical model. Several studies have shown that isotopically expanding bilayers prefer to roll along their longitudinal axis than to develop a double-curved shape [71, 72]. For increasing amounts of expansion (*i.e.*,  $\alpha > 1.2$ ) and large aspect ratios (*i.e.*,  $b/L_0 \gg 1$ ), the dominant curvature is found to approach the curvature predicted using the plane-strain theory [72]. This can be explained based on energy considerations as bending is energetically more favorable than the in-plane stretching required for the development of a double curvature. When combined with the effects of clamping, no significant curvature in the width direction is expected.

The performed bifurcation analysis does not predict the wrinkling amplitude but only the onset of wrinkling. The effects of wrinkling on the amount of bending cannot, thus, be determined using the model presented here. While limiting the design space of self-folding bilayers to ensure wrinkling is avoided may, in theory, exclude some high stiffness configurations, the results presented in Figure 3.5 indicate that the actual drop in the maximum achievable stiffness is in practice quite limited. In addition, this effect is limited to low-expansion values (Figure 3.5d).

The stiffness of curved bilayer elements was predicted using a model based on a beam theory. In general, however, such models are only accurate for slender structures (*i.e.*,  $\kappa H \ll 1$ ). Comparing the FEA results with the predictions of the stiffness model indicates that, indeed, larger discrepancies are observed for the larger values of the normalized curvature (Figure 3.3b). Especially for hydrogels with large expansion coefficients (*i.e.*,  $\alpha \sim 3.0$ ), the normalized curvature  $\kappa H$  may even exceed 1 and the beam stiffness will be significantly underestimated (Figure 3.5b). For the other types of active materials with smaller amounts of expansion (*i.e.*,  $\alpha < 2.0$ ), the discrepancies between the stiffness model and the computational results are  $< 20\%$  (Figure 3.5b). A comparison of the stiffness limits for the various types of different active materials shows that the stiffness of hydrogel-based bilayer elements is at least 2 orders of magnitude lower than that of SMP bilayers. Therefore, the underestimation of the stiffness of self-folding hydrogel elements does not affect the overall theoretical stiffness limit of  $\approx 1.5$  GPa.

Finally, the theoretical stiffness limit of bilayer elements highly depends on the specific properties of the selected stimuli-responsive materials. Here, we have only included the properties of active materials that have been used in the literature for the fabrication of self-folding bilayers. However, other types of stimuli-responsive materials with superior mechanical properties may have been

reported in the literature for other applications. Even though the presented list of active materials is not exhaustive, it clearly shows that the application of SMP-based self-folding elements results in significantly higher stiffness values as compared to the other types of activate materials included here.

In conclusion, we developed an analytical model for evaluating the stiffness of bilayer self-folding elements. We then used the developed models to establish the theoretical stiffness limits of self-folding bilayers. Considering the usual materials used for that purpose, the maximum stiffness reached in practice is estimated to be around 1.5 GPa for SMP-based self-folding elements. The stiffness of SMP bilayers is significantly higher than the stiffness of any other bilayer element based on the other types of active materials. The presented models could be also used for optimizing the stiffness of self-folding bilayers. In general, a thickness ratio between 2 and 10 and a stiffness ratio of around  $10^{-2}$  would result in a near-optimal stiffness of the bilayer construct. Given the fact that these results are length scale-independent, they could be applied to various types of self-folding origami lattices.

## 3.4 Materials and methods

### 3.4.1. Finite-deformation bending model

We start our analysis by considering the plane strain bending of a thick incompressible beam. The following kinematic relations (normality conditions [37]) are imposed (Figure 3.7):

$$r = f(y) \quad (3.8a)$$

$$\theta = g(x) \quad (3.8b)$$

Based on this assumption, the deformation gradient  $\mathbf{F}$  can be written as follows [32]:

$$\mathbf{F} = \frac{df(y)}{dy} \mathbf{e}_r \otimes \mathbf{e}_y + f(y) \frac{dg(x)}{dx} \mathbf{e}_\theta \otimes \mathbf{e}_x \quad (3.9)$$

Applying the incompressibility condition (*i.e.*,  $J = |\mathbf{F}| = 1$ ) gives:

$$\frac{df(y)}{dy} f(y) \frac{dg(x)}{dx} = 1 \quad (3.10)$$

To solve Equation 3.10, the following boundary conditions can be applied:

$$f\left(y = -\frac{h}{2}\right) = r_i \quad (3.11a)$$



$$f\left(y = \frac{h}{2}\right) = r_o \quad (3.11b)$$

$$g\left(x = -\frac{L}{2}\right) = -\bar{\theta} \quad (3.11c)$$

$$g\left(x = \frac{L}{2}\right) = \bar{\theta} \quad (3.11d)$$

where  $r_i$  is the inner radius and  $r_o$  is the outer radius (Figure 3.7). By solving Equation 3.10, the principle stretches in the deformed configuration are obtained as [37]:

$$\lambda_r = \frac{dr}{dy} = \frac{df(y)}{dy} = \frac{L_o}{2\bar{\theta}r} \quad (3.12a)$$

$$\lambda_\theta = r \frac{d\theta}{dx} = f(y) \frac{dg(x)}{dx} = \frac{2\bar{\theta}r}{L_o} \quad (3.12b)$$

As a next step, the balance equations need to be derived. Assuming that the hyperelastic behavior of the involved materials can be described using an incompressible Neo-Hookean material model, the strain energy density function  $W$  can be written as:

$$W = \frac{G}{2}(\mathbf{I}_1 - 3) \quad (3.13)$$

where  $G$  is the shear modulus and  $\mathbf{I}_1$  is the first invariant of the left Cauchy-Green strain tensor,  $\mathbf{B} = \mathbf{F}\mathbf{F}^T$ . The transversal and radial stresses as a function of the principal stretches can be calculated from  $\boldsymbol{\sigma} = \frac{1}{J} \frac{\partial W}{\partial \mathbf{F}} \mathbf{F}^T$ :

$$\sigma_r = -p + G\lambda_r^2 \quad (3.14a)$$

$$\sigma_\theta = -p + G\lambda_\theta^2 \quad (3.14b)$$

The pressure field  $p(r)$  can be obtained up to an integration constant  $C$  by substituting Equation 3.14 in the static balance equation ( $\nabla \cdot \boldsymbol{\sigma} = 0$ ) [32]:

$$p(r) = \frac{G}{2}(\lambda_r^2 - \lambda_\theta^2) + C \quad (3.15)$$

Finally, we consider a bilayer constituting of two layers of an incompressible Neo-Hookean material. The volumetric constraint equations ( $J = 1$ ) for both layers yields the following:

$$L_1 h = \bar{\theta}(r_m^2 - r_i^2) \quad (3.16a)$$

$$\alpha L_1 \beta h = \bar{\theta}(r_o^2 - r_m^2) \quad (3.16b)$$

where  $r_i$  is the inner radius,  $r_m$  is the interface radius, and  $r_o$  is the outer radius. Enforcing the zero radial stress condition at the inner and outer radii of the bilayer beam yields the integration constants  $C_i$  of both layers. For finding the equilibrium configuration, the net forces and moments must vanish at both ends of the beam:

$$N(\theta = \pm\bar{\theta}) = \int \sigma_\theta dr = \int_{r_1}^{r_2} \sigma_\theta^1 dr + \int_{r_2}^{r_3} \sigma_\theta^2 dr = 0 \quad (3.17a)$$

$$M(\theta = \pm\bar{\theta}) = \int r \sigma_\theta dr = \int_{r_1}^{r_2} \sigma_\theta^1 r dr + \int_{r_2}^{r_3} \sigma_\theta^2 r dr = 0 \quad (3.17b)$$

Equations 3.16 and 3.17 form a set of 4 equations that can be solved numerically to calculate the normalized unknowns  $r_i/H$ ,  $r_m/H$ ,  $r_o/H$ , and the ratio  $\bar{\theta}/L_0$ . The normalized results are independent from the initial total thickness,  $H$ .

### 3.4.2. Stability model

Using a bending analysis, we derived the static equilibrium shape of a particular self-folding bilayer element. We now aim to find the onset of instability by applying the method of incremental deformations [73]. This method involves the superposition of an incremental displacement field on the bended configuration and calculating the corresponding incremental stresses using [74]:

$$\Sigma = -\delta p \mathbf{I} + p \mathbf{L}^T + G \mathbf{L} \mathbf{B} \quad (3.18)$$

where  $\Sigma$  is the first Piola Kirchhoff stress tensor,  $\delta p$  is the pressure increment,  $\mathbf{L}$  is the gradient of the incremental displacement field,  $\mathbf{u}$  ( $\mathbf{L} = \nabla \cdot \mathbf{u}$ ), and  $\mathbf{B} = \mathbf{F} \mathbf{F}^T$ . Following Roccabianca *et al.* [33, 34], we propose the following incremental displacement fields:

$$u_r = f(r) \cos(n\theta) \quad (3.19a)$$

$$u_\theta = g(r) \sin(n\theta) \quad (3.19b)$$

$$\delta p = k(r) \cos(n\theta) \quad (3.19c)$$

The incompressibility conditions (*i.e.*,  $\text{tr}(\mathbf{L}) = 0$ ) allows us to write the unknown function  $g(r)$  as a function  $f(r)$ :

$$g = \frac{f + f'r}{n} \quad (3.20)$$

By combining Equations 3.18 and 3.19, the incremental equilibrium equations (*i.e.*,  $\nabla \cdot \Sigma = 0$ ) can be solved to derive the unknown function  $k(r)$  as a function of both  $f(r)$  and  $g(r)$ . The subsequent substitution of Equation 3.20 yields the two following equations [33]:

$$k' = [a^2(1 - n^2)]f + \left[a^2r - \frac{2}{a^2r^3}\right]f' + \left[\frac{1}{a^2r^2}\right]f'' \quad (3.21a)$$

$$k = \left[\frac{-1}{a^2r^3}\left(1 - \frac{1}{n^2}\right)\right]f - \left[a^2r^2 + \frac{1}{n^2a^2r^2}\right]f' + \left[\frac{2}{n^2a^2r}\right]f'' + \left[\frac{1}{a^2n^2}\right]f''' \quad (3.21b)$$

where  $a = 2\bar{\theta}/L_0$ . The differentiation of Equation 3.21b with respect to  $r$  and its subsequent substitution into Equation 3.21a results in a single differential equation for the function  $f(r)$ :

$$\begin{aligned} f'''' + \left[\frac{2}{r}\right]f''' - \left[n^2a^4r^2 + \frac{3 - n^2}{r^2}\right]f'' + \left[\frac{3 - n^2}{r^3} + 3n^2a^4r\right]f' \\ + \left[\left(\frac{3}{r^4} + n^2a^4\right)(n^2 - 1)\right]f = 0 \end{aligned} \quad (3.22)$$

The function  $f$  within each layer can be obtained by enforcing the continuity conditions at the interface of both layers:

$$\Sigma_{rr}^{(1)}(r = r_m) = \Sigma_{rr}^{(2)}(r = r_m) \quad (3.23a)$$

$$\Sigma_{\theta r}^{(1)}(r = r_m) = \Sigma_{\theta r}^{(2)}(r = r_m) \quad (3.23b)$$

$$u_r^{(1)}(r = r_m) = u_r^{(2)}(r = r_m) \quad (3.23c)$$

$$u_\theta^{(1)}(r = r_m) = u_\theta^{(2)}(r = r_m) \quad (3.23d)$$

as well as imposing zero force condition at the inner and outer radii:

$$\Sigma_{rr}^{(1)}(r = r_i) = 0 \quad (3.24a)$$

$$\Sigma_{rr}^{(2)}(r = r_o) = 0 \quad (3.24b)$$

$$\Sigma_{\theta r}^{(1)}(r = r_i) = 0 \quad (3.24c)$$

$$\Sigma_{\theta r}^{(2)}(r = r_o) = 0 \quad (3.24d)$$

The incremental shear forces and normal displacements should also vanish at both ends of the beam:

$$\Sigma_{\theta r}^{(1)}(\theta = \pm\bar{\theta}) = 0 \quad (3.25a)$$

$$\Sigma_{\theta r}^{(2)}(\theta = \pm\bar{\theta}) = 0 \quad (3.25b)$$

$$u_\theta^{(1)} = 0 \quad (3.25c)$$

$$u_\theta^{(2)} = 0 \quad (3.25d)$$

Finally, to avoid numerical ill-conditioning in the cases where large differences between the properties (mechanical, geometrical) of both layers exist, we used the compound matrix method to search for an expansion value  $\alpha$  that results in a non-trivial solution of  $\mathcal{F}^{(i)}$ , given the thickness ratio,  $\beta$ , and stiffness ratio,  $\gamma$  [33].

### 3.4.3. Derivation of the thick-beam stiffness model

Consider a segment of a curved beam loaded in pure bending (Figure 3.9a). We assume that a plane cross-section remains plain after bending. Based on geometrical considerations, the tangential strain at a distance  $r - r_n$  from the neutral axis is given by:

$$\epsilon_\theta(r, \theta) = \frac{(r - r_n)d\theta}{r \theta} \quad (3.26)$$

Neglecting the radial stresses, the tangential stress for a linear elastic material is:

$$\sigma_\theta(r, \theta) = E \epsilon_\theta = E \frac{(r - r_n)d\theta}{r \theta} \quad (3.27)$$

In the case of pure bending, the total tangential stress across a specific cross-section equals zero ( $\int_A \sigma_\theta dA = 0$ , where  $A$  is the cross-section area). As a result, the neutral axis of a curved beam can be derived as a function from the cross-section geometry and material properties as:

$$r_n = \frac{E_1 A_1 + E_2 A_2}{E_1 \int_{A_1} \frac{1}{r} dA + E_2 \int_{A_2} \frac{1}{r} dA} \quad (3.28)$$

where subscripts 1 and 2 refer to the different layers of the beam. The applied moment  $M$  is defined to be positive for increasing curvatures. Combined with Equation 3.27, the moment resulting from the tangential stress is given by:

$$M(\theta) = \int_A (r - r_n) \sigma_\theta dA = \frac{d\theta}{\theta} [(r_{c,1} - r_n) E_1 A_1 + (r_{c,2} - r_n) E_2 A_2] = \frac{d\theta}{\theta} C_M \quad (3.29)$$

Combining Equation 3.29 with Equation 3.27 and adding a term related to the normal force  $N$ , the tangential stress in layer  $i$  can be written as a function of the applied loads as:

$$\sigma_{\theta,i}(r, \theta) = \left( \frac{r - r_n}{r} \right) \frac{M E_i}{C_M} + \frac{N E_i}{C_N} \quad (3.30)$$

where  $C_N = E_1 A_1 + E_2 A_2$ . The next step is to consider the average transverse shear stress along the width of the beam due to an applied bending moment. Writing the net force in the tangential direction of a beam element with the length  $r_c d\theta$  from height  $r$  till the outer radius  $r_0$  gives (see Figure 3.9b):

$$\tau_2(r, \theta) = \frac{V E_2}{C_M} \left[ r_0 - r + r_n \ln \left( \frac{r}{r_0} \right) \right] \quad (3.31)$$

for  $r > r_m$ . The shear stress in the bottom layer can be obtained in a similar way but by integrating from the inner radius  $r_i$  till height  $r$ . Neglecting the radial stresses, the total internal energy is then obtained as:

$$U = \frac{1}{2} \int_V \frac{\sigma_\theta^2}{E} dV + \frac{1}{2} \int_V \frac{\tau^2}{G} dV \quad (3.32)$$

Substituting Equations 3.30 and 3.31 into Equation 3.32 gives the strain energy as a function of the applied loads:

$$U = \frac{1}{2} \int_\theta \frac{M^2}{C_M} d\theta + \int_\theta \frac{MN}{C_N} d\theta + \frac{1}{2} \int_\theta \frac{N^2 C_C}{C_N^2} d\theta + \frac{1}{2} \int_\theta \frac{V^2 C_S}{C_M^2} d\theta \quad (3.33)$$

where  $C_C = r_{c,1} E_1 A_1 + r_{c,2} E_2 A_2$  and  $C_S = E_1(1 + \nu) C_{S1} + E_2(1 + \nu) C_{S2}$ . The constants  $C_{S1}$  and  $C_{S2}$  are as follows:

$$\begin{aligned} C_{S1} = & -\frac{r_i^4}{6} + \frac{5r_n r_i^3}{9} - \frac{r_n^2 r_i^2}{2} \\ & + \left( r_i^2 r_m^2 - \frac{4r_i r_m^3}{3} + \frac{r_m^4}{2} - r_n r_m^2 \left( \left( -2r_i + \frac{4r_m}{3} \right) \ln \left( \frac{r_m}{r_i} \right) + r_i - \frac{4r_m}{9} \right) \right. \\ & \left. + r_n^2 r_m^2 \left( \ln \left( \frac{r_m}{r_i} \right)^2 - \ln \left( \frac{r_m}{r_i} \right) + \frac{1}{2} \right) \right) \end{aligned} \quad (3.34a)$$

$$\begin{aligned} C_{S2} = & \frac{r_o^4}{6} - \frac{5r_n r_o^3}{9} + \frac{r_n^2 r_o^2}{2} \\ & - \left( r_o^2 r_m^2 - \frac{4r_o r_m^3}{3} + \frac{r_m^4}{2} - r_n r_m^2 \left( \left( -2r_o + \frac{4r_m}{3} \right) \ln \left( \frac{r_m}{r_o} \right) + r_o - \frac{4r_m}{9} \right) \right. \\ & \left. + r_n^2 r_m^2 \left( \ln \left( \frac{r_m}{r_o} \right)^2 - \ln \left( \frac{r_m}{r_o} \right) + \frac{1}{2} \right) \right) \end{aligned} \quad (3.34b)$$

where the results of the bending analysis are used to derive explicit relationships for  $C_M$ ,  $C_N$ ,  $C_C$ , and  $C_S$ .

For the curved beam shown in Figure 3.3, the relationships between the applied force  $P$  and the cross-sectional loads can be established as:

$$M(\theta) = P r_c (1 - \cos(\theta)) \quad (3.35a)$$

$$N(\theta) = P \cos(\theta) \quad (3.35b)$$

$$V(\theta) = -P \sin(\theta) \quad (3.35c)$$

where  $r_c$  is the centroid of the composite bilayer beam. The substitution of Equation 3.34 into the strain energy function (Equation 3.33) and subsequent

differentiation with respect to the force  $P$  ( $\delta = \frac{\partial U}{\partial P}$ , Castigliano's second theorem) yields the displacement  $\delta$  as a linear function of  $P$ . The initial stiffness  $k$  of the curved bilayer can, therefore, be calculated as:

$$k = \frac{P}{\delta} \quad (3.36)$$

### 3.4.4. Finite element analysis

FEA was performed using the commercial software package Abaqus (Abaqus 6.14, Simulia, US). Static plane strain analyses were performed for both the bending and stiffness steps using an implicit nonlinear solver (Abaqus Standard, full Newton integration). Full-integration hybrid plane strain elements (*i.e.*, CPE4H) were used for modelling the incompressible behavior of the materials. The constitutive behavior of the bilayer during the bending analysis was captured using an incompressible Neo-Hookean material model. The Neo-Hookean material constant  $C_{10}$  was calculated based on the selected Young's modulus as:

$$C_{10}^{(i)} = \frac{G_i}{2} = \frac{E_i}{6} \quad (3.37)$$

In order to allow for instabilities to be triggered, imperfections were introduced through the perturbation of the elastic properties of few elements at the interface of both layers [75, 76] (see Table 3.2). The expansion of the active layer was modelled through the inclusion of a predefined stress field. The individual stress components were calculated as:

$$\sigma_x = 2C_{10}^{(2)} \left( \frac{1}{\alpha^2} - \alpha^2 \right) \quad (3.38a)$$

$$\sigma_y = 0 \quad (3.38b)$$

$$\sigma_z = 2C_{10}^{(2)} (1 - \alpha^2) \quad (3.38c)$$

$$\sigma_{xy} = 0 \quad (3.38d)$$

For the stiffness analysis, an incompressible linear elastic material model was used. One side of the curved beam was clamped while a small compressive displacement of 0.1% of the beam radius was applied at the centroid axis of the beam. The resulting reaction force was divided by the applied displacement to calculate the stiffness of the bilayer element.

### 3.4.5. Bilayer bending experiments

Bilayer samples were fabricated from polylactic acid (PLA) filaments using a fused deposition modeling (FDM) 3D printer (Ultimaker 2+, Ultimaker, The Netherlands). During the process of filament extrusion and the subsequent cooling of the printed material, pre-stresses are stored as memory inside the structure of the printed material [17]. Upon exposure to high temperatures, the printed filament shrinks along the length direction accompanied with expansion in the

other directions. Bilayers were produced by printing several layers with filaments aligned in the longitudinal direction on top of a series of layers with filaments perpendicular to the length direction. A nozzle diameter of 0.25 mm and a printing speed of 50 mm/s was used while the layer thickness and extrusion temperature were varied to program the different amounts of longitudinal shrinkage (see Table 3.3).

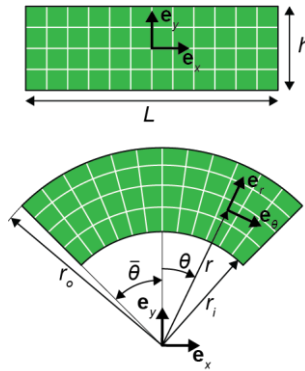
The polymer-metal bilayers samples were fabricated from polyolefin (G. Apex, Taiwan Yun Lin Electronic Co. Taiwan) with a nominal thickness of 1.0 mm. The stiffness of the polyolefin layer was obtained from the literature [77, 78]. The bilayer samples were produced through adhesive bonding (Loctite 401, Henkel, Ireland) of the polyolefin layer to a thin stainless steel foil (AISI 316, annealed, Goodfellow, UK) with a thickness of 50  $\mu\text{m}$ . The specimens were cured for at least 24 h at room temperature.

All the specimens were activated through submersion in a transparent container filled with hot water for at least 60 s to ensure the completeness of the shape-shifting process. The 4D printed samples were activated at a temperature of 90  $^{\circ}\text{C}$  while the activation temperature for the polymer-metal bilayer samples was varied to achieve different amounts of longitudinal shrinkage (see Table 3.4). The deformed configuration of the activated bilayers was captured using digital cameras. A custom MATLAB (Mathworks, version R2020b, US) code was used for image processing. A circle was fit to the detected interface radius to obtain the curvature of the specimens.

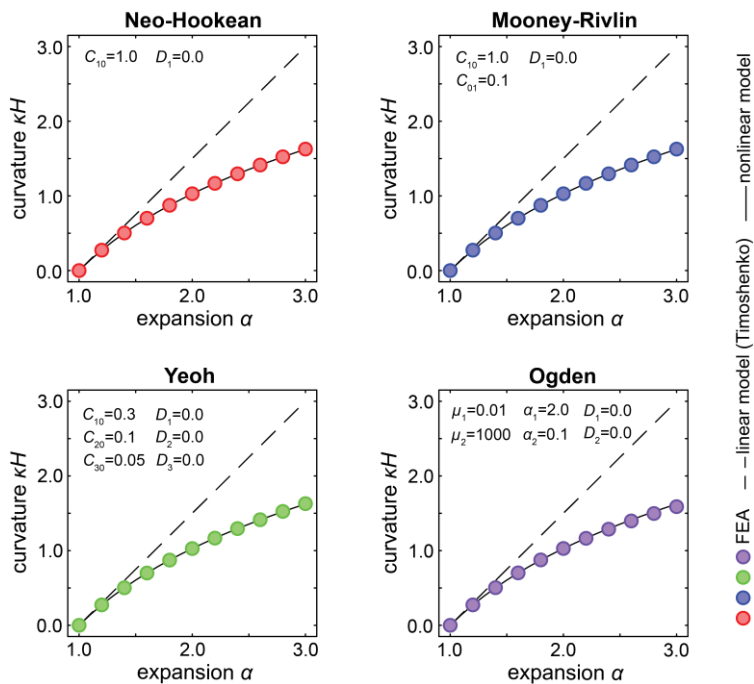
### 3.4.6. Stiffness experiments

The specimens were produced using a multi-material polyjet 3D printer (Object500 Connex3, StratasyS). Different combinations of hard (VeroCyan<sup>TM</sup>) and soft (Agilus30<sup>TM</sup> Clear) photo polymeric materials were used for the fabrication of bilayer beams with various stiffness ratios (see Table 3.5 and 3.6). The beams were fabricated with a beam thickness varying between 2.0 and 10.0 mm. The beams were fabricated with a radius of 10.0 mm and a beam thickness varying between 2.0 and 10.0 mm ( $\beta = 1$ ). The specimens were then mechanically tested under compression (maximum displacement = 2.0 mm and compression rate = 5 mm/min, see Figure 3.11) using a Lloyd LR5K mechanical testing machine equipped with a 100 N load cell. For all the experiments, a linear relationship between the load and displacement could be observed. A MATLAB code was used to fit a line to the experimental data, thereby obtaining the stiffness of the specimens.

### 3.5 Supplementary information



**Figure 3.7:** Schematic representation of the bending of a thick elastic block into a curved beam.

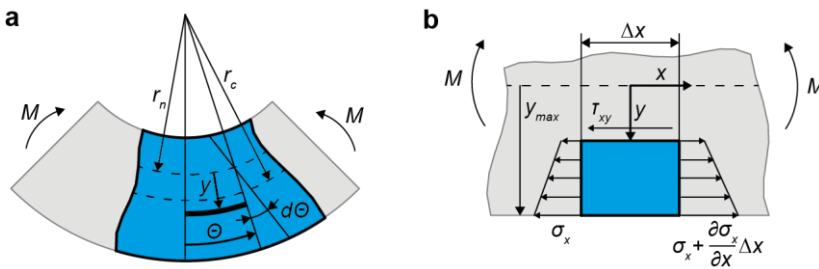


**Figure 3.8:** Theoretical and FEA results for the bending of bilayer beams using different incompressible hyperelastic material models.



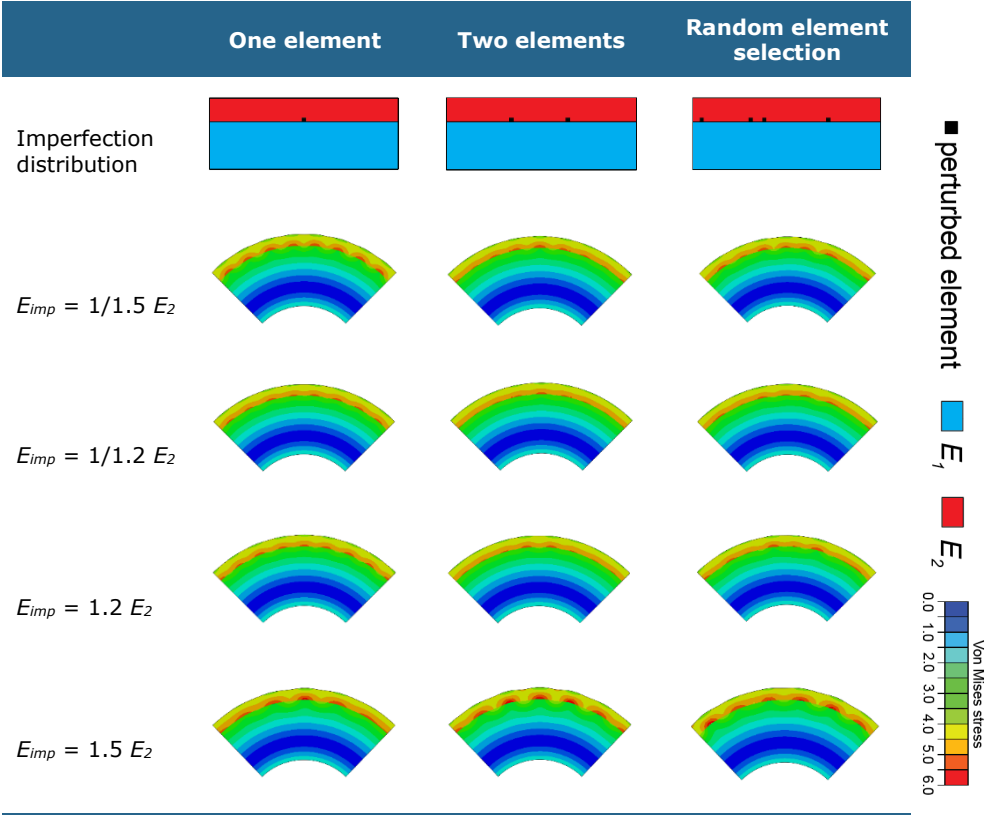
**Table 3.1:** Comparison of the wrinkling theory and FEA for multiple combinations of thickness ratio and stiffness ratio. Both the expansion values at the onset of wrinkling  $\alpha_{\text{wrinkling}}$  and the number of wrinkles  $n_{\text{wrinkles}}$  are listed while the maximum value of  $\alpha$  was set to 3.0.

Parameters		Theory		FEA	
$\beta$	$\gamma$	$\alpha_{\text{wrinkling}}$	$n_{\text{wrinkles}}$	$\alpha_{\text{wrinkling}}$	$n_{\text{wrinkles}}$
1/100	1/100	>3	n/a	>3	n/a
1/100	1/10	>3	n/a	>3	n/a
1/100	1	1.9	151	2.0	148
1/100	10	1.2	134	1.3	85
1/100	100	1.2	22	1.2	22
1/10	1/100	3.0	170	2.1	140
1/10	1/10	2.1	88	2.3	70
1/10	1	2.6	6	2.5	7
1/10	10	2.9	2	2.7	2
1/10	100	2.6	2	2.9	2
1	1/100	>3	n/a	>3	n/a
1	1/10	>3	n/a	>3	n/a
1	1	>3	n/a	>3	n/a
1	10	>3	n/a	>3	n/a
1	100	>3	n/a	>3	n/a
10	1/100	1.05	2	1.1	2
10	1/10	>3	n/a	>3	n/a
10	1	>3	n/a	>3	n/a
10	10	>3	n/a	>3	n/a
10	100	>3	n/a	>3	n/a
100	1/100	1.03	2	1.07	2
100	1/10	>3	n/a	>3	n/a
100	1	>3	n/a	>3	n/a
100	10	>3	n/a	>3	n/a
100	100	>3	n/a	>3	n/a



**Figure 3.9:** Schematic illustrations of beam segments. (a) A curved beam loaded in pure bending. (b) A straight beam loaded in bending. The net force in x-direction over the beam element in blue equals zero.

**Table 3.2:** The effects of the imperfection distribution and amplitude on the onset of wrinkling in a bilayer self-folding sample ( $a = 2.6$ ,  $\beta = 1/10$ , and  $\gamma = 1$ ).



**Table 3.3:** The programmed deformation for different printer settings (layer thickness and extrusion temperature).

Printer setting	$L/L_0$	$h/h_0$
Extrusion temp: 225 °C Layer thickness: 0.1 mm	0.86	1.16
Extrusion temp: 225 °C Layer thickness: 0.05 mm	0.78	1.25
Extrusion temp: 210 °C Layer thickness: 0.05 mm	0.68	1.46
Extrusion temp: 195 °C Layer thickness: 0.05 mm	0.58	1.59
Extrusion temp: 185°C Layer thickness: 0.05 mm	0.53	1.67

**Table 3.4:** The temperature-dependent deformation of the heat shrinking polymer.

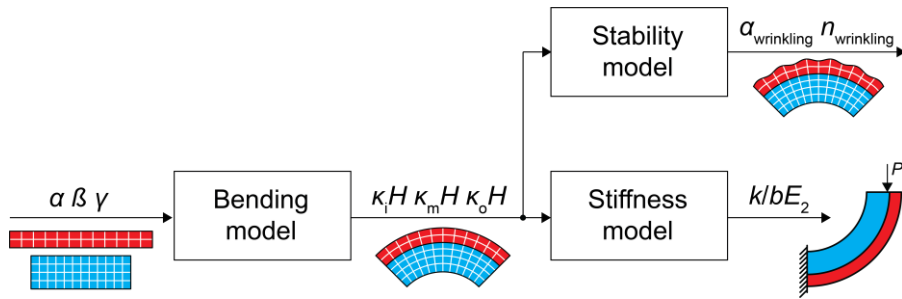
Activation temperature (°C)	$L/L_0$	$h/h_0$
75	0.92	1.11
80	0.86	1.26
82.5	0.82	1.30
85	0.73	1.53
87.5	0.65	1.61
90	0.59	1.88

**Table 3.5:** The Young's modulus of the Polyjet 3D printed materials with different combinations of hard (VeroCyan™) and soft (Agilus30™ Clear) photopolymeric materials.

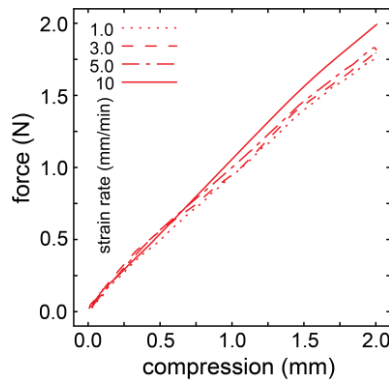
Hard volume fraction $\rho$ (%)	$E$ (MPa)
0	0.84
10	3.2
20	15.4
30	103
100	2552

**Table 3.6:** The fabrication parameters of the samples used for the stiffness experiment.

	$\rho$ outer layer (%)	$\rho$ outer layer (%)
Figure 4c-i	0	0
Figure 4c-ii	10	30
Figure 4c-iii	10	20
Figure 4c-iv	10	20



**Figure 3.10:** A block diagram showing how the different models are combined. The input parameters include the three dimensionless parameters  $\alpha$ ,  $\beta$ , and  $\gamma$ . The output of the models are the dimensionless stiffness of the 90°-folded bilayer as well as the onset of wrinkling.



**Figure 3.11:** The effects of the compression rate on the stiffness of the 3D printed curved bilayer elements.

## Bibliography

1. Meloni, M., et al., *Engineering Origami: A comprehensive review of recent applications, design methods, and tools*. Advanced Science, 2021. **8**(13): p. 2000636.
2. Gracias, D.H., et al., *Forming electrical networks in three dimensions by self-assembly*. science, 2000. **289**(5482): p. 1170-1172.
3. Cho, J.-H., et al., *Nanoscale origami for 3D optics*. Small, 2011. **7**(14): p. 1943-1948.
4. Jamal, M., A.M. Zarafshar, and D.H. Gracias, *Differentially photo-crosslinked polymers enable self-assembling microfluidics*. Nature communications, 2011. **2**(1): p. 1-6.
5. Jamal, M., et al., *Directed growth of fibroblasts into three dimensional micropatterned geometries via self-assembling scaffolds*. Biomaterials, 2010. **31**(7): p. 1683-1690.
6. Janbaz, S., et al., *Origami lattices with free-form surface ornaments*. Science advances, 2017. **3**(11): p. eaao1595.
7. Ionov, L., *Polymeric actuators*. Langmuir, 2015. **31**(18): p. 5015-5024.
8. Liu, Y., J. Genzer, and M.D. Dickey, *"2D or not 2D": Shape-programming polymer sheets*. Progress in Polymer Science, 2016. **52**: p. 79-106.
9. van Manen, T., S. Janbaz, and A.A. Zadpoor, *Programming the shape-shifting of flat soft matter*. Materials Today, 2018. **21**(2): p. 144-163.
10. Zhang, Y., et al., *Printing, folding and assembly methods for forming 3D mesostructures in advanced materials*. Nature Reviews Materials, 2017. **2**(4): p. 1-17.
11. Wei, M., et al., *Stimuli-responsive polymers and their applications*. Polymer Chemistry, 2017. **8**(1): p. 127-143.
12. Liu, F. and M.W. Urban, *Recent advances and challenges in designing stimuli-responsive polymers*. Progress in polymer science, 2010. **35**(1-2): p. 3-23.
13. Gracias, D.H., *Stimuli responsive self-folding using thin polymer films*. Current Opinion in Chemical Engineering, 2013. **2**(1): p. 112-119.
14. Ding, Z., et al., *Direct 4D printing via active composite materials*. Science advances, 2017. **3**(4): p. e1602890.
15. Gladman, A.S., et al., *Biomimetic 4D printing*. Nature materials, 2016. **15**(4): p. 413-418.
16. Kim, Y., et al., *Printing ferromagnetic domains for untethered fast-transforming soft materials*. Nature, 2018. **558**(7709): p. 274-279.
17. Van Manen, T., S. Janbaz, and A.A. Zadpoor, *Programming 2D/3D shape-shifting with hobbyist 3D printers*. Materials horizons, 2017. **4**(6): p. 1064-1069.
18. van Manen, T., et al., *4D printing of reconfigurable metamaterials and devices*. Communications Materials, 2021. **2**(1): p. 1-8.
19. Filipov, E.T., T. Tachi, and G.H. Paulino, *Origami tubes assembled into stiff, yet reconfigurable structures and metamaterials*. Proceedings of the National Academy of Sciences, 2015. **112**(40): p. 12321-12326.
20. Overvelde, J.T., et al., *Rational design of reconfigurable prismatic architected materials*. Nature, 2017. **541**(7637): p. 347-352.
21. Zhai, Z., Y. Wang, and H. Jiang, *Origami-inspired, on-demand deployable and collapsible mechanical metamaterials with tunable stiffness*. Proceedings of the National Academy of Sciences, 2018. **115**(9): p. 2032-2037.
22. Bertoldi, K., et al., *Flexible mechanical metamaterials*. Nature Reviews Materials, 2017. **2**(11): p. 1-11.
23. Kim, Y.-J., et al., *A novel layer jamming mechanism with tunable stiffness capability for minimally invasive surgery*. IEEE Transactions on Robotics, 2013. **29**(4): p. 1031-1042.
24. Ou, J., et al. *jamSheets: thin interfaces with tunable stiffness enabled by layer jamming*. in *Proceedings of the 8th International Conference on Tangible, Embedded and Embodied Interaction*. 2014.

25. Kim, S.-J., et al., *An origami-inspired, self-locking robotic arm that can be folded flat*. Science Robotics, 2018. **3**(16): p. eaar2915.
26. Nojima, T. and K. Saito, *Development of newly designed ultra-light core structures*. JSME International Journal Series A Solid Mechanics and Material Engineering, 2006. **49**(1): p. 38-42.
27. van Manen, T., et al., *Kirigami-enabled self-folding origami*. Materials Today, 2020. **32**: p. 59-67.
28. Randhawa, J.S., et al., *Importance of surface patterns for defect mitigation in three-dimensional self-assembly*. Langmuir, 2010. **26**(15): p. 12534-12539.
29. Tien, J., T.L. Breen, and G.M. Whitesides, *Crystallization of millimeter-scale objects with use of capillary forces*. Journal of the American Chemical Society, 1998. **120**(48): p. 12670-12671.
30. Abdolahi, J., et al., *Analytical and numerical analysis of swelling-induced large bending of thermally-activated hydrogel bilayers*. International Journal of Solids and Structures, 2016. **99**: p. 1-11.
31. Morimoto, T. and F. Ashida, *Temperature-responsive bending of a bilayer gel*. International Journal of Solids and Structures, 2015. **56**: p. 20-28.
32. Nardinocchi, P. and E. Puntel, *Finite bending solutions for layered gel beams*. International Journal of Solids and Structures, 2016. **90**: p. 228-235.
33. Roccabianca, S., D. Bigoni, and M. Gei, *Long wavelength bifurcations and multiple neutral axes of elastic layered structures subject to finite bending*. Journal of Mechanics of Materials and Structures, 2011. **6**(1): p. 511-527.
34. Roccabianca, S., M. Gei, and D. Bigoni, *Plane strain bifurcations of elastic layered structures subject to finite bending: theory versus experiments*. IMA journal of applied mathematics, 2010. **75**(4): p. 525-548.
35. Budynas, R.G., *Advanced strength and applied stress analysis*. 1999: McGraw-Hill.
36. Budynas, R.G., J.K. Nisbett, and K. Tangchaichit, *Shigley's mechanical engineering design*. 2005: McGraw Hill New York.
37. Rivlin, R., *Large elastic deformations of isotropic materials. V. The problem of flexure*. Proceedings of the Royal Society of London. Series A. Mathematical and Physical Sciences, 1949. **195**(1043): p. 463-473.
38. Cendula, P., et al., *Bending and wrinkling as competing relaxation pathways for strained free-hanging films*. Physical Review B, 2009. **79**(8): p. 085429.
39. Timoshenko, S., *Analysis of bi-metal thermostats*. Josa, 1925. **11**(3): p. 233-255.
40. Bassik, N., et al., *Patterning thin film mechanical properties to drive assembly of complex 3D structures*. Advanced Materials, 2008. **20**(24): p. 4760-4764.
41. Arora, W.J., et al., *Membrane folding to achieve three-dimensional nanostructures: Nanopatterned silicon nitride folded with stressed chromium hinges*. Applied physics letters, 2006. **88**(5): p. 053108.
42. Pinto, R.M., V. Chu, and J.P. Conde, *Amorphous Silicon Self-Rolling Micro Electromechanical Systems: From Residual Stress Control to Complex 3D Structures*. Advanced Engineering Materials, 2019. **21**(9): p. 1900663.
43. Schmidt, O., et al., *Self-assembled nanoholes, lateral quantum-dot molecules, and rolled-up nanotubes*. IEEE Journal of selected topics in quantum electronics, 2002. **8**(5): p. 1025-1034.
44. Vaccaro, P.O., K. Kubota, and T. Aida, *Strain-driven self-positioning of micromachined structures*. Applied Physics Letters, 2001. **78**(19): p. 2852-2854.
45. Pi, C.-H. and K.T. Turner, *Design, analysis, and characterization of stress-engineered 3D microstructures comprised of PECVD silicon oxide and nitride*. Journal of Micromechanics and Microengineering, 2016. **26**(6): p. 065010.
46. Cheng, X., et al., *Surface chemical and mechanical properties of plasma-polymerized N-isopropylacrylamide*. Langmuir, 2005. **21**(17): p. 7833-7841.
47. Bassik, N., et al., *Photolithographically patterned smart hydrogel based bilayer actuators*. Polymer, 2010. **51**(26): p. 6093-6098.

48. Kim, J., et al., *Reversible self-bending soft hydrogel microstructures with mechanically optimized designs*. Chemical Engineering Journal, 2017. **321**: p. 384-393.
49. Naficy, S., et al., *4D printing of reversible shape morphing hydrogel structures*. Macromolecular Materials and Engineering, 2017. **302**(1): p. 1600212.
50. Na, J.H., et al., *Programming reversibly self-folding origami with micropatterned photo-crosslinkable polymer trilayers*. Advanced Materials, 2015. **27**(1): p. 79-85.
51. Hu, Z., X. Zhang, and Y. Li, *Synthesis and application of modulated polymer gels*. Science, 1995. **269**(5223): p. 525-527.
52. Morales, D., et al., *Ionoprinted multi-responsive hydrogel actuators*. Micromachines, 2016. **7**(6): p. 98.
53. Wang, X., et al., *Multi-Responsive Bilayer Hydrogel Actuators with Programmable and Precisely Tunable Motions*. Macromolecular Chemistry and Physics, 2019. **220**(6): p. 1800562.
54. Jamal, M., et al., *Bio-origami hydrogel scaffolds composed of photocrosslinked PEG bilayers*. Advanced healthcare materials, 2013. **2**(8): p. 1142-1150.
55. Janbaz, S., R. Hedayati, and A. Zadpoor, *Programming the shape-shifting of flat soft matter: from self-rolling/self-twisting materials to self-folding origami*. Materials Horizons, 2016. **3**(6): p. 536-547.
56. Felton, S.M., et al., *Self-folding with shape memory composites*. Soft Matter, 2013. **9**(32): p. 7688-7694.
57. Ge, Q., H.J. Qi, and M.L. Dunn, *Active materials by four-dimension printing*. Applied Physics Letters, 2013. **103**(13): p. 131901.
58. Ge, Q., et al., *Active origami by 4D printing*. Smart materials and structures, 2014. **23**(9): p. 094007.
59. Liu, Y., et al., *Self-folding of polymer sheets using local light absorption*. Soft matter, 2012. **8**(6): p. 1764-1769.
60. Mailen, R.W., et al., *Modelling of shape memory polymer sheets that self-fold in response to localized heating*. Soft Matter, 2015. **11**(39): p. 7827-7834.
61. Wang, H., et al., *Shape-Controlled, Self-Wrapped Carbon Nanotube 3D Electronics*. Advanced Science, 2015. **2**(9): p. 1500103.
62. Liu, Y., et al., *Sequential self-folding of polymer sheets*. Science Advances, 2017. **3**(3): p. e1602417.
63. Shaha, R.K., A.H. Torbati, and C.P. Frick, *Body-temperature s hape-shifting liquid crystal elastomers*. Journal of Applied Polymer Science, 2021. **138**(14): p. 50136.
64. An, N., M. Li, and J. Zhou, *Instability of liquid crystal elastomers*. Smart Materials and Structures, 2015. **25**(1): p. 015016.
65. Kim, H., et al., *Tough, shape-changing materials: crystallized liquid crystal elastomers*. Macromolecules, 2017. **50**(11): p. 4267-4275.
66. Agrawal, A., et al., *Shape-responsive liquid crystal elastomer bilayers*. Soft Matter, 2014. **10**(9): p. 1411-1415.
67. Barnes, M. and R. Verduzco, *Direct shape programming of liquid crystal elastomers*. Soft Matter, 2019. **15**: p. 870-879.
68. Boothby, J. and T. Ware, *Dual-responsive, shape-switching bilayers enabled by liquid crystal elastomers*. Soft Matter, 2017. **13**(24): p. 4349-4356.
69. Yuan, C., et al., *3D printed reversible shape changing soft actuators assisted by liquid crystal elastomers*. Soft Matter, 2017. **13**(33): p. 5558-5568.
70. Meng, H. and G. Li, *A review of stimuli-responsive shape memory polymer composites*. Polymer, 2013. **54**(9): p. 2199-2221.
71. Alben, S., B. Balakrishnan, and E. Smela, *Edge Effects Determine the Direction of Bilayer Bending*. Nano Letters, 2011. **11**(6): p. 2280-2285.
72. Finot, M. and S. Suresh, *Small and large deformation of thick and thin-film multilayers: effects of layer geometry, plasticity and compositional gradients*. Journal of the Mechanics and Physics of Solids, 1996. **44**(5): p. 683-721.
73. Ogden, R.W., *Non-linear elastic deformations*. 1997: Courier Corporation.

74. Su, Y., et al., *Pattern evolution in bending dielectric-elastomeric bilayers*. Journal of the Mechanics and Physics of Solids, 2020. **136**: p. 103670.
75. Nikraves, S., D. Ryu, and Y.-L. Shen, *Direct numerical simulation of buckling instability of thin films on a compliant substrate*. Advances in Mechanical Engineering, 2019. **11**(4): p. 1687814019840470.
76. Nikraves, S., D. Ryu, and Y.-L. Shen, *instabilities of thin films on a compliant Substrate: Direct numerical Simulations from Surface Wrinkling to Global Buckling*. Scientific reports, 2020. **10**(1): p. 1-19.





# Programming 2D/3D shape-shifting with hobbyist 3D printers

# 4

Materials and devices with advanced functionalities often need to combine complex 3D shapes with functionality-inducing surface features. Precisely controlled bio-nanopatterns, printed electronic components, and sensors/actuators are all examples of such surface features. However, the vast majority of the refined technologies that are currently available for creating functional surface features only work on flat surfaces. Here we present initially flat constructs that upon triggering by high temperatures change their shape to a pre-programmed 3D shape, thereby enabling the combination of surface-related functionalities with complex 3D shapes. A number of shape shifting materials have been proposed during the last few years based on various types of advanced technologies. The proposed techniques often require multiple fabrication steps and special materials, while being limited in terms of the 3D shapes they could achieve. The approach presented here is a single-step printing process that only requires a hobbyist 3D printer and inexpensive off-the-shelf materials. It also lends itself to a host of design strategies based on self-folding origami, instability-driven pop-up, and 'sequential' shape shifting to unprecedentedly expand the space of achievable 3D shapes. This combination of simplicity and versatility is a key to widespread applications.

T. van Manen, S. Janbaz & A.A. Zadpoor. (2017). *Programming 2D/3D shape-shifting with hobbyist 3D printers*. Materials horizons, **4**(6): p. 1064-1069.

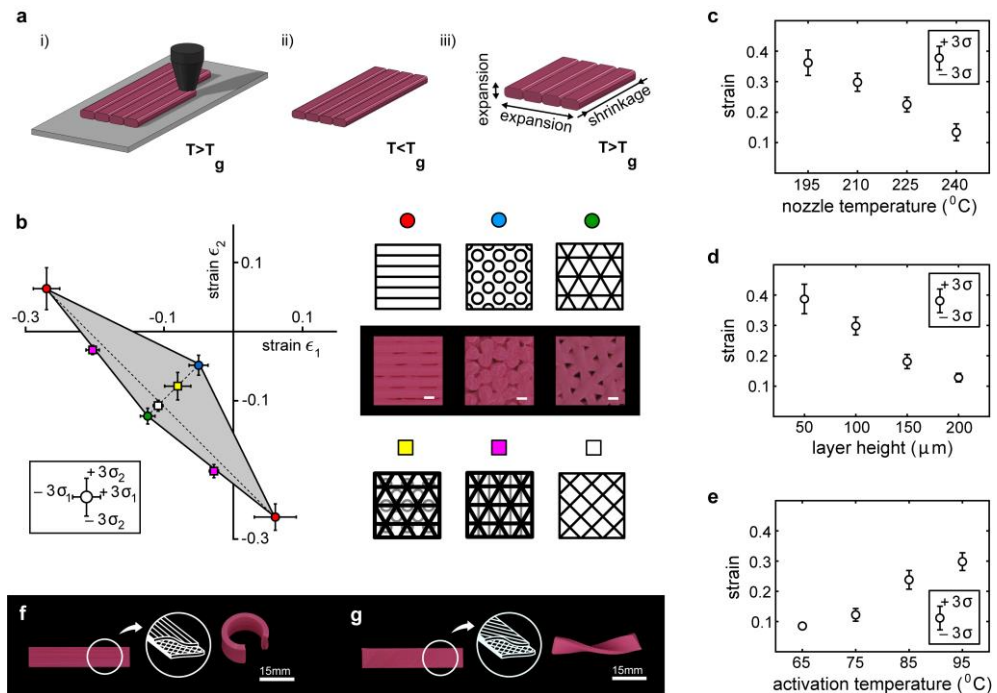
## 4.1 Introduction

Materials that are programmed to develop 3D configurations from initially flat states propound a revolutionary approach with applications in biotechnology [1], electronics [2], and engineering of complex metamaterials [3]. Combining passive and stimuli-triggered active layers into a multilayer construct is often used for programming the basic modes of shape-shifting such as bending and twisting [4–8]. Swellable and shape memory polymers (SMP) are widely used as the active elements in such designs. Triggered by different stimuli such as increase in temperature, humidity, or light, active elements can drive the process of shape-shifting [9–12]. Temporal shape transition of programmed SMP without any external stimuli is reported as well [13]. Dimensional parameters and programming procedure as well as the activation conditions can control the quality of the deformations [8]. Complex 3D structures are then obtained through the rational arrangement of active elements in multi-ply constructs [4]. For example, active hinges can control the folding state of origami [5, 14]. As an alternative to multi-layers, compressive stresses generated in swellable polymers could be used to induce complex shape-shiftings [15, 16]. The sequence of folding may be tuned to avoid locking and could be used as a tool to drive the folding kinematics of highly complex structures and improve the integrity of the target configurations [17, 18].

3D printing provides an alternative route to the programming of shape shifting: spatial arrangement of active (and passive) elements. In particular, sophisticated multi-material printing techniques could be used to combine different materials (e.g. hydrogel/polymer or polymer/polymer) to achieve multi-shape [19] or reversible shape-shifting [19, 20]. Anisotropic addition of properties (e.g. swelling ratio or stiffness) can include a fourth dimension into 3D printing techniques to achieve the so-called 4D printing [21, 22]. In a sharp contrast to the previously proposed techniques that require sophisticated or custom-made printers and spatial materials, here we present a versatile approach that requires no more than a hobbyist 3D printer and inexpensive off-the-shelf materials to implement many of the above-mentioned design routes and more.

## 4.2 Results and Discussion

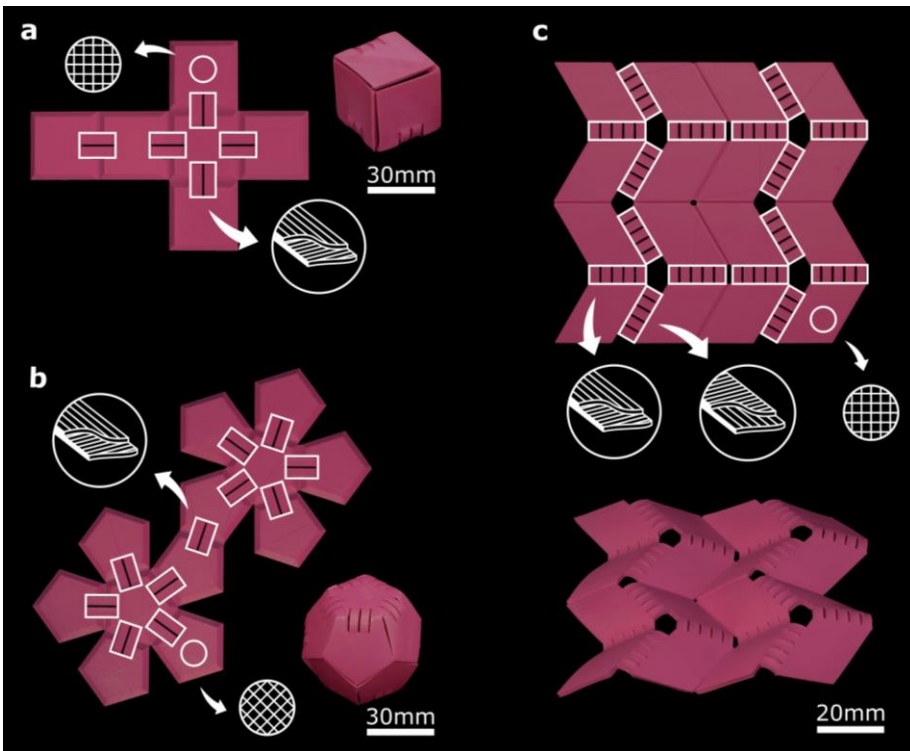
Hobbyist 3D printers generally work on the basis of extrusion of polymeric filaments, a technology called fused deposition modeling (FDM) (Figure 4.1a). During the printing process, the filament experiences temperatures above its melting temperature while being stretched. The high temperature allows for stretching and alignment of polymer chains along the direction of extrusion, which due to the constraints applied during the printing process (see the supplementary information, Section 4.4), is stored in the material as memory. Polylactic acid (PLA), a shape memory polymer with a melting temperature  $>180\text{ }^{\circ}\text{C}$ , is the most widely used material in hobbyist FDM printers. 3D printed (*i.e.*, extruded) PLA



**Figure 4.1:** (a) As the filament is extruded during the printing process, it stretches and bonds with the previously printed layer. After cooling down below  $T_g$ , the stretching of the filament is stored as memory in the material. Upon heating above  $T_g$ , the material relaxes, resulting in shrinkage in the longitudinal direction and expansion in both other directions. (b) The printing pattern of multi-ply square panels regulates their in-plane strains. The grey area shows the range of possible directional strains that we measured for multipattern panels. (c-e) Both printing and activation parameters control the shrinkage of multi-ply panels. (f) Basic shape shifting in self-bending strips made by combining a longitudinal shrinking toplayer with a semi-passive bottom layer. (g) Changing the orientation of the toplayer results in self-twisting.

filaments simultaneously decrease in length and thicken once heated above their glass transition temperature,  $T_g$  (Figure 4.1a). The percentage of decrease in the filament length could be controlled through adjustment of the printing parameters including the extrusion and activation (*i.e.*, triggering) temperatures as well as the layer thickness (Figure 4.1c-e). The flat surfaces are made of a number of layers with small thicknesses (50-200  $\mu\text{m}$ ). We used layers with identical patterns as well as stacks of layers with different patterns (Figure 4.6) to fabricate flat surfaces that show different combinations of directional strains ( $\epsilon_1$  and  $\epsilon_2$ ) upon exposure to temperatures exceeding  $T_g$  (Figure 4.1b). The negative planar strains are quite large (up to 0.27) while smaller positive strains (up to 0.06) are possible too (Figure 4.1b).

Flat surfaces (plies) with the desired deformation characteristics (i.e.  $\epsilon_1$ ,  $\epsilon_2$  duos) were then printed on top of each other for programming the desired shape transformation in the final multi-ply flat construct. The most basic mode of shape-shifting, i.e. a self-bending (self-rolling) strip, is achieved when a ply with relatively large anisotropic deformation characteristics (e.g.  $\epsilon_1 = -0.27$ ,  $\epsilon_2 = 0.06$ ) is printed on top of a ply with relatively small isotropic deformation characteristics (e.g.  $\epsilon_1 = -0.11$ ,  $\epsilon_2 = -0.11$ ) (Figure 4.1f). The main straining direction of the ply with large deformation characteristics must be chosen to be in parallel with the length of the strip. The out-of-plane deformation occurs due to the resistance of the semi-passive ply against deformation of the active ply. If the main straining direction makes an angle with the length of the strip, a self-twisting (self-helicing) strip is made (Figure 4.1g). Both self-bending and self-twisting elements were used as actuating elements in the shape-shifting designs described below.



**Figure 4.2:** Self-bending elements (annotated on the figure as white rectangles) connect the semi-passive panels of origami structures. (a) A flat printed construct, consisting of 6 square panels connected by a thin layer to preserve the integrity of the structure, is folded into a cubic box upon activation (Video 4.1 [23]). The printing patterns of the active bilayers and semi-passive panels are shown schematically. (b) Using the same method, a self-folding dodecahedron folds to its 3D shape (Video 4.2 [23]). (c) The well-known Miura-ori folding pattern was printed and activated using two different types of self-bending elements (with different bending directions). The initially flat structure made of four Miura-ori units transforms its shape to the desired folded state upon activation (Video 4.3 [23]).

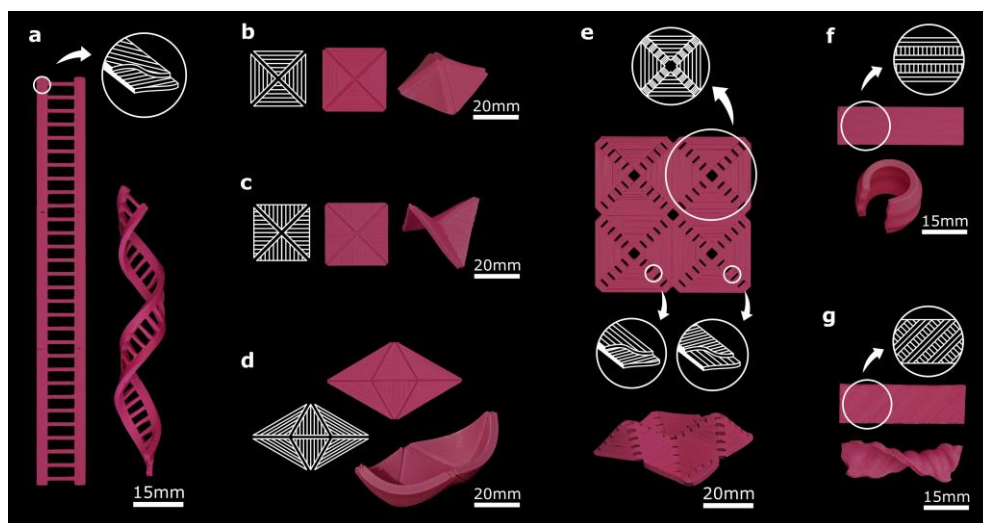
Self-folding origami is one of the areas where semi-passive multi-ply panels with minimal deformation characteristics (e.g.  $\epsilon_1 = -0.11$ ,  $\epsilon_2 = -0.11$ ) that represent the rigid parts of the origami are combined with actuating elements that exhibit large out-of-plane deformations (Figure 4.2). The self-bending elements described above are the simplest types of such actuators. The width and thickness of the strips strongly affect the deformation characteristics (e.g. radius of curvature, Figure 4.8) and could therefore be used to adjust the actuation behavior of self-bending elements, thereby enabling a wide range of 3D shapes. Using multiple actuating elements -with different widths and thickness- in the same joint of a rigid origami not only allows for achieving different ultimate positions but also enables separation of the actuations kinematics from the actuation kinetics (i.e., actuation force). A self-folding box is the simplest type of self-folding origami that can be made with the above-mentioned techniques (Figure 4.2a). These design principles were found to be highly scalable and were, thus, applied to shapes with larger number of folds and more complex topologies such as a self-folding dodecahedron (Figure 4.2b). An example of a technically relevant 3D shape is the Miura-ori origami that has received much attention recently [24, 25] and is studied as a model of rigid origami. Manual folding of Miura-ori origami is challenging, making it difficult to perform extensive and consistent experiments. We combined two types of self-bending actuators, which bend in different directions, with semi-passive panels representing the rigid parts of the design to make a self-folding Miura-ori origami (Figure 4.2c). Four actuators were used at each joint to increase the bending moment and overcome the locking caused by slight asynchronicities in the start of the bending of two or more actuators.

Derivatives of the basic shape-shifting modes could be used for obtaining more complex shapes. For example, two narrow self-helixing strips connected by a number of semi-passive horizontal elements were used to fabricate a DNA-inspired structure (Figure 4.3a).

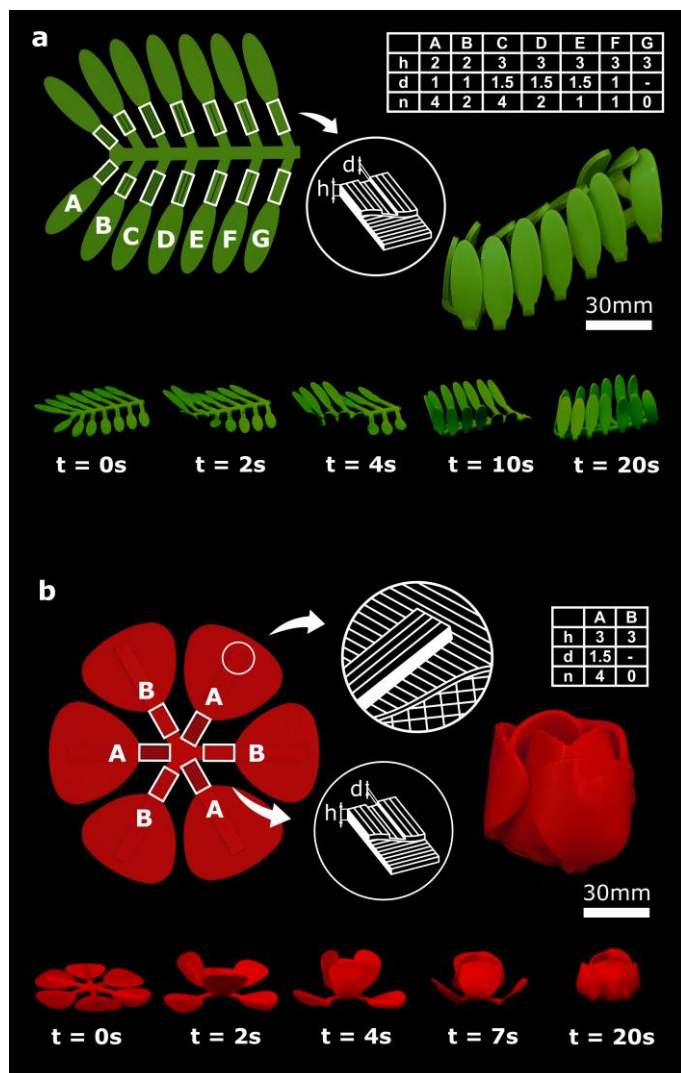
Every shape-shifting design demonstrated so far has been based on combination of semi-passive panels with actuators. An alternative approach is to combine active panels that shrink in one direction and expand in another. In such a scenario, exposure to high temperatures creates compressive stresses that force some of the panels to buckle out of plane. The active panels are connected via thin printed layers that act as joints and folding lines. The buckling caused by externally applied compressive forces have been recently proposed as an effective way for transforming 2D shapes to complex 3D shapes [26, 27]. The methodology we present here preserves the versatility of the buckling-induced 2D/3D shape transformations while taking it one step further by incorporating active elements, meaning not only that no external compressive forces are required but also that the number and complexity of the applied compressive forces could be drastically increased. To demonstrate some of the shapes that could be achieved through this approach, we designed self-folding pyramids (Figure 4.3b), saddle shapes

(Figure 4.3c), and boats (Figure 4.3d). To control the direction of the out-of-plane buckling, the thin connection between the panels could be replaced by some active bending elements. Using that approach, we assembled four pyramids (similar to Figure 4.3b) of which, after activation, two popped-up in one direction and the other two in the other direction (Figure 4.3e).

In an alternative approach to multi-ply panels, we used single-ply strips to induce out-of-plane shape shifting. As opposed to the through-the-thickness arrangement of semi-passive and active plies used so far, the side-by-side alignment of shrinking and expanding monolayer strips can achieve self-bending (Figure 4.3f) and self-twisting when the direction of monolayer strips is oblique (Figure 4.3g). After activation, parallel buckling lines appear on the surface of these monolayer strips as a consequence of energy minimization in their constituting micro-elements. This single-ply approach provides an additional shape-shifting avenue that could be potentially integrated into multi-ply designs to extend the space of achievable 3D shapes.



**Figure 4.3:** (a) Two initially flat self-twisting (bilayer) strands together with semi-passive connectors result in a DNA-inspired shape after activation (Video 4.4 [23]). (b-d) The schematic of the monolayer panels with small grooves that were used to determine the folding lines. Compressive stresses generated by the anisotropic in-plane shrinkage of the panels result in out-of-plane buckling patterns that create the desired 3D shapes (Video 4.5-4.6 [23]). (e) Self-bending elements were placed at the folding lines of a shrinking panel to control the direction of buckling (i.e. upward vs. downward) (Video 4.8 [23]). (f) Parallel arrangement of expanding and shrinking strips results in a monolayer self-rolling element (Video 4.7 [23]). (g) Arrangement of the expanding and shrinking strips with a 45° angle with respect to the longitudinal direction results in a monolayer self-twisting element (Video 4.7 [23]).



**Figure 4.4:** Sequential shape-shifting in two nature-inspired design. The active regions in both structures are highlighted by white rectangles while the geometry and printing patterns are shown schematically. Dimensions ( $h$ : thickness,  $d$ : groove depth) and number of grooves,  $n$  of the active elements are tabulated for both structures. (a) Gradual closure of the leaves of a structure resembling the shy plant. Sequential shape shifting was controlled by the thickness and the dimensions of the grooves in the bilayer active elements (Video 4.9 [23]). (b) Two-step folding of the initially flat petals to create a tulip. The time-lapses illustrate the sequence of folding for both designs (Video 4.10 [23]).

The most complex types of 2D/3D shape shifting need to be performed in an ordered sequence of steps. In self-folding origami, for example, some folds need to occur before others, necessitating the ability to program 'sequential folding'. We used two strategies, namely variable porosity and variable thickness, to adjust the activation times of the active elements.



Porosity was introduced to the panels by printing an array of grooves. We changed the depth and number of grooves to make panels with different porosities. Heat transfer occurs more readily in panels with higher porosity, which in turns results in faster activation. Thickness variation could be also used to adjust the time of activation, because it takes more time for the thicker panels to reach  $T_g$  and go into the soft glassy state. Activation will not commence before almost the entire thickness of the panel has reached the glass transition temperature, as the stiffness of the panel is much higher at low temperatures [28]. Using both above-mentioned strategies, we incorporated sequential folding into two designs. The first design imitates the gradual closing of the leaves of the shy (*i.e.*, *Mimosa pudica*) plant (Figure 4.4a). The second design (Figure 4.4b) is a self-folding tulip with initially flat petals that sequentially fold to create the multiple layers seen in natural tulips. When incorporated into the previously discussed design paradigms, time delays could tremendously enrich the programmability of initially flat constructs by enabling multiple shape-shifting steps.

### 4.3 Outlook and Conclusions

A number of points need to be discussed with respect to the shape-shifting behaviour of the structures developed here. First, the results of the current study clearly show that different printing parameters results in different shape-shifting behaviours (Figures 4.1b and 4.7). Changing the printing parameters could, among other effects, result in altered microstructure. Somewhat similar effects have been found in other studies [29]. The micro-architectural parameters of the printed structures such as the porosity could also affect the shape-shifting behaviour and were, for example, used for creating sequential folding. Second, the shape shifting behaviour of 3D printed PLA is activated by exposure to high temperatures. However, the homogeneity of the temperature field as well as the specific heat transfer conditions might be different based on the surrounding media. In addition, the other conditions of the surrounding environment such as humidity, pH, or liquid type could potentially affect the shape-shifting behaviour by changing the microstructure of the printed material. Similar effects have been observed in other kinds of shape-shifting materials [30]. Third, we used different in-plane arrangements of the 3D printed shrinking polymer to create shrinkage or expansion in lattice structures in response to the activation stimulus (e.g. Figure 4.9b-c). It would be also interesting to expand the current designs to create other kinds of negative/positive structural expansions similar to those reported in the literature [31]. There are, however, some limitations such as the resolution of FDM printing and the layer-by-layer manner of printing that could limit the range of achievable structural expansion coefficients. Finally, although the approach presented here is aimed at achieving permanent shape-shifting, similar designs based on multiple responsive materials could be also used for programming reversible shape transformations [32].

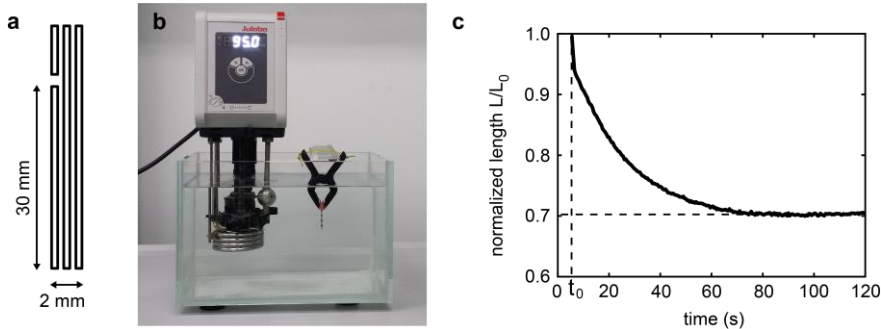
Given that a host of inexpensive 3D printers and PLA filaments similar to the ones used here are available in the market and that very complex 3D shapes could be achieved, there is no to little practical barrier to the widespread application of the proposed shape shifting techniques. Advanced technologies that primarily work in 2D such as nanolithography, electron beam induced deposition [33], microarray printing [34], and direct-write electrospinning [35] together with the functionalities they offer could then be easily incorporated into 3D devices. The design principles and fabrication techniques presented here could be transferred and scaled to serve as a general platform for programming the shape shifting of flat materials and address the requirements of other printing technologies and materials.

## 4.4 Supplementary information

### 4.4.1. General methods

3D printers (Ultimaker 2+, Ultimaker, The Netherlands) working on the basis of fused deposition modelling (FDM) and polylactic acid (PLA) polymeric filaments (Ultimaker, diameter = 2.85 mm,  $T_g$  = 60-65 °C) were used for fabrication of all designs presented in this work. PLA generally has good shape memory properties [36]. Samples were produced in the room temperature while the temperature of the glass print bed was set to 60 °C in order to improve the adhesion between the samples and the print bed. The PLA filaments were extruded through a standard 0.4 mm nozzle. A nozzle temperature of 210 °C, printing speed of 60 mm/s, filament flow of 2.1 mm<sup>3</sup>/s, and layer thickness of 0.1 mm were used. Good adhesion between the fixed print bed and extruded material and the small gap between the nozzle and print bed, which result in swiping of the extruded filament by the moving nozzle tip, make sure that the melted material is stretched during printing. The stretched state of the melted filament will be frozen after cooling down and remains as memory in the body of the printed constructs. Should it not have been for the combined effects of swiping and material adhesion, no stress would have been accumulated and stored in the material. That was confirmed by a simple experiment in which PLA filaments extruded through the 3D printer nozzle using the same parameters as described above exhibited no memory.

The memory stored in the materials can be released by increasing the temperature above  $T_g$  while not constraining the printed structure at its boundaries. Printing patterns prescribe the directions of shrinkage and expansion into the body of printed constructs, which could be used as a tool for programming the shape-shifting of polymeric structures. A cubic glass water bath suitable for temperatures higher than  $T_g$  was used for activation of the printed structures, allowing us to track the deformations of the structures. The temperature of the water was controlled using a heating immersion circulator (CORIO CD, Julabo, Germany). Digital cameras were used to track the deformation of the studied specimens and a Matlab (Mathworks, version R2016b) code was used for image processing.

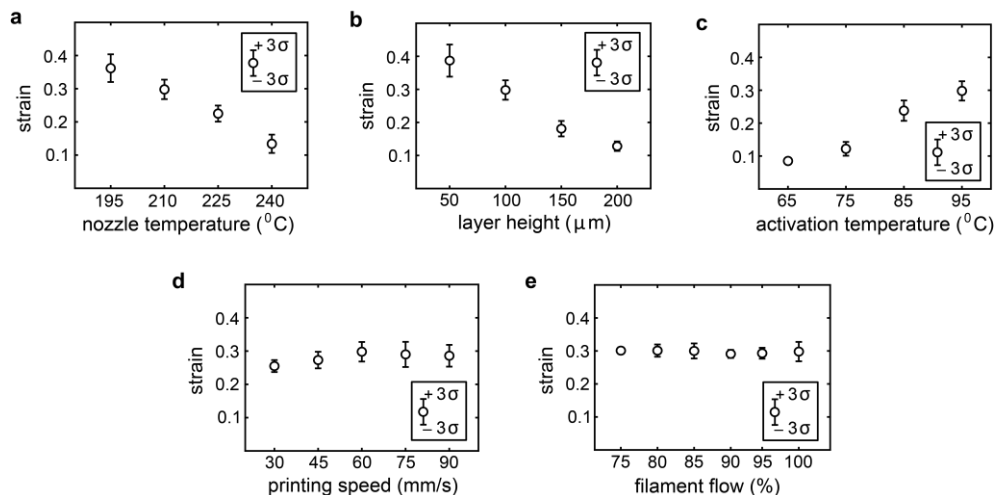


**Figure 4.5:** (a) The print path of each printed layer of the specimens. (b) The experimental setup used for activation of the specimens. The specimens were held by a gripper. (c) Change in the length of one sample specimen. The deformation starts at time  $t_0$  after activation.

#### 4.4.2. Effects of printing parameters on the directional strains of flat specimens

A number of test specimens ( $30 \times 10 \times 2$  mm) were 3D printed with PLA filaments (color: silver). The extruded filaments were aligned in the longitudinal direction (the print path is shown in Figure 4.5a). The specimens were activated at  $95^\circ\text{C}$  for at least 2 min to ensure the completion of the shape-shifting process. To provide free boundary conditions at both ends of the specimens, a weak connection was printed between the testing part of the specimen and its fixed end, which was attached to a gripper to keep the specimen in place (Figure 4.5b). The specimens were marked with black dots in order to easily track the change in length with image processing. The effects of nozzle temperature, printing speed, filament flow, and layer thickness were experimentally studied where each parameter was independently varied from the standard settings set by the manufacture (see Section 4.4.1). In addition, the effects of activation temperature were experimentally investigated.

The strain vs. time curves followed similar paths (Figure 4.5c) but with different onset times,  $t_0$ , and maximum strains. Three of the five studied parameters were found to highly influence the strain induced in the specimens (Figure 4.6). Both reduction in the nozzle temperature and layer thickness increase the maximum strain. The maximum strain could be increased from 13% to 36% by lowering the nozzle temperature from  $240^\circ\text{C}$  to  $195^\circ\text{C}$  (Figure 4.6a). Decreasing the layer thickness from 0.2 mm to 0.05 mm results in a 3-fold increase in the maximum strain (38% for 0.05 mm, Figure 4.6b). The activation temperature also strongly affected the contraction in the longitudinal direction (Figure 4.6c). The amount of shrinkage increased from about 13% to 29% when the activation temperature increased from  $65^\circ\text{C}$  to  $95^\circ\text{C}$ . The printing speed and filament flow did not significantly influence the shrinkage of the specimens (Figure 4.6d-e). The filament flow is expressed as a percentage of the standard material flow of  $2.1 \text{ mm}^3/\text{s}$  (at a printing speed of  $60 \text{ mm/s}$ ).



**Figure 4.6:** The effects of the printer settings and activation temperature on the shrinkage of the specimens. The average shrinkage over four tested specimens is plotted with the error bars representing three times the standard deviation from the mean.

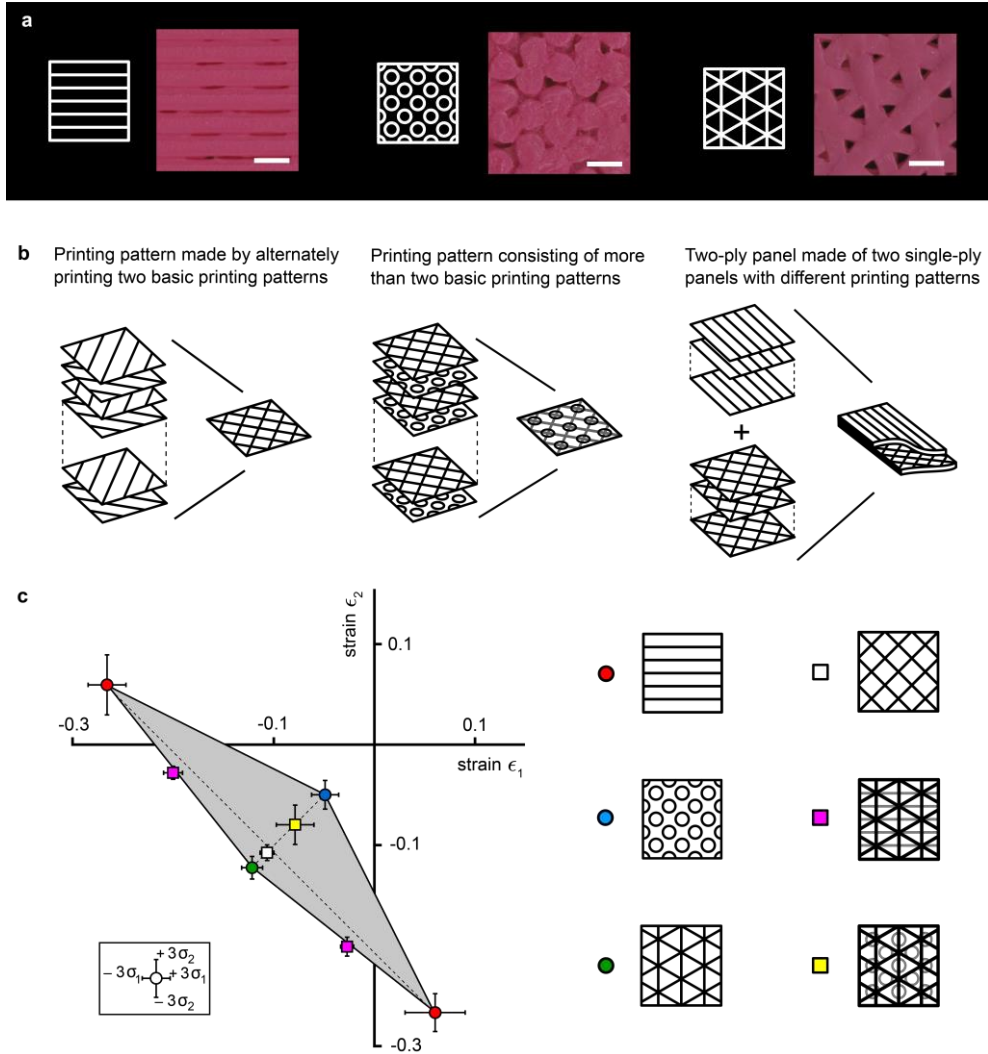
The nozzle temperature highly influenced the shrinkage of the specimens. As the extruded filament cools down, some relaxation of the stretched polymeric chains happens before the temperature drops below  $T_g$ . Printing at higher temperatures gives more time for relaxation and less stress will be stored inside the printed samples. Increasing the layer thickness has a similar effect, because it increases the cooling time. Moreover, reducing the layer thickness enhances the level of stretching of the polymer chains during the printing process.

#### 4.4.3. Effects of the printing pattern on the in-plane deformation of rectangular specimens

Different printing patterns were used for production of rectangular specimens (30×30×2 mm) from PLA filaments (color: silver). Three basic pattern designs, made by printing a stack of layers with identical patterns, were used (Figure 4.7a) together with a number of composite patterns, which were produced by printing a stack made of layers with different patterns (Figure 4.7b). The standard printer settings (see Section 1 of this document) were used. Activation was done at 95  $^{\circ}\text{C}$  for at least 2 min to ensure shape-shifting was complete. The length and width of the specimens before and after activation were measured using a caliper.

The deformation duos (normalized change in the length of the specimens in both in-plane directions) are plotted in Figure 4.7c. The alignment of the filament in one direction resulted in 27% shrinkage and 6% expansion in both orthogonal in-plane directions. Both circular and triangular printing patterns showed isotropic in-plane shrinkage (5% and 12%, respectively). Alternating the printing direction between consecutive layers resulted in 11% shrinkage in both directions.

Combining linear and triangular printing patterns resulted in highly anisotropic strains ( $\epsilon_1 = -0.20$ ,  $\epsilon_2 = -0.03$ ). On the other hand, the composite of triangular and circular printing patterns resulted in isotropic contractions equal to 8%.



**Figure 4.7:** (a) Schematic representation and detailed images of the three basic printing patterns (scale bar = 0.5 mm). (b) Complex printing patterns and two-ply structures were made by combining basic patterns. (c) The effects of printing pattern on in-plane deformation. The average of four tested specimens is plotted and the error bars represent three times the standard deviation.

A wide range of both isotropic and anisotropic in-plane deformation duos could be achieved by varying the printing pattern. Anisotropic deformations predominantly require layers with filaments aligned in one direction. Printing small circles

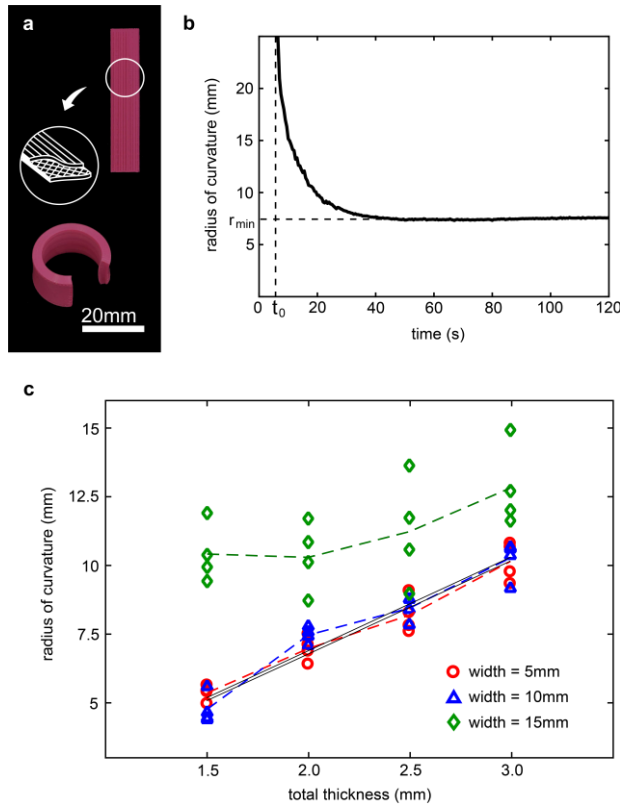
severely limits the amount of stored deformation, reducing the shrinkage to only 5% in both directions. The triangular printing pattern shows the largest isotropic shrinkage of 12%. These three cases show some of the extremes of anisotropic and isotropic in-plane deformation that could be achieved by combining basic printing patterns into a composite pattern. The tested composite patterns showed in-plane deformations that were in-between those of the basic patterns they were made of.

The triangular pattern could be seen as a composite of three linear patterns rotated by 120°, although the triangular pattern is printed within one layer instead of printing three separate linear patterns on top of each other. However, the shrinkage is significantly different from the grid infill pattern (composite of two orthogonal linear patterns). The insets of Figure 4.7a show that the triangular pattern is more porous as compared with the grid infill pattern, which was confirmed by comparing the weights of both types of specimens. The average mass of a 30×10×2 mm specimen with triangular pattern and grid infill pattern were respectively 2.0 and 2.3 g. The larger porosity of the triangular infill pattern allows for more deformation (shrinkage) as compared with the grid pattern. Further increasing the porosity might result in larger deformations but will also reduce the stiffness of the panels.

#### 4.4.4. Parametric study on two-ply strips

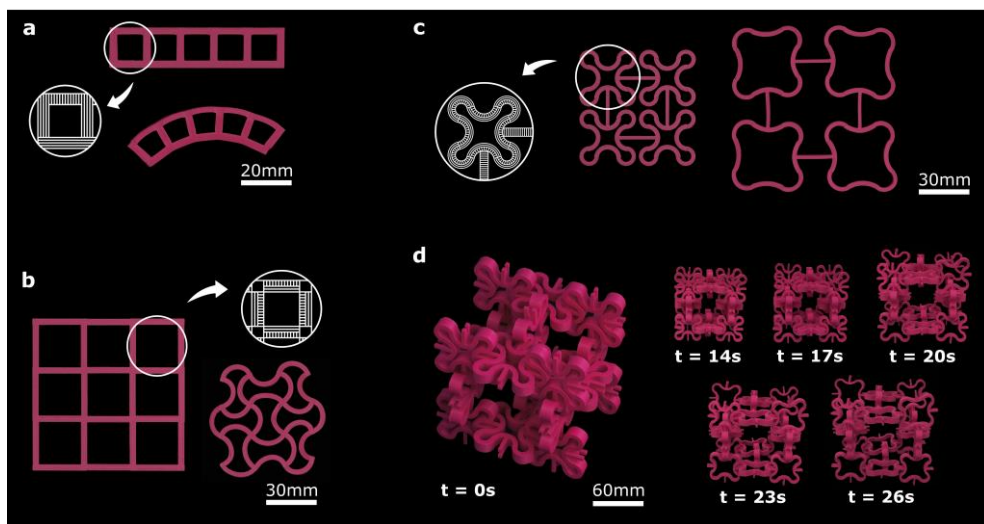
Two-ply specimens with a length of 30 mm were 3D printed from PLA (color: silver) to study the effects of dimensions (thickness, width) on their final shape. The printing patterns of the top and bottom plies are schematically shown in Figure 4.8a. The thickness of both plies was equal. Activation was done at 95 °C for at least 2 min to make sure the activation process was complete. One end of each specimen was fixed using a gripper and the free boundary was provided by a weak connection between the self-bending specimen and the fixed end. Marking the specimen with black dots allowed us to use image processing techniques for tracking the changes in the radius of curvature during the experiment.

Experimentally determined changes in the radius of curvature of one of the specimens is plotted in Figure 4.8b. The other specimens exhibited similar trends of deformation with the main difference being in their onset time,  $t_0$ , and minimum radius of curvature,  $r_{\min}$ . Both thickness and width of the specimens significantly influenced the shape-shifting of the two-ply specimens (Figure 4.8c). The results show radii of curvature in the range of 4.3 mm – 14.9 mm. The slender specimens (width = 5-10 mm) showed a 2-fold increase in their radius of curvature by increasing the thickness from 1.5 mm to 3 mm. Increasing the width from 5 mm to 10 mm did not change the results. Further increasing the width to 15 mm resulted in a 30% - 100% increase in the radius of curvature, dependent on the thickness.



**Figure 4.8:** (a) Schematic representation of the two-ply specimen. A cut-out of the top layer is made to show the printing pattern of the bottom ply. (b) A sample curve representative of the tested specimens showing the change in the radius of curvature with time. The onset time of bending is denoted by  $t_0$  and the minimum radius of curvature is denoted by  $r_{min}$ . (c) Experimental results show the radius of curvature of two-ply specimens with different sizes. Four specimens from each configuration were tested.

Increasing both the thickness and width of the two-ply strips resulted in larger radii of curvature after activation. According to the Timoshenko's bilayer bending model, the radius of curvature increases linearly as the thickness increases [37]. Fitting this linear relation between the radius and thickness to the experimental data showed that the experiments are in good agreement with the model for slender specimens ( $R^2 = 0.99$  and  $R^2 = 0.97$  for widths of 5 mm and 10 mm, respectively). By further increasing the width to 15 mm, the edge effects, which are not captured by the Timoshenko's bilayer model, started to become more prominent. The Poisson's effect causes the difference in the longitudinal strains of the top and bottom plies to be accompanied with an opposite difference in the transverse strains of both plies, resulting in the transverse bending of the two-ply strips. This double curvature increases the bending moment of inertia in the longitudinal direction, thereby increasing the radius of curvature.



**Figure 4.9:** 2D to 2D and 3D to 3D shape-shifting of cellular structures. (a) Bending of a 5×1 square array upon activation (Video 4.11 [23]). (b) Pattern transformation from a 3×3 square array to a 3×3 hourglass-shaped array (Video 4.12 [23]). (c) A 2×2 expanding cellular structure (Video 4.13 [23]). (d) The volumetric expansion of an assembly of 20 expanding unit-cells (Video 4.14 [23]). Unit-cells with the same printing patterns as the expanding structure (Figure 4.9c) were used.

#### 4.4.5. Shape-shifting of cellular structures

Cellular 2D structures were printed from PLA (color: magenta) using the standard printing settings. All specimens were produced with an edge thickness of 3.2 mm and a height of 7.5 mm. Two mechanisms of shape-shifting in the cellular structure were used to program both 2D to 2D and 3D to 3D shape-shifting. Printing of a 5×1 square array was performed with filament extrusion along the edge to program reduction in the edge length or in transverse direction to program increase in the edge length (Figure 4.9a). The programmed expansion and shrinkage of the edges results in the bending of the structure. Alternative to programming the change in the length of the edges, bending of the edges can be programmed by printing an expanding and shrinking strip side-by-side in one edge. This method is illustrated by a 3 x 3 array which shows pattern transformation from rectangular cells to hour-glass-shaped cells (Figure 4.9b). Expansion of a 2×2 cellular structure is achieved by straightening some initially curved edges using the same method (Figure 4.9c). 3D to 3D shape-shifting is illustrated with a cellular cubic structure made through manual assembly of 2D cellular unit-cells, which shows volumetric expansion upon activation (Figure 4.9d). Both the 5×1 and 3×3 square arrays were activated at 95 °C while other cellular structures were activated at 85 °C to avoid excessive deformations. Movies capturing the shape-shifting of the cellular structures were recorded and can be found as electronic supplementary material.



#### 4.4.6. Printing and activation parameters

**Table 4.1:** The printing parameters and activation conditions which were used for production and activation of the designs presented in this work.

Structure	Figure	Printing speed (mm/s)	Nozzle temperature (°C)	Layer height (μm)	Activation temperature (°C)
Box	4.2a	60	210	100	95
Dodecahedron	4.2b	60	210	100	95
Miura-ori	4.2c	60	210	100	95
DNA	4.3a	60	210	100	95
Pyramid	4.3b	60	210	100	95
Saddle	4.3c	60	210	100	95
Boat	4.3d	60	210	100	95
4 pyramids	4.3e	60	210	100	95
Bending strip	4.3f	60	195	50	95
Twisting strip	4.3g	60	195	50	95
<i>Mimosa pudica</i>	4.4a	60	210	100	90
Tulip	4.4b	60	210	100	90
5 x 1 array	4.9a	60	210	100	95
3 x 3 array	4.9b	60	210	100	95
2 x 2 array	4.9c	60	210	100	85
3D cellular structure	4.9d	60	210	100	85

## Bibliography

1. Randall, C.L., E. Gultepe, and D.H. Gracias, *Self-folding devices and materials for biomedical applications*. Trends in biotechnology, 2012. **30**(3): p. 138-146.
2. Gracias, D.H., et al., *Forming electrical networks in three dimensions by self-assembly*. science, 2000. **289**(5482): p. 1170-1172.
3. Xia, F., et al., *Two-dimensional material nanophotonics*. Nature Photonics, 2014. **8**(12): p. 899-907.
4. Liu, Y., J. Genzer, and M.D. Dickey, "2D or not 2D": *Shape-programming polymer sheets*. Progress in Polymer Science, 2016. **52**: p. 79-106.
5. Felton, S.M., et al., *Self-folding with shape memory composites*. Soft Matter, 2013. **9**(32): p. 7688-7694.
6. Stoychev, G., et al., *Hierarchical multi-step folding of polymer bilayers*. Advanced Functional Materials, 2013. **23**(18): p. 2295-2300.
7. Mu, J., et al., *Origami-inspired active graphene-based paper for programmable instant self-folding walking devices*. Science advances, 2015. **1**(10): p. e1500533.
8. Janbaz, S., R. Hedayati, and A.A. Zadpoor, *Programming the shape-shifting of flat soft matter: from self-rolling/self-twisting materials to self-folding origami*. Materials Horizons, 2016. **3**(6): p. 536-547.
9. Liu, Y., et al., *Self-folding of polymer sheets using local light absorption*. Soft matter, 2012. **8**(6): p. 1764-1769.
10. Jamal, M., A.M. Zarafshar, and D.H. Gracias, *Differentially photo-crosslinked polymers enable self-assembling microfluidics*. Nature communications, 2011. **2**: p. 527.
11. Zhao, Q., H.J. Qi, and T. Xie, *Recent progress in shape memory polymer: New behavior, enabling materials, and mechanistic understanding*. Progress in Polymer Science, 2015. **49**: p. 79-120.
12. Huang, L., et al., *Ultrafast digital printing toward 4D shape changing materials*. Advanced Materials, 2016: p. 1605390.
13. Hu, X., et al., *Programming temporal shapeshifting*. Nature Communications, 2016. **7**: p. 12919.
14. Na, J.H., et al., *Programming reversibly self-folding origami with micropatterned photo-crosslinkable polymer trilayers*. Advanced Materials, 2015. **27**(1): p. 79-85.
15. Kim, J., et al., *Designing responsive buckled surfaces by halftone gel lithography*. Science, 2012. **335**(6073): p. 1201-1205.
16. Wu, Z.L., et al., *Three-dimensional shape transformations of hydrogel sheets induced by small-scale modulation of internal stresses*. Nature communications, 2013. **4**: p. 1586.
17. Mao, Y., et al., *Sequential self-folding structures by 3D printed digital shape memory polymers*. Scientific Reports, 2015. **5**: p. 13616.
18. Ge, Q., et al., *Multimaterial 4D printing with tailorable shape memory polymers*. Scientific Reports, 2016. **6**: p. 31110.
19. Wu, J., et al., *Multi-shape active composites by 3D printing of digital shape memory polymers*. Scientific Reports, 2016. **6**: p. 24224.
20. Raviv, D., et al., *Active printed materials for complex self-evolving deformations*. Scientific reports, 2014. **4**: p. 7422.
21. Kokkinis, D., M. Schaffner, and A.R. Studart, *Multimaterial magnetically assisted 3D printing of composite materials*. Nature Communications, 2015. **6**: p. 8643.
22. Gladman, A.S., et al., *Biomimetic 4D printing*. Nature Materials, 2016. **15**: p. 413-418.
23. Van Manen, T., S. Janbaz, and A.A. Zadpoor, *Programming 2D/3D shape-shifting with hobbyist 3D printers*. Materials horizons, 2017. **4**(6): p. 1064-1069.
24. Chen, Y., R. Peng, and Z. You, *Origami of thick panels*. Science, 2015. **349**(6246): p. 396-400.
25. Schenk, M. and S.D. Guest, *Geometry of Miura-folded metamaterials*. Proceedings of the National Academy of Sciences, 2013. **110**(9): p. 3276-3281.

26. Xu, S., et al., *Assembly of micro/nanomaterials into complex, three-dimensional architectures by compressive buckling*. Science, 2015. **347**(6218): p. 154-159.
27. Yan, Z., et al., *Controlled mechanical buckling for origami-inspired construction of 3D microstructures in advanced materials*. Advanced Functional Materials, 2016. **26**: p. 2629-2639.
28. Ratna, D. and J. Karger-Kocsis, *Recent advances in shape memory polymers and composites: a review*. Journal of Materials Science, 2008. **43**(1): p. 254-269.
29. Malinauskas, M., et al., *3D microporous scaffolds manufactured via combination of fused filament fabrication and direct laser writing ablation*. Micromachines, 2014. **5**(4): p. 839-858.
30. Rekštytė, S., et al., *Microactuation and sensing using reversible deformations of laser-written polymeric structures*. Nanotechnology, 2017. **28**(12): p. 124001.
31. Qu, J., et al., *Micro-Structured Two-Component 3D Metamaterials with Negative Thermal-Expansion Coefficient from Positive Constituents*. Scientific reports, 2017. **7**: p. 40643.
32. Mao, Y., et al., *3D printed reversible shape changing components with stimuli responsive materials*. Scientific reports, 2016. **6**.
33. Van Dorp, W.F., et al., *Approaching the resolution limit of nanometer-scale electron beam-induced deposition*. Nano letters, 2005. **5**(7): p. 1303-1307.
34. Harris, T.M., A. Massimi, and G. Childs, *Injecting new ideas into microarray printing*. Nature biotechnology, 2000. **18**(4): p. 384-385.
35. Lee, J., et al., *Fabrication of patterned nanofibrous mats using direct-write electrospinning*. Langmuir, 2012. **28**(18): p. 7267-7275.
36. Senatov, F.S., et al., *Mechanical properties and shape memory effect of 3D-printed PLA-based porous scaffolds*. Journal of the mechanical behavior of biomedical materials, 2016. **57**: p. 139-148.
37. Timoshenko, S., *Analysis of bi-metal thermostats*. Josa, 1925. **11**(3): p. 233-255.





# 4D printing of reconfigurable metamaterials and devices **5**

Shape-shifting materials are a powerful tool for the fabrication of reconfigurable materials. Upon activation, not only a change in their shape but also a large shift in their material properties can be realized. As compared with the 4D printing of 2D-to-3D shape-shifting materials, the 4D printing of reconfigurable (i.e., 3D-to-3D shape-shifting) materials remains challenging. That is caused by the intrinsically 2D nature of the layer-by-layer manner of fabrication, which limits the possible shape-shifting modes of 4D printed reconfigurable materials. Here, we present a single-step production method for the fabrication and programming of 3D-to-3D shape-changing materials, which requires nothing more than a simple modification of widely available fused deposition modeling (FDM) printers. This simple modification allows the printer to print on curved surfaces. We demonstrate how this modified printer can be combined with various design strategies to achieve high levels of complexity and versatility in the 3D-to-3D shape-shifting behavior of our reconfigurable materials and devices. We showcase the potential of the proposed approach for the fabrication of deployable medical devices including deployable bifurcation stents that are otherwise extremely challenging to create.

## 5.1 Introduction

Shape-shifting empowers the development of designer materials with advanced functionalities and properties. For example, a flat mechanism can shift its shape into a fully functional robot [1, 2]. Other examples are origami-based metamaterials [3-5] or self-folding bio-scaffolds made from (nano-)patterned 2D sheets [6]. There are two major categories of shape-shifting: 2D-to-3D and 3D-to-3D. 2D-to-3D shape-shifting enables flat constructs to fold themselves into geometrically-complex 3D objects. The main advantage lies in the ability to employ planar fabrication techniques for affording an ultimately 3D object with functionalities that originate from micro-/nanoscale surface features [7-9]. 3D-to-3D shape-shifting, on the other hand, is particularly useful for the fabrication of reconfigurable materials [10, 11]. The 3D configuration of such materials changes upon activation, thereby altering their functions and properties (*e.g.*, stiffness or wave propagation properties [12, 13]).

Several strategies for the fabrication of shape-shifting structures are reported in the literature. The vast majority of the existing techniques rely on the use of active materials that change their dimensions upon activation [14-16]. Examples include the swelling of hydrogels submerged in water [17] and the shrinkage of pre-strained shape-memory polymers exposed to high temperatures [18, 19]. 4D printing allows for the single-step manufacturing of complex shape-shifting structures [20-22]. The simplest type of 4D printing relies on the introduction of some sort of anisotropy in the material during the printing process [23-27]. Recently, we demonstrated how hobbyist FDM 3D printers and widely available, inexpensive materials can be used to program complex shape-shifting behaviors [26]. This approach, which has received much attention since and makes 4D printing accessible to a wide range of users, is cost-effective, highly scalable, and applicable to many materials.

The main working principle is the introduction of a rationally designed pattern of spatially varying anisotropies into the material. Such a pattern of anisotropy together with the memory stored in the extruded deposited filaments makes it possible to program complex 2D-to-3D shape-shifting behaviors into the fabric of the 4D printed object. The memory stored in the printed polymers (*e.g.*, polylactic-acid (PLA) filaments) is a result of simultaneous extrusion during the printing process and the rapid cooling of the extruded filaments under the physical constraints imposed by the neighboring filaments [26]. When heated above their glass transition temperature ( $T_g$ ), each deposited filament shrinks along its longitudinal direction while expanding in the other directions. The combined, concerted actions of all anisotropically deposited filaments lead to the desired shape-shifting behavior.

While highly effective for 2D-to-3D shape-shifting, our previously proposed approach as well as similar approaches proposed by others [28, 29] are seriously limited by the in-plane nature of their introduced anisotropies, which makes it very challenging to create reconfigurable materials. Here, we circumvent this limitation by printing otherwise planar structures on curved surfaces. We present a simple design of an add-on device, which makes it possible for hobbyist 3D printers to 4D-print on curved surfaces. We use computational models to simulate the shape-shifting behavior of the printed structures and to better understand the underlying mechanisms. Moreover, we demonstrate the potential of our proposed approach through the design and fabrication of various types of reconfigurable materials and devices, including a number of deployable cardiovascular stents.

## 5.2 Results and Discussion

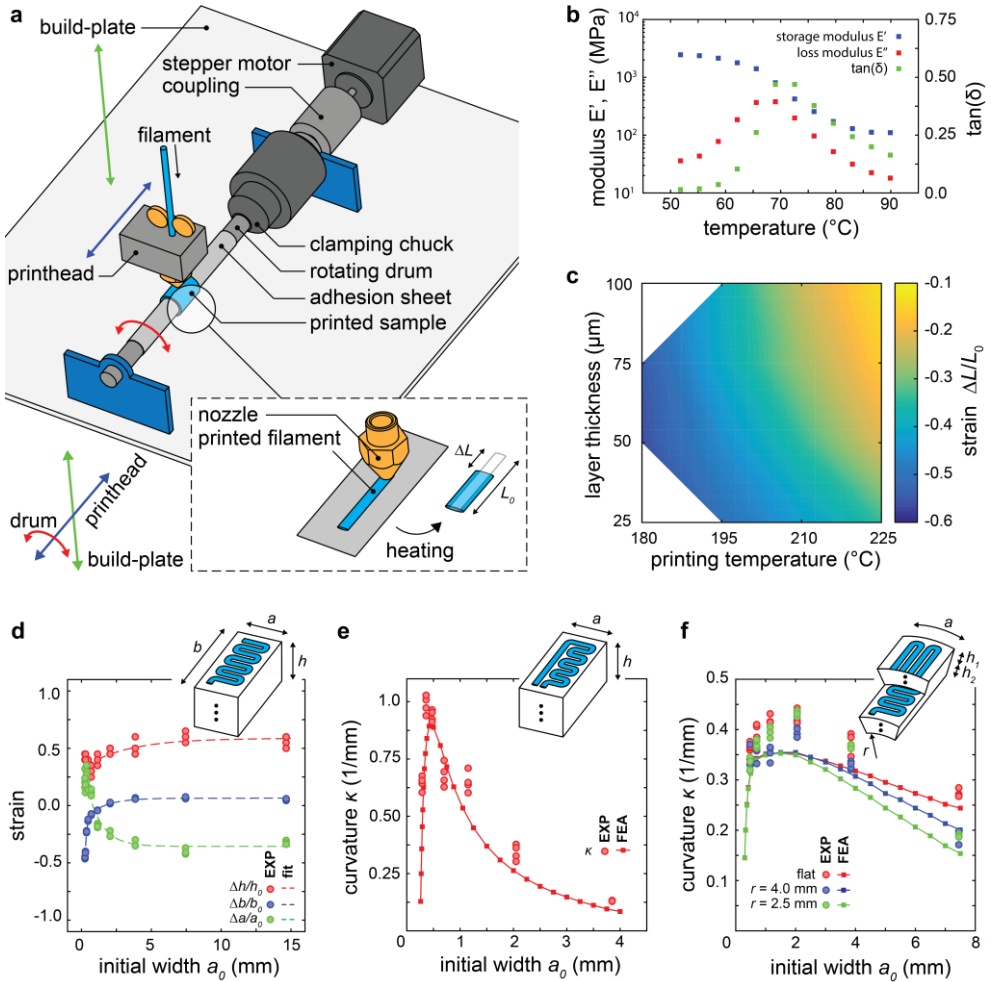
### 5.2.2 Basic shape-shifting elements

We designed and fabricated a simple add-on device, which was then mounted on an inexpensive hobbyist 3D printer (Figure 5.5). The add-on device employs a stepper motor to rotate a drum on which the specimens are printed. Combined with the three degrees-of-freedom offered by the linear motion system of the 3D printer, the rotating drums allows for the deformation patterns to be programmed along both longitudinal and circumferential directions. This new concept for the fabrication of curved 3D-to-3D shape-shifting structures is schematically illustrated in Figure 5.1a. More details can be found in Section 5.5.1.

To demonstrate the utility of the proposed approach, we used PLA filaments. First, we studied the material properties and deformation characteristics of basic shape-shifting elements. The thermomechanical properties of the PLA filaments were characterized using dynamic mechanical analysis (DMA). Molded PLA specimens were used in order to study the material properties independent from the 3D printing process. The DMA test results reveal a  $T_g$  of 70 °C while a clear drop in the mechanical properties upon heating above  $T_g$  can be observed (Figure 5.1b). Based on the experimental data, a temperature-dependent viscoelastic material model was fitted to be used for finite element analysis (FEA). The model parameters are listed in Table 5.1, 5.2 and 5.4. More methodological details can be found in Section 5.5.2.

We then studied the shape transformation of individually printed filaments as a function of the printing parameters. Both the layer thickness and extrusion temperature were varied to find the optimal combination of printing parameters. A lower printing temperature and, to a lesser extent, a smaller layer thickness were found to result in an increased filament shrinkage (Figure 5.1c and Figure 5.7a). An extrusion temperature of 180 °C was selected as the lower bound,





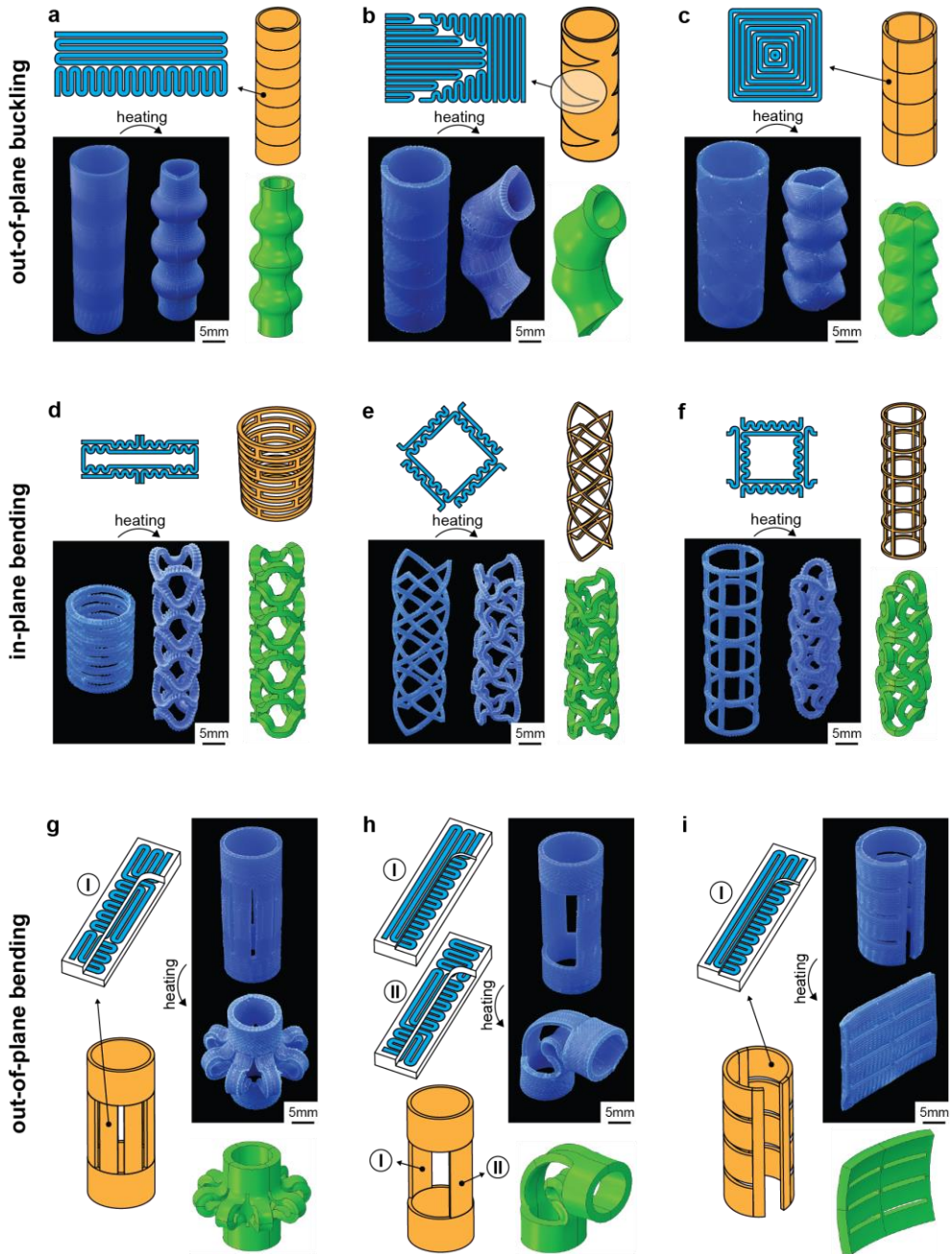
**Figure 5.1:** 4D printing concept. a) A schematic illustration of the methodology used for the fabrication of curved shape-shifting specimens. b) The storage modulus, loss modulus, and  $\tan(\delta)$  of the molded PLA specimens for a frequency of 10 Hz. c) The effects of the layer thickness and printing temperature on the longitudinal shrinkage of the printed filaments. d-f) The deformation characteristics of the basic building blocks as a function of the initial width.

because PLA filaments do not fully melt below this temperature, rendering the extrusion process very challenging especially for very thin and very thick layers.

The effective programmed deformation of printed constructs is the combined effect of the introduced molecular orientation along the direction of printing and the cooling history of the material. The molecular orientation is dependent on several factors, such as the molecular alignment introduced within the nozzle and the additional straining caused by the velocity differences between the print-head

and rotating shaft. Only the accumulated results of the printing parameters were studied here. These results were, however, consistent between the prints performed on a flat bed and those carried out using a rotating shaft. Reheating and subsequent cooling of the PLA filaments may cause additional relaxation, thereby limiting the magnitude of the programmed deformation. We, therefore, studied the effects of the printing path too. Only for parallel filaments with lengths less than 5 mm, a significant effect of the printing path on the shape-shifting behavior was observed (Figure 5.1d and Figure 5.7b-c). Curves were fit to the experimental data to serve as input to the finite element analysis (FEA) calculations that were performed to describe the shape-shifting behavior of the reconfigurable materials and devices studies here (Table 5.3). More methodological details can be found in Section 5.5.3.

Based on the knowledge gained regarding the effects of the printing parameters and printing path on the programmed deformations, basic bending elements were designed. The smallest possible in-plane bending element consists of one shrinking line parallel to an expanding block wave pattern (Figure 5.1e). Upon increasing the width of the expanding block-wave, the expansion ratio of the elements increases but at the cost of an increase in the bending stiffness. The maximum curvature was found for bending elements with a width of 0.5 mm. Out-of-plane bending elements were fabricated by printing parallel filaments in the longitudinal direction on top of layers with parallel filaments in the transverse direction (Figure 5.1f). Again, the degree of the longitudinal expansion of the bottom layers increases for larger widths ( $a$ ) of the out-of-plane bending elements. However, the increased difference in the longitudinal expansion between the top and bottom layers is accompanied with an opposite difference in the transverse expansion. As the width of the element increases, the bending due to the transverse expansion becomes more dominant, thereby increasing the second moment of inertia in the longitudinal direction. This effect is larger for the specimens with a smaller initial radius of curvature (Figure 5.1f). Regardless of the initial curvature, however, the maximum curvature was achieved for a width of 2.0 mm (Figure 5.1f). Both for the in-plane and out-of-plane bending elements, FEA was performed in which dimensional changes were calculated with the aid of empirical deformation curves (Figure 5.1d). In general, a good agreement between the experiments and FEA simulations was found (Figure 5.1e-f). The discrepancies between the experiments and the FEA results may be attributed to the manufacturing imperfections, such as the porosity of the 3D printed specimens, that are not implemented in the computational model. Such porosities may introduce anisotropies in the stiffness of the bending elements while also affecting the amount of (transverse) expansion [26, 30-33]. As a result, the bending stiffness of the elements reduces, resulting in an underestimation of the bending curvature in the computational models. More details on the FEA results can be found in Section 5.5.4.



**Figure 5.2:** Shape-shifting of a variety of curved samples. a-c) Three examples of out-of-plane buckling specimens employing in-plane deformation patterns. d-f) The shape-shifting behavior of cylindrical lattices with in-plane bending elements. g-i) The shape-shifting specimens made of different arrangements of out-of-plane bending elements. In all cases, experimental and computational results are presented side by side.

### 5.2.2 Reconfigurable materials

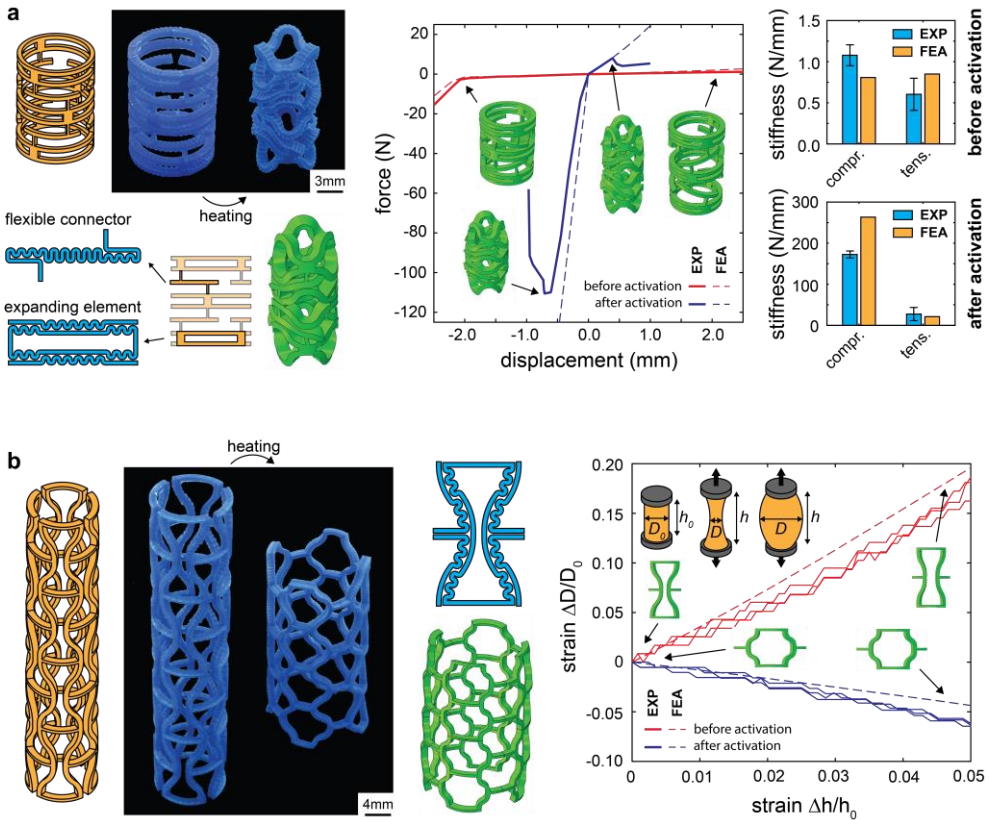
The next step is to apply the developed approach and the basic elements presented above for the design and fabrication of more complex reconfigurable structures. We employed three different design strategies to fabricate a variety of curved shape-changing specimens (Figure 5.2). The first strategy is based on introducing spatial variations in the orientation of the printing path along the circumferential or longitudinal directions, which was used to create multiple sample objects with out-of-plane shape-shifting behaviors caused by buckling (Figure 5.2a-c). Using this approach, both the bending of a cylinder as well as various other types of shape transformations can be programmed in the structure of the material. The second shape-shifting strategy relies on the positioning of in-plane bending elements within lattice structures. Three different types of unit cells were designed, resulting in a variety of shape deformations (Figure 5.2d-f). Finally, multiple arrangements of out-of-plane elements connected by semi-passive cylinders (*i.e.*, elements displaying limited amounts of deformation upon activation) were used for the manufacturing of a third series of shape-shifting tubes (Figure 5.2g-i). Tubes that shrink along their longitudinal direction (Figure 5.2g), bend (Figure 5.2h), or unfold (Figure 5.2i) were fabricated. For all the designed specimens, there is a good agreement between the experiments and the FEA results, indicating the effectiveness of the FEA models in predicting the shape-shifting behavior of our 4D printed curved specimens. Videos 2-4 [34] show the shape-shifting patterns as well as the FEA results of the samples presented in Figure 5.2.

### 5.2.3 Adaptive materials

The method we present here for the fabrication of reconfigurable materials, which requires nothing more than a simple modification of widely available FDM 3D printers and inexpensive PLA filaments paves the way for different types of potential applications. Here, we highlight two classes of potential applications, including adaptive materials (*i.e.*, adaptive stiffness and Poisson's ratio) and deployable (medical) devices.

A rational design of the shape-shifting behavior can be used to change specific properties of a material, including its stiffness and Poisson's ratio. We present two such designs. The first design is a compliant structure made of stiff rings connected by flexible elements (Figure 5.3a). When subjected to tensile, compressive, twisting, or shearing loads, the dominant deformation mode is the bending of the thin flexures. The stiffness of the specimens, therefore, does not exceed  $\approx 1.0 \text{ N mm}^{-1}$  (Figure 5.3a). Upon activation, the flexible connectors and expanding rings come into contact with each other. Once those contacts are established, the dominant deformation mode switches to the stretching of the flexures combined with the compression of the stiff rings (Figure 5.3a). This programmed change in the deformation regimen results in a shift from a highly

compliant structure to a semi-rigid one. In the case of tensile loading, a 30-fold increase in the stiffness is achieved while the compressive stiffness increases even more, by more than 2 orders of magnitude (Figure 5.3a). The computational models developed using the material characteristics and shape-memory behavior of simple configurations (Figure 5.1) are capable of capturing the constitutive response as well as the shape-shifting behavior of the adaptive-stiffness specimens designed here (Figure 5.3a). The relatively small differences between the experiments and FEA can be attributed to the local failure of the specimens, which is not included in the FEA models. The second design of adaptive materials presented here consists of a regular assembly of re-entrant honeycomb unit cells (Figure 5.3b). The bending of the arms, upon activation, results in switching from a re-entrant unit cell (with auxetic behavior) to conventional honeycomb unit cells



**Figure 5.3:** Switching of mechanical properties. a) Shape-shifting structure that switch their mechanical behavior from highly compliant to semi-rigid upon activation. The error bars represent the standard deviation ( $n = 3$  per group). b) The switching of the Poisson's ratio of a 4D printed specimen made using re-entrant unit-cells. Upon activation, the specimen switches its mechanical behavior from conventional (*i.e.*, a positive value of the Poisson's ratio) to auxetic (*i.e.*, a negative value of the Poisson's ratio). In all cases, experimental and computational results are presented side by side.

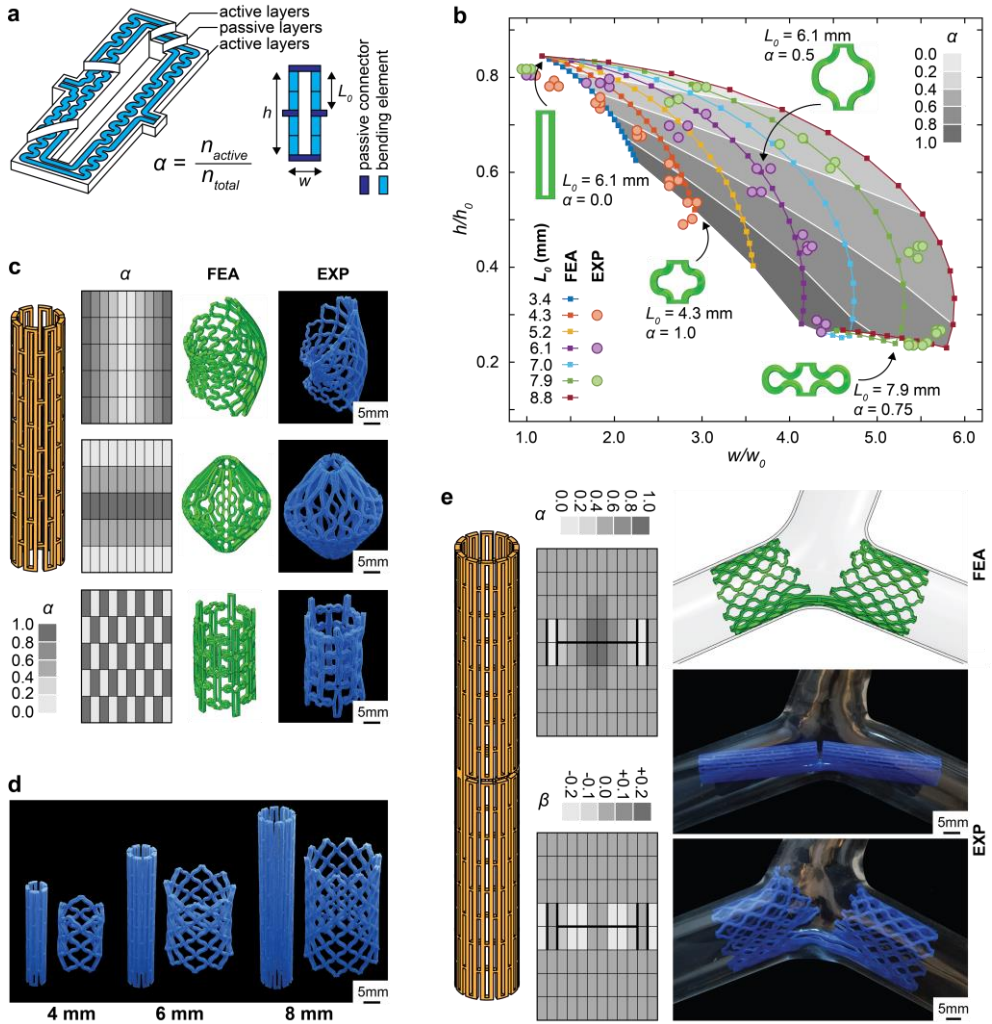
(with positive values of the Poisson's ratio) (Figure 5.3b). We conducted experiments in which the specimens were subjected to tensile loading both before and after the activation of the shape-shifting behavior. The change in the diameter as a function of the applied stretch is plotted in Figure 5.3b. A switch from a negative to a positive Poisson's ratio can, indeed, be observed in these results. This shift in the Poisson's ratio was also captured by our computational model (Figure 5.3b). While we only demonstrated two examples of adaptive mechanical behavior, many other types of adaptive behavior are possible. Examples include opposite switching behaviors (*i.e.*, from stiff to compliant or from conventional to auxetic) as well as the switching of other structural properties. Video 5 [34] shows the activation of the samples presented in Figure 5.3.

### 5.2.4 Deployable devices

Deployable devices are another interesting area of potential application for the approach presented here. Deployable devices can be transported to otherwise inaccessible places (*e.g.*, in the human body). Subsequently, the device is deployed to fulfil its desired function. Here, we use a specific design of the unit cell to program the shape-shifting behavior of a large variety of deployable structures. The unit cell consists of in-plane bending elements that are joined through small connectors (Figure 5.4a). In addition to the initial length of the bending arms ( $L_0$ ), the amount of bending can be programmed by introducing a number of so-called passive layers within the bending arms. The printing paths of both passive and active layers are illustrated in Figure 5.4a. As opposed to active layers, passive layers are designed to remain straight upon activation. The competition between the active and passive layers determines the final curvature of the bending elements. Both experiments and finite element simulations were conducted to study the effects of the number of passive layers (described by the parameter  $\alpha$ ) and  $L_0$  on the in-plane deformation of the unit cell (see Figure 5.4b). As  $\alpha$  and  $L_0$  increase, the lateral expansion of the unit cell increases at the cost of an increased longitudinal shrinkage. Upon activation, unit cells with a larger  $\alpha$  and  $L_0$  experience some levels of contact between their bending arms, which limits their expansion (Figure 5.4b). The results presented in Figure 5.4b can be used as a design map to program a large variety of deployable structures. We designed and fabricated three types of deployable cylinders consisting of an array of  $5 \times 10$  unit cells. Multiple gradients of  $\alpha$  were used, resulting in different deployed geometries even though the initial geometry is the same in all cases (Figure 5.4c). Video 6 [34] shows the deployment of these three samples.

One important application of deployable structures is in the development of medical devices, including cardiovascular stents. Polymeric stents are particularly interesting because of their superior ability to serve as a drug delivery vehicle [35, 36]. Moreover, bioresorbable polymers can be used to eliminate some of the risks





**Figure 5.4:** Deployable materials and devices. a) An illustration of the design strategy and printing path of a shape-shifting unit cell made of in-plane bending elements and passive connectors. b) Computationally and experimentally obtained deformation characteristics of the expandable unit-cell. c) Deployable cylinders made of different combinations of unit cells. d) The dimensional scaling of the deployable stents. e) The deployment of a bifurcation stent within a model artery.

associated with permanent stents, such as late stent thrombosis [37-39]. Here, we demonstrate the potential of the presented shape-shifting approach to serve as a platform for the fabrication of self-expandable polymeric stents. Based on the same unit cell design (Figure 5.4a), three uniformly expandable stents were fabricated in different sizes (Figure 5.4d). Miniaturized stents can be fabricated using rotating rods with smaller diameters. Upon activation, the stents expand into their permanent shape (Figure 5.4d). We designed the stents to show an

approximately three-fold increase in diameter. Depending on the selected dimensions of the unit cells, smaller or larger amounts of radial expansion can be achieved as well.

As a final demonstration of the versatility of the presented 4D printing approach, a bifurcation stent was designed and fabricated. The design is based on the same expandable unit cell as described above (Figure 5.4a). In addition to  $\alpha$ , there are two other design features that affect the shape-shifting behavior of unit cells with a length of  $L_0$ . First, some of the connections between neighboring unit cells were removed in order to decouple the expansion in the tangential and longitudinal directions. Second, a degree of out-of-plane bending of individual unit cells was introduced by off-center positioning of the passive layers. The amount of the programmed out-of-plane actuation is described by the dimensionless parameter  $\beta$ :

$$\beta = \frac{n_{\text{active,top}} - n_{\text{active,bottom}}}{n_{\text{total}}} \quad (5.1)$$

where  $n_{\text{active,top}}$  is the number of active layers on top of the passive layers while  $n_{\text{active,bottom}}$  is the number of active layers underneath the passive layers. The spatial control of  $\alpha$  and  $\beta$  as well as the connections between unit cells allows for the programming of even more complex shape-shifting patterns. We designed a bifurcation stent by assembling an array of  $8 \times 12$  unit cells (Figure 5.4e). The removed connections are indicated by a thick black line. Upon activation, the bifurcation stent expands and an anchor point for the connection of a side-branch stent opens up. We used a model artery to activate the bifurcation stent and demonstrate its flexibility in morphing the geometry of the artery (Figure 5.4e). Video 7 [34] shows the activation of both a conventional as well as a bifurcation stent.

### 5.3 Outlook and conclusions

In summary, we presented a method for the fabrication of reconfigurable materials. Commercially available FDM 3D printers were modified through the addition of a simple device that can be easily manufactured in most basic workshops (if not domestic kitchens). By printing the specimens on a rotating shaft, we could incorporate both in-plane and on-curvature anisotropies into the fabric of 4D printed constructs. We then used the proposed approach to demonstrate the high level of geometrical complexity that can be achieved in the 3D-to-3D shape-shifting behavior of reconfigurable materials and devices. We also demonstrated some potential applications of the proposed reconfigurable materials, including those with adaptive effective properties (*i.e.*, adaptive stiffnesses and switchable auxeticity) as well as deployable (medical) devices. While we only used PLA filaments in the current study, a wide range of shape



memory polymers with highly variable values of the glass transition temperatures can be used for the fabrication of 4D printed devices. Polymers with lower values of the glass transition temperature already exist [40] and can be used in low-temperature applications. The underlying concepts of the approach proposed here remain valid regardless of the material used. While we performed most of our experiments using a hot water bath, not all potential applications are compatible with a liquid activation medium. We, therefore, conducted a number of experiments using hot air as the activation medium to understand the effects of the activation medium on the resulting shape-shifting behavior. The results of our experiments confirmed that the shape-shifting behavior of the specimens fabricated using the presented 4D printing approach are largely independent from the activation medium (Figure 5.8). In any case, short activation times (typically less than 30s) were sufficient to complete the shape-shifting process, which is highly beneficial for most practical applications. We believe that the development of such types of low-entry-barrier 4D printing technologies is essential for the democratization of emerging digital fabrication technologies and ensures they remain globally accessible including in low-resource settings.

## 5.4 Materials and methods

### 5.4.1 Sample fabrication

All the specimens were fabricated from PLA filaments using a FDM 3D printer (Ultimaker 2+, Ultimaker, The Netherlands). The add-on device (Figure 5.1a) was designed as a rotating drum mounted on a frame made from laser-cut acrylic sheets. The design and manufacturing details are presented Section 5.5 (Table 5.5 and 5.6). Good adhesion between the rotating drum and the printing specimens was guaranteed by the means of adhesion sheets. Both the printing paths and GCode files were generated using custom programs written in MATLAB (Mathworks, US). Sections 5.5.1, 5.5.5 and 5.5.7 can be consulted for extensive details on the fabrication process including the specific fabrication parameters for all the specimens presented in this study.

### 5.4.2 Sample activation

Samples were activated using a transparent container filled with hot water. The temperature was controlled by a heating immersion circulator (CORIO CD, Julabo, Germany). The deformations of the specimens were captured using digital cameras. The specimens were submerged in the water bath with a temperature of 90 °C for at least 30 s to ensure the shape-shifting process was complete (see Section 5.5.6).

### 5.4.3 Characterization of the constitutive behavior

The temperature-dependent mechanical properties of PLA were measured by performing dynamic mechanical analysis (DMA) measurements using a TA-Instruments Q-800 machine (TA Instruments, US). Assuming the material to be

thermorheologically simple, the time-temperature superposition principle was applied. A master curve was constructed by shifting the measured storage modulus at different temperatures along the frequency axis. The resulting master curve with the corresponding shift factors ( $a_T$ ) were then obtained. The Williams-Landel-Ferry (WLF) equation was fit to the experimental results and was used for the further analyses performed here (Figure 5.6).

#### 5.4.4 Finite element analysis

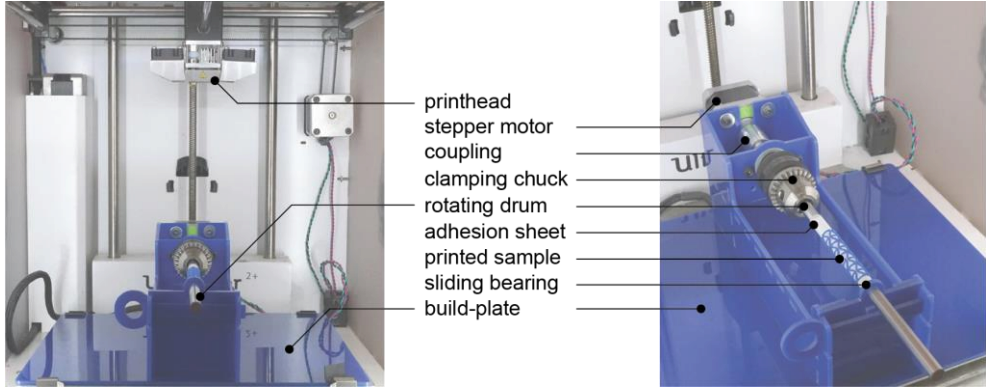
FEA was performed using the commercial software Abaqus (Abaqus 6.14, Simulia, US). A transient coupled temperature-displacement analysis was performed (Abaqus Standard, nonlinear implicit solver, full Newton integration) in order to also capture the time-dependent material behavior. The geometries of the computational models were discretized using full-integrated solid temperature-displacement elements (*i.e.*, C3D8T in Abaqus). The viscoelastic behavior of PLA was modelled using a Prony series. The simulation time was set to 2 min to ensure the completeness of the shape-shifting process. For some of the models, a surface-to-surface contact definition was implemented to prevent the penetration of different parts of the structure. A penalty contact enforcement algorithm was used for that purpose. The full details of the material characterization using DMA, material models, computational procedures, and the other methodological aspects of the computational modeling approach are presented in Section 5.5.2 and 5.5.4.

### 5.5 Supplementary material

#### 5.5.1 Fabrication process

A standard commercially available FDM 3D printer (Ultimaker 2+, Ultimaker, The Netherlands) was used for the fabrication of all the specimens. The 3D printer was modified to enable the 4D printing of curved specimens (Figure 5.5). A frame made from laser-cut acrylic sheets was attached to the build-plate of the printer. On top of this frame, a rotating shaft was mounted. Both the slider bearing and rotating drum are interchangeable allowing for the fabrication of specimens with diameters in the range of 3-10 mm. Adhesive sheets were attached to the rotating shaft in order to enhance the adhesion of the specimens to the shaft.

The frame with rotating drum could be installed simply by replacing the glass bed with this add-on device. Moreover, the connector cable of the original x-direction stepper motor needs to be replaced by the connector cable of the added motor that drives the rotating shaft. No other changes to the hardware are required. In order to account for the transmission from the stepper motor rotation to circumferential displacement, the number of steps per mm for the stepper motor needs to be adjusted. This could be simply done by inserting the GCode command 'M92 Xs' to the GCode file, where s is the number of steps per mm. Of course, the number of steps is dependent on the radius and could be adjusted for different rotating shafts as well as for every printing layer.



**Figure 5.5:** Production method. The modified FDM 3D printer used for 4D printing on curved surfaces.

### 5.5.2 Material characterization and constitutive modelling

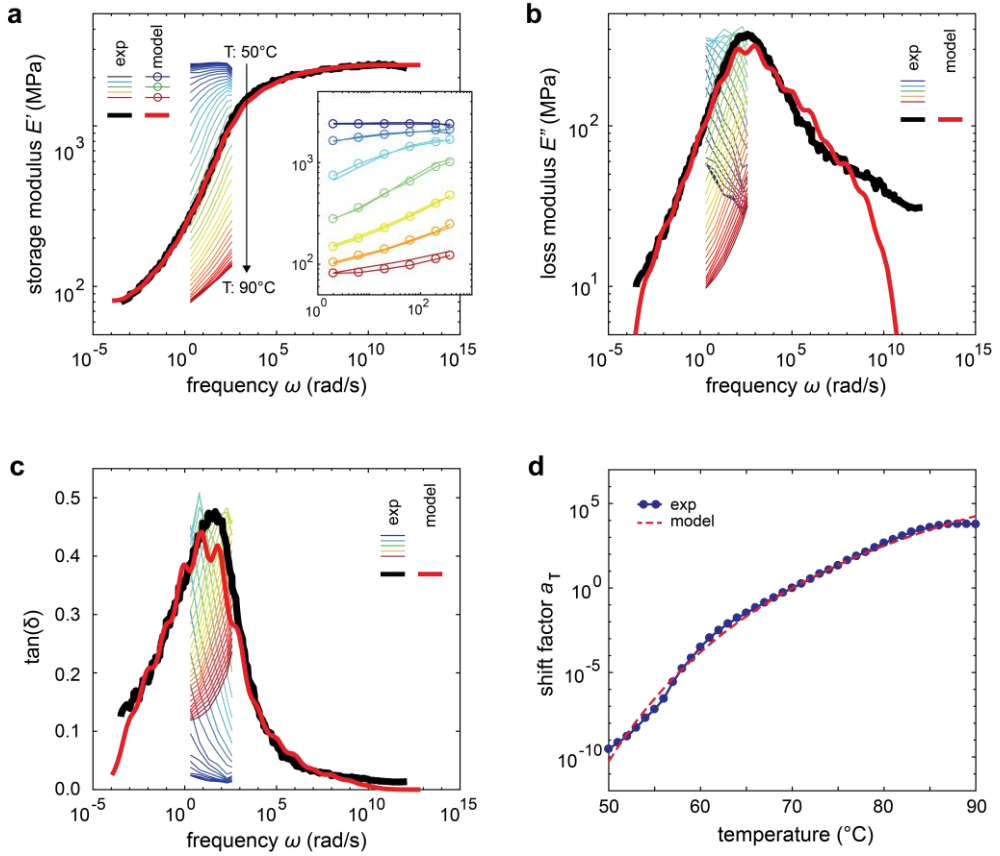
The temperature-dependent mechanical properties of PLA were measured by performing dynamic mechanical analysis (DMA) measurements using a TA-Instruments Q-800 machine (TA Instruments, US). While slowly increasing the temperature at a constant rate of 1°C/min, the PLA specimens were subjected to an oscillatory strain of +/- 0.015% across a frequency sweep (0.32, 1, 3.2 10, 32, 60 Hz). Based on the measured reaction force, the temperature- and frequency-dependent storage modulus ( $E'$ ), loss modulus ( $E''$ ), and phase angle ( $\tan(\delta)$ ) were obtained (Figure 5.6a-c). Assuming the material to be thermorheologically simple, the time-temperature superposition principle could be applied [41]. A master curve was constructed by shifting the linearly interpolated values of the measured storage modulus at different temperatures along the frequency axis. The resulting master curve with the corresponding shift factors ( $a_T$ ) are presented in Figure 5.6d.

Fitting the Williams-Landel-Ferry (WLF) equation allows for determining the empirical constants  $C_1$  and  $C_2$  (Table 5.1):

$$\log a_T = \frac{-C_1(T - T_{ref})}{C_2 + T - T_{ref}} \quad (5.2)$$

The viscoelastic behavior of PLA was modelled using a Prony series. Upon fitting the master curve (storage modulus  $E'$ ) to a Prony series model, the long-term modulus  $E_0$ , relaxation moduli  $e_n$ , and relaxation times  $\tau_n$  were determined (Table 5.2) as:

$$E'(\omega) = E_0 + \sum_{n=1}^N \frac{e_n \omega^2 \tau_n^2}{1 + \omega^2 \tau_n^2} \quad (5.3)$$



**Figure 5.6:** The DMA results and fitted model. (a-c) The rainbow-colored lines depict the experimental results for different temperatures ranging between 50 °C (blue lines) and 90 °C (red lines). A master curve (black line) was built from the storage modulus results, (d) using the measured shift factors (blue dots). The model (red lines) was constructed by fitting a Prony series to the master curve, using the WLF equation.

Having determined the moduli and the relaxation times, the loss modulus ( $E''$ ) and phase angle ( $\tan(\delta)$ ) were calculated as (Figure 5.6):

$$E''(\omega) = \sum_{n=1}^N \frac{e_n \omega \tau_n}{1 + \omega^2 \tau_n^2} \quad (5.4)$$

$$\tan \delta(\omega) = \frac{E''(\omega)}{E'(\omega)} \quad (5.5)$$

The model is fitted to the storage modulus data. Therefore, errors for both the loss modulus and  $\tan(\delta)$  curve are expected. Especially in the glassy state ( $\omega > 108$  rad/s), the storage modulus is almost constant and relatively large fitting errors can be observed in Figure 5.6. However, an accurate viscoelastic model is

only of importance in the transition region between the glassy and rubbery material behavior. Outside this region, the material behavior is largely independent from time. As a result, somewhat larger errors for the lower and higher frequencies are not expected to markedly influence the constitutive behavior.

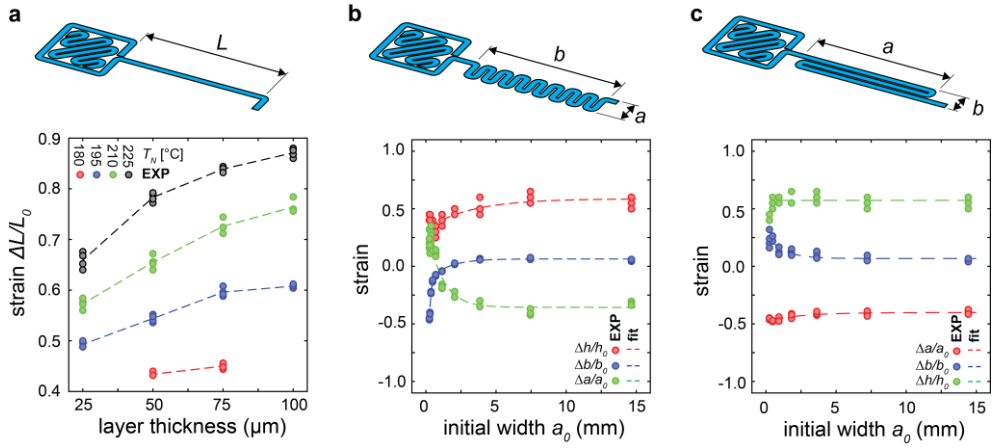
The mechanical properties used as input for the finite element analysis are listed in Table 5.1.

**Table 5.1:** The viscoelastic properties of PLA.

	$T_{ref}$ (°C)	70
WLF parameters	$C_1$ (-)	14.59
	$C_2$ (K)	48.43
	$E_0$ (MPa)	80.59
long term modulus	$E_0$ (MPa)	80.59
instantaneous modulus	$E_\infty$ (MPa)	2394
density	$\rho$ (kg/m <sup>3</sup> )	1.24

**Table 5.2:** The Prony series coefficients identified for PLA.

$\tau_n$ (s)	$e_n$ (MPa)
$1 \cdot 10^{-11}$	0.00
$1 \cdot 10^{-10}$	20.12
$1 \cdot 10^{-9}$	50.31
$1 \cdot 10^{-8}$	81.37
$1 \cdot 10^{-7}$	97.02
$1 \cdot 10^{-6}$	173.70
$1 \cdot 10^{-5}$	225.60
$1 \cdot 10^{-4}$	292.64
$1 \cdot 10^{-3}$	474.56
$1 \cdot 10^{-2}$	449.43
$1 \cdot 10^{-1}$	237.98
$1 \cdot 10^0$	114.16
$1 \cdot 10^1$	51.82
$1 \cdot 10^2$	29.98
$1 \cdot 10^3$	14.40
$1 \cdot 10^4$	0.00
$1 \cdot 10^5$	0.72



**Figure 5.7:** Dependency of the strain on printer settings and printing path. The experimentally determined values of the strain during the shape-shifting process (a) depending on the printer settings and (b-c) for different printing paths.

### 5.5.3 Basic elements

Three series of experiments were conducted to study the behavior of self-folding basic elements. First, the effects of the printing temperature and layer thickness on the programmed deformations were investigated. Specimens with a width of a single filament, a height of 2 mm, and a length of 25 mm were fabricated. The printing path is depicted in Figure 5.7a. The printing speed was set to 50 mm/s and the specimens were printed on a flat build-plate. The layer thickness was varied in steps of 25  $\mu\text{m}$  while the nozzle temperature was adjusted in steps of 15 °C. In total, 16 groups of specimens ( $n = 4$  per group) were fabricated. Based on a linear interpolation of the experimental results, the plot in Figure 5.3a was generated. Decreasing the layer thickness and nozzle temperature resulted in an increase in the amount of filament shrinkage. Both of those parameters reduce the cooling time of the extruded filaments, thereby limiting the relaxation of the introduced stresses. As a result, the filament shrinkage upon activation increases. Another parameter effecting the cooling history of extruded filaments is the printing path. The reheating and cooling of the filaments by the passing nozzle may result in additional relaxation, which decreases the final amount of programmed memory.

In a second series of experiments, the effects of the printing path on the shape-shifting characteristics of the specimens were characterized. Specimens with a layer thickness of 50  $\mu\text{m}$ , a printing temperature of 195 °C, and a printing speed of 50 mm/s were fabricated on a flat build-plate. Both the filament length and the number of parallel filaments were varied. The applied printing patterns are presented in Figures 5.7b-c. Especially for the filaments with a length below 5 mm, an effect of the printing path on the programmed deformation was found.

The dependency of in-plane deformation on the printing path could be described by the following equation:

$$y(x) = a_0 + \sum_{i=1}^n a_i b_i^x \quad (5.6)$$

in which the function  $y(x)$  can be replaced by one of the three shrinkage parameters (*i.e.*,  $\Delta a/a_0$ ,  $\Delta b/b_0$ , or  $\Delta h/h_0$ ) as a function of either the length ( $a$ ) or width ( $b$ ) of the specimens. The fitting coefficients are listed in Table 5.3. The fitted equations were used as input for the computational modeling of more complex shape-shifting elements. In the third series of experiments, the shape-shifting behavior of bending elements was studied and a comparison was performed between FEA and experimental results. Both the in-plane and out-of-plane bending elements were designed. The printing temperature was set to 195 °C, the layer thickness to 50  $\mu\text{m}$ , and a printing speed of 50 mm/s was used. The specimens were fabricated on a flat build plate except for the initially curved specimens. For both the in-plane and out-of-plane bending elements, the maximum bending curvature was found by varying the width.

**Table 5.3:** The curve fitting parameters (Equation 5.6).

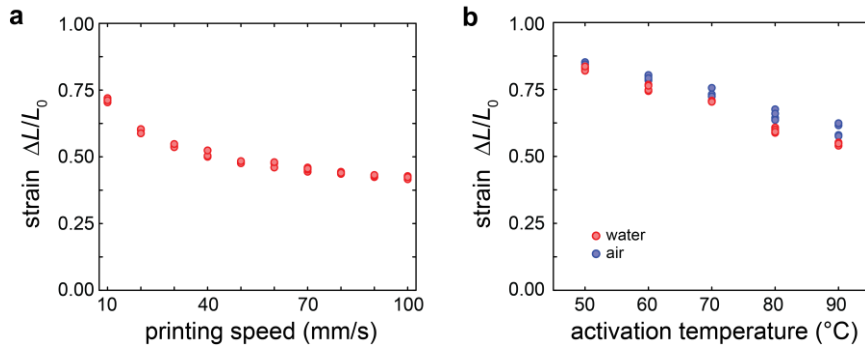
	$a_0(-)$	$a_1(-)$	$b_1(1/\text{mm})$	$a_2(-)$	$b_2(1/\text{mm})$	$R^2$
$\frac{\Delta a}{a_0}(a_0)$	0.644	0.606	0.386	-	-	0.95
$\frac{\Delta b}{b_0}(a_0)$	1.06	-0.359	$2.21 \cdot 10^{-4}$	-0.181	0.480	0.99
$\frac{\Delta h}{h_0}(a_0)$	1.59	-0.245	0.732	-	-	0.76
$\frac{\Delta a}{a_0}(b_0)$	0.599	$-6.89 \cdot 10^{-2}$	0.670	-	-	0.89
$\frac{\Delta b}{b_0}(b_0)$	1.07	0.171	0.426	-	-	0.89
$\frac{\Delta h}{h_0}(b_0)$	1.57	-0.160	$1.11 \cdot 10^{-3}$	-	-	0.94

#### 5.5.4 Finite element analysis

FEA was performed based on the viscoelastic material properties described in the Section 5.5.1. The programmed deformation characteristics were included in the model by the means of different thermal expansion coefficients. These coefficients were acquired from the curves fitted to the measured deformations of the basic building-blocks (Section 5.5.3). Complex shape-shifting structures were modelled by splitting the geometry into its basic building-blocks, each of which exhibiting different thermal expansion coefficients. The heat transfer properties of PLA were obtained from the literature and are summarized in Table 5.4.

**Table 5.4:** The heat transfer properties of PLA.

thermal conductivity	$k$ (W/mK)	0.18
convective heat transfer coefficient	$h$ (W/m <sup>2</sup> K)	2000
specific heat	$c$ (J/kgK)	1800



**Figure 5.8:** Dependency of the strain on printer settings and activation conditions. The experimentally determined values of the strain during the shape-shifting process (a) for different printing speeds and (b) different activation temperatures.

### 5.5.5 Printing speed

The stepper motors used in the 3D printer are limited in terms of their maximum rotational speed. Given a certain rotational speed, the maximum printing speed drops for rotating drums with smaller diameters. Therefore, the effects of the printing speed on the shape-shifting characteristics were studied as well. The specimens with a printing path similar to the specimens shown in Figure 5.7a were fabricated with a layer thickness of 50  $\mu\text{m}$  and a printing temperature of 185  $^{\circ}\text{C}$ . The results indicate a significant effect of the printing speed on the filament shrinkage for very low printing speeds (Figure 5.8a). A lower printing speed allows for more relaxation of the extruded filaments, thereby reducing the final amount of frozen-in molecular orientation.

### 5.5.6 Sample activation

All the specimens were activated in a hot water bath primarily because it is relatively simple to accurately control the temperature of water. The use of a transparent container for the activation of the specimens allowed for tracking the deformation of the specimens with digital cameras. However, some applications of the presented 4D printed reconfigurable materials may not allow for sample activation by the means of a liquid medium. Therefore, a series of experiments were conducted to compare the shape-shifting behaviors of specimens activated using hot water and hot air. Specimens with a printing path similar to those printed in Figure 5.7a were fabricated with a layer thickness of 50  $\mu\text{m}$ , a printing temperature of 195  $^{\circ}\text{C}$ , and printing speed of 50 mm/s. For a range of different activation temperatures, only small differences were observed between the different activation media (Figure 5.8b).



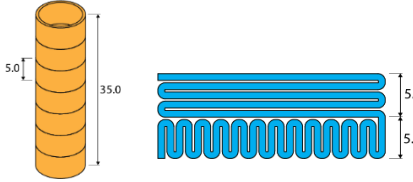
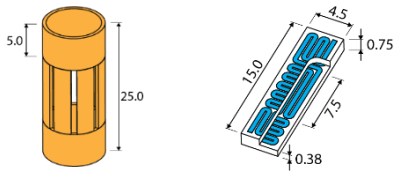
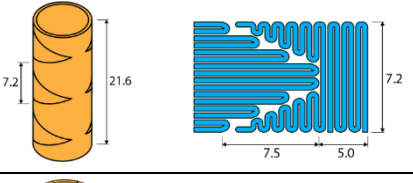
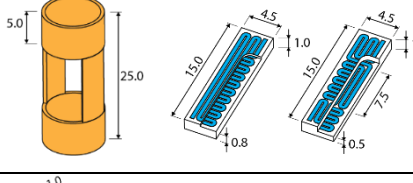
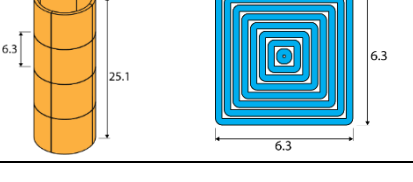
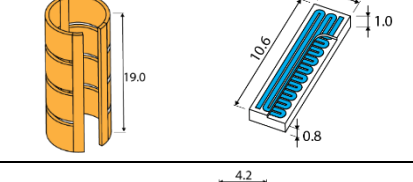
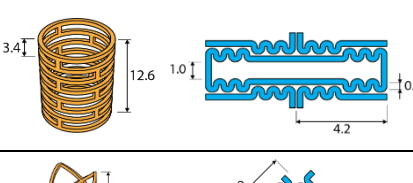
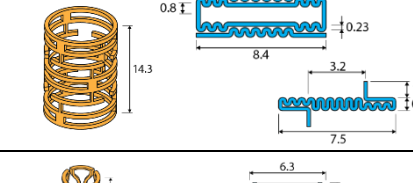
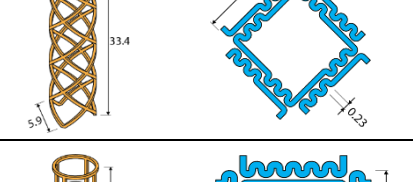
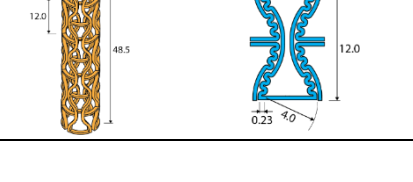
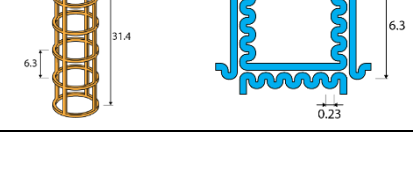
**Table 5.5:** The fabrication parameters for all the specimens presented in this study.

Structure	Figure	Printing speed (mm/s)	Layer thickness (mm)	Printing temperature (°C)	Shaft diameter (mm)	Number of layers
Out-of-plane buckling	2a	30	0.05	195	8	10
	2b	30	0.05	185	8	20
	2c	30	0.05	195	8	10
In-plane bending	2d	50	0.05	195	8	20
	2e	50	0.05	195	8	15
	2f	50	0.05	195	8	15
Out-of-plane bending	2g	50	0.05	195	8	15
	2h	50	0.05	195	8	20
	2i	30	0.05	195	8	20
Switching in mechanical properties	3a	50	0.05	195	8	20
	3b	50	0.05	195	8	20
Deployable samples	4b	50	0.05	185	flat	20
	4c-i	50	0.05	185	8	20
	4c-ii	50	0.05	185	8	20
	4c-iii	50	0.05	185	8	20
Cardiovascular stents	4d-i	25	0.05	185	4	20
	4d-ii	37.5	0.05	185	6	20
	4d-iii	50	0.05	185	8	20
	4e	50	0.05	185	10	20

### 5.5.7 Fabrication parameters

The parameters used for the fabrication of the shape-shifting samples presented in this study are listed in Table 5.5. The other geometrical parameters are listed in Table 5.6. All the specimens were activated using hot water at a temperature of 90 °C.

**Table 5.6:** Dimensions (in mm) for the specimens presented in this study.

<p><b>2a</b></p> 	<p><b>2g</b></p> 
<p><b>2b</b></p> 	<p><b>2h</b></p> 
<p><b>2c</b></p> 	<p><b>2i</b></p> 
<p><b>2d</b></p> 	<p><b>3a</b></p> 
<p><b>2e</b></p> 	<p><b>3b</b></p> 
<p><b>2f</b></p> 	

## Bibliography

1. Felton, S., et al., *A method for building self-folding machines*. Science, 2014. **345**(6197): p. 644-646.
2. Rus, D. and M.T. Tolley, *Design, fabrication and control of origami robots*. Nature Reviews Materials, 2018. **3**(6): p. 101-112.
3. Filipov, E.T., T. Tachi, and G.H. Paulino, *Origami tubes assembled into stiff, yet reconfigurable structures and metamaterials*. Proceedings of the National Academy of Sciences, 2015. **112**(40): p. 12321-12326.
4. Overvelde, J.T., et al., *Rational design of reconfigurable prismatic architected materials*. Nature, 2017. **541**(7637): p. 347-352.
5. Ning, X., et al., *Assembly of advanced materials into 3D functional structures by methods inspired by origami and kirigami: a review*. Advanced Materials Interfaces, 2018. **5**(13): p. 1800284.
6. Jamal, M., et al., *Directed growth of fibroblasts into three dimensional micropatterned geometries via self-assembling scaffolds*. Biomaterials, 2010. **31**(7): p. 1683-1690.
7. Cho, J.-H., et al., *Nanoscale origami for 3D optics*. Small, 2011. **7**(14): p. 1943-1948.
8. Janbaz, S., et al., *Origami lattices with free-form surface ornaments*. Science advances, 2017. **3**(11): p. eaao1595.
9. van Manen, T., et al., *Kirigami-enabled self-folding origami*. Materials Today, 2020. **32**: p. 59-67.
10. Bobbert, F., et al., *Russian doll deployable meta-implants: Fusion of kirigami, origami, and multi-stability*. Materials & Design, 2020: p. 108624.
11. Haghpahan, B., et al., *Multistable shape-reconfigurable architected materials*. Advanced Materials, 2016. **28**(36): p. 7915-7920.
12. Overvelde, J.T., et al., *A three-dimensional actuated origami-inspired transformable metamaterial with multiple degrees of freedom*. Nature communications, 2016. **7**(1): p. 1-8.
13. Yang, C., et al., *4D printing reconfigurable, deployable and mechanically tunable metamaterials*. Materials Horizons, 2019. **6**(6): p. 1244-1250.
14. Liu, Y., J. Genzer, and M.D. Dickey, "2D or not 2D": *Shape-programming polymer sheets*. Progress in Polymer Science, 2016. **52**: p. 79-106.
15. van Manen, T., S. Janbaz, and A.A. Zadpoor, *Programming the shape-shifting of flat soft matter*. Materials Today, 2018. **21**(2): p. 144-163.
16. Zhang, Y., et al., *Printing, folding and assembly methods for forming 3D mesostructures in advanced materials*. Nature Reviews Materials, 2017. **2**(4): p. 1-17.
17. Ionov, L., *Polymeric actuators*. Langmuir, 2015. **31**(18): p. 5015-5024.
18. Lendlein, A. and R. Langer, *Biodegradable, elastic shape-memory polymers for potential biomedical applications*. Science, 2002. **296**(5573): p. 1673-1676.
19. Zhao, Q., H.J. Qi, and T. Xie, *Recent progress in shape memory polymer: New behavior, enabling materials, and mechanistic understanding*. Progress in Polymer Science, 2015. **49**: p. 79-120.
20. Ding, Z., et al., *Direct 4D printing via active composite materials*. Science advances, 2017. **3**(4): p. e1602890.
21. Raviv, D., et al., *Active printed materials for complex self-evolving deformations*. Scientific reports, 2014. **4**: p. 7422.
22. Zhao, Z., et al., *Desolvation induced origami of photocurable polymers by digit light processing*. Macromolecular rapid communications, 2017. **38**(13): p. 1600625.
23. Ambulo, C.P., et al., *Four-dimensional printing of liquid crystal elastomers*. ACS applied materials & interfaces, 2017. **9**(42): p. 37332-37339.
24. Gladman, A.S., et al., *Biomimetic 4D printing*. Nature materials, 2016. **15**(4): p. 413-418.
25. Kotikian, A., et al., *3D printing of liquid crystal elastomeric actuators with spatially programed nematic order*. Advanced materials, 2018. **30**(10): p. 1706164.

26. Van Manen, T., S. Janbaz, and A.A. Zadpoor, *Programming 2D/3D shape-shifting with hobbyist 3D printers*. Materials horizons, 2017. **4**(6): p. 1064-1069.
27. Kim, Y., et al., *Printing ferromagnetic domains for untethered fast-transforming soft materials*. Nature, 2018. **558**(7709): p. 274-279.
28. Lewis, J.A. and G.M. Gratson, *Direct writing in three dimensions*. Materials today, 2004. **7**(7-8): p. 32-39.
29. Truby, R.L. and J.A. Lewis, *Printing soft matter in three dimensions*. Nature, 2016. **540**(7633): p. 371-378.
30. Song, Y., et al., *Measurements of the mechanical response of unidirectional 3D-printed PLA*. Materials & Design, 2017. **123**: p. 154-164.
31. Liao, Y., et al., *Effect of porosity and crystallinity on 3D printed PLA properties*. Polymers, 2019. **11**(9): p. 1487.
32. Lubombo, C. and M.A. Huneault, *Effect of infill patterns on the mechanical performance of lightweight 3D-printed cellular PLA parts*. Materials Today Communications, 2018. **17**: p. 214-228.
33. Le Duigou, A., et al., *3D printing of wood fibre biocomposites: From mechanical to actuation functionality*. Materials & Design, 2016. **96**: p. 106-114.
34. van Manen, T., et al., *4D printing of reconfigurable metamaterials and devices*. Communications Materials, 2021. **2**(1): p. 1-8.
35. Im, S.H., Y. Jung, and S.H. Kim, *Current status and future direction of biodegradable metallic and polymeric vascular scaffolds for next-generation stents*. Acta biomaterialia, 2017. **60**: p. 3-22.
36. Peng, T., P. Gibula, and M.F. Goosen, *Role of polymers in improving the results of stenting in coronary arteries*. Biomaterials, 1996. **17**(7): p. 685-694.
37. Stefanini, G.G., et al., *Biodegradable polymer drug-eluting stents reduce the risk of stent thrombosis at 4 years in patients undergoing percutaneous coronary intervention: a pooled analysis of individual patient data from the ISAR-TEST 3, ISAR-TEST 4, and LEADERS randomized trials*. European heart journal, 2012. **33**(10): p. 1214-1222.
38. Ang, H.Y., et al., *Bioresorbable stents: Current and upcoming bioresorbable technologies*. International Journal of Cardiology, 2017. **228**: p. 931-939.
39. Iqbal, J., et al., *Bioresorbable scaffolds: rationale, current status, challenges, and future*. European heart journal, 2014. **35**(12): p. 765-776.
40. Meng, Y., J. Jiang, and M. Anthamatten, *Body temperature triggered shape-memory polymers with high elastic energy storage capacity*. Journal of Polymer Science Part B: Polymer Physics, 2016. **54**(14): p. 1397-1404.
41. Ferry, J.D., *Viscoelastic properties of polymers*. 1980: John Wiley & Sons.



# Kirigami-enabled self-folding origami

# 6

Self-folding of complex origami-inspired structures from flat states allows for the incorporation of a multitude of surface-related functionalities into the final 3D device. Several self-folding techniques have therefore been developed during the last few years to fabricate such multi-functional devices. The vast majority of such approaches are, however, limited to simple folding sequences, specific materials, or large length scales, rendering them inapplicable to microscale (meta)materials and devices with complex geometries, which are often made from materials other than the ones for which these approaches are developed. Here, we propose a mechanical self-folding technique that only requires global stretching for activation, is applicable to a wide range of materials, allows for sequential self-folding of multi-storey constructs, and can be downscaled to microscale dimensions. We combined two types of permanently deforming kirigami elements, working on the basis of either multi-stability or plastic deformation, with an elastic layer to create self-folding basic elements. The folding angles of these elements could be controlled using the kirigami cut patterns as well as the dimensions of the elastic layer and be accurately predicted using our computational models. We then assembled these basic elements in a modular manner to create multiple complex 3D structures (*e.g.*, multi-storey origami lattices) in different sizes including some with microscale feature sizes. Moreover, starting from a flat state enabled us to incorporate not only precisely controlled, arbitrarily complex, and spatially varied micropatterns but also flexible electronics into the self-folded 3D structures. In all cases, our computational models could capture the self-folding behavior of the assemblies and the strains in the connectors of the flexible electronic devices, thereby guiding the rational design of our specimens. This approach has numerous potential applications including fabrication of multi-functional and instrumented implantable medical devices, steerable medical instruments, and microrobots.

T. van Manen, S. Janbaz, M. Ganjian & A.A. Zadpoor (2020). *Kirigami-enabled self-folding origami*. *Materials Today*, **32**: p. 59-67.

## 6.1 Introduction

Self-folding origami [1-3] has a myriad of potential applications in the development of designer materials with advanced functionalities including robotic materials [4-7], thin film materials [8], mechanical metamaterials [9-13], optical metamaterials [14], electronic devices [15], antennas [16], space structures [17, 18], and biomaterials [19-21]. Self-folding origami can, therefore, be seen as an alternative fabrication strategy with advantages that range from lower manufacturing costs to enabling the combination of the favorable properties offered by 2D materials with those of bespoke 3D structures. In particular, shape-shifting materials that allow for the formation of complex 3D geometries from initially flat materials offer a promising strategy for the fabrication of surface-functionalized lattice structures [20]. Given the fact that the geometrical design of many metamaterials with various types of rare or unprecedented properties are based on regular lattice structures [22-27], self-folding origami lattices hold particular promise in this regard. For this type of advanced metamaterials, starting from a flat state would also allow for the use of advanced production techniques that are usually only applicable to flat surfaces, such as electron beam nanolithography [28-30], dip pen nanolithography [31, 32], and direct-write atomic layer deposition [33]. These techniques could then be used to embed a variety of complex surface features in the flat material prior to the assembly into a 3D structure. That may include printable electronic devices that incorporate sensors and actuators into the ultimate (wearable) 3D object [15, 16, 34, 35], surface nanopatterns that determine stem cell fate [36-38] or kill bacteria to prevent implant-associated infections [39, 40], or surface nano-features that manipulate the surface properties to create superhydrophobicity or superhydrophilicity [41-43] for such applications as self-cleaning surfaces. In this approach, once the incorporation of the surface-related functionalities is concluded, a self-folding behavior is initiated using a triggering stimulus.

Different strategies based on either internally generated stresses or externally applied forces have been proposed for the fabrication of stimuli-responsive materials that shift their shape from a flat state to a 3D geometry [44-46]. Internal stresses could be generated using shape-memory polymers or alloys that exhibit dimensional changes upon activation by a variety of stimuli including temperature [47, 48] and humidity [49]. Based on the arrangement of those active materials, out-of-plane deformations can be programmed into a flat material [1, 3]. However, the application of these approaches is limited by the type of activation stimulus. For example, active materials that require high temperatures for activation cannot be used inside the human body. Moreover, this strategy requires the use of specific materials, which is an important limiting factor for many applications. Finally, this approach is not suited for the fabrication of self-folding origami (lattices) at smaller scales, as accurate positioning and/or training of (shape-memory) materials at the microscale may be needed. In the

case of 4D printing approaches [50, 51], the dimensional accuracy required for microscale fabrication of self-folding origami often exceeds the resolution of the available 3D printing technologies.

The alternative approach of working with external forces could help overcome most of the above-mentioned challenges. However, design flexibility is much reduced when working with a few globally applied forces. It is therefore extremely challenging to program complex shape-shifting behaviors such as those required for the folding of regular lattices from flat states. A variety of shape-shifting techniques based on externally applied forces have been reported in the literature [52]. For example, capillary forces have been utilized for the folding of polyhedral structures [53]. Nevertheless, only simple 3D geometries comprising a single polyhedral unit cell have, thus far, been demonstrated [54]. Compressive buckling of thin stiff constructs on top of a pre-stressed elastomeric substrate has also been used for the fabrication of 3D geometries from initial flat state [55]. However, the actuation forces have to be applied locally through a precisely controlled pattern of bonding sites between the construct and substrate, which limits the fabrication of complex freestanding and multi-storey constructs.

Here, we propose a new kirigami-based approach for the design and fabrication of complex self-folding origami-like structures (*e.g.*, origami lattices) that are activated with externally-applied (*i.e.*, global) mechanical forces. The presented approach is suitable for the fabrication of self-folding origami at the microscale and is applicable to a wide range of materials. Furthermore, we work with tensile forces as opposed to the buckling-inducing compressive forces that had been used in the previous studies [55] and whose behavior may be challenging to predict in the nonlinear post-buckling regimen. Taking advantage of the multi-stability [56–58] and highly localized out-of-plane buckling, our approach also lends itself to sequential self-folding that is crucial for multi-step folding strategies.

## 6.2 Results and Discussion

### 6.2.1 Self-folding elements

We used a combination of experimental techniques and computational models to design, fabricate, and analyze our self-folding origami-inspired structures (see Materials and Methods). The main concept in this approach is a through-the-thickness combination of an elastic layer with a layer exhibiting permanent deformation. The permanent deformation may arise from multi-stability or from the plastic deformation of the material. The presented shape-shifting concepts could, therefore, be applied to different types of materials (*e.g.*, metals and polymers). When stretched, both layers will elongate. Upon the release of the force, the elastic layer tends to contract back to its original length, while the permanently-deformed layer opposes that recovery. The mismatch between the



tendencies of both layers causes an out-of-plane deformation that could be exploited to self-fold initially flat constructs.

We implemented this approach by designing two types of kirigami elements that exhibited permanent deformations upon stretching (Figure 6.1a). We then combined the kirigami elements with a layer of an elastomeric material (*i.e.*, PDMS) to create self-folding bilayers (Figure 6.1a). Shape transformations could be programmed using different arrangements of these basic elements. We fabricated our kirigami elements from both multi-stable polymer sheets (Figure 6.1b) as well as from metal foils (Figure 6.1b). A pattern of mutually orthogonal cuts into a polyolefin sheet caused the material to exhibit a multi-stable mechanical response. Upon stretching above a critical strain value, the four square elements present within the kirigami element rotated far enough to 'snap' into their other stable position, thereby elongating the kirigami strip permanently (Figure 6.1c). The amount of the permanent elongation could be adjusted by changing the dimensions of the elements constituting the kirigami strip such as the dimensions of the square elements (Figure 6.1c).

In the case of metal foils, high levels of plastic deformation were achieved by incorporating a pattern of parallel grooves into a titanium foil (Figure 6.1d). Using this approach, the maximum amount of the allowable permanent deformation was increased by more than two orders of magnitude to values  $>100\%$  strain (Figure 6.1d). In these kirigami patterns, the deformation is localized at the edges of the cut patterns (Figure 6.1d). The thinly cut ribbons stretch up to the point where localized deformation leads to a highly localized out-of-plane buckling at the sharp corners of the cut pattern (Figure 6.1d). Given that this deformation is plastic in the case of metal foils, the kirigami strip is permanently elongated. Our experiments showed that the amount of permanent elongation equals the level of stretching, except for a small offset caused by the recovery of the initial elastic response of the material (Figure 6.1d). Depending on the applied stretching, the thickness of the elastic layer, and the dimensions of the kirigami cutting patterns, folding angles up to  $100^\circ$  could be achieved (Figure 6.1e-g). The folding angles generally increased with the applied stretching (Figure 6.1e). The folding angles predicted by our finite element analysis (FEA) models were in excellent agreement with the experimentally observed values (Figure 6.1e), meaning that these models could be used for the rational design of the self-folding elements (*e.g.*, dimensions, cut-patterns, *etc.*). In general, a larger width of the self-folding elements resulted in higher folding angles (Figure 6.1f). The thickness-dependency of the folding angle was much more severe in the case of plastically deforming kirigami elements, while there was little to no such dependency in the case of the multi-stable elements (Figure 6.1g). Video 6.1 demonstrates how both types of basic elements work in practice [59].

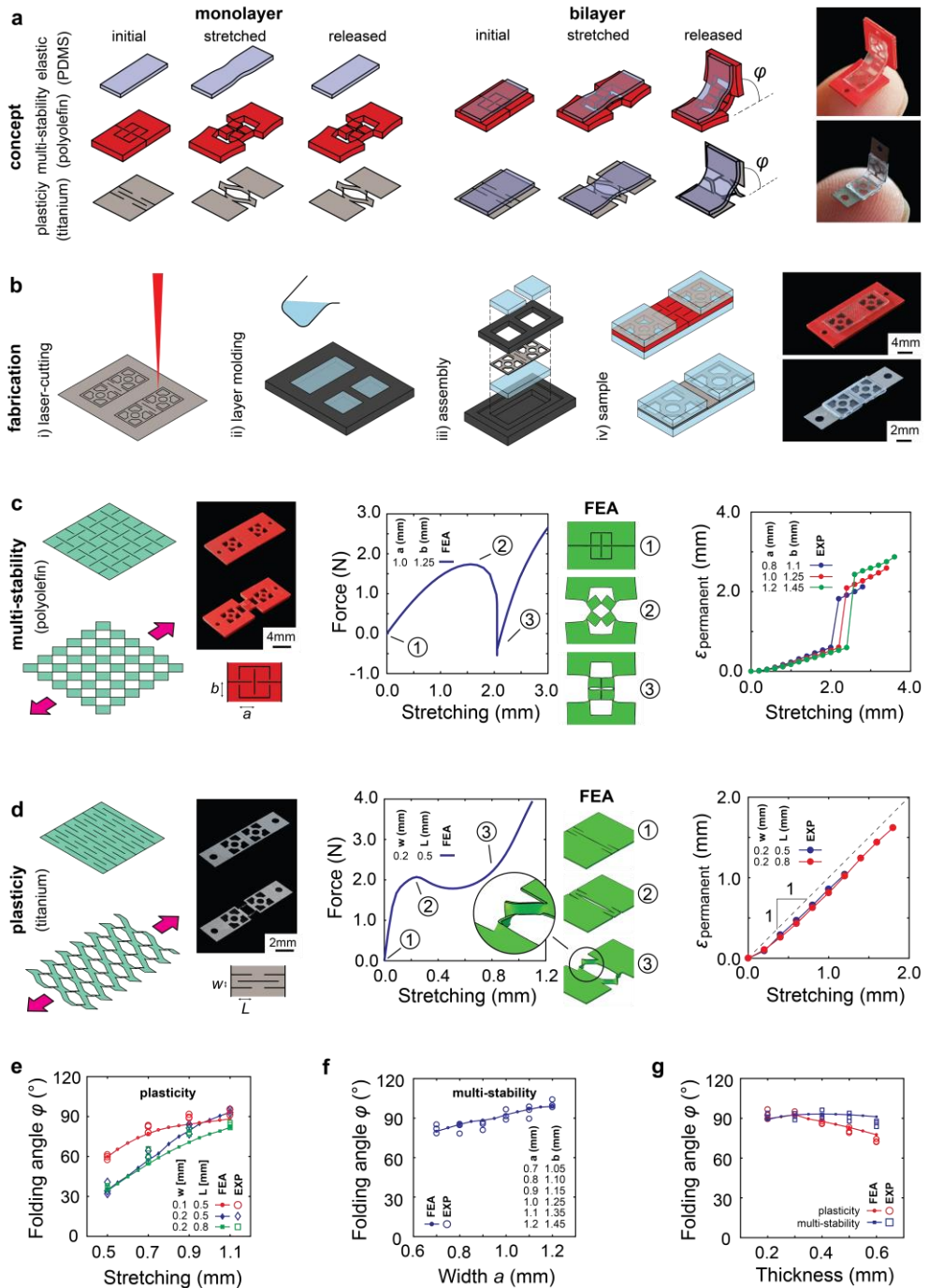


Figure 6.1: See next page for Figure caption.

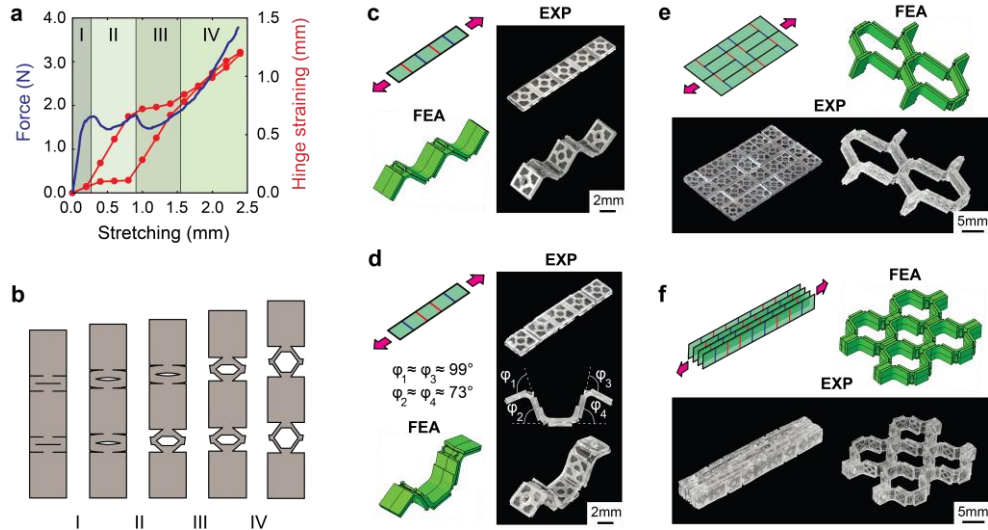
**Figure 6.1:** The main concepts and methods used for the design and fabrication of self-folding elements. (a) Two types of basic elements were designed by combining two types of permanently-deforming kirigami-based layers monolayers with an elastic layer to create bilayers (left). Stretching the bilayers resulted in self-folding elements that exhibited out-of-plane bending upon releasing the force (right). (b) The kirigami elements were made by laser cutting after which they were assembled with molded PDMS layers to create the basic elements. (c) One type of the kirigami elements were made from a polymeric material and worked through multi-stability (left). In this design, the four squares constituting the middle part of the kirigami element rotated as the force gradually increased until they snapped to another position at which point the force drops (middle). The amount of permanent deformation as a function of the design parameters and stretching was measured (right). (d) The other type of kirigami elements was made from a metallic foil (left) and worked on the basis of plastic deformation resulting from localized out-of-plane buckling (middle). Permanent deformation as a function of the design parameters and stretching was measured (right). (e-g) The folding angle as a function of design parameters and stretching (e), width (f), and thickness of the elastic layer (g) (both experimental and FEA values). See Video 6.1 [59].

### 6.2.2 Arrays of self-folding elements

To create more complex shape-shifting behaviors, one needs to use assemblies of these two basic elements. The advantage of the plastically deformed kirigami elements is that they allow for a continuous range of elongations, while multi-stable elements work on the on-off basis, meaning that only certain discrete values of elongation are admissible. Moreover, multi-stable elements require a minimum ratio of their thickness to the other dimensions to exhibit the specific snap-through instability behavior required for permanent elongation. Nevertheless, multi-stable elements have an important feature that makes them particularly useful for complex assemblies of basic elements, namely the elongation of the multi-stable elements assembled in-series is largely independent of each other. That does not hold for the plastically deforming kirigami elements, where four stages of deformation are observed in the simplest case of two in-series assembled elements (Figure 6.2a-b). In the first stage (stage I, Figure 6.2a-b), both elements elongate together until one of them experiences localized buckling after which elongation will occur mostly in that element (stage II, Figure 6.2a-b). This continues up to the point where the second element also experiences localized buckling following which only the second element will elongate (stage III, Figure 6.2a-b). Once both elements have equally elongated, they will again start to elongate together (stage IV, Figure 6.2a-b). Our experimental measurements clearly showed the presence of these four stages and the difference between the assembled elements in terms of their individual elongations (Figure 6.2a).

We assembled the basic building blocks described above in series and in parallel (Figure 6.2c-f). In-series positioning of the self-folding elements allowed for the formation of linear patterns with the same (Figure 6.2c) and different folding angles (Figure 6.2d). A combination of in-parallel and in-series assembly of the basic elements allowed for the fabrication of more complex 3D shapes with

complex planar patterns (Figure 6.2e-f). These patterns could be also stacked to create multi-storey constructs possibly with patterns that vary from one story to another. Video 6.2 shows the self-folding behavior of the samples presented in Figure 6.2 [59].

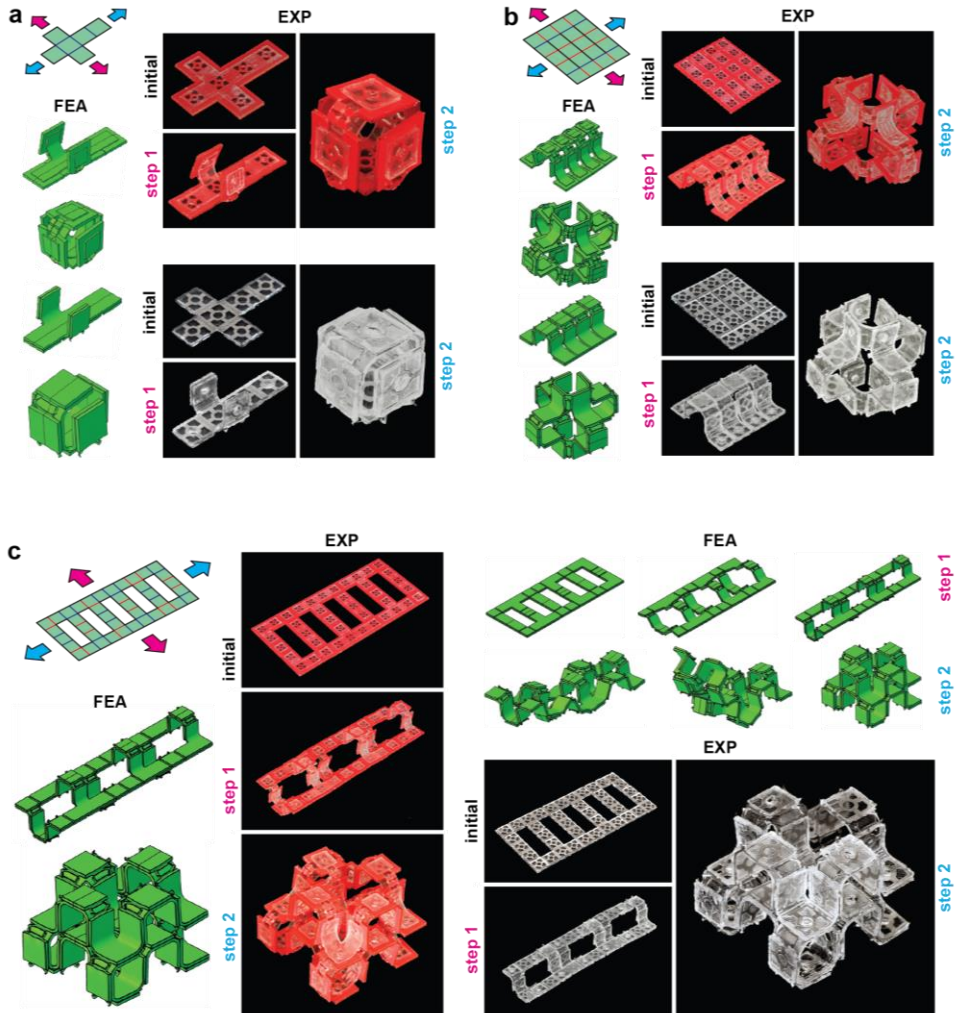


**Figure 6.2:** The self-folding behavior of the arrays of self-folding elements connected to each other in series and in parallel as predicted with FEA models and observed in our experiments. (a-b) Force and hinge straining as functions of stretching in the case of two basic elements connected to each other in series (a). Both basic elements do not deform simultaneously and four different stages of deformation can be identified (b). (c-d) Self-folding elements connected to each other in series with similar (c) and different (d) folding angles. (e-f) An array of self-folding elements connected in parallel and in-series to create more complex patterns of shape-shifting behavior. See Video 6.2 [59].

### 6.2.3 Complex assemblies

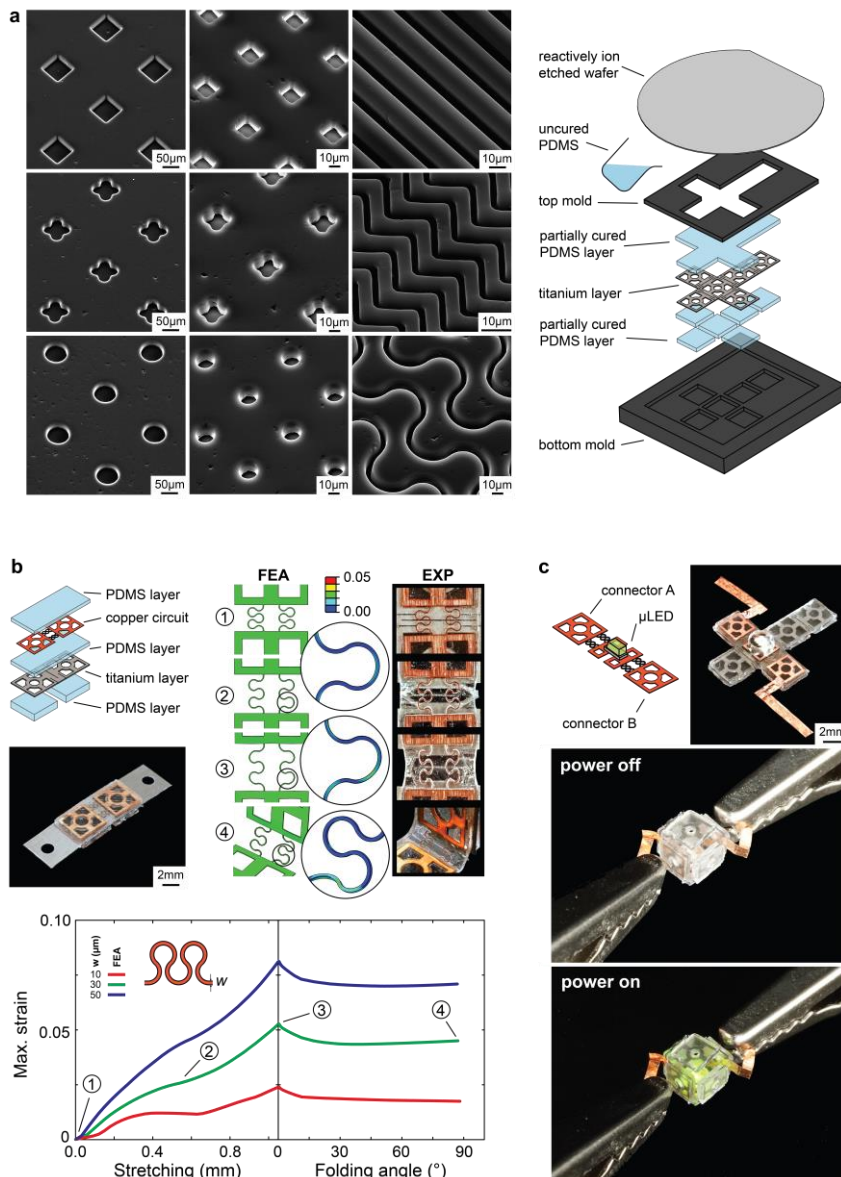
The real challenge, however, is in the design of fully self-folding multi-storey structures. Indeed, the folding sequences devised for such multi-storey constructs as lattice origami require sequential folding [20]. We combined orthogonal assemblies of the basic elements with stiff panels to enable the sequential self-folding of multi-storey constructs (Figure 6.3). In this approach, stretching is performed sequentially: first along one of the orthogonal directions and, then, along the other. We fabricated three types of self-folding 3D designs including a cube and two multi-storey structures (Figure 6.3). In all cases, we fabricated the specimens using both multi-stable and plastically deformed kirigami elements (Figure 6.3). The deformed shapes of all structures were accurately predicted by our FEA models (Figure 6.3), meaning that they could be used as a predictive tool for the rational design of complex assemblies of basic elements in general and for

the design of the critical dimensions of both basic elements and orthogonal assemblies. We, therefore, chose the design parameters of the individual basic elements making up the assemblies such that they exhibited the differential self-folding response required for creating the multi-storey constructs. The activation sequences and self-folding behavior of the specimens presented in Figure 6.3 can be seen in Video 6.3 [59].



**Figure 6.3:** Complex shape-shifting behavior for three different designs as predicted with FEA models and observed in our experiments. (a-c) Self-folding of a cube from a flat state (a) as well as sequential shape-shifting from flat states to complex multi-storey shapes (b-c). All designs were realized using both multi-stable (red) and plastically deforming (gray) kirigami elements. See Video 6.3 [59].





**Figure 6.4:** Surface-related functionalities added to our shape-shifting designs. (a) Precisely controlled, arbitrarily complex, and spatially varied micropatterns (left) created using optical lithography and molding in the elastic layer of our self-folding elements (right). (b) Flexible electronics incorporated into the design of the basic elements (top). FEA simulations were used to predict the strain in the flexible connectors and to study the effects of design parameters (e.g., the width of the ribbons) on the experienced strain values (middle). Experimentally observed and predicted shape-shifting behavior of the specimens incorporating flexible electronics agreed with each other (bottom). (c) A micro-LED was incorporated into a self-folding cube to demonstrate the feasibility of incorporating electronic devices in the presented designs. The micro-LED was lit to check the connectivity of the connectors after self-folding. See Video 6.4 [59].

### 6.2.4 Surface-related functionalities

To demonstrate some of the functionalities that could be incorporated into the self-folding origami-inspired structures developed here, we created specimens with two different types of surface-related functionalities including precisely-controlled surface micro-patterns and flexible electronics. Starting from a flat state enabled us to use optical lithography for incorporating a wide range of arbitrarily complex, precisely controlled, and spatially varied micropatterns (Figure 6.4a) onto the PDMS layer during the curing process. The flexible electronics were incorporated into our specimens using highly stretchable copper connectors that could accommodate the applied stretching during the self-folding process (Figure 6.4b). Our coil-like designs of the connectors (Figure 6.4b) was also effective in reducing the amount of strain that they underwent during the self-folding process. Our FEA models predicted that the dimensions of the connectors strongly affect the strains they experience during the self-folding process (Figure 6.4b). For example, the maximum strain values predicted for the connectors increased by up to  $\approx 3$  folds when the width of the ribbon increased from 10  $\mu\text{m}$  to 50  $\mu\text{m}$  (Figure 6.4b). This clearly shows the importance of high cutting precisions that allowed us to choose a width of 30  $\mu\text{m}$  to simultaneously limit the maximum strain experienced by the connectors while avoiding the risk of failure in very thin connectors (*e.g.*, connectors with a width of 10  $\mu\text{m}$ ). The amount of strain sustained by the connectors significantly decreased with the folding angle, and reached values  $\leq 5\%$  for folding angles between  $45^\circ$  and  $90^\circ$  (Figure 6.4b). A micro-LED was incorporated in the design of a self-folding box to demonstrate the feasibility of integrating electronic devices into these origami-inspired self-folding structures (Figure 6.4c). The micro-LED was then lit to confirm the proper connectivity of the circuits after self-folding (Figure 6.4c, see Video 6.4 [59]).

## 6.3 Outlook and conclusions

In summary, we presented an approach for the fabrication of complex (*e.g.*, multi-storey) self-folding origami-inspired structures that works on the basis of bilayers of permanently deforming kirigami elements and an elastic layer. Global mechanical forces activate the self-folding behavior. Given the highly mechanical nature of these elements, they could be made from a very wide range of materials at the micro-scale, which distinguishes this method from most other shape-shifting techniques that are either limited to specific materials or are limited to large-scale constructs (or both). We also demonstrated the possibility of incorporating bespoke micropatterns and flexible electronics into a number of 3D constructs made using this approach.

The two types of the basic kirigami elements used here harness either 'highly localized' mechanical instability or plastic deformations to create the desired patterns of self-folding. This allows us to create basic elements with easily

predictable mechanical responses that could be assembled in a modular way to create more complex shape-shifting behavior without having to worry about the nonlinear post-buckling behavior of the geometrical designs resulting from such assemblies.

The feature sizes of the smallest specimens presented here (*e.g.*, Figure 3) are in the micrometer range and are not far from the length-scales required for creating the 3D porous structures that could be used as tissue engineering scaffolds. This is the first time ever that such self-folding 3D porous structures are fabricated at this scale from biocompatible materials (*e.g.*, titanium foils) and with the possibility of directly incorporating micro-/nanopatterns that could influence stem cell differentiation [36–38] and kill bacteria to prevent implant-associated infections [39, 40]. The demonstrated possibility to integrate flexible electronics could also pave the way for the development of smart implantable devices with sensing and on-demand drug delivery mechanisms. Such level of multifunctionality is unprecedented for implantable medical devices. This type of fabrication techniques could also be used in many other areas of advanced functional materials including micro-robotics, miniaturized steerable medical instruments, and precision devices. Finally, the mechanical nature of the proposed self-folding process also means that the functionality-inducing features or devices present on the surface are not affected by the chemicals or the high temperatures used in the activation process. This could be of importance for many of the application areas mentioned above.

## 6.4 Materials and methods

### 6.4.1 Sample fabrication

The multi-stable specimens were fabricated from polyolefin polymers (polyolefin, thickness = 0.65 mm; G. Apex, Taiwan Yun Lin Electronic Co. Taiwan) while plastically deforming kirigami were made from pure titanium foils (titanium foil, purity = 99.6+%, annealed, thickness = 50  $\mu\text{m}$ ; Goodfellow, UK). In both cases, the specimens were cut using laser micromachining (Optec Laser Micromachining Systems, Belgium). The permanently deforming kirigami constructs were then molded into a polydimethylsiloxane (PDMS) elastomer matrix (Sylgard 184, Dow Corning, USA). The PDMS was thoroughly mixed (mixing ratio 7.5:1 between prepolymer and curing agent) for at least 3 min followed by degassing for 10 min before being poured into the mold. The molds were made from acrylonitrile butadiene styrene (ABS) using 3D printers (Ultimaker 2+, Ultimaker, The Netherlands) that worked on the basis of fused deposition modeling (FDM). Both the polyolefin and titanium specimens were covered by a thin layer of a release agent (polyvinylalcohol (PVA), Polyestershoppen BV, The Netherlands) in order to minimize the adhesion between the kirigami specimens and the elastomeric layers. The individual layers of PDMS were (partially) cured for 60 min at 55 °C. In a second step, the individual layers together with the metal or polymer layer



were assembled into another mold while some uncured PDMS was added to bond the partially cured PDMS layers together. As a final step, the specimens were fully cured for 24 h at 55 °C.

### 6.4.2 Micro-patterning

Various micro-scale patterns were produced on the surface of PDMS layers using replication of negatively designed micropatterns on a silicon wafer. The designed patterns were used to fabricate a photomask (optical photomask, feature size accuracy = 0.5  $\mu\text{m}$ , Computographics Photomask Solutions, UK). A polished silicon wafer (4 inches, thickness =  $525 \pm 25$   $\mu\text{m}$ , p-type) was then cleaned with nitric acid (Merck, Darmstadt, Germany) followed by baking for 10 min in an oven at 110 °C for dehydration. Hexamethyldisilazane (HMDS) (BASF, Ludwigshafen, Germany) was poured on the surface at 150 °C for 45 sec to improve the adhesion between the silicon substrate and photoresist. The process followed by spin coating a Shipley S1813 photoresist (MicroChem Corp., Newton, MA, USA) onto the wafer and baking at 115 °C on a hotplate for 60 s. Optical lithography was then carried out by an EVG 620 mask aligner (EVGroup, St. Florian, Austria), and the exposed resist was developed in MF-321 (Shipley, Microposit Developer, USA) at room temperature for 1.5 min, and rinsed in deionized water.

The patterns were transferred into the silicon wafer using an inductive coupled plasma reactive ion etching (ICP RIE) (Adixen, AMS100 Bosch, I-speeder) with  $\text{SF}_6$  = 200 sccm,  $\text{C}_4\text{F}_8$  = 100 sccm, ICP power = 2000 W, CCP = 80 W, temperature = 10 °C, and for five min. The specimens were finally cleaned in acetone. To remove the HMDS layer, the samples were soaked in n-methylpyrrolidone (NMP, Merck, Darmstadt, Germany) at 70 °C for 5 min and then in resist stripper (PRS-3000, JTBaker, The Netherlands) for 10 min and at 80 °C. Finally, the specimens were rinsed thoroughly in DI water and then spin-dried. The final cleaning process was done by oxygen plasma (Tepla M4L Gas Plasma System, Corona, CA, USA) with  $\text{O}_2$  flow = 200 sccm, power = 600 W, and for 10 min.

### 6.4.3 Flexible electronics

Conductive circuits were made from a copper foil (copper foil, purity = 99.9+%, annealed, thickness = 25  $\mu\text{m}$ ; Goodfellow, UK) using laser micromachining. Electrical components were adhesively bonded to the circuit using conductive glue (wire glue, Anders Products, MA, USA). A layer of ethyl cyanoacrylate (LOCTITE 401, Loctite, Germany) adhesive was added to increase the bonding strength between the circuit and the electronic devices.

### 6.4.4 Mechanical activation

The self-folding specimens were stretched using a Lloyd LR5K mechanical testing machine equipped with either a 5 N or 100 N load cell (depending on the range of

the measured forces). The deformations experienced by the specimens were captured using a high-resolution digital camera (Sony A7R with a Sony FE 90-mm f/2.8 macro OSS lens). Image processing was used for measuring the folding angle of the basic elements.

#### 6.4.5 Finite element analysis

FEA was performed using the commercial software Abaqus (Abaqus 6.14). A nonlinear implicit solver (Abaqus Standard) was used to simulate both the stretching and folding of the plastically deforming self-folding constructs. First, a linear buckling analysis was performed to find the buckling modes of the specimens. The first buckling mode predicted by the linear buckling analysis was then introduced as an imperfection to predict the post-buckling behavior of the specimens. Full-integrated solid elements (*i.e.*, C3D8 or C3D20) were used to model the titanium specimens. The PDMS layers were modeled using eight-node hybrid solid elements (*i.e.*, C3D8H). A surface-to-surface contact definition between the titanium and PDMS layers was implemented using a penalty contact enforcement algorithm. For the complex assemblies, the contact definition was replaced by a number of constraint equations, thereby enhancing the convergence while limiting the required computational cost.

A dynamic analysis using the same nonlinear implicit solver was performed to model the multi-stable behavior of the self-folding hinges. Eight-node hybrid solid elements (*i.e.*, C3D8H) were used for modeling both polyolefin and PDMS layers. A self-contact definition was implemented in order to prevent self-penetration of the polyolefin surfaces. Similar to the case of titanium specimens, a penalty contact enforcement algorithm was used.

The stretching and folding of the self-folding hinges embedded with an electrical circuit were also analyzed using FEA (Abaqus Standard). The copper circuit was modeled using eight-node solid elements (*i.e.*, C3D8) and an elastoplastic material model (von Mises yield function, tabular input of strain hardening data) based on a stress-strain curve reported in the literature [60]. Constraint equations between the adjacent nodes of the PDMS and the copper layers were applied to ensure the embedding of the copper circuit inside the PDMS matrix.

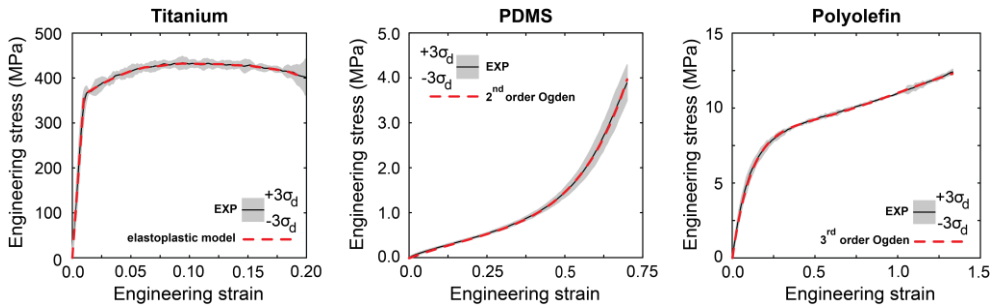
#### 6.4.6 Material models

Uniaxial tensile tests were performed to characterize the mechanical properties of titanium, polyolefin, and PDMS using the same mechanical testing machine (100 N load cell). An elastoplastic material model (von Mises yield function, tabular input of strain hardening data) was fitted to model the mechanical behavior of titanium. Incompressible hyperelastic material models were used for the modeling of both polyolefin (3<sup>rd</sup> order Ogden model) and PDMS (2<sup>nd</sup> order Ogden model). More details can be found in Section 6.5.1.

## 6.5 Supplementary material

### 6.5.1 Material models and material properties

Strips of titanium, polyolefin, and PDMS were produced using laser micromachining or molding. Three identical samples of each material were mechanically tested under tension using a Lloyd LR5K machine equipped with either a 5 N or 100 N load cell (Figure 6.5).



**Figure 6.5:** Uniaxial tensile tests. The average stress data over three samples are plotted with the error bars representing three times the standard deviation from the mean. The fitted material models are plotted using dashed red lines.

An elastoplastic material model (von Mises yield function, tabular input of strain hardening data) was used to model the mechanical behavior of titanium. Both PDMS and polyolefin were modeled using an incompressible hyperelastic model (2<sup>nd</sup> order and 3<sup>rd</sup> order Ogden model, respectively). The obtained material parameters are listed in Table 6.1. An elastoplastic material model (von Mises yield function, tabular input of strain hardening data) was used for modeling the copper connectors. The stress-strain curve of copper was adopted from the literature [60].

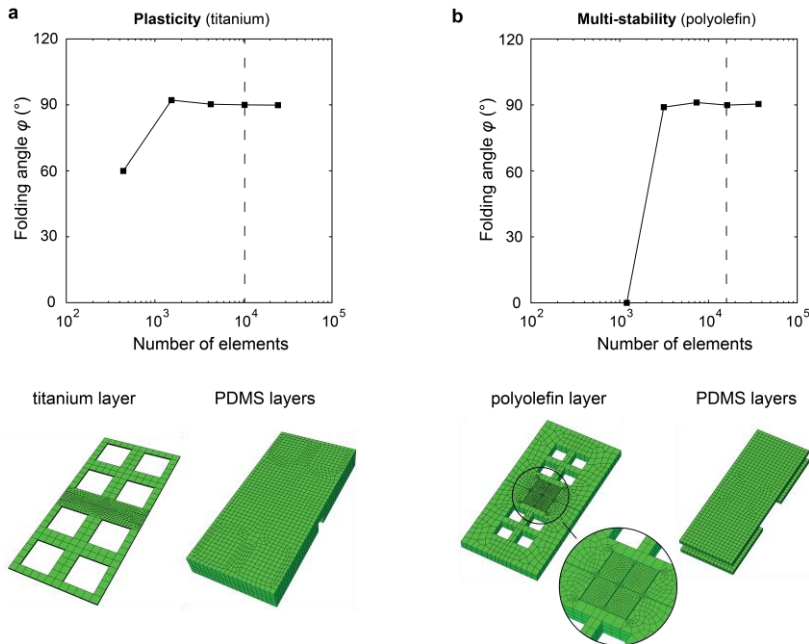
**Table 6.1:** The parameters of the material models used for the finite element analyses presented in this study.

<b>Titanium</b>	$E = 36.7 \text{ GPa}$	$\nu = 0.35$
<b>PDMS</b>	$\mu_1 = 5.895 \cdot 10^{-2} \text{ MPa}$	$\alpha_1 = 11.91$
	$\mu_2 = 7.917 \cdot 10^{-1} \text{ MPa}$	$\alpha_2 = 4.611 \cdot 10^{-6}$
<b>Polyolefin</b>	$\mu_1 = -7.398 \text{ MPa}$	$\alpha_1 = 4.490 \cdot 10^{-2}$
	$\mu_2 = -15.45 \text{ MPa}$	$\alpha_2 = 3.113$
	$\mu_3 = 49.25 \text{ MPa}$	$\alpha_3 = -5.498$
<b>Copper</b>	$E = 38.1 \text{ GPa}$	$\nu = 0.35$

### 6.5.2 Mesh convergence study

A mesh convergence analysis was performed in order to ensure the accuracy of the finite element models. The analysis was conducted only for the basic elements after which a similar mesh size was used for the modeling of the more complex assemblies of basic elements. Coarse meshes were used as the starting points for

both analyses. The folding angle rapidly converged upon decreasing the mesh size (Figure 6.6). The dashed lines in the left and right subfigures of Figure 6.6 indicate the mesh sizes used for the finite element analyses presented in this work.



**Figure 6.6:** Mesh convergence analysis. Mesh convergence analysis for self-folding basic elements working either on the basis of plasticity or multi-stability. The mesh size used for the simulations presented in this work is indicated with dashed lines.

**Table 6.2:** The parameters that were used for activation (*i.e.*, stretching) of the designs presented in this work.

Structure	Figure	Stretching (mm)
Series of identical basic elements	6.2c	4.2
Series of different basic elements	6.2d	4.0
Parallel strips of self-folding basic elements	6.2e	4.0
Stacked strips of self-folding basic elements	6.2f	8.0

Structure	Figure	Stretching – step 1 (mm)	Stretching – step 2 (mm)
Cubic box – multi-stability	6.3a	5.0	7.5
Cubic box – plasticity	6.3a	2.1	3.15
Tubular construct – multi-stability	6.3b	10.0	7.5
Tubular construct – plasticity	6.3b	4.2	3.15
Multi-storey lattice – multi-stability	6.3c	10.0	25.0
Multi-storey lattice – plasticity	6.3c	4.2	10.5

### **6.5.3 Activation parameters**

The parameters that were used for the mechanical activation of all the specimens presented in this Chapter are listed in Table 6.2.

## Bibliography

1. Liu, Y., J. Genzer, and M.D. Dickey, "2D or not 2D": Shape-programming polymer sheets. *Prog Polym Sci*, 2016. **52**: p. 79-106.
2. Santangelo, C.D., *Extreme mechanics: self-folding origami*. Annual Review of Condensed Matter Physics, 2017. **8**: p. 165-183.
3. van Manen, T., S. Janbaz, and A.A. Zadpoor, *Programming the shape-shifting of flat soft matter*. Materials Today, 2018. **21**(2): p. 144-163.
4. Boyvat, M., J.-S. Koh, and R.J. Wood, *Addressable wireless actuation for multijoint folding robots and devices*. Science Robotics, 2017. **2**: p. 1544eaan.
5. Felton, S., et al., *A method for building self-folding machines*. Science, 2014. **345**(6197): p. 644-646.
6. Mu, J., et al., *Origami-inspired active graphene-based paper for programmable instant self-folding walking devices*. Science Advances, 2015. **1**(10): p. e1500533.
7. Teoh, Z.E., et al., *Rotary-actuated folding polyhedrons for midwater investigation of delicate marine organisms*. Science Robotics, 2018. **3**(20): p. eaat5276.
8. Shenoy, V.B. and D.H. Gracias, *Self-folding thin-film materials: From nanopolyhedra to graphene origami*. MRS Bulletin, 2012. **37**(9): p. 847-854.
9. Bertoldi, K., et al., *Flexible mechanical metamaterials*. Nature Reviews Materials, 2017. **2**(11): p. 17066.
10. Overvelde, J.T., et al., *A three-dimensional actuated origami-inspired transformable metamaterial with multiple degrees of freedom*. Nature Communications, 2016. **7**: p. 10929.
11. Silverberg, J.L., et al., *Using origami design principles to fold reprogrammable mechanical metamaterials*. Science, 2014. **345**(6197): p. 647-650.
12. Wang, Z., et al., *Origami-Based Reconfigurable Metamaterials for Tunable Chirality*. Advanced Materials, 2017. **29**(27): p. 1700412.
13. Yasuda, H. and J. Yang, *Reentrant origami-based metamaterials with negative Poisson's ratio and bistability*. Physical Review Letters, 2015. **114**(18): p. 185502.
14. Cho, J.H., et al., *Nanoscale origami for 3D optics*. Small, 2011. **7**(14): p. 1943-1948.
15. Sundaram, S., et al., *3D-printed self-folding electronics*. ACS Applied Materials & Interfaces, 2017. **9**(37): p. 32290-32298.
16. Hayes, G.J., et al., *Self-folding origami microstrip antennas*. IEEE Transactions on Antennas and Propagation, 2014. **62**(10): p. 5416-5419.
17. Hartl, D., K. Lane, and R. Malak. *Computational design of a reconfigurable origami space structure incorporating shape memory alloy thin films*. in ASME 2012 Conference on Smart Materials, Adaptive Structures and Intelligent Systems. 2012. American Society of Mechanical Engineers.
18. Hartl, D., K. Lane, and R. Malak. *Design of a massively reconfigurable origami space structure incorporating shape memory alloys*. in ASME 2012 International Mechanical Engineering Congress and Exposition. 2012. American Society of Mechanical Engineers.
19. Janbaz, S., R. Hedayati, and A. Zadpoor, *Programming the shape-shifting of flat soft matter: from self-rolling/self-twisting materials to self-folding origami*. Materials Horizons, 2016. **3**(6): p. 536-547.
20. Janbaz, S., et al., *Origami lattices with free-form surface ornaments*. Science advances, 2017. **3**(11): p. eaao1595.
21. Kuribayashi-Shigetomi, K., H. Onoe, and S. Takeuchi, *Cell origami: self-folding of three-dimensional cell-laden microstructures driven by cell traction force*. PloS one, 2012. **7**(12): p. e51085.
22. Chen, Y., et al., *Lattice metamaterials with mechanically tunable Poisson's ratio for vibration control*. Physical Review Applied, 2017. **7**(2): p. 024012.
23. Hedayati, R., A. Leeflang, and A. Zadpoor, *Additively manufactured metallic pentamode meta-materials*. Applied Physics Letters, 2017. **110**(9): p. 091905.
24. Kadic, M., et al., *On the practicability of pentamode mechanical metamaterials*. Applied Physics Letters, 2012. **100**(19): p. 191901.

25. Lee, J.-H., et al., *Periodic bicontinuous composites for high specific energy absorption*. Nano Letters, 2012. **12**(8): p. 4392-4396.
26. Wang, Q., et al., *Lightweight mechanical metamaterials with tunable negative thermal expansion*. Physical Review Letters, 2016. **117**(17): p. 175901.
27. Zheng, X., et al., *Ultralight, ultrastiff mechanical metamaterials*. Science, 2014. **344**(6190): p. 1373-1377.
28. Kim, D.H., et al., *Biomimetic nanopatterns as enabling tools for analysis and control of live cells*. Advanced Materials, 2010. **22**(41): p. 4551-4566.
29. Kim, S.O., et al., *Epitaxial self-assembly of block copolymers on lithographically defined nanopatterned substrates*. Nature, 2003. **424**(6947): p. 411.
30. Yang, S., et al., *Template-Confined Dewetting Process to Surface Nanopatterns: Fabrication, Structural Tunability, and Structure-Related Properties*. Advanced Functional Materials, 2011. **21**(13): p. 2446-2455.
31. Narui, Y. and K.S. Salaita, *Dip-pen nanolithography of optically transparent cationic polymers to manipulate spatial organization of proteolipid membranes*. Chemical Science, 2012. **3**(3): p. 794-799.
32. Wu, C.C., et al., *Strategies for Patterning Biomolecules with Dip-Pen Nanolithography*. Small, 2011. **7**(8): p. 989-1002.
33. Mackus, A., et al., *Nanopatterning by direct-write atomic layer deposition*. Nanoscale, 2012. **4**(15): p. 4477-4480.
34. Du, J., et al. *ShapeTex: Implementing shape-changing structures in fabric for wearable actuation*. in *Proceedings of the Twelfth International Conference on Tangible, Embedded, and Embodied Interaction*. 2018. ACM.
35. Rus, S., et al. *Prototyping Shape-Sensing Fabrics Through Physical Simulation*. in *European Conference on Ambient Intelligence*. 2018. Springer.
36. Chen, W., et al., *Nanotopographical surfaces for stem cell fate control: Engineering mechanobiology from the bottom*. Nano Today, 2014. **9**(6): p. 759-784.
37. Dalby, M.J., N. Gadegaard, and R.O. Oreffo, *Harnessing nanotopography and integrin-matrix interactions to influence stem cell fate*. Nature Materials, 2014. **13**(6): p. 558.
38. Dobbenga, S., L.E. Fratila-Apachitei, and A.A. Zadpoor, *Nanopattern-induced osteogenic differentiation of stem cells—A systematic review*. Acta biomaterialia, 2016. **46**: p. 3-14.
39. Linklater, D.P., S. Juodkazis, and E.P. Ivanova, *Nanofabrication of mechano-bactericidal surfaces*. Nanoscale, 2017. **9**(43): p. 16564-16585.
40. Modaresifar, K., et al., *Bactericidal effects of nanopatterns: A systematic review*. Acta biomaterialia, 2019. **83**: p. 29-36.
41. Bhushan, B. and Y.C. Jung, *Wetting, adhesion and friction of superhydrophobic and hydrophilic leaves and fabricated micro/nanopatterned surfaces*. Journal of Physics: Condensed Matter, 2008. **20**(22): p. 225010.
42. Bhushan, B., Y.C. Jung, and K. Koch, *Micro-, nano- and hierarchical structures for superhydrophobicity, self-cleaning and low adhesion*. Philosophical Transactions of the Royal Society of London A, 2009. **367**(1894): p. 1631-1672.
43. Martines, E., et al., *Superhydrophobicity and superhydrophilicity of regular nanopatterns*. Nano Letters, 2005. **5**(10): p. 2097-2103.
44. Callens, S.J. and A.A. Zadpoor, *From flat sheets to curved geometries: Origami and kirigami approaches*. Materials Today, 2018. **21**(3): p. 241-264.
45. Liu, Y., J. Genzer, and M.D. Dickey, *"2D or not 2D": Shape-programming polymer sheets*. Progress in Polymer Science, 2016. **52**: p. 79-106.
46. Van Manen, T., S. Janbaz, and A.A. Zadpoor, *Programming the shape-shifting of flat soft matter*. Materials Today, 2018. **21**: p. 144-163.
47. Shen, X., et al., *Large negative thermal expansion of a polymer driven by a submolecular conformational change*. Nat Chem, 2013. **5**(12): p. 1035-41.
48. Behl, M. and A. Lendlein, *Shape-memory polymers*. Materials today, 2007. **10**(4): p. 20-28.

49. Ma, M., et al., *Bio-inspired polymer composite actuator and generator driven by water gradients*. Science, 2013. **339**(6116): p. 186-9.
50. Gladman, A.S., et al., *Biomimetic 4D printing*. Nature Materials, 2016. **15**(4): p. 413.
51. Van Manen, T., S. Janbaz, and A.A. Zadpoor, *Programming 2D/3D shape-shifting with hobbyist 3D printers*. Materials Horizons, 2017. **4**(6): p. 1064-1069.
52. Zhang, Y., et al., *Printing, folding and assembly methods for forming 3D mesostructures in advanced materials*. Nature Reviews Materials, 2017. **2**(4): p. 17019.
53. Gracias, D.H., et al., *Fabrication of Micrometer-Scale, Patterned Polyhedra by Self-Assembly*. Advanced Materials, 2002. **14**(3): p. 235-238.
54. Pandey, S., et al., *Algorithmic design of self-folding polyhedra*. Proc Natl Acad Sci U S A, 2011. **108**(50): p. 19885-90.
55. Xu, S., et al., *Assembly of micro/nanomaterials into complex, three-dimensional architectures by compressive buckling*. Science, 2015. **347**(6218): p. 154-159.
56. Fu, H., et al., *Morphable 3D mesostructures and microelectronic devices by multistable buckling mechanics*. Nature Materials, 2018. **17**(3): p. 268.
57. Waitukaitis, S., et al., *Origami multistability: From single vertices to metasheets*. Physical Review Letters, 2015. **114**(5): p. 055503.
58. Yang, Y., M.A. Dias, and D.P. Holmes, *Multistable kirigami for tunable architected materials*. Physical Review Materials, 2018. **2**(11): p. 110601.
59. van Manen, T., et al., *Kirigami-enabled self-folding origami*. Materials Today, 2020. **32**: p. 59-67.
60. Simons, G., et al., *Size effects in tensile testing of thin cold rolled and annealed Cu foils*. Materials Science and Engineering: A, 2006. **416**(1-2): p. 290-299.





# Automated folding of origami lattices: from nanopatterned sheets to stiff meta-biomaterials



Folding nanopatterned flat sheets into complex 3D structures enables the fabrication of meta-biomaterials that combine a rationally designed 3D architecture (e.g., to tune mechanical and mass transport properties) with nanoscale surface features (e.g., to guide the differentiation of stem cells). Self-folding is an attractive approach for realizing such materials. However, self-folded lattices are generally too compliant as there is an inherent competition between the ease-of-folding requirements and the final load-bearing characteristics. Inspired by sheet metal forming, we propose an alternative route for the fabrication of origami lattices. This 'automated folding' approach allows for the introduction of sharp folds into thick metal sheets, thereby enhancing their stiffness. We then demonstrate the first time ever realization of automatically folded origami lattices with bone-mimicking mechanical properties (elastic modulus = 0.5 GPa). The proposed approach is highly scalable given that the unit cells making up the meta-biomaterial can be arbitrarily large in number and small in dimensions. To demonstrate the scalability and versatility of the proposed approach, we fabricated origami lattices with > 100 unit cells, lattices with unit cells as small as 1.25 mm, and auxetic lattices. We then used inductively coupled plasma reactive ion etching to nanopattern the surface of the sheets prior to folding. Protected by a thin layer of coating, these nanoscale features remained intact during the folding process. A cell culture assay was then used to assess the bone tissue regeneration performance of the folded origami. We found that the nanopatterned folded specimens exhibit significantly increased mineralization as compared to their non-patterned counterparts.

T. van Manen, M. Ganjian, K. Modaresifar, L.E. Fratila-Apachitei & A.A. Zadpoor (2021). *Automated folding of origami lattices: from nanopatterned sheets to stiff meta-biomaterials*. Small (Accepted).

## 7.1 Introduction

Architected materials that combine volume-related functionalities with surface-related functionalities often cannot be manufactured using the currently available 3D printing techniques. An important category of such materials are meta-biomaterials in which complex 3D shapes need to be combined with complex and precisely controlled surface nanopatterns. Much of the surface area of such highly porous materials is internal, meaning that they are inaccessible for nanopatterning once the 3D printing process has been finished. Moreover, nanopatterning techniques that can create geometrically complex and precisely controlled nanopatterns generally only work on flat surfaces. A promising approach [1-3] to combine volume-related with surface-related in such materials is to start from a flat state to make sure the entire surface of the biomaterial is available for nanopatterning. Once the nanopatterning step is concluded, the material self-folds into a complex 3D shape. Such an approach, therefore, allows for the fabrication of multi-functional meta-biomaterials blending the advantages of a fully-accessible flat surface with those of a rationally designed 3D architecture. The precisely controlled nanopatterns can, for example, kill bacteria [4, 5] and cause the osteogenic differentiation of stem cells [6], while the 3D porous architecture can adjust the mechanical [7-9] and mass transport [10, 11] properties of the obtained lattices while also affecting the curvature sensed by the cells [12]. The incorporation of multiple functionalities through the folding of flat constructs has applications in other areas as well, including flexible electronics [3, 13] and soft robotics [14].

Given the numerous advantages of such origami lattices, many dedicated self-folding techniques have been developed in the recent years [15-17]. Nevertheless, several major challenges remain unresolved. Most importantly, self-folded origami lattices are usually too compliant to be suitable for such applications as load-bearing bone substitutes. To avoid stress shielding and stimulate bone tissue regeneration, the mechanical properties of bone substitutes should match those of their surrounding bone tissue [18]. Dependent on the type and location of the bony defect, an elastic modulus of 0.1-20 GPa may be required [19, 20]. Second, it remains highly challenging to self-fold origami lattices whose unit cells are large in number (*i.e.*, hundreds to thousands) and small in dimensions (*i.e.*, meso/microscale range). The second challenge can, in principle, be addressed within the paradigm of self-folding materials, for example, by developing 4D printing techniques with finer resolutions [21, 22] and synthesizing shape memory polymers with higher magnitudes of generated forces [23]. The first challenge, however, is inherent to self-folding processes. That is because there is an inherent competition between the ease-of-folding requirements on the one hand and the final load-bearing characteristics of self-folded lattices on the other. For the fabrication of high-modulus self-folding structures, sharp folds need to be realized in thick sheets of flat material. The realization of such sharp folds

requires the use of active materials that display large deformations upon activation. Such active materials (*e.g.*, both hard shape memory polymers and hydrogels) are too compliant for the fabrication of high-modulus origami lattices. Indeed, we have recently demonstrated that there exist theoretical boundaries limiting the stiffness of self-folded origami [24].

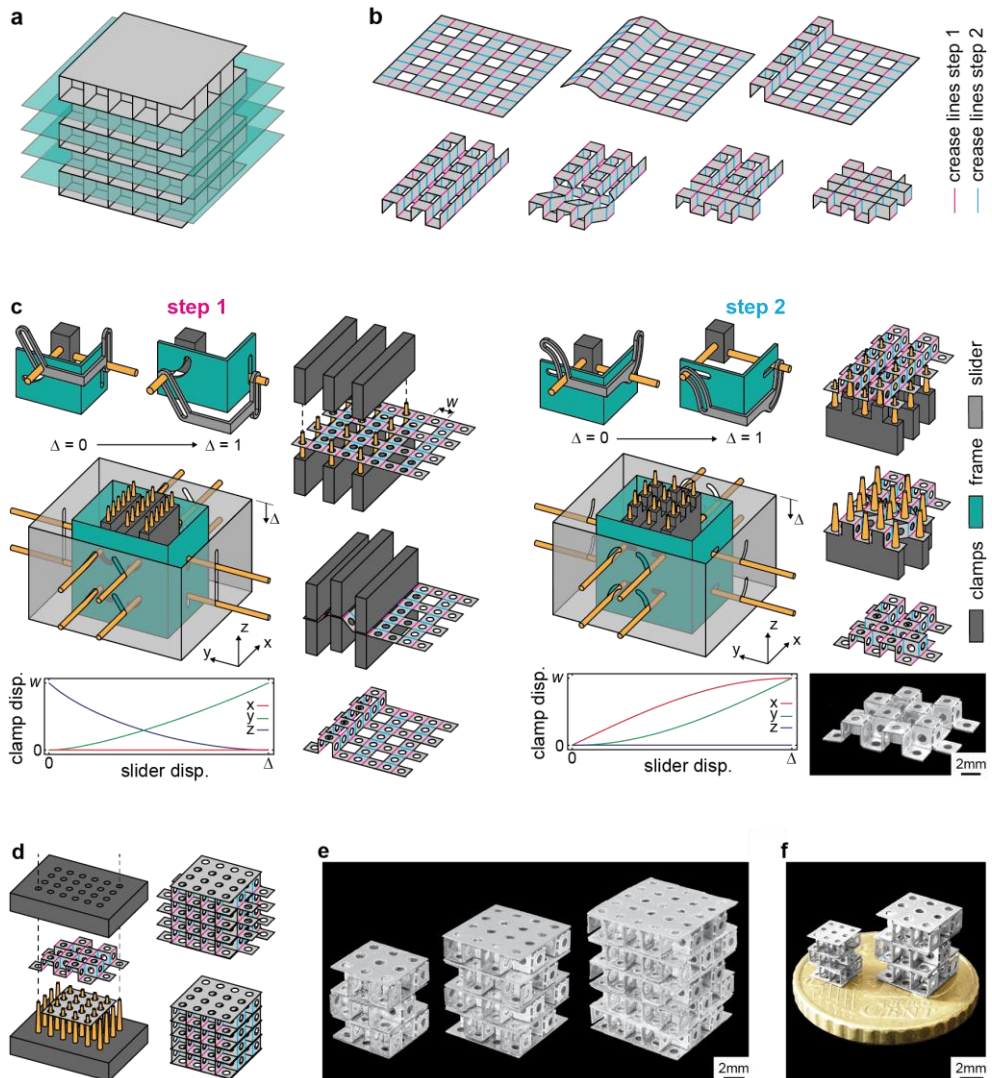
One approach to address the first limitation is to use an additional (locking) mechanism to enhance the mechanical properties of the folding elements after completing the self-folding process. For example, separate locking elements are used in a few studies to increase the stiffness of the folded structure [25-27]. Another method includes the so-called 'layer-jamming mechanisms' in which a stack of self-folding elements is compressed after folding to enhance their combined stiffness [28-30]. However, both techniques highly limit the design freedom and scalability.

Here, we propose the alternative approach of 'automated folding' to address both abovementioned limitations of self-folding processes. Inspired by sheet metal forming processes, we developed miniaturized folding devices that can fold origami lattices made from a large number of small unit cells. This approach allows for realizing sharp permanent folds in thick (metallic) sheets. The sharpness of the folds, the large thickness of the sheets (as compared to the curvature of the folds), and the freedom in using any material including metals translates to high, bone-mimicking stiffness values while also enabling the inclusion of pore sizes that are suitable for bone tissue regeneration (*i.e.*, 300-900  $\mu\text{m}$  [31-33]). The afforded scalability in the design of meta-biomaterials also extends to the dimensions of the unit cells, as the proposed approach is highly amenable to miniaturization. Indeed, the primary factor limiting the unit cell dimensions is the precision of the applied micromachining technique. We use the proposed approach to demonstrate the first ever realization of automatically folded origami lattices with bone-mimicking mechanical properties. To showcase the versatility of the unit cells that can be realized, we also fold origami lattices with auxetic properties (*i.e.*, a negative Poisson's ratio). Finally, we demonstrate the entire process of fabricating origami-based meta-biomaterials by micromachining thick titanium sheets followed by surface nanopatterning using inductively coupled plasma reactive ion etching (ICP RIE), application of a protective layer to preserve the nanopatterns during the folding process, and the biological evaluation of the folded specimens using *in vitro* cell culture assays.

## 7.2 Results and Discussion

### 7.2.1 Automated folding of 3D lattices

We start by considering regular lattices made of an identical unit cell repeated along the three orthogonal axes (Figure 7.1a). Such lattices can be unfolded by slicing their 3D geometry into 'storeys' whose thickness equals that of a single



**Figure 7.1:** Fabrication of stiff cubic lattices. (a) The 'slicing' of a cubic lattice structure. (b) The folding sequences of an array of cubic unit cells. (c) A schematic illustration of the two-step folding process of cubic 'storeys' using external folding devices. (d) The assembly of the folded 'storeys' into a cubic lattice structure. (e) The photographs of the folded cubic lattices with different numbers of unit cells. (f) The cubic lattices with different unit cell dimensions ( $w = 1.25$  mm and  $w = 2.0$  mm) are shown on top of a 10 Euro cent coin.

unit cell (Figure 7.1a). Depending on the type of the unit cell, different folding patterns have been proposed in the literature for the folding of such storeys [2, 34]. Here, we will be focusing on one such folding strategy (Figure 7.1b) while keeping in mind that the other folding strategies can, in principle, be realized as well. First, a series of collinear hinges along the  $y$ -direction are simultaneously folded into a corrugated sheet, in a row-by-row manner (Figure 7.1b). Upon the

completion of the first stage, all the remaining (*i.e.*, unfolded) crease lines align along the z-direction. Second, the corrugated sheet is folded into the final array of cubes (Figure 7.1b). This step can be repeated sequentially to achieve the desired array of the unit cells. The main advantage of this particular folding sequence is that the folding steps can be decoupled into multiple non-interfering stages. Consequently, a simple, yet highly scalable folding device can be designed to automate the folding process. In addition, the selected folding pattern is rigid-foldable, meaning that the deformation is localized at the crease lines. The faces are, therefore, not stretched or twisted during the folding process, ensuring that the applied surface ornaments remain intact. Finally, the lattices can be folded from a single sheet, further improving their structural integrity.

We designed two sets of folding devices (*i.e.*, one for each folding step, Figure 7.1c). Stereolithography (SLA) 3D printing was used for the fabrication of the folding devices (see Section 7.4, Figure 7.6). First, we designed clamps that use small pins to hold the flat sheets. Circular holes were, therefore, incorporated into the design of the initially flat sheets. The clamps can be actuated using a mechanism that is made of a frame with fixed slots and an outer slider containing a number of guiding slots (Figure 7.1c). The frame and sliders are linked through the pins connected to the two moving clamps. The middle clamp is fixed to the frame. Only actuated by the downward displacement of the slider,  $\Delta$ , the clamps make the desired movement that is encoded into the geometry of the slots (Figure 7.1c). In the first folding step, the specimen is clamped between two similar folding devices to constrain the displacement of the specimen in the z-direction. For the second folding step, no constraints in the z-direction need to be applied and a single folding device is sufficient for the folding of the specimen. Because the folding sequence is composed of two independent steps, large arrays of polyhedra can be folded provided that the widths of the folding devices are large enough.

Following the folding process, the individual 'storeys' need to be assembled into a cubic lattice. Additional flat sheets were designed that provided the surface area for the adhesive bonding of the folded 'storeys' (Figure 7.1d). A special device made of an array of pins and holes was used to align the folded specimens and to press them together during the curing time of the adhesive. The assembled cubic lattices still contain a few protruding panels that were needed for the clamping of the specimen during the folding process. Upon the manual removal of these panels, the final cubic lattice is obtained (Figure 7.1d). Multiple cubic lattices with different numbers of unit cells ( $w = 2.0$  mm) were folded and assembled using the proposed approach (Figure 7.1e). In addition, smaller folding devices were used for the fabrication of a cubic lattice structure with  $w = 1.25$  mm (Figure 7.1f and Figure 7.9), demonstrating the scalability of the developed folding technique.

Some amount of elastic springback is inherent to the described folding process. Both experiments and FEA simulations were performed to quantify the amount of springback of the titanium sheets used in this study. For folding angles of  $90^\circ$ , the amount of elastic springback is found to be around  $10^\circ$  (Figure 7.10). Two strategies were employed to minimize the effects of springback on the geometry of the folded cubic 'storeys'. First, the crease lines of the first folding step are perpendicular to the crease lines of the second folding step which prohibits the springback of the folds of the first step (Figure 7.1b). Second, during the assembly of individual 'storeys', the springback of the vertical folds (second folding step) is restrained by the assembly tooling (Figure 7.1d). Because of these two strategies, elastic springback did not cause any significant deviations from the desired geometry in the cubic lattices (Figure 7.1e).

### 7.2.2. Mechanical properties of cubic lattices

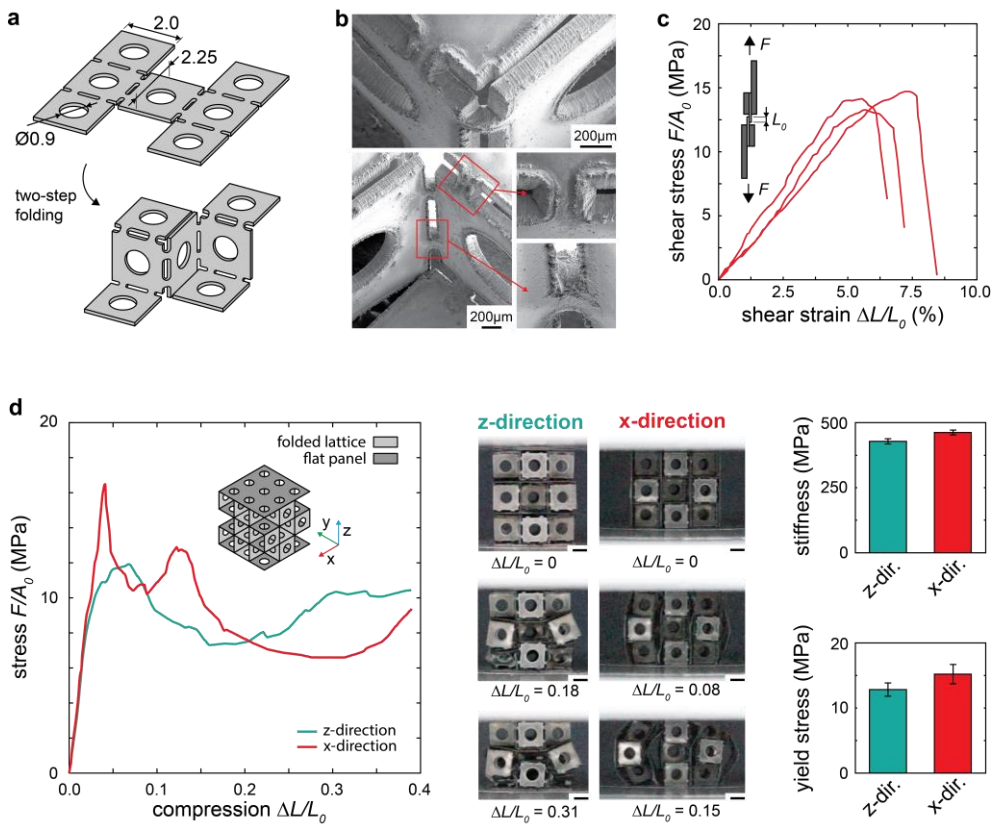
Given the importance of mechanical properties in determining the performance of load-bearing meta-biomaterials, we studied how origami lattices respond to mechanical loads. Initially flat sheets with a panel width ( $w$ ) of 2.0 mm were laser-cut from titanium foils with a thickness of 125  $\mu\text{m}$ . Crease lines were integrated into the design in order to concentrate the deformation at the folding lines (Figure 7.2a). The length of one of the panels was slightly extended (Figure 2a) such that the edges of this panel aligned with the top and bottom panels and could, thus, contribute to the load-bearing capacity of the specimens when loaded in compression. Circular holes were incorporated into the design to not only serve as the clamping sites for the folding devices but to also produce an interconnected array of cubic unit cells. In general, meta-biomaterials need to be permeable to enable both cell migration and the transport of oxygen and nutrients [18]. Scanning electron microscope (SEM) images were used to assess the quality of the specimens after folding. We found that the deformations were localized at the crease lines without any signs of cracks (Figure 7.2b).

For the assembly of the folded lattices, a biocompatible cyanoacrylate-based adhesive was selected. The mechanical performance of the adhesive was assessed by performing a series of lap shear tests (Figure 7.2c). The results reveal an average shear strength of 14.1 MPa and an average shear modulus of 270 MPa, which are in the same range as other cyanoacrylate-based adhesives [35-37] and are expected to be sufficient for carrying the shear loads developed within the storeys due to the potential misalignments and the other unforeseen causes of shear loading.

Subsequently, compression tests were performed on the lattices made from an array of  $3 \times 3 \times 3$  cubic unit cells. For the first set of experiments, the specimens were oriented along the z-direction. The specimens failed though the sequential collapse of individual 'storeys' (Figure 7.2d). We also compressed the specimens



along the x-direction and observed that the dominant failure mode shifts to the failure of the adhesive accompanied by the outward buckling of the outer storeys (Figure 7.2d). Regardless of the loading direction, the effective elastic modulus was 400-500 MPa while the yield strength was around 15 MPa (Figure 7.2d). These values are in the same range as the mechanical properties of the cancellous bone (typically between 50-1000MPa) [38] and confirm the bone-mimicking mechanical properties of the folded lattice structures. Samples containing more unit cells are expected to exhibit even higher stiffness values because the panels located on the edges of the specimens carry less loads (Figure 7.1e). For larger lattice structures (*i.e.*, those comprising more unit-cells), a higher stiffness will be reached as the boundary effects will be smaller as compared to the  $3 \times 3 \times 3$  lattice structures fabricated here. Both FEA simulations and an analytical scaling analysis were performed to study the effective elastic properties of a cubic lattice structures with  $n \times n \times n$  unit-cells both of which indicated an effective elastic modulus of  $\sim 700$  MPa



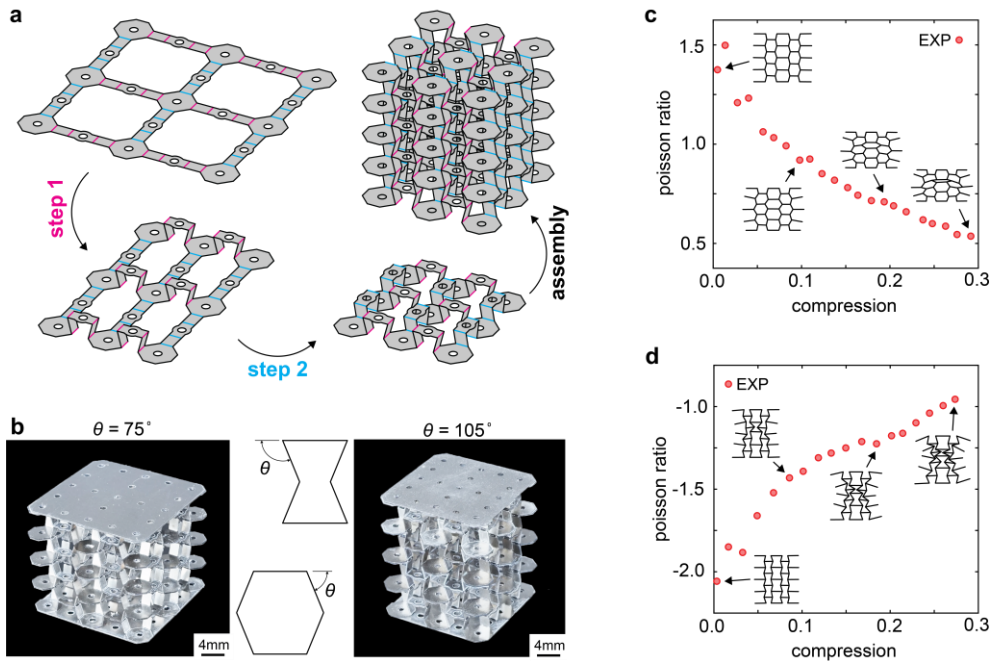
**Figure 7.2:** The mechanical properties of the folded cubic lattices. (a) A schematic representation of the initial geometry of the flat material and the folded structure. (b) The SEM images of a folded cubic structure showing the sharp folding lines. (c) The lab shear test results for the biocompatible adhesive ( $n = 3$ ). (d) The compression test results of the folded lattices containing  $3 \times 3 \times 3$  cubic unit cells ( $n = 3$ ).



for  $n \gg 3$  (see Section 7.5.2). Confining the folded lattices within the boundaries of a cavity may also increase their effective stiffness, as outward buckling would be suppressed. Finally, the buckling load of the vertical panels is dependent on the design of the crease lines that connect these panels. A larger number of connections as well as larger connections will decrease the effective panel height, thereby increasing the buckling load. The design of the crease lines can, therefore, be further optimized to increase both the stiffness and the buckling load of individual storeys.

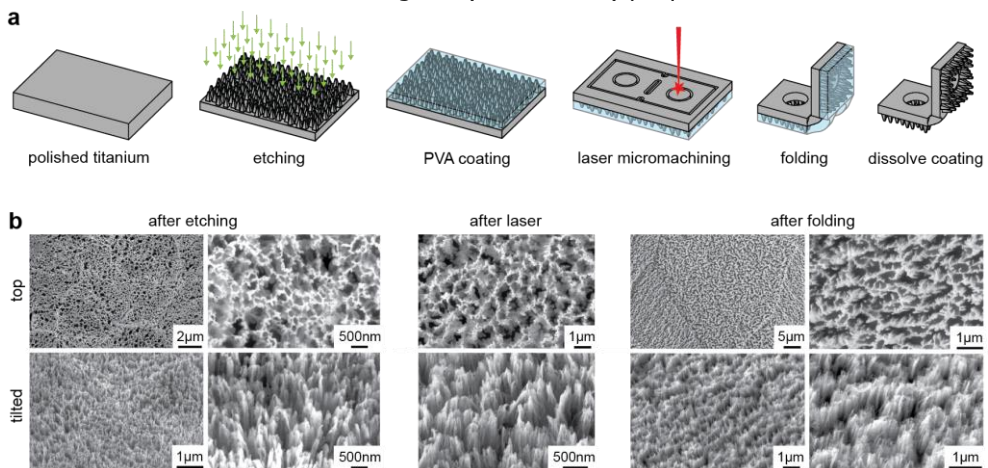
### 7.2.3. Auxetic and non-auxetic hexagonal lattices

In addition to cubic lattices, several other types of origami can be automatically folded using the proposed approach. Given the importance of auxetic structures in the design of meta-biomaterials [39], we folded origami lattices based on the re-entrant unit cell. Similar to the previous designs, the storeys were folded in two independent steps (Figure 7.3a), meaning that the automated folding method is equally scalable and the maximum number of unit cells is only limited by the width of the folding device. Figure 7.7 (Section 7.5) presents additional details regarding the design of the folding devices. From the same initially flat sheet, specimens with different re-entrant angles ( $\theta$ ) can be folded using a single set of



**Figure 7.3:** Folded re-entrant structures. (a) A schematic representation of the two-step folding process and the subsequent assembly of the re-entrant lattice structures. (b) The photographs of the fabricated auxetic lattices with different values of the re-entrant angle,  $\theta$ . The Poisson's ratio as a function of the compressive strain for lattices with  $\theta$  angles of (c)  $75^\circ$  and (d)  $105^\circ$ .

folding devices. The re-entrant angle can be controlled depending on the amount of the downward displacement of the slider,  $\Delta$ . As a demonstration, two specimens were fabricated with  $\theta$  angles equal to  $75^\circ$  and  $105^\circ$  (Figure 7.3b). Both specimens were compressed to measure their Poisson's ratios. Image processing was used to determine how the mean value of the Poisson's ratio evolves as the compressive load gradually increases. Indeed, the specimen with a  $\theta$  angle equal to  $75^\circ$  exhibited a positive Poisson's ratio ranging between 0.5 and 1.5 depending on the magnitude of the applied strain (Figure 7.3c). A negative Poisson's ratio between -2.0 and -1.0 was observed for the sample with a  $\theta$  angle equal to  $105^\circ$  (Figure 7.3d). These results clearly show the potential of the proposed approach for folding origami lattices based on various other types of unit cells. The ability to adjust the type of the unit cell means that automatically folded meta-biomaterials can offer a wide range of (mechanical) properties and functionalities.



**Figure 7.4:** Surface functionalization. (a) A schematic illustration of the nanopatterning and surface protection steps. (b) The SEM images of the bTi surface at different stages of the production process.

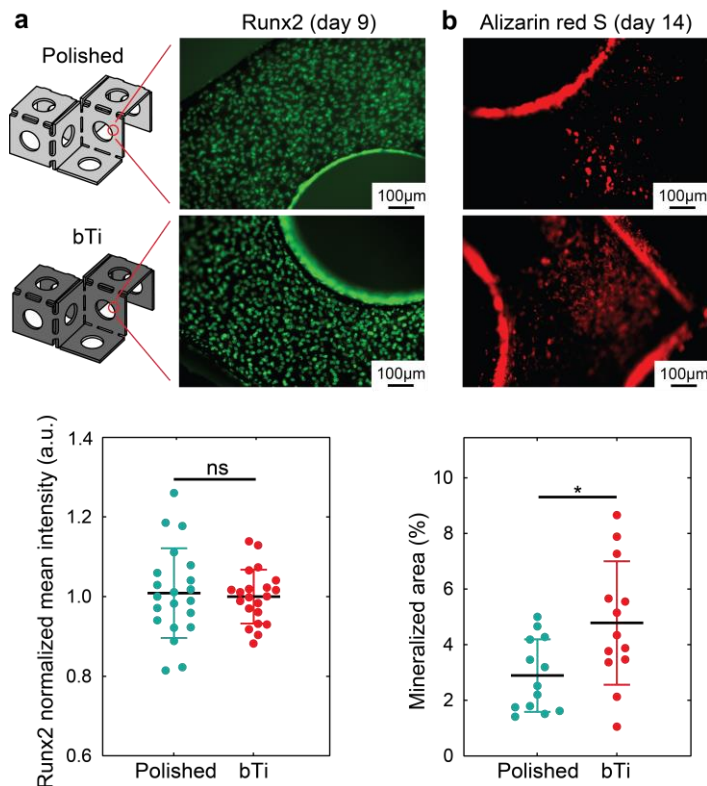
#### 7.2.4. Nanopatterning

The main advantage of the lattices folded from initially flat sheets is the ability to functionalize the entire surface of the final implant using advanced nanopatterning techniques. During the folding process, the functionalized surface needs to be protected to prevent it from being damaged by the folding tools and the self-contact of the sheet. We, therefore, applied a thin layer of polyvinyl alcohol (PVA) coating to the nanopatterned specimens [40]. Upon the completion of the folding process, the coating was dissolved by immersing the specimens in hot water (Figure 7.4a). We used dry etching (ICP RIE) to pattern the surface of the polished flat specimens with nanopillars and create the so-called black titanium (bTi) specimens. The parameters of the ICP RIE were selected such that the resulting nanopillars had dimensions in the range known to be both osteogenic and bactericidal [41]. Evaluating the generated bTi nanopillars by SEM and AFM (data

not shown) revealed that they had a tip diameter below 100 nm and a height between 700 nm and 1000 nm. These dimensions have been previously shown to induce both osteogenic and bactericidal properties [41]. After each production step, SEM images were made of the nanopatterned samples to determine whether the applied nanostructures were still intact. These images confirmed that the patterns remain unaffected by the different production steps (Figure 7.4b), save for a small laser heat-affected zone (Figure 7.2b).

### 7.2.5. Cell culture

We performed biological assays to compare the osteogenic properties of the nanopatterned lattices with their non-patterned polished counterparts. Both patterned and non-patterned specimens supported the attachment of the preosteoblasts onto their surface and did not hinder the expression of Runx2 as an osteogenic marker (Figure 7.5a). There was no significant difference in the intensity of the Runx2 signal between the patterned and non-patterned specimens (Figure 7.5a). The results obtained here for 3D specimens is in line with the results of a previous *in vitro* study on 2D substrates covered with different configurations of bTi pillars [41] in which we found that a configuration of pillars similar to the present study did not downregulate the expression of Runx2 while other nanopattern designs (*e.g.*, taller and more separated pillars) significantly impaired it. Furthermore, in agreement with the previous studies [41, 42], the percentage of the area containing mineralized nodules was significantly higher for the nanopatterned origami lattices as compared to the non-patterned specimens (Figure 7.5b). The enhanced mineralization induced by bTi nanopillars has been argued to be associated with the early stage changes in the adaptation of the cells to the surface, including the changes in the formation and distribution of focal adhesions as well as changes in the cell morphology [41, 42]. The full consistency of the results obtained in the current 3D experiments with those of our previous 2D studies suggest that the functionalities observed in flat specimens carry over to the folded origami lattices. This is an important conclusion that, if supported by further evidence, could greatly simplify the process of evaluating the biological response of origami-based meta-biomaterials. Further studies, including experiments using *in vivo* animal models, are required to explain the effects of such nanopatterned constructs on the bone tissue regeneration process. Moreover, nanopatterns such as those applied here have the potential to induce additional functionalities, such as bactericidal properties [41]. Combining an osteogenic response with bactericidal properties would enable the origami-based meta-biomaterials to both improve bony ingrowth and prevent implant-associated infections.



**Figure 7.5:** The osteogenic response of the preosteoblast cells cultured on the folded lattice structures. (a) The representative immunofluorescent images of Runx2 after 9 days of culture. No significant difference between the polished and bTi lattices was found. (b) The representative images of the mineralized nodules after Alizarin red S staining after (day 14). The mineralized area is significantly larger for the bTi lattices as compared with the polished specimens. Unpaired *t*-test with the Welch correction,  $*p < 0.05$ .

### 7.3 Outlook and conclusions

In summary, we presented a methodology for the fabrication of high-modulus origami lattices whose (internal) surfaces were decorated with nanoscale surface ornaments. While this method could, in principle, be applied to a wide range of materials, we demonstrated automatically folded cubic lattices with an effective modulus of up to 0.5 GPa, automatically folded auxetic and non-auxetic hexagonal lattices, and folded lattices with osteogenic surface nanopatterns. The application of a thin coating layer was sufficient to protect the surface nanopatterns during the laser cutting and subsequent folding steps. Finally, our *in vitro* assays confirmed that the nanopatterned origami lattices exhibit enhanced osteogenic response as compared to their non-patterned counterparts, including a significantly higher degree of mineralization.

The proposed folding method is highly scalable in terms of the number of unit-cells. Specific folding patterns were selected that allowed for the decoupling of the folding process in two separate steps that could be performed in a row-by-row manner. A simple folding device could then be used for the folding of lattice structures with a large number of unit-cells. Indeed, the requirement that it should be possible to decouple the folding process in two separate steps limits the design freedom of the proposed folding method. A larger design freedom can be reached when we relax this requirement. This, however, will limit the scalability of the proposed folding method in terms of the number of the incorporated unit-cells.

Bone-substituting meta-biomaterials require a pore size within the range 200-2000  $\mu\text{m}$  [43, 44], although the optimum pore size is generally believed to be between 300-900  $\mu\text{m}$  [31-33]. To demonstrate the scalability of the presented folding strategy, we folded a cubic lattice with a unit cell size of 1250  $\mu\text{m}$  from a 50  $\mu\text{m}$  thick titanium sheet (Figure 7.1f). In principle, further miniaturization would be possible provided that more advanced production techniques, such as micro-milling [45, 46], are used for the fabrication of the folding devices.

We reported the fabrication of lattice structures with an effective modulus of 0.5 GPa, which is in the range of the values reported in the literature for the trabecular bone [38]. One method to increase the elastic modulus of the folded structures is to reduce the size of the unit-cells so as to fit more unit-cells in a similar volume. This will increase the load-bearing capacity of the structure [24]. An alternative strategy would be to stack several loosely connected sheets with relatively smaller thicknesses that are simultaneously folded to achieve the desired combination of large thickness values and an increased bend sharpness [24].

We only applied the surface nanopatterns to one side of the sheets used here. Applying the nanopatterns to both sides of the sheets is expected to further enhance the osteogenic potential of the resulting meta-biomaterials. While there is no fundamental reason why this may not be possible, there are a few practical challenges that need to be overcome first. In particular, bespoke techniques need to be developed to protect the already patterned side while the other side is being patterned.

Given that high-modulus biofunctionalized origami lattices comprising large arrays of small interconnected unit-cells can be fabricated, the described approach paves the way for the application of folded lattices as load-bearing meta-biomaterials. Such metamaterials can be fabricated from a wide range of materials while the different types of surface-related functionalities could be embedded into the initially flat material. Even though some aspects of the applied methodology could benefit from further optimization, the proposed approach satisfies all the primary design objectives of a meta-biomaterial, including biocompatibility, fully customizable surface nanopatterns, bone-mimicking mechanical properties,

osteogenic behavior, appropriate range of pore sizes, and scalability. The presented production technique could, therefore, serve as a platform for further biological evaluation of origami-inspired meta-biomaterials, including both *in vitro* and *in vivo* experiments.

## 7.4 Materials and methods

### 7.4.1. Folding devices

Folding devices were manufactured using a stereolithography (SLA) 3D printer (Form 3, Formlabs, Massachusetts, US). CNC milling was used for the precise drilling of the holes in the frame and the clamps for the clamping pins. Finally, the clamps, frame, and slider were assembled using steel rods (diameter = 2.0 mm).

### 7.4.2. Sample fabrication

The specimens were produced from pure titanium sheets (titanium foil, purity = 99.6+%, annealed, Goodfellow, UK) with a thickness of either 50  $\mu\text{m}$  or 125  $\mu\text{m}$ . The specimens were laser cut using laser micromachining equipment (Optec Laser Micromachining Systems, Belgium). A biocompatible cyanoacrylate-based adhesive (ethyl cyanoacrylate, MB297Med-2, MasterBond, US) was used for to assemble the folded storeys. After the application of the adhesive, the specimens were compressed for at least 2 minutes to guarantee the sufficient fixation of the components. The mechanical tests were performed after at least 48 h to ensure the adhesive was fully cured. Figure 7.8 (Section 7.5) illustrates the various steps of the production process.

### 7.4.3. Mechanical testing

A Lloyd-LR5K mechanical testing machine equipped with a 100 N load-cell was used for the compressive mechanical testing of the folded specimens. The resulting deformations were captured using a high-resolution digital camera (Sony A7R, lens = Sony FE 90-mm f/2.8 macro OSS). Lines were fit to the experimental data using a custom MATLAB (Mathworks, version R2020b, US) code to determine the stiffness of the folded lattices. Custom MATLAB codes were used for image processing in order to obtain the Poisson's ratio of the lattices made using the re-entrant unit cells (Figure 7.3). For the measurement of the Poisson's ratio, only the middle unit-cells in the front plane of the specimens were considered in order to minimize the effects of boundary conditions on the results.

### 7.4.4. Nanopatterning

Annealed titanium sheets (titanium foil, purity = 99.6+%, annealed; Goodfellow, UK) with a thickness of 125  $\mu\text{m}$  were used for the fabrication of the bTi samples. The sheets were cut to the size of a 4-inch (diameter = 101.6mm) silicon wafer and were polished by chemical mechanical polishing (CMP Mecapol E460, Saint-Martin-le-Vinoux, France). The 4-inch titanium sheets were then cut into 10×14 mm<sup>2</sup> pieces using the laser micromachine. Consequently, the samples were

cleaned in acetone, ethanol, and isopropyl alcohol (IPA) (consecutive steps of 30 min each), and were spin-dried.

The polished Ti specimens were nanopatterned using an ICP RIE machine (PlasmaLab System 100, Oxford Instruments, UK) to create the so-called black titanium (bTi) specimens. First, the Ti specimens were glued with a thermal joint compound (type 120, Wakefield Engineering, USA) to a 4-inch fused silica carrier wafer. The etching gasses included  $\text{Cl}_2$  and Ar. The etching process was performed under the following condition: ICP power = 600 W, RF power = 100 W,  $\text{Cl}_2$  flow rate = 30 sccm, Ar flow rate = 2.5 sccm, chamber pressure = 0.02 mbar, temperature = 40 °C, and etching time = 10 minutes. Following the etching process, the specimens were cleaned in acetone, ethanol, and IPA (consecutive steps of 30 min each), and were then spin-dried. High-resolution scanning electron microscopy (SEM) images were taken with a Helios (FEI Helios G4 CX dual-beam workstation, Hillsborough, OR, USA) microscope at 10 kV and 43 pA. SEM and atomic force microscopy (AFM, JPK Nanowizard 4, Bruker, Germany) were used to measure the height and tip diameter of the nanopillars as described before [41]. To prevent the bTi nanopatterns from being damaged during the following laser-cut and folding processes, the specimens were coated two times with polyvinyl alcohol (PVA) (Resin Technology, France), each step followed by thermal treatment at 50 °C for 1 hour. The PVA coating was applied by dipping the sample within the PVA solution. This layer was removed prior to the cell culture experiments by placing the folded specimens in hot water (temperature = 70 °C) overnight.

#### 7.4.5. Cell culture

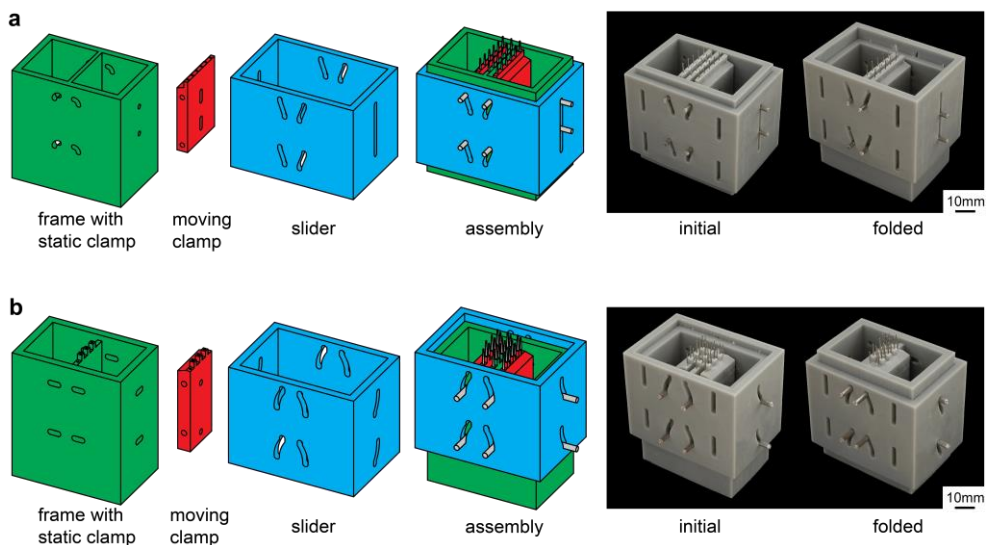
Prior to cell seeding, all the fabricated specimens were sterilized through immersion in 70% ethanol and exposure to UV light for 20 minutes. Preosteoblast MC3T3-E1 cells (Sigma-Aldrich, Germany) were cultured in alpha minimum essential medium ( $\alpha$ -MEM) supplemented with 10% (v/v) fetal bovine serum (FBS) and 1% (v/v) penicillin-streptomycin (all from Thermo Fisher Scientific, US). After reaching confluence, the cells were seeded on both types of constructs ( $n = 4$ ) with a density of  $2 \times 10^4$  cells per construct in a 48 well-plate, and were incubated at 37 °C and 5%  $\text{CO}_2$ . The cell culture medium was refreshed every 2 days by adding 50  $\mu\text{g/ml}$  ascorbic acid (1:1000) and 4 mM  $\beta$ -glycerophosphate (1:500) (both from Sigma-Aldrich, Germany) to  $\alpha$ -MEM. After 9 days of culture, the cells adhered to the constructs were washed with phosphate buffered saline (PBS) and were fixated using a 4% (v/v) formaldehyde solution (Sigma-Aldrich, Germany). The cell membrane was permeabilized by adding 0.5% Triton X-100/PBS (Sigma-Aldrich, Germany) at 4 °C for 5 min. Subsequently, the constructs were incubated in 1% BSA/PBS (Sigma-Aldrich, Germany) at 37 °C for 5 min. Then, the cells were incubated in recombinant anti-Runx2 rabbit monoclonal primary antibody (1:250 in 1% BSA/PBS, Abcam, UK) for 1 h at 37



°C. Following three times washing with 0.5% Tween-20/PBS (Sigma-Aldrich, Germany), the cells were incubated in Alexa Fluor 488, donkey anti-rabbit polyclonal secondary antibody (1:200 in 1% BSA/PBS, Thermo Fisher Scientific, US) for 1 h at room temperature. The constructs were finally washed three times with 0.5% Tween-20/PBS and once with 1X PBS. Fluorescent images were acquired from different panels of the constructs using a fluorescence microscope (ZOE™ fluorescent cell imager, Bio-Rad, The Netherlands). Ten images from each study group (*i.e.*, patterned and non-patterned constructs) were randomly selected for further analysis. Three regions of interest (ROIs) with an area of  $500 \times 500 \mu\text{m}^2$  were analyzed for the intensity of Runx2 using ImageJ 1.53c (NIH, US). Finally, the mean intensity of each ROI was normalized with respect to the mean intensity of all ROIs within the same image.

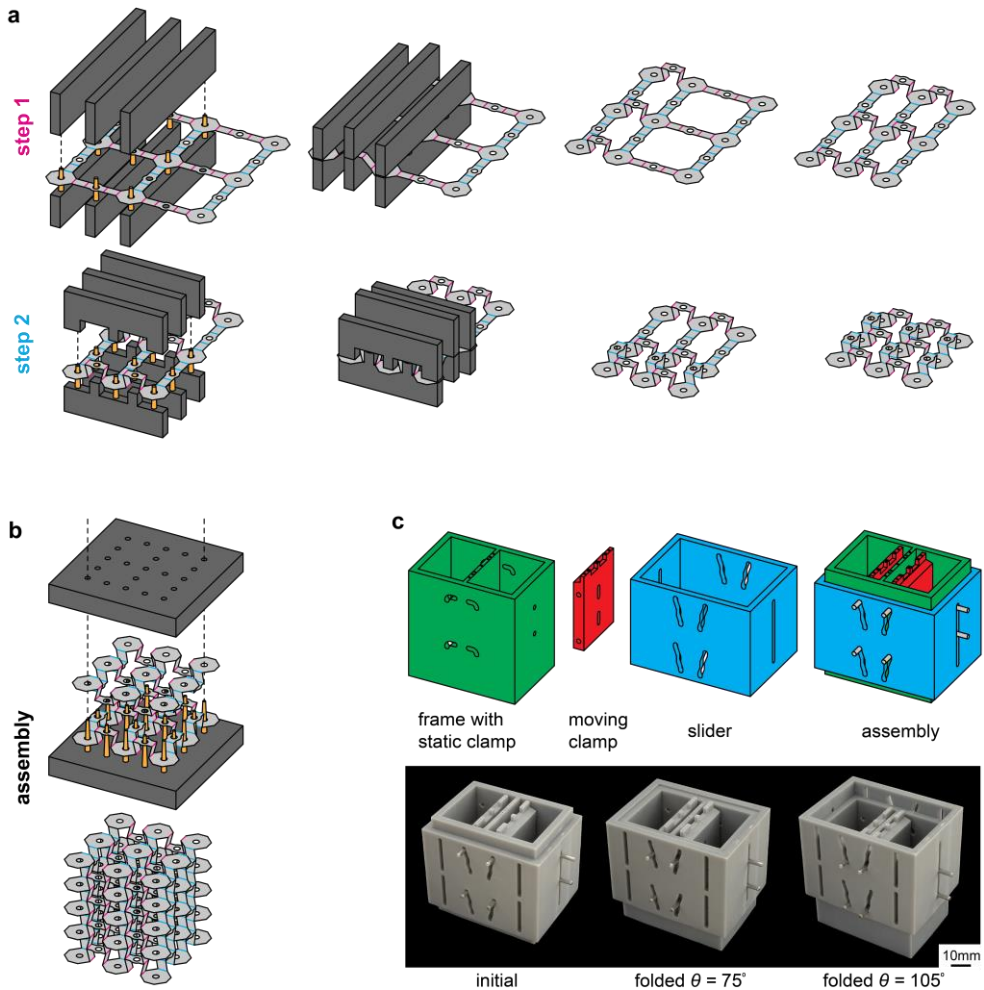
To analyze the matrix mineralization induced by the constructs, the Alizarin red S assay was performed after 14 days of culture. The cells were washed and fixated as described above. The constructs were then incubated in 2% (w/v) Alizarin red S solution (Sigma-Aldrich, Germany) for 30 min in the dark. The constructs were then rinsed 5 times with distilled water before being imaged by a ZOE™ fluorescent cell imager (Bio-Rad, The Netherlands). The total area of the mineralized nodules on the surface was quantified by running the Analyze Particles command in ImageJ then normalized with respect to the area of the surface on which the nodules were observed.

## 7.5 Supplementary information

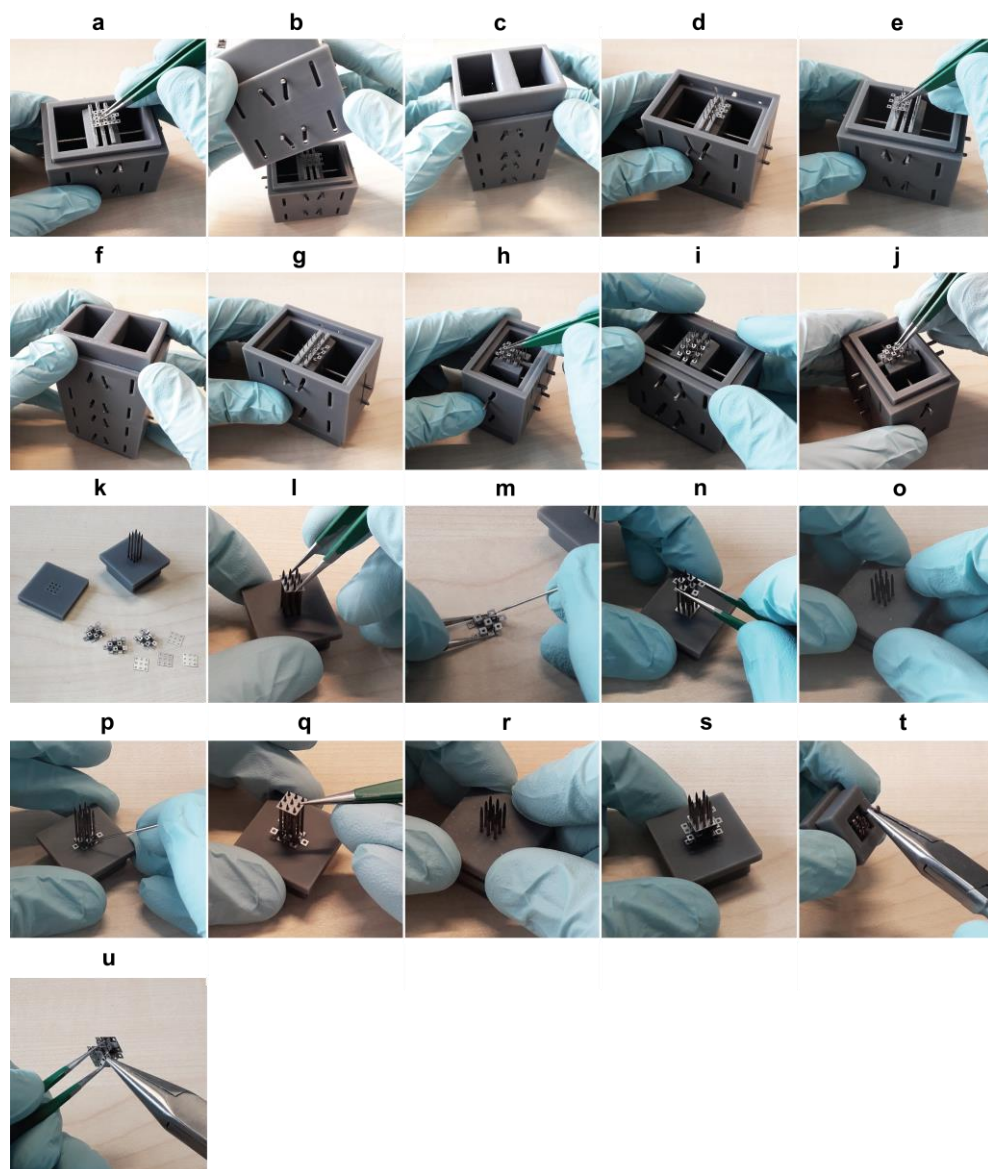


**Figure 7.6:** Folding devices for the folding of cubic lattice structures. Schematic representations and pictures of the folding devices used for the folding of cubic lattices for folding step 1 (a) and folding step 2 (b).

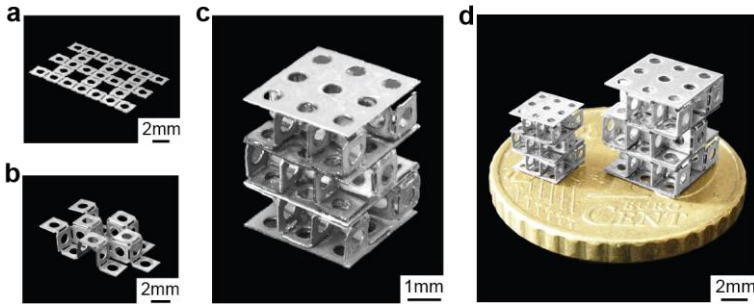




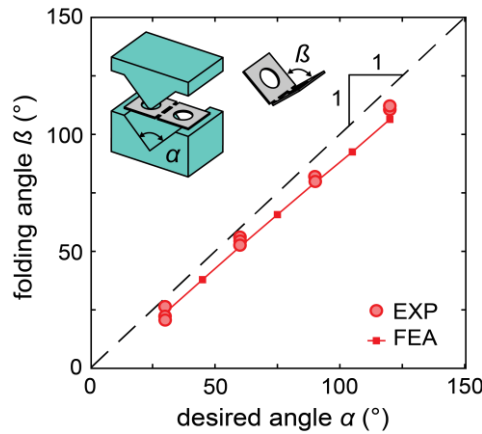
**Figure 7.7:** Folding of re-entrant structures. (a) Schematic illustration of the folding of re-entrant 'storeys'. (b) Assembly of the folded structures into a re-entrant lattice. (c) Schematic representation and pictures of the folding devices used for the folding re-entrant lattice structures. The same folding device can be used for both folding steps. The re-entrant angle  $\theta$  can be varied based on the slider displacement.



**Figure 7.8:** Pictures showing the production of cubic lattices. (a-g) The first folding step. (h-j) The second folding step. (k-t) Assembly of the folded 'storeys'. (u) Removal of the protruding panels.



**Figure 7.9:** Fabrication of cubic lattices with unit cell dimensions of 1.25 mm. (a) Initial flat titanium sheet with thickness of 50  $\mu\text{m}$ . (b) One folded 'storey'. (c) Cubic lattice of  $3 \times 3 \times 3$  unit cells. (d) Cubic lattices with different unit cell dimensions ( $w = 1.25$  mm and  $w = 2.0$  mm) are shown side by side with a ten euro cent coin for scale.



**Figure 7.10:** Elastic springback. The final folding angle as a function of the angle of the folding apparatus. The difference between desired angle  $\alpha$  and achieved folding angle  $\beta$  equals the elastic springback.

### 7.5.1. Elastic springback

The elastic springback of the titanium sheets after folding was studied both experimentally and numerically. The experiments were performed using titanium specimens with similar panel and crease line dimensions as those of the cubic lattice structures (Figure 7.2a). Punches and dies with angles  $\alpha$  of  $30^\circ$ ,  $60^\circ$ ,  $90^\circ$ , and  $120^\circ$  were fabricated from acrylic sheets using laser cutting. An optical microscope was used to measure the folding angle  $\beta$  of the folded specimens. Finite element analysis (FEA) was performed using the open-source software FEBio [47]. The punch and die were modelled as rigid materials. Four-node linear tetrahedron elements were used for the discretization of the specimen geometry. The constitutive behavior of the titanium sheets was captured using an elastoplastic material model ( $E = 36.7\text{GPa}$ ,  $\nu = 0.35$ ,  $\sigma_y = 350\text{MPa}$ , yield function: von Mises). The material model was fitted to the experimental data obtained in a previous study of ours where the same material was used (tabular input of strain

hardening data) [3]. A surface-to-surface penalty contact enforcement algorithm was implemented between the rigid punch and die and the titanium sample. The simulation of both the folding step and the release of the specimens was done using an implicit non-linear solver (full Newton method). The results of the experiments ( $n = 4$ ) and FEA simulations are presented side-by-side in Figure 7.10. The simulation results were in good agreement with the experiments. It can be observed that the amount of elastic springback is, in general, limited to around  $10^\circ$ .

### 7.5.2. Scaling lattice stiffness

Boundary effects influence the effective elastic properties of  $n \times n \times n$  cubic lattice structures, especially for the small values of  $n$ . FEA simulations were performed to find the effective elastic moduli of lattices with different numbers of unit-cells. The open-source software FEBio [47] was used. The lattices structures were discretized using four-node linear tetrahedron elements. Because only the initial stiffness was considered here, a linear elastic material model ( $E = 36.7\text{GPa}$ ,  $\nu = 0.35$ ) was used. An implicit non-linear solver (full Newton method) was employed for the simulations.

In addition, a scaling analysis was performed. For this analysis, the assumption was made that all vertical panels have an identical stiffness of  $k$ . In addition, the panels positioned at the boundaries of the specimens were assumed to have negligible stiffness as compared to the other vertical panels because these panels are only connected to one of the adjacent horizontal panels. Given these assumptions, the number of the vertical load-bearing panels of a  $n \times n$  cubic 'storey' equals  $n(n-1)$ . The stiffness  $k_n$  of a  $n \times n \times n$  cubic lattice can then be written as:

$$k_n = \frac{n(n-1)}{n} k \quad (7.1)$$

The modulus of such a lattice is given as:

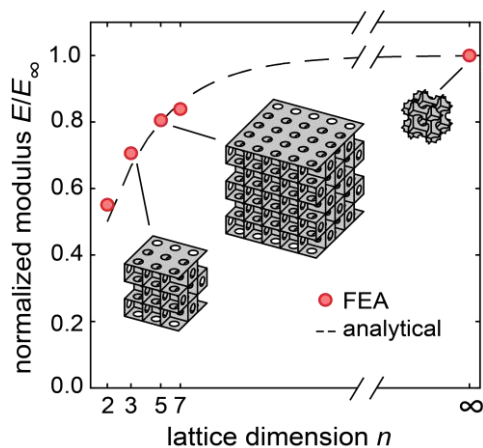
$$E_n = k_n \frac{h}{A} = \frac{n(n-1)}{n} \frac{n d}{n^2 d} k = \frac{n-1}{n} k \quad (7.2)$$

where  $h$  is the height of the total lattice,  $A$  is the cross-sectional area of the lattice structures, and  $d$  is the size of each unit-cell. Normalizing the modulus gives:

$$\frac{E_n}{E_\infty} = \frac{n-1}{n} \quad (7.3)$$

Both the results of the FEA simulations and the scaling analysis are plotted in Figure 7.11. The results of the simulations and those of the scaling analysis

generally agreed. The results indicate that the measured stiffness of the  $3 \times 3 \times 3$  cubic lattice structures is around 70% of the modulus of similar lattice structures comprising much more unit-cells.



**Figure 7.11:** The normalized lattice modulus as a function of the lattice dimension  $n$ .

## Bibliography

1. Jamal, M., et al., *Directed growth of fibroblasts into three dimensional micropatterned geometries via self-assembling scaffolds*. Biomaterials, 2010. **31**(7): p. 1683-1690.
2. Janbaz, S., et al., *Origami lattices with free-form surface ornaments*. Science advances, 2017. **3**(11): p. eaao1595.
3. van Manen, T., et al., *Kirigami-enabled self-folding origami*. Materials Today, 2020. **32**: p. 59-67.
4. Modaresifar, K., et al., *Bactericidal effects of nanopatterns: A systematic review*. Acta biomaterialia, 2019. **83**: p. 29-36.
5. Modaresifar, K., et al., *Deciphering the roles of interspace and controlled disorder in the bactericidal properties of nanopatterns against Staphylococcus aureus*. Nanomaterials, 2020. **10**(2): p. 347.
6. Dobbenga, S., L.E. Fratila-Apachitei, and A.A. Zadpoor, *Nanopattern-induced osteogenic differentiation of stem cells-A systematic review*. Acta biomaterialia, 2016. **46**: p. 3-14.
7. Zheng, X., et al., *Ultralight, ultrastiff mechanical metamaterials*. Science, 2014. **344**(6190): p. 1373-1377.
8. Berger, J., H. Wadley, and R. McMeeking, *Mechanical metamaterials at the theoretical limit of isotropic elastic stiffness*. Nature, 2017. **543**(7646): p. 533-537.
9. Tancogne-Dejean, T., et al., *3D Plate-Lattices: An Emerging Class of Low-Density Metamaterial Exhibiting Optimal Isotropic Stiffness*. Advanced Materials, 2018. **30**(45): p. 1803334.
10. Callens, S.J., et al., *Decoupling Minimal Surface Metamaterial Properties Through Multi-Material Hyperbolic Tilings*. Advanced Functional Materials, 2021: p. 2101373.
11. Montazerian, H., et al., *Permeability and mechanical properties of gradient porous PDMS scaffolds fabricated by 3D-printed sacrificial templates designed with minimal surfaces*. Acta biomaterialia, 2019. **96**: p. 149-160.
12. Callens, S.J., et al., *Substrate curvature as a cue to guide spatiotemporal cell and tissue organization*. Biomaterials, 2020. **232**: p. 119739.
13. Nan, K., et al., *Compliant and stretchable thermoelectric coils for energy harvesting in miniature flexible devices*. Science advances, 2018. **4**(11): p. eaau5849.
14. Rus, D. and M.T. Tolley, *Design, fabrication and control of origami robots*. Nature Reviews Materials, 2018. **3**(6): p. 101-112.
15. Ionov, L., *Polymeric actuators*. Langmuir, 2015. **31**(18): p. 5015-5024.
16. Liu, Y., J. Genzer, and M.D. Dickey, *"2D or not 2D": Shape-programming polymer sheets*. Progress in Polymer Science, 2016. **52**: p. 79-106.
17. van Manen, T., S. Janbaz, and A.A. Zadpoor, *Programming the shape-shifting of flat soft matter*. Materials Today, 2018. **21**(2): p. 144-163.
18. Koons, G.L., M. Diba, and A.G. Mikos, *Materials design for bone-tissue engineering*. Nature Reviews Materials, 2020. **5**(8): p. 584-603.
19. Bose, S., M. Roy, and A. Bandyopadhyay, *Recent advances in bone tissue engineering scaffolds*. Trends in biotechnology, 2012. **30**(10): p. 546-554.
20. Wu, S., et al., *Biomimetic porous scaffolds for bone tissue engineering*. Materials Science and Engineering: R: Reports, 2014. **80**: p. 1-36.
21. Huang, T.-Y., et al., *Four-dimensional micro-building blocks*. Science advances, 2020. **6**(3): p. eaav8219.
22. Spiegel, C.A., et al., *4D printing at the microscale*. Advanced Functional Materials, 2020. **30**(26): p. 1907615.
23. Hassanzadeh-Aghdam, M.K., R. Ansari, and M.J. Mahmoodi, *Thermo-mechanical properties of shape memory polymer nanocomposites reinforced by carbon nanotubes*. Mechanics of Materials, 2019. **129**: p. 80-98.
24. van Manen, T., et al., *Theoretical stiffness limits of 4D printed self-folding metamaterials*. Communications Materials, 2022. **3**(1): p. 1-12.
25. Felton, S.M., et al., *Self-folding with shape memory composites*. Soft Matter, 2013. **9**(32): p. 7688-7694.



26. Kim, S.-J., et al., *An origami-inspired, self-locking robotic arm that can be folded flat*. Science Robotics, 2018. **3**(16).
27. Mao, Y., et al., *Sequential self-folding structures by 3D printed digital shape memory polymers*. Scientific reports, 2015. **5**(1): p. 1-12.
28. Ou, J., et al. *jamSheets: thin interfaces with tunable stiffness enabled by layer jamming*. in *Proceedings of the 8th International Conference on Tangible, Embedded and Embodied Interaction*. 2014.
29. Kim, Y.-J., et al., *A novel layer jamming mechanism with tunable stiffness capability for minimally invasive surgery*. IEEE Transactions on Robotics, 2013. **29**(4): p. 1031-1042.
30. Kuder, I.K., et al., *Variable stiffness material and structural concepts for morphing applications*. Progress in Aerospace Sciences, 2013. **63**: p. 33-55.
31. Putra, N., et al., *Multi-material additive manufacturing technologies for Ti-, Mg-, and Fe-based biomaterials for bone substitution*. Acta biomaterialia, 2020. **109**: p. 1-20.
32. Burg, K.J., S. Porter, and J.F. Kellam, *Biomaterial developments for bone tissue engineering*. Biomaterials, 2000. **21**(23): p. 2347-2359.
33. Salgado, A.J., O.P. Coutinho, and R.L. Reis, *Bone tissue engineering: state of the art and future trends*. Macromolecular bioscience, 2004. **4**(8): p. 743-765.
34. Nojima, T. and K. Saito, *Development of newly designed ultra-light core structures*. JSME International Journal Series A Solid Mechanics and Material Engineering, 2006. **49**(1): p. 38-42.
35. Shantha, K., S. Thennarasu, and N. Krishnamurti, *Developments and applications of cyanoacrylate adhesives*. Journal of adhesion science and technology, 1989. **3**(1): p. 237-260.
36. de Souza Vieira, J., et al., *Bond strength evaluation of cyanoacrylate-based adhesives and screws for bone fixation*. Oral and maxillofacial surgery, 2016. **20**(2): p. 157-160.
37. Kandalam, U., et al., *Novel bone adhesives: a comparison of bond strengths in vitro*. International journal of oral and maxillofacial surgery, 2013. **42**(9): p. 1054-1059.
38. Gibson, L., *The mechanical behaviour of cancellous bone*. Journal of biomechanics, 1985. **18**(5): p. 317-328.
39. Kolken, H.M. and A. Zadpoor, *Auxetic mechanical metamaterials*. RSC advances, 2017. **7**(9): p. 5111-5129.
40. Ganjian, M., et al., *Controlled metal crumpling as an alternative to folding for the fabrication of nanopatterned meta-biomaterials*. Submitted, 2021.
41. Modaresifar, K., et al., *On the Use of Black Ti as a Bone Substituting Biomaterial: Behind the Scenes of Dual-Functionality*. Small, 2021: p. 2100706.
42. Clainche, T.L., et al., *Mechano-Bactericidal Titanium Surfaces for Bone Tissue Engineering*. ACS Applied Materials & Interfaces, 2020. **12**(43): p. 48272-48283.
43. Murphy, C.M., M.G. Haugh, and F.J. O'brien, *The effect of mean pore size on cell attachment, proliferation and migration in collagen-glycosaminoglycan scaffolds for bone tissue engineering*. Biomaterials, 2010. **31**(3): p. 461-466.
44. Hollister, S.J., *Porous scaffold design for tissue engineering*. Nature materials, 2005. **4**(7): p. 518-524.
45. Aurich, J.C., et al., *Surface quality in micro milling: Influences of spindle and cutting parameters*. CIRP Annals, 2017. **66**(1): p. 101-104.
46. Chen, N., et al., *Advances in micro milling: From tool fabrication to process outcomes*. International Journal of Machine Tools and Manufacture, 2020: p. 103670.
47. Maas, S.A., et al., *FEBio: finite elements for biomechanics*. Journal of biomechanical engineering, 2012. **134**(1).







Outlook and conclusions

8

## 8.1. Main findings

This thesis covered the fabrication of functionalized self-folding meta-materials with the aim of developing synthetic bone-substituting materials. Here, we summarize the main findings of each chapter.

In **Chapter 2**, we reviewed the different mechanisms that could be used for the programming of 2D-to-3D shape-shifting. These programming strategies are independent from the underlying molecular mechanisms of specific stimuli-responsive materials and could, therefore, be applied to a wide range of material combinations. In general, two categories of shape-shifting materials were identified: (i) programming of stress gradients through the thickness of material and (ii) the introduction of in-plane stress gradients. Stress gradients through the thickness of the material can be programmed either by varying the through-the-thickness variation of the material properties or by localized activation of the material. As a result, out-of-plane bending moments are generated upon activation. This strategy is especially suitable for the fabrication of self-rolling (*i.e.*, bending) elements. More complex geometries can be realized by combining self-rolling elements with (semi-)passive panels. Through the spatial variation of the material properties or by localized activation of a uniform material, in-plane stress gradients can be generated upon activation. Once the generated compressive stresses exceed a critical threshold, the stresses could be released through the out-of-plane buckling of the shape-shifting material. The main advantage of this programming strategy is that shapes with non-zero Gaussian curvatures (*i.e.*, doubly-curved structures) can be fabricated from initially flat sheets.

Once concern regarding the fabrication of self-folding metamaterials are the intrinsically conflicting stiffness requirements: to allow for self-folding, the folding elements need to be flexible while a high stiffness is required for the application of the metamaterial in a load-bearing structure. In **Chapter 3**, we optimized the design of bilayer self-folding elements using a combination of analytical and numerical modelling techniques. Our analysis indicates that a maximum effective stiffness of 1.5 GPa can be realized for shape-memory polymer (SMP) bilayers. For the other classes of stimuli-responsive materials, a significantly lower stiffness was found.

In **Chapter 4**, we reported on the development of a novel production technique for the fabrication of shape-shifting samples. Requiring nothing more than a hobbyist 3D printer and off-the-shelf materials, complex shape-shifting patterns were programmed through the spatial control of the orientation of SMP filaments. During the process of extrusion, individual filaments are being stretched and their deformation is stored as memory inside the structure of the material. Upon activation by heat, the programmed stresses is released. Based on the arrangement of the extruded filaments, highly complex shape-shifting patterns can be programmed. In **Chapter 4**, we demonstrated the shape-shifting of a

variety of geometries based on the programming of in-plane stress gradients as well as stress variations through the thickness of the material. In addition, heat transfer can be controlled by adjusting the porosity of the 3D printed structures, thereby enabling the programming of sequential (*i.e.*, time-dependent) shape-shifting behaviours.

The shape-shifting technique presented in **Chapter 4** only allows for the in-plane control of the filament alignment owing to the layer-by-layer manner of fabrication. The programming of 3D-to-3D shape-shifting, therefore, remains a challenge. In **Chapter 5**, we developed a method to extend the presented 4D printing technique to the programming of 3D-to-3D shape-shifting structures. A number of simple modifications to the 3D printer allowed for the printing of self-folding constructs on curved surfaces. As a demonstration of the versatility of the presented method, a cardiovascular bifurcation stent was fabricated and deployed within a dummy artery.

By combining origami and kirigami techniques, a purely mechanical method for the programming of shape-shifting was developed (**Chapter 6**). The described methodology works on the basis of (mechanically) programming of permanent and reversible deformations (upon stretching) of self-folding materials. Upon the release of the pre-stretch, the recovery of the elastic deformations drives the shape-shifting of the entire structure. The presented method could be applied to many different combinations of metallic and polymeric materials. A variety of 3D geometries, including a multi-storey lattice, were fabricated from initially flat materials. As a proof-of-concept, different types of surface functionalities, including flexible electronics, were incorporated into the structure of material.

In **Chapter 7**, we described the development of an automated folding method inspired by sheet metal forming techniques. Folding devices were designed to clamp and fold an initially flat metal sheet. Specific folding patterns were selected that enabled the folding to be decoupled in multiple distinct steps. Owing to this decoupling, the folding of large arrays of interconnecting unit-cells was realized. In addition, the presented folding technique enables the realization of sharp folds within thick sheets which results in a high stiffness of the folded lattice. An effective stiffness of  $\approx 0.5$  GPa was achieved for cubic lattices folded from titanium sheets. Finally, lattices with embedded surface nano-patterns were fabricated and cell culture experiments were performed to demonstrate the potential of the functionalized metamaterials to be used as a synthetic bone-substituting material.

## 8.2. General discussion

The development of several different shape-shifting techniques was described in this thesis. In general, each technique has its specific advantages and disadvantages as compared with other self-folding methods. Here, we discuss the

three reported shape-shifting techniques in relation to the formulated research objectives.

### 8.2.1. 4D printing (Chapters 4 and 5)

The main advantage of using additive manufacturing techniques for the programming of shape-shifting structures is the flexibility it affords regarding the design of the to-be-printed construct. The developed 4D printing technique allows for the programming of a large variety of geometries within a single production step. Complex patterns of both in-plane and through-the-thickness stress gradients could be programmed in the structure of the as-printed construct (**objective I**).

The presented 4D printed specimens were fabricated from poly-lactic acid (PLA) that is a widely used 3D printing filament. PLA is considered to be both biocompatible and biodegradable and is, therefore, a suitable material for biomedical applications [1, 2]. For some biomedical applications, however, the self-folding material needs to be activated inside the human body and the allowed activation temperatures are limited. Examples are drug delivery systems or miniaturized biopsy devices [3-5]. Because the underlying programming mechanism remains valid regardless of the type of the SMP material, the presented 4D printing technique is not limited to the use of PLA (**objective II**). For specific applications, therefore, SMPs triggered by lower temperatures may be a better alternative [6]. For the production of functionalized bio-scaffolds, however, the activation occurs outside the human body and high activation temperature are not a limitation.

The theoretical stiffness analysis (Chapter 3) indicates that the highest stiffness can be realized using SMP self-folding elements. Following this analysis, the presented 4D printing method should be able to fabricate self-folding lattices with a stiffness up to 1.5 GPa (**objective IV**). Depending on the site of the bone defect, bone scaffolds with a stiffness of 1.5 GPa could closely match the mechanical properties of the surrounding bony tissue [7, 8]. 4D printing of SMP self-folding structures is, therefore, a promising route towards the fabrication of synthetic bone substituting materials.

### 8.2.2. Mechanically activated self-folding (Chapter 6)

The presented mechanically activated shape-shifting technique utilized specific kirigami patterns to enable the large and permanent deformations of the specimens upon stretching. When combined with a layer of elastic material, mechanically activated self-folding elements could be fabricated. The main advantage of this approach is that it could be applied to a wide range of both materials, including both metals and polymers (**objective II**). Depending on the application and the desired surface-related features, a specific combination of

materials can be selected. In this case, using a polydimethylsiloxane (PDMS) elastic layer allowed for the incorporation of micro-patterns as well as flexible electronics in the self-folding specimens. The integration of other functionalities, such as microfluidic devices would be possible as well [9].

We also demonstrated the production of multi-storey structures made of multiple cubic unit-cells (**objective III**). Samples were fabricated with unit-cell dimensions in the range of 3.0-5.0 mm. Because of the mechanical nature of the shape-shifting strategy, the presented method is highly scalable. It is, therefore, possible, at least in principle, to fabricate lattices comprising arrays of smaller unit-cells.

One of the limitations of the mechanical folding techniques presented in this thesis is that the range of the achievable geometries is limited to the folding of rigid panels connected by self-folding elements (**objective I**). Because self-folding needs to be activated by globally applied forces, the range of 3D geometries is further constrained. In addition, the flexibility in programming different folding angles in a series of self-folding hinges is restricted by the mechanical behaviour of the individual bending elements. Another limitation of the presented self-folding method is the stiffness of the folded constructs (**objective IV**). The introduction of cuts in the initial flat material is required for the realization of large permanent deformation. These cuts also highly reduces the effective stiffness of the resulting metamaterial [10].

### 8.2.3. Mechanically supported folding (Chapter 7)

The use of external folding devices for the folding of lattice structures enabled the introduction of sharp folds in initially flat sheets. In addition to the optimization of self-folding bilayer elements (Chapter 3), the presented approach offers another strategy for the fabrication of stiff lattice structures (**objective IV**). Mechanical properties in the same range of the cancellous bone were realized [11, 12]. Combined with the ability to embed surface features onto the initially flat material, the presented folding method could serve as a platform for the fabrication of functionalized metamaterials.

The described approach could be applied to a wide range of materials (**objective II**). The applied deformation is highly localized and large amounts of strain are experienced by the material at the folding lines. Therefore, the thickness of the flat sheets needs to be carefully adjusted dependent on the mechanical properties of the selected material in order to not exceed the failure strain.

In terms of the achievable folding geometries, this approach is restricted to the folding patterns that are both rigid-foldable and allow for the decoupling of the folding pattern in distinct steps (**objective I**). Decoupling of the folding pattern,

however, enabled the fabrication of large arrays of unit-cells (**objective III**). The number of unit-cells is, in principle, only limited by the width of the folding device. The presented folding technique could, therefore, be used for the mass production of metamaterials comprising arrays with a large number of unit-cells.

#### 8.2.4 Broader perspective

In general three different approaches for the production of 3D porous materials from decorated flat materials have been presented in the literature. In this thesis, only folding as a route towards the production of functionalized metamaterials has been presented. One of the alternative approaches is the (self-)assembly of flat panels into 3D constructs [13-15]. Usually capillary forces are utilized to assemble rigid panels into polyhedral blocks [13, 16, 17]. Upon release of the panels from a substrate, the surface tension of applied liquid droplets at the interface of these panels drives the assembly into 3D building blocks. This approach is especially applicable at small length-scale (*i.e.*, nano- and microscale) as capillary forces scale with length contrary to elastic force that scale with area or inertia forces that scale with volume [16]. Self-assembly using capillary forces is, however, limited to the folding of single unit-cells and further assembly steps will be required for the fabrication of lattice structures comprising multiple unit-cells [18].

Crumpling of flat sheets into 3D porous construct is the third approach for the fabrication of functionalized metamaterials. In contrast to the well-controlled folding procedures, crumpling is a much more random process. Several attempts have been made to establish the relationships between the geometry and mechanical of the initial flat materials and the resulting properties of the crumpled matter [19-21]. The main advantages of crumpling-based metamaterials is the relative ease of fabrication. A similar pattern protection method to the approach presented in Chapter 7 could be applied to the crumpling of functionalized flat sheets. Indeed, the crumpling of patterned flat materials into 3D meta-biomaterials has been demonstrated [22]. However, compared with folding structural integrity is lacking and the realization of spatially controlled properties in the 3D metamaterial is much more challenging.

### 8.3. Future research directions

The research presented in this thesis contributed to the development of self-folding materials to be applied as meta-biomaterials. However, many opportunities and challenges remain unexplored regarding the application of the presented techniques in clinical settings. Here, we present several opportunities for future research that might contribute to the understanding and application of self-folding meta-biomaterials.

### 8.3.1. Stiffness of self-folding materials

The analysis on the theoretical stiffness limits of self-folding metamaterials primarily focussed on the stiffness of individual self-folding elements. In general, the effective stiffness of self-folding meta-biomaterials depends both on the arrangement of the folding elements and the stiffness of the constituting bending elements. In this regard, it would be interesting to generalize the presented results to different self-folding geometries.

Another limitation of the stiffness analysis is that the results were derived using 2D plane strain models. Therefore, the curvature along the width direction of the bilayer elements was disregarded. In practice, however, the development of a doubly curved shape is expected under certain conditions [23, 24], which could enhance the stiffness of the curved bilayer element. The development of more sophisticated models would allow to study the effects of double-curvature on the bending behaviour and stiffness of bilayer self-folding elements.

### 8.3.2. 4D printing

The main challenge for the application of the 4D printing of shape-memory polymer filaments is the miniaturization of the presented techniques. To fabricate self-folding metamaterials with unit-cell dimensions  $<2.0$  mm, nozzle diameters well below 0.1 mm are required. Future developments towards that direction are, therefore, needed.

Another challenge regarding the production of self-folding metamaterials is the limited stiffness of the SMP during the process of activation. The actuation force of the shape-shifting elements dramatically drops when the temperature exceeds the glass transition temperature. As a result, the activated specimens may be distorted due to the presence of relatively small forces, such as gravity or other external factors. Advanced computational modelling techniques as well as extensive experimentation should be employed to optimize the process of 4D printing of large arrays of small interconnecting unit-cells and to minimize the effects of such forcers.

A good understanding of the thermomechanical processes experienced by the extruded filaments is also essential for the further development of similar 4D printing techniques. The amount of programmed strain is dependent both on the extrusion parameters and the heating/cooling history of the filaments (Chapter 5). Sophisticated thermomechanical modelling techniques need to be employed in order to better understand how exactly the methods proposed in this thesis work. The availability of such model could, for example, be used to optimize the printing path and to minimize the effects of the heating and cooling cycles on the amount of programmed strain.



Finally, the distortion of embedded surface-related functionalities may arise as a result of (small) deformations of the (semi-)passive panels during the process of activation. The effects of panel deformation on the surface features should, therefore, be investigated. The shrinkage of panels, however, could be employed as well for further miniaturization of the unit-cell dimensions as well as for the creation of embedded nanostructures [25].

### 8.3.3. Mechanically activated self-folding

Mechanical self-folding techniques offer several advantages over shape-shifting materials made from stimuli-responsive materials. First of all, they could be applied to a wide range of materials. However, the mechanical response of different materials as well as the different designs of the kirigami elements highly affect the shape-shifting behaviour of the resulting constructs. Computational modelling should, therefore, be employed to optimize the design of the constructs such that the best possible shape-shifting behaviour for each combinations of materials is achieved.

The second advantage of a mechanical shape-shifting approach is that, depending on the desired surface-related functionalities, a specific substrate material can be selected. Here, we used a polydimethylsiloxane (PDMS) substrate embedded with micro-patterns as well as flexible electronics. A combination of electronics and surface nanopatterning can be used for the fabrication of multi-functional smart implants that are capable of both sensing [26] and guiding the formation of tissues. Similar functionalities may be applied in on-demand drug delivery systems [27]. The fabrication and demonstration of such a sophisticated device would be an interesting research direction.

### 8.3.4. Mechanical supported folding

First of all, several opportunities exist for the improvement of the folding technique presented in Chapter 7. One direction for future research would be the optimization of the design of the crease lines in order to enhance the stiffness of the folded lattice structures. Both computational and experimental methods could be employed towards that purpose. Other research directions are the further miniaturization of the folded metamaterials as well as the introduction of anisotropy to better mimic the mechanical properties of the surrounding bony tissue.

Secondly, the presented folding technique could serve as a platform for cell culture experiments. This opens up the opportunity to study the biological response to a variety of surface-related functionalities in a 3D environment. Extensive *in vivo* and *in vitro* experiments need to be performed to optimize the scaffold design as well as to investigate the interplay between the scaffold geometry, surface topography, and tissue formation.

## 8.5 Concluding remarks

This thesis described the development of several shape-shifting techniques. The mechanically supported folding technique is the most successful in achieving the formulated requirements for synthetic bone-substituting materials. Although further optimization of the scaffold design as well as folding devices is required, the proposed folding method enables extensive biological testing of nanopatterns in a 3D environment.

Finally recurring to the aim of this thesis: indeed, a platform for the fabrication of stiff functionalized metamaterials comprising large arrays of small unit-cells has been developed. The proposed folding methods could serve as a starting point for extensive biological testing.

## Bibliography

1. Bergstroem, J.S. and D. Hayman, *An overview of mechanical properties and material modeling of polylactide (PLA) for medical applications*. Annals of biomedical engineering, 2016. **44**(2): p. 330-340.
2. Hamad, K., et al., *Properties and medical applications of polylactic acid: A review*. Express Polymer Letters, 2015. **9**(5).
3. Azam, A., et al., *Self-folding micropatterned polymeric containers*. Biomedical microdevices, 2011. **13**(1): p. 51-58.
4. Randall, C.L., E. Gultepe, and D.H. Gracias, *Self-folding devices and materials for biomedical applications*. Trends in biotechnology, 2012. **30**(3): p. 138-146.
5. Cianchetti, M., et al., *Biomedical applications of soft robotics*. Nature Reviews Materials, 2018. **3**(6): p. 143-153.
6. Meng, Y., J. Jiang, and M. Anthamatten, *Body temperature triggered shape-memory polymers with high elastic energy storage capacity*. Journal of Polymer Science Part B: Polymer Physics, 2016. **54**(14): p. 1397-1404.
7. Lin, C.Y., N. Kikuchi, and S.J. Hollister, *A novel method for biomaterial scaffold internal architecture design to match bone elastic properties with desired porosity*. Journal of biomechanics, 2004. **37**(5): p. 623-636.
8. Maggi, A., H. Li, and J.R. Greer, *Three-dimensional nano-architected scaffolds with tunable stiffness for efficient bone tissue growth*. Acta biomaterialia, 2017. **63**: p. 294-305.
9. Jamal, M., A.M. Zarafshar, and D.H. Gracias, *Differentially photo-crosslinked polymers enable self-assembling microfluidics*. Nature communications, 2011. **2**(1): p. 1-6.
10. Shyu, T.C., et al., *A kirigami approach to engineering elasticity in nanocomposites through patterned defects*. Nature materials, 2015. **14**(8): p. 785-789.
11. Bose, S., M. Roy, and A. Bandyopadhyay, *Recent advances in bone tissue engineering scaffolds*. Trends in biotechnology, 2012. **30**(10): p. 546-554.
12. Wu, S., et al., *Biomimetic porous scaffolds for bone tissue engineering*. Materials Science and Engineering: R: Reports, 2014. **80**: p. 1-36.
13. Gracias, D.H., et al., *Fabrication of Micrometer-Scale, Patterned Polyhedra by Self-Assembly*. Advanced Materials, 2002. **14**(3): p. 235-238.
14. Cho, J.-H., et al., *Nanoscale origami for 3D optics*. Small, 2011. **7**(14): p. 1943-1948.
15. Randall, C.L., et al., *Three-dimensional microwell arrays for cell culture*. Lab on a Chip, 2011. **11**(1): p. 127-131.
16. Kwok, K.S., et al., *Self-Folding Using Capillary Forces*. Advanced Materials Interfaces, 2020. **7**(5): p. 1901677.
17. Kuribayashi-Shigetomi, K., H. Onoe, and S. Takeuchi, *Cell origami: self-folding of three-dimensional cell-laden microstructures driven by cell traction force*. PloS one, 2012. **7**(12): p. e51085.
18. Randhawa, J.S., et al., *Importance of surface patterns for defect mitigation in three-dimensional self-assembly*. Langmuir, 2010. **26**(15): p. 12534-12539.
19. Mirzaali, M., et al., *Crumpling-based soft metamaterials: the effects of sheet pore size and porosity*. Scientific reports, 2017. **7**(1): p. 1-7.
20. Fokker, M., S. Janbaz, and A. Zadpoor, *Crumpling of thin sheets as a basis for creating mechanical metamaterials*. RSC advances, 2019. **9**(9): p. 5174-5188.
21. Habibi, M., M. Adda-Bedia, and D. Bonn, *Effect of the material properties on the crumpling of a thin sheet*. Soft matter, 2017. **13**(22): p. 4029-4034.
22. Ganjian, M., et al., *Controlled metal crumpling as an alternative to folding for the fabrication of nanopatterned meta-biomaterials*. Materials & Design, 2022. **220**: p. 110844.
23. Mirzaali, M.J., et al., *Curvature Induced by Deflection in Thick Meta-Plates*. Advanced Materials: p. 2008082.
24. Alben, S., B. Balakrishnan, and E. Smela, *Edge effects determine the direction of bilayer bending*. Nano letters, 2011. **11**(6): p. 2280-2285.
25. Bauer, J., et al., *Approaching theoretical strength in glassy carbon nanolattices*. Nature materials, 2016. **15**(4): p. 438-443.
26. Han, M., et al., *Three-dimensional piezoelectric polymer microsystems for vibrational energy harvesting, robotic interfaces and biomedical implants*. Nature Electronics, 2019. **2**(1): p. 26-35.

27. Fernandes, R. and D.H. Gracias, *Self-folding polymeric containers for encapsulation and delivery of drugs*. Advanced drug delivery reviews, 2012. **64**(14): p. 1579-1589.



# Acknowledgement

Writing these final pages of my thesis means that the work of the last couple of years has come to an end. The moment I sat down to write this pages I realized that finishing my thesis marks the end of an even longer period. For more than a decade the TU Delft has been part of my life. Back in 2010 I started with the bachelor program Mechanical Engineering. And now, twelve years later, I am about to finish my PhD. A lot has happened during that period.

In 2015 I stepped into the office of **Amir** for the first time. I still remember you showed me some videos of colourful samples that changed their shape once emerged in a hot water bath. That is how I came across the topic of this thesis for the first time. Your enthusiasm was infectious and soon I started my master thesis on exactly this subject. Later on you offered me a PhD position to continue this research for another four years. Amir, I would like to thank you for your support during these years. I really appreciate the responsibilities and freedom that you gave me to find my own way into this large and complicated subject. At the same time you were always there to provide guidance, to discuss the research or just to have a chat.

This journey wouldn't have been the same without my office-mate, colleague and friend **Shahram**. From the moment that I started my master thesis project till the last year of my PhD we shared the same office. I really enjoyed our daily discussions on science but especially our numerous coffee breaks. A few months before the end of my PhD you accepted another position at a different university. During these last couple of months I fully realized how important it is to have a colleague like you. Thank you!

My research topic was part of a broader project together with **Françoise, Khashayar, Mahya** and **Sebastien**. We started our PhD within the same year. If I look back it's amazing to see how we all found our own way into this topic. Thank you all for your support and kindness.

At the beginning of the covid lockdowns some great initiatives emerged from our faculty. Within our lab we decided to develop an emergency ventilator for covid patients. It was truly amazing to see how much can be achieved with an enthusiastic team in such a supportive environment. Although we may have been a bit naïve in underestimating the amount of regulations involved, we were able to build a working prototype within a matter of weeks. Thank you **Amir, Mauricio, Mohammad, Pier, Sander, Sebastien** and **Yageng** for the enthusiasm and energy you all brought into this project.

I would also like to thank **Angelique, Eline, Fabian, Gerwin, Helda, Iulian, Ingmar, Jiahui, Jie, Juan, Lidy, Mahdiyeh, Marike, Marjolijn, Michelle, Nazli, Niko, Paul, Pedro, Sabrina** and all my colleagues of our department. Thank you for all the moments that we share together over the past five years.

Here, I would also like to express my gratitude to my lovely wife **Janneke**. For us personally the last couple of years have been a great time as well. We married before the start of my PhD project and both of our children were born during the past years. Thank you for your love and support.

I would like to conclude by citing a verse from Scripture. In some universities it is common to start official ceremonies with exactly these words. Words that express a trust and dependence in God. Words that also deeply resonate with me:

*Our help is in the name of the Lord, the Maker of heaven and earth.*

Psalm 124:8







# Publications

**T. van Manen**, S. Janbaz & A.A. Zadpoor. (2017). *Programming 2D/3D shape-shifting with hobbyist 3D printers*. Materials horizons, **4**(6): p. 1064-1069.

**T. van Manen**, S. Janbaz & A.A. Zadpoor. (2018). *Programming the shape-shifting of flat soft matter*. Materials Today, **21**(2): p. 144-163.

S. Janbaz, K. Narooei, **T. van Manen** & A.A. Zadpoor. (2020). *Strain rate-dependent mechanical metamaterials*. Science advances, **6**(25): eaba0616.

**T. van Manen**, S. Janbaz, M. Ganjian, & A.A. Zadpoor. (2020). *Kirigami-enabled self-folding origami*. Materials Today, **32**: p. 59-67.

F.S.L. Bobbert, S. Janbaz, **T. van Manen**, Y. Li & A.A. Zadpoor. (2020). *Russian doll deployable meta-implants: Fusion of kirigami, origami, and multi-stability*. Materials & Design, **191**: 108624.

**T. van Manen**, S. Janbaz, K. M. B. Jansen & A.A. Zadpoor. (2021). *4D printing of reconfigurable metamaterials and devices*. Communications Materials, **2**: 56.

M. Ganjian, S. Janbaz, **T. van Manen**, N. Tümer, K. Modaresifar, M. Minneboo & A.A. Zadpoor (2022). *Controlled metal crumpling as an alternative to folding for the fabrication of nanopatterned meta-biomaterials*. Materials & Design, **220**: 110844.

**T. van Manen**, V.M. Dehabadi, M. C. Saldívar, M.J. Mirzaali & A.A. Zadpoor (2022). *Theoretical stiffness limits of 4D printed self-folding metamaterials*. Communications Materials, **3**: 43.

S. Janbaz, D. Fan, M. Ganjian, **T. van Manen**, U. Staufer & A.A. Zadpoor (2022). *3D printable strain rate-dependent machine-matter* (Submitted).

**T. van Manen**, M. Ganjian, K. Modaresifar, L.E. Fratila-Apachitei & A.A. Zadpoor (2022). *Automated folding of origami lattices: from nanopatterned sheets to stiff meta-biomaterial*. Small (Accepted).

V.M. Dehababi, E. Yarali, A. Ghalayaniesfahani, S.J.P. Callens, **T. van Manen**, A. Accardo, S. Ghodrat, J. Bico, M. Habibi, M.J. Mirzaali & A.A. Zadpoor (2022). *Curvature tuning through defect-based 4D printing* (Submitted).